Optical and non-equilibrium properties of graphene

PhD thesis

by

Ulf Briskot

15.10.2015

Instructor: Prof. Dr. Alexander D. Mirlin

Optische und Nichtgleichgewichtseigenschaften von Graphen

Zur Erlangung des akademischen Grades eines

DOKTORS DER NATURWISSENSCHAFTEN

von der Fakultät für Physik
des Karlsruher Instituts für Technologie

genehmigte

DISSERTATION

von

Dipl. Phys. Ulf Briskot
aus Köln

To my family.

Introduction

A decade has passed since the discovery of graphene [1]. Since then, it has stimulated active research in condensed matter and material science and triggered numerous discoveries [2, 3]. However it still gives rise to open questions from a very broad spectrum. Among those are very fundamental ones in the context of the quantum field-theoretical description of many-particle systems as well as application oriented problems regarding the fabrication of actual devices and the description of transport and optical properties of these systems.

Graphene properties sometimes read like a list of superlatives. First of all being a single-atom-thick layer of carbon atoms it is the first truly two-dimensional material. It occurs naturally in graphite which consists of multiple layers of carbon atoms. Within each layer the sp_2 hybridized carbon atoms arrange in a honeycomb lattice. Graphene was first synthesized using an exfoliation technique with adhesive tape on graphite to isolate a single layer of carbon atoms that we now call graphene.[1] It is also the strongest known material on earth. Measurements of the Young's modulus yield a value of $1\,$TPa [4]. Furthermore it shows exceptional heat conductivity as well as remarkable electronic transport properties [5–7]. More specifically, the mobilities in graphene are of the order $\sim 2 \times 10^5\,\mathrm{cm}^2/\mathrm{Vs}$ [3]. In suspended graphene, mobilities of even $\sim 10^6\,\mathrm{cm}^2/\mathrm{Vs}$ have been measured [8]. Here suspended means that graphene is placed on a scaffold formed by the contact electrodes for example. If graphene is placed on a gate the carrier density can be tuned down to very small values for a semimetal [1].

The pristine graphene exhibits a gapless band structure which renders it a semimetal. Remarkably the band structure is not only gapless. At the nodal points, where the conduction and valence band touch, the energy dispersion becomes linear in the momentum signifying the emergence of massless quasiparticles. More specifically, the low energy excitations of graphene are massless Dirac fermions. The latter fact has been found theoretically even before the actual synthesis of graphene [9, 10]. Graphene is therefore an experimental test ground for quasirelativistic physics. The Dirac nature is also responsible for an unconventional quantum Hall effect that persists even up to room temperatures [11]. This unconventional Hall effect serves as a clear evidence for Dirac fermions.

Moreover, graphene does not only host Dirac fermions. Since they are intrinsically interacting, it is considered a condensed matter realization of two-dimensional quantum electrodynamics. However the massless Dirac carriers do not move with the speed of light c which is the characteristic velocity of the electromagnetic field but rather with the Fermi velocity $v_F \sim c/300$. Therefore the interaction can be regarded instantaneous. Due to the ratio $v_F/c \sim 1/300$ the dimensionless coupling constant α_g of the electron-electron interaction in graphene is correspondingly $\alpha_g \sim 2.2$ for suspended graphene instead of the well-known value of $\alpha_{\mathrm{QED}} \sim 1/137$ for the high energy quantum electrodynamics. It becomes clear that the study of interaction in graphene is not only interesting it is even necessary to include interactions.

First of all, suspended graphene is genuinely strongly correlated. Moreover it exhibits a quantum critical point. The critical point is situated between the electron-doped and the hole-doped Fermi liquid. Both phases are separated by the critical region for finite temperatures. In this critical region

---

[1] Ironically, in contrast to graphene adhesive tape is in fact roughly hundred years old. Graphite is known to mankind far beyond that.

the system is described by a relativistic Dirac liquid and the low-frequency response is determined by relativistic hydrodynamics. Correspondingly graphene is exactly at criticality at zero temperature and half filling, i.e. when the chemical potential is situated exactly at the Dirac points where the conduction and valence band touch. In this case the system is charge neutral. In the quantum critical regime the relaxation rates in graphene deviate from the Fermi liquid expectation. Although we emphasized that the suspended graphene is apparently strongly interacting, the weak coupling analysis seems to explain all experimental data so far even for the suspended graphene.

In other experimental realizations the dielectric screening of a substrate can lead to a weak Coulomb interaction with $\alpha_g < 1$. However, instantaneous Coulomb interaction can affect transport properties at the Dirac point significantly. In particular in the regime of high temperatures and in clean samples. The high-temperature regime is certainly realized in experiments under strong driving [12]. Here Coulomb interaction will eventually dominate over disorder and phonon processes. On the other hand interaction induced scattering rates will limit the transport characteristics of very clean samples and therefore pose limits on the intrinsic properties of graphene. The latter fact is also important to understand limitations for possible devices in optical and optoelectronic applications.

In the context of optical experiments the interaction is not merely a limiting factor. It is also the fastest scattering mechanism determining the equilibration of optically excited carriers in graphene. More specifically, it is responsible for the thermalization of high energy electrons as they are created in time resolved pump-probe measurements. The understanding of the short-time dynamics is mandatory for applications of graphene in laser physics and photovoltaics. As an example graphene has already been used in mode-locked lasers as a saturable absorber [13]. The relaxation dynamics of electrons in particular in the presence of high-energy photons is a genuine non-equilibrium situation. A theoretical description of this non-equilibrium needs to describe the evolution of the microscopic degrees of freedom and the effect of interactions on the microscopic population. Recently there has also been an increasing interest in post-quench dynamics of systems driven out of equilibrium by a sudden quench in system parameters. This sudden change can be realized in optical lattices where specific parameters of the Hamiltonian describing the particles in the lattice can be tuned by modifying the confining traps. However the laser excitation in pump-probe measurements, where graphene is excited by a pump pulse, can also be considered a sudden quench of the system. In particular systems close to critical points are expected to give nontrivial relaxation dynamics [14]. All these topics need to take into account interactions in the evolution of microscopic quantities.

On the other hand we mentioned high field experiments as reported in Ref. [12]. In order to understand such experiments taking into account finite size effects and electrostatic surroundings it is advantageous to develop an effective macroscopic description that does not rely on the microscopic details as it is unavoidable for optical frequencies. Still this effective description needs to take into account scattering properly. In order to do so one starts from a microscopic description as one would employ for the pump-probe setup and has to develop an effective non-equilibrium description for large length scales. Graphene in the interaction-dominated regime enables such an effective hydrodynamic description on large length scales. The emerging hydrodynamics is controlled by electron-electron interaction and moreover is given by relativistic hydrodynamics as was pointed out in pioneering works by Sachdev and Müller [15] (see also Ref. [16]).

These two regimes of non-equilibrium phenomena in graphene, the microscopic description for optical experiments and the effective collision-dominated hydrodynamics for graphene are the main topics of this thesis. In both cases we will in particular be concerned with the relaxation dynamics due to electron-electron interactions. In the microscopic theory for pump-probe measurements in graphene

we will study the relaxation of high energy electrons in phase space. The microscopic analysis in the presence of interaction is motivated by a number of pump-probe experiments performed in recent years. Within the hydrodynamic theory we study the relaxation of a macroscopic perturbation in the energy density, i.e. a hot spot, in real space. While the microscopic theory is suitable for high frequencies and short pulses the hydrodynamics deals with low-frequency perturbations.

Pump-probe experiments on graphene started with the early works by Dawlaty et al [17] and Sun et al [18]. In general, optical pump-probe measurements are a versatile tool to study short-time dynamics of physical systems. The system is initially driven out of equilibrium by the pump laser. Subsequently the probe yields a snapshot of the system's state and allows experiments to track the evolution of chemical reactions and relaxation of solid state systems. Developments and improvements over the last years in mode-locked lasers for example have led to temporal resolution in the femtosecond regime. In this regard, free-electron lasers certainly hold the record of the shortest pulse duration since they achieve attosecond pulse lengths. Semiconductors have been studied by means of optical pump-probe measurements before the above mentioned works reported in Refs [17, 18].

The early stage of the temporal evolution that is initialized by the excitation of the system by the pulse is characterized by a coherent evolution of the microscopic polarization and population. Within this first regime there is no mixing of different momentum states [19, 20]. With the achievement of femtosecond time resolution the coherent regime becomes accessible by experiments. Subsequently the fastest scattering mechanism leads to a redistribution of the population and finally to the thermalization of graphene electrons.

The theoretical description of these processes is largely based on numerical methods to simulate the coherent dynamics of populations and polarizations as well as the decay and thermalization due to different scattering mechanisms like electron-electron interaction and phonons [21]. These numerical simulations are usually based on the optical semiconductor Bloch equations [20] including various different stages of approximations. In Ref. [22] it was theoretically predicted that electron-electron interaction in graphene leads to the fast redistribution of electrons in momentum space on the time scale of 250 fs. After this interaction-dominated regime phonons cool the system on a picosecond time scale.

Following active experimental [21, 23–26] and theoretical work [22, 27–29] in the field of pump-probe spectroscopy on graphene another aspect of interaction in the relaxation dynamics was uncovered in Ref. [30]. It was found that optical excited electrons in graphene relax towards lower energies in a cascade with on average constant step size determined by the equilibrium parameters of the graphene. A first theoretical zero temperature analysis of the cascade was performed in Ref. [31]. The cascade emerges due to Coulomb interaction with only little influence of phonons [30, 31].

In view of these experimental and theoretical findings this thesis will study the relaxation dynamics of high-energy electrons as they are created in optical pump-probe measurements. First of all the characteristics of the relaxation cascade due to electron-electron interaction needs to be studied beyond the zero temperature analysis. Moreover, the relaxation cascade can be reformulated as a random walk. However this description necessitates a detailed analysis of the statistics of the relaxation process. While Ref. [31] was primarily concerned with the average step size in the cascade this work presents a detailed statistical description. This includes the specific distribution of the step sizes in the cascade. The central question this thesis is going to address in the context of pump-probe measurements is whether the relaxation cascade of high-energy electrons in graphene can be understood in terms of a diffusive motion in energy space. More specifically, what are the characteristics of this diffusive motion deriving from the microscopics of the Coulomb interaction in graphene. Moreover, how do the diffusive

parameters change with temperature. To answer these questions we are going to develop an analytical model for the microscopic evolution of photoexcited high-energy electrons in graphene including relaxation due to electron-electron interaction.

The second main topic of this thesis is the emergent hydrodynamics in graphene due to Coulomb scattering. On the one hand the hydrodynamic theory in graphene is an effective description for transport, in particular nonlinear transport. Furthermore, it represents a macroscopic description of relaxation processes whenever the system is driven out of global equilibrium. From another perspective, graphene can serve as a test ground for relativistic hydrodynamics.

Testing hydrodynamics also became feasible not only due to increasing device quality but also due to the implementation of experimental techniques to locally map the charge densities. For example the scanning near-field microscopy (SNOM) enables the measurement of optical near-fields. Here an AFM tip is used as an antenna to convert optical near fields that are a measure of the local charge density into far-fields that can be detected using standard optical techniques. The SNOM technique in particular found applications in the study of plasmons in graphene [32, 33]. In fact graphene promises to be an excellent platform for plasmonics [34]. Plasmons, the collective excitations of coupled electromagnetic fields and density fluctuations are very long-lived in graphene and tunable [32–36]. In view of the description of nonlinear transport, high-field experiments like the one reported in Ref. [12] naturally entail very high temperatures. In Ref. [12] electronic temperatures up to 1200 K have been measured. In this high-temperature regime interactions become the dominant scattering mechanism. The hydrodynamic description can serve as an effective theory in this regime.

Hydrodynamic transport simulations have been applied to semiconductor field-effect transistors [37] explaining for example current saturation due to channel depletion. It is therefore interesting to develop an equivalent theory for graphene. Previous theoretical approaches have often employed phenomenological hydrodynamic models [38–40] or considered the dissipationless limit [41].

Within linear response the hydrodynamic theory has been developed from the Boltzmann equation in Ref. [42]. This thesis pursues a similar approach deriving the nonlinear hydrodynamics in the collision-dominated regime from the microscopic kinetic equation. In the context of the hydrodynamic description of transport in graphene this thesis addresses a description of the low-frequency optical response by hydrodynamics. More specifically this work investigates the influence of interaction-limited transport coefficients as for example the viscosity in the nonlocal optical response.

Moreover, we study the relaxation of graphene driven out of equilibrium. We investigate the relaxation of a hot spot. Such a hot spot might occur after excitation by a laser pulse. Therefore the relaxation dynamics in the hydrodynamic regime represent a natural extension of our study of relaxation processes in graphene after laser excitation. Whereas the first part is concerned with the relaxation in phase space for ultra short pulses, the hydrodynamics describes the relaxation in real space. Such systems far away from global equilibrium have also been studied theoretically in one-dimensional systems [43, 44].

Structure of the thesis

The structure of the thesis is the following:

In **Chapter 1** we give a brief introduction to the properties of graphene that are relevant for our theoretical studies. In particular we describe the field theoretical description of its electronic properties. We emphasize the relevance of the Coulomb interaction. Furthermore we discuss the peculiarities of the electron-electron interaction in graphene. Finally we discuss the notion of criticality in graphene

and review the Wilson renormalization group (RG) calculation for the Coulomb interaction.

The **Chapter 2** summarizes some of the results on the linear transport properties of graphene. Here the linear response transport is conveniently calculated in the Kubo formalism. Interestingly, graphene exhibits universal values of conductivity in different regimes of frequencies. We also explain the connection between the optical conductivity and optical transmission. The latter is a relevant observable in pump-probe measurements. We close the discussion of the linear transport in graphene within the Kubo formalism with a review on our results for the linear magnetotransport including disorder.

While Chapt. 2 was devoted to the computation of the linear conductivity in the Kubo formalism we develop the kinetic equation for graphene in **Chapter 3**. The latter is more convenient to describe interaction effects and in particular non-equilibrium setups. We give a brief introduction to the non-equilibrium field theory which we then apply to graphene taking into account the specialties due to the Dirac nature of low energy excitations. We also study the coherent regime of particle-hole pair creation by a laser pulse. Along those calculations we derive the effective rate equation for the generation of photoexcited carriers that will be employed in the following chapter.

The **Chapter 4** analyses the relaxation of high energy electrons due to Coulomb interaction in view of the cascade picture as explained above. We study first a single cascade step for finite temperatures. In order to describe the relaxation cascade as a diffusive process we give a brief introduction to the theory of stable distributions and Lévy processes. After this excursion we reformulate the relaxation cascade in terms of anomalous diffusion culminating in the formulation of the fractional Fokker-Planck equation (FFPE) for the relaxation of high energy electrons in graphene due to Coulomb interaction. We also combine the effective rate equation derived in Chapt. 3 with the FFPE. This allows us to make the connection to experiments and discuss the differential change in transmission as well as the time evolution of the distribution of photoexcited electrons.

The **Chapter 5** describes the derivation of the nonlinear collision-dominated hydrodynamics in graphene. We discuss the plasmon spectrum as well as the nonlocal optical conductivity. Finally we show results from numerical simulations of nonlinear hydrodynamics in graphene driven out of global equilibrium. Furthermore we explain the relevant numerical techniques employed in those simulations.

Contents

List of Figures

1

Field theory and Coulomb interaction in graphene

In this section we recall, mainly for notational purpose, the basic properties of graphene and its field theoretical description. We will also review the results on the effects of electron-electron interaction in graphene. In this context we discuss the RG analysis of graphene, the notion of criticality and the quantum critical point (QCP). We also discuss the random phase approximation (RPA) at finite temperatures as well as chemical potentials.

1.1 Field theory in graphene

Nowadays graphene is widely known in the condensed matter community as one of the first strictly two-dimensional materials. In contrast to two-dimensional electron gases in semiconductor heterostructures [45] graphene was for a long time not even believed to exist, since the Mermin-Wagner theorem forbids the breaking of long-range order in two dimensions [2]. However graphene exists in three dimensional space. Therefore the bending of the graphene into the third dimension the so-called ripples and the presence of a substrate lead to the stability of the graphene and many of its relatives derived from Van der Waals heterostructures, for example the transition metal dichalcogenides [46].

Graphene has been studied theoretically long before its actual synthesis in 2004 [1].[1] Those early studies of the hexagonal carbon lattices revealed that the low energy theory of graphene is described in terms of massless Dirac fermions [9, 10]. This made it promising from a theoretical as well as from the application oriented standpoint.

The theoretical interest was primarily triggered by the fact that electrons in graphene are described by massless fermions which in addition to this interact intrinsically by Coulomb interaction, in other words by the electromagnetic field. This renders the graphene system a solid state toy model for quantum electrodynamics. However, when it comes to the comparison between graphene and high energy QED (2+1) one has to emphasis two major differences.

It must be noted that electrons in graphene are only quasi-relativistic. They do not move with the speed of light but rather with the Fermi velocity v_F as we will see below. The latter is approximately 300 times smaller than the speed of light c and is roughly given by $v_F \simeq 10^6 \ m/s$ [3]. Thus due to the small ratio v_F/c, relativistic retardation effects in the electromagnetic field are usually ignored and the Coulomb interaction in graphene is assumed to be instantaneous. This limit however is fulfilled

---

[1] A patent on a production method of graphene has been filed in 2002, see "United States Patent: 7071258".

only for the bare Fermi velocity. For a large renormalized value of v_F in the infrared this assumption of instantaneous Coulomb interaction might break down. However this does not lead to any practical problems if finite temperature cuts off the RG flow before the Fermi velocity reaches the speed of light. More specifically the RG flow is terminated when the renormalized temperature reaches the cut-off [47]. We will discuss the Wilson-RG for graphene in more detail in Sec. 1.3.

Another difference between the field theory in graphene and QED (2+1) is that in the case of graphene the electrodynamic field lives in three spatial dimensions. Thus the effective Coulomb potential between two electrons in graphene, the propagator of the electromagnetic field, is given by

$$V(\vec{q}) = \frac{2\pi e^2}{|\vec{q}|} \, . \tag{1.1}$$

Here $\vec{q} = (q_x, q_y)^T$ is the transferred in-plane momentum. If this is Fourier-transformed into real space one obtains $V(\vec{r}) = e^2/|\vec{r}|$. It is this difference in the photon propagator, compared to the truly two-dimensional electrodynamics where $V_{2D}(\vec{r}) \sim \ln(r)$, that leads to the special features in the interacting graphene that distinguish it from real QED(2+1). The system is rather similar to QED (3+1) since it exhibits scale invariance with the dimensionless coupling constant given by the graphene fine structure constant

$$\alpha_g = \frac{e^2}{v_F \hbar} \, , \tag{1.2}$$

where we have restored $\hbar$. Due to the fact that $c/v_F \sim 300$, we have $\alpha_g \simeq 2.2$ for graphene in vacuum. Therefore freestanding graphene is generically a strongly interacting system. All this said, one can conclude that graphene is rather similar to QED (3+1). It can also be shown that it exhibits a critical point [48]. We will come back to that in Sec. 1.3, where we review the RG in graphene that is the systematic way to sum up the logarithmic self-energy corrections expected for a system at criticality.

1.1.1 The Hamiltonian of the non-interacting graphene

In this section we are going to introduce the necessary notations and the methodological framework for the subsequent chapters. Our approach towards the description of transport phenomena and non-equilibrium dynamics in graphene will largely be based on the field-theoretical method. We assume that the reader is familiar with basic concepts of the afore mentioned method. A useful introduction can be found for example in Refs. [49, 50].

As was pointed out by early works [9, 10] and already hinted at in the introduction of this chapter, the low-energy physics of the electrons in graphene is described in terms of massless Dirac electrons. This is in fact a consequence of the symmetry of the graphene lattice shown in Fig. 1.1(a) and also tightly connected to the fact that the honeycomb lattice is a lattice with a basis of two atoms [51]. As we will explain later in more detail, there are in fact two species of Dirac electrons present in graphene, see Eq. (1.5) and the following discussion. Both species are eigenstates with definite and most importantly opposite chirality. In this sense the presence of two species is also necessary to fulfill the fermion doubling theorem lattice theories with chiral symmetry [52]. Furthermore, the relativistic nature of the theory, thus the presence of Dirac electrons, is robust against perturbations that do not violate parity, time reversal and do not mix the two Dirac species [53], i.e. break the chiral symmetry in graphene [see Eq. (1.5) and the following discussion].

In the Figure 1.1(b) we show the first Brillouin zone of graphene and the band structure. The graphene Bravais-lattice is the triangular lattice as depicted in Fig. 1.1(a), where the blue diamond illustrates the primitive unit cell. Hence the reciprocal lattice is also a triangle lattice with a hexagon
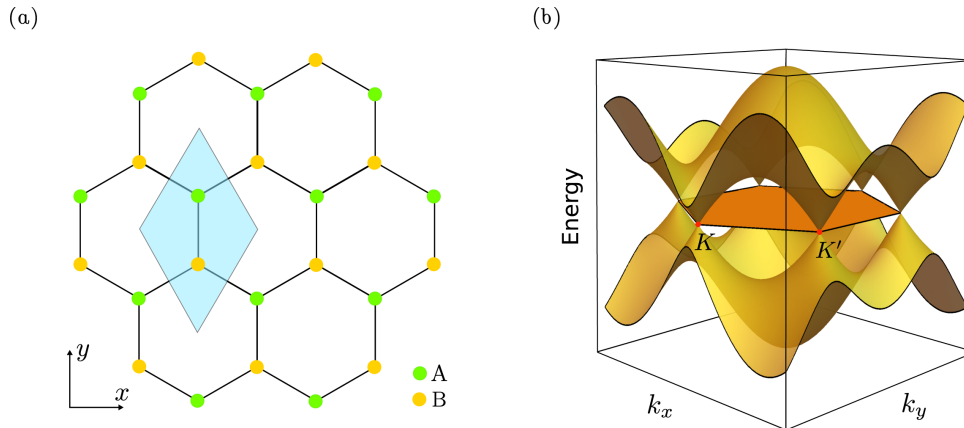
Figure 1.1: *(a) The honeycomb lattice of graphene with inequivalent lattice sites A and B forming two shifted triangular lattices. (b) The schematic band structure of graphene and the first Brillouin zone. The two inequivalent Dirac points are denoted as K and K'. Close to them the dispersion becomes linear.*

as a first Brillouin zone. The high symmetry points of importance for the low energy theory are the so-called Dirac points, of which we find two inequivalent called K and K'. In Fig. 1.1(b), we show the resulting band structure of the graphene honeycomb lattice [see Fig. 1.1(a)] derived from a nearest-neighbor tight-binding description [3]. We observe that the band structure shows two bands which are particle-hole symmetric if one takes into account only nearest neighbor hopping in the tight-binding description. More importantly the two bands touch at the Dirac points and close to them the dispersion of electrons is linear in momentum, i.e. the energy of the low energy quasi-particles is $\varepsilon_{\lambda,\vec{k}} = \lambda v_F |\vec{k}|$ with the Fermi velocity $v_F = 10^6\,m/s$ [3] and we introduced the band index $\lambda = +1$ for the conduction band and $\lambda = -1$ for the valence band. Note also that at half-filling the Fermi energy lies exactly at zero energy thus at the nodal point where the two bands touch [see Fig. 1.1(b)]. Starting from a tight-binding description of the graphene lattice as depicted in Fig. 1.1(a) the low energy Hamiltonian of the free theory in the continuum limit reads as

$$\hat{H} = \int \mathrm{d}^2r \, \Psi^\dagger(\vec{r})(-\mathrm{i}v_F \vec{\sigma} \cdot \nabla)\Psi(\vec{r}) \,. \tag{1.3}$$

Here the field Ψ is a two component spinor in sublattice space. The Pauli matrices $\vec{\sigma} = (\sigma_x, \sigma_y)^T$ in Eq. (1.3) operate in the sublattice space. Furthermore $\nabla = (\partial_x, \partial_y)^T$ is the in-plane derivative. For simplicity we only consider one Dirac cone and extend the theory to both cones at the end of this section. In the low energy continuum limit the sublattice degree of freedom takes the role of the so-called pseudo-spin in analogy to the spinor character of the electronic wave function in the Dirac equation that encodes the electron spin in relativistic quantum mechanics. For the spinor fields in graphene we have the commutation relations

$$\{\Psi_\alpha(\vec{r}), \Psi^\dagger_\beta(\vec{r}\,')\} = \delta_{\alpha\beta}\delta(\vec{r} - \vec{r}\,') \,. \tag{1.4}$$

In the following we choose dimensionless units for which $v_F = 1$.

The fact that we have two Dirac cones that are connected by time reversal symmetry, see e.g. Ref. [54], can be taken into account by writing the low energy theory in terms of an additional set of

Pauli matrices τ_i acting in valley space,[2]

$$\hat{H}' = \int d^2r \, \Psi^\dagger(\vec{r})[-iv_F(\tau_3 \otimes \vec{\sigma}) \cdot \nabla]\Psi(\vec{r}) \,. \tag{1.5}$$

For the resulting four component spinors Ψ in Eq. (1.5) one can define the familiar Dirac matrices $\vec{\gamma} = -i\tau_2 \otimes \vec{\sigma}$ and $\gamma_0 = \tau_1 \otimes \sigma_0$, where σ_0 is the 2×2 unit matrix. From these we can furthermore construct the matrix $\gamma_5 = i\gamma_0\gamma_1\gamma_2\gamma_3$. Chirality is then defined as the eigenvalues of the matrix $\gamma_5 = \tau_3$ and indeed the two Dirac points do have opposite chirality [54]. However, we are not considering any chirality breaking perturbations in this work. For example we do not assume that the electron-electron interaction leads to chiral symmetry breaking (see Sec. 1.2). The latter assumption is valid in the weak coupling regime where the graphene is infrared stable in the presence of Coulomb interaction even at the Dirac point (see Sec. 1.2). In the absence of chiral symmetry breaking the two Dirac points are equivalent and together with the real spin of the electrons they merely lead to a degeneracy factor of $N = 4$ for all practical purposes.

1.1.2 Non-interacting eigenstates

The Hamiltonian of the non-interacting graphene was introduced in the previous section. We will briefly introduce the single-particle eigenstates and eigenenergies as we will need them later on. The single-particle Hamiltonian

$$\mathcal{H} = -i\vec{\sigma} \cdot \nabla \,, \tag{1.6}$$

possesses the following set of eigenstates

$$\phi_{\lambda,\vec{k}}(\vec{r}) = e^{+i\vec{k}\cdot\vec{r}} \, u_{\lambda,\vec{k}}(\vec{r}) \,, \tag{1.7}$$

where the eigenspinors u are given by

$$u_{\lambda,\vec{k}} = \frac{1}{\sqrt{2}} \begin{pmatrix} e^{-i\varphi_{\vec{k}}/2} \\ \lambda \, e^{+i\varphi_{\vec{k}}/2} \end{pmatrix} \,. \tag{1.8}$$

Here we have introduced the angle $\varphi_{\vec{k}}$ of the momentum $\vec{k}$ in addition to the already familiar band index $\lambda = \pm 1$. Furthermore, we used our personally preferred choice of gauge. We will sometimes use the Dirac notation $|\lambda, \vec{k}\rangle$ for the basis independent representation of the eigenstates (1.7). The energy corresponding to the state $|\lambda, \vec{k}\rangle$ are $\varepsilon_{\lambda,\vec{k}} = \lambda|\vec{k}|$, as was mentioned in Sec. 1.1.1. All this leads us to the density of states of the clean graphene [3], which reads as

$$\nu(\varepsilon) = \frac{|\varepsilon|}{2\pi v_F^2} \,. \tag{1.9}$$

Furthermore the retarded Green's function is readily obtained as

$$G^R(\varepsilon, \vec{p}) = \frac{\varepsilon + \vec{\sigma} \cdot \vec{p}}{(\varepsilon + i0)^2 - \varepsilon_k^2} \,. \tag{1.10}$$

Here $\vec{\sigma}$ is the vector of Pauli matrices acting in sublattice space, and we have the advanced Green's function $G^A = [G^R]^\dagger$.

---

[2]We have chosen the ordering A, B, B, A for the columns of the matrix $\tau_3 \otimes \sigma$ in Eq. (1.5), where A and B denote the sublattice A and B in Fig.1.1(a)

The velocity associated with an electronic state $|\lambda, \vec{k}\rangle$ is given by

$$\hat{v}_{\lambda,\vec{k}} = \lambda \vec{k}/k \; . \tag{1.11}$$

Note that in contrast to a Galilean invariant system the velocity is up to a sign fully determined by the direction of the momentum. And the absolute value of the velocity is always given by the Fermi velocity. For a parabolic spectrum of massive particles with mass m the velocity would simply be proportional to the momentum in the form $\vec{v} \sim \vec{k}/m$. This difference is at the heart of the relativistic hydrodynamics close to the Dirac point and more importantly it explains why electron interactions in graphene can lead to a finite dc conductivity right at the Dirac point (see Chapt. 5).

The fact that Dirac electrons are described by spinors encodes their nontrivial topological character. Due to this, for example the matrix elements of Coulomb scattering in the eigenbasis (1.7) contain the nontrivial overlap of the eigenspinors (1.8) in the form

$$\Theta_{\lambda,\vec{k};\lambda',\vec{k}'} = u^\dagger_{\lambda,\vec{k}} u_{\lambda',\vec{k}'} = \frac{1}{2}\left(1 + \hat{v}_{\lambda,\vec{k}} \cdot \hat{v}_{\lambda',\vec{k}'}\right) \; . \tag{1.12}$$

We will refer to them as the so-called Dirac factors. The Dirac factors encode the nontrivial Berry phase of Dirac particles. It is well known that Dirac particles acquire an additional minus sign under 2π rotations. Likewise backscattering can be expressed as a π-rotation that creates an orthogonal spinor to the initial one and hence the matrix element vanishes. Therefore backscattering is suppressed for Dirac particles, a fact that leads for example to the phenomenon of Klein tunneling [2].

1.2 Aspects of electron-electron interaction in graphene

In the context of short-time dynamics after laser excitations for example as well as in the interaction-dominated transport regime electron-electron interaction plays an important role in graphene. Regarding the first point, interactions are probably the fastest process and important for the thermalization of carriers. Secondly, electron-electron interaction is an intrinsic property of graphene that behaves slightly different at the Dirac point compared to usual Fermi liquids. This is revealed in particular in the RG analysis as discussed in Sec. 1.3. Interactions can be tuned to some extend by the dielectric environment but it will still limit specific properties of graphene and also graphene devices.

We already mentioned in the beginning of this chapter that it is the similarity to QED that makes the interacting graphene so interesting also from a purely theoretical standpoint. We will relegate a discussion of the physical details mainly to Sec. 1.3 while we first introduce the technical framework to deal with electron-electron interaction in the following chapters.

The interaction Hamiltonian of the Coulomb interaction with the instantaneous Coulomb potential given by Eq. (1.1) reads as

$$H_{\text{int}} = \frac{1}{2}\int_{\vec{r}}\int_{\vec{r}'} \Psi^\dagger(\vec{r})\Psi^\dagger(\vec{r}') \, \frac{e^2}{|\vec{r}-\vec{r}'|} \, \Psi(\vec{r}')\Psi(\vec{r}) \; . \tag{1.13}$$

The fact that the Coulomb interaction is taken to be instantaneous leads to a peculiar result in the Keldysh theory (see Chapt. 3 and Appendix B). This peculiar result concerns the propagator of the electromagnetic field. More precisely, the bare propagator of the electromagnetic field which describes the plasmons can be obtained from a Hubbard-Stratonovich transformation of the four-fermion interaction (1.13). To do so we use the path integral representation of the partition function in graphene

$$Z = \int \mathcal{D}(\Psi, \Psi^\dagger) \, e^{-S[\Psi, \Psi^\dagger]} \; , \tag{1.14}$$

where the action in imaginary time is given by

$$S[\Psi, \Psi^\dagger] = \int_1 \Psi^\dagger(1)[\partial_\tau - i\vec{\sigma} \cdot \nabla - \mu]\Psi(1) + \frac{e^2}{2\epsilon} \int_{1,2} \frac{\Psi^\dagger(1)\Psi^\dagger(2)\Psi(2)\Psi(1)}{|\vec{r}_1 - \vec{r}_2|} \ . \tag{1.15}$$

Here we used the short-hand notation $\int_i = \int_0^\beta d\tau_i \int_{\vec{r}_i}$. We omitted an explicit sum over spin and valley degrees of freedom for each fermion since they effectively lead to a degeneracy factor of $N = 4$ in the final result as discussed in the previous section. Similarly we simply wrote $\Psi(1)$ for $\Psi(\vec{r}_1, \tau_1)$ and $\Psi(2)$ for $\Psi(\vec{r}_2, \tau_2)$ respectively.

We also introduced the dielectric constant $\epsilon = (\epsilon_1 + \epsilon_2)/2$ in Eq. (1.15), where $\epsilon_{1,2}$ are the dielectric constants of the materials on either side of the graphene sheet. For suspended graphene $\varepsilon = 1$, while for SiO$_2$ $\epsilon_i \simeq 3.9$ [45] and for SiC $\epsilon_i \simeq 10$ [55]. The presence of the dielectric screening can be easily understood if one solves the electrostatic problem of the interaction between two charges in the graphene sheet embedded in two dielectric media. The presence of the substrate therefore also allows a weak coupling analysis, since, due to the substrate, the previously given value $\alpha_g \simeq 2.2$ can be tuned to $\alpha_g \ll 1$.

If we decouple the four-fermion interaction in Eq. (1.15) by means of a Hubbard-Stratonovich transformation using the real scalar field Φ, i.e. we decouple in the density-density channel, we end up with the action

$$S_2[\Psi, \Psi^\dagger, \Phi] = \int_1 \Psi^\dagger(1)[\partial_\tau - i\vec{\sigma} \cdot \nabla - \mu + \Phi(1)]\Psi(1) + \int_q \int_0^\beta d\tau \, \frac{q}{4\pi} \, \Phi_{-q}(\tau)\Phi_q(\tau) \ . \tag{1.16}$$

The corresponding bare propagator of the plasmon field in the Keldysh theory (see Sect. 3.1)

$$D(1,2) = -i\langle T_c \Phi(1)\Phi(2)\rangle \ , \tag{1.17}$$

has no Keldysh component since the interaction is instantaneous, i.e. $V(q)$ is independent of ω. However, in perturbation theory the plasmon propagator acquires a finite Keldysh or $D^{\gtrless}$ component through the interaction with the fermions and the resulting retardation effects. This is illustrated in Fig. 1.2(b) where the leading order diagram contributing to the plasmon propagator is illustrated. The triangles in the same figure denote the vertex in the Keldysh space of forward and backward time contour[3] (see Chapt. 3) that reads as [56],

$$\gamma_{ij}^k = \delta_{ij}[\sigma_3]_{jk} \ , \tag{1.18}$$

where i and j are the contour index of the electron field Ψ, σ_3 is here the third Pauli matrix acting in the space of forward and backward contour and the index k is related to the contour index of the plasmon field Φ. This said, it immediately follows that the plasmon temperature for example is given by the electron temperature in equilibrium.

1.2.1 Kinematics of electron-electron interaction

The electron-electron interaction in graphene includes a couple of peculiarities. Among those are foremost the kinematic constraints on scattering processes that govern the physics for example in the Boltzmann collision integral that will be discussed in Sec. 3.2.4 and derived in more detail in the Appendix B. We will start with the simple analysis of kinematics of two-particle scattering in graphene.

---

[3] Here we consider the Keldysh space before rotating to the Larkin-Ovchinnikov representation [56]. That means we are dealing with the Green's function $G^{T,\tilde{T}}$ and $G^{\gtrless}$ as in Chapt. 3.

(a)   (b)
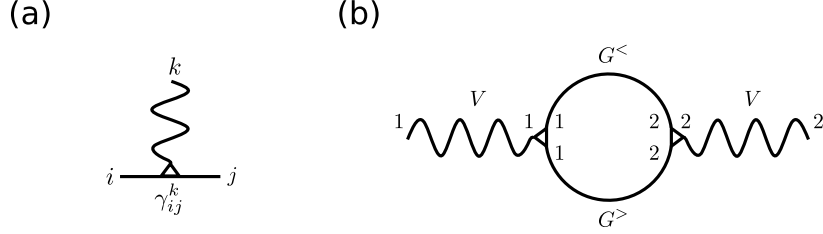
Figure 1.2: *(a) The interaction vertex in the double-time contour space as given in Eq. (1.18). See also Sec. 3.1 and in particular Fig. 3.1 for more details on the Keldysh theory. (b) The RPA bubble of Coulomb interaction on the contour. The indices 1 and 2 denote the forward and backward part of the contour. As the bare Coulomb interaction V is instantaneous, thus diagonal in Keldysh space, we see that the off-diagonal component in Keldysh space is only generated by the interaction with the electrons as described in the main text.*

Suppose we are considering the following real scattering event due to electron-electron interaction in graphene,

$$|\lambda_1, \vec{k_1}\rangle \otimes |\lambda_3, \vec{k_3}\rangle \to |\lambda_2, \vec{k_2}\rangle \otimes |\lambda_4, \vec{k_4}\rangle \,. \tag{1.19}$$

Momentum is always conserved by electron-electron scattering while for the real process also energy is conserved. We introduce the transferred momentum $\vec{q} = \vec{k_2} - \vec{k_1}$. Since all particles are assumed to be on-shell and due to the linear dispersion relation there is, up to a sign, no difference in energy and absolute value of momentum. Thus if one combines the conservation of momentum with the conservation of energy one obtains the relation

$$\lambda_1|\vec{p_1}| + \lambda_3|\vec{p_3}| = \lambda_2|\vec{p_1} + \vec{q}| + \lambda_4|\vec{p_3} - \vec{q}| \,, \tag{1.20}$$

between initial and final state energies. We can then classify the possible scattering processes according the the combinations of $(\lambda_1, \lambda_3; \lambda_2, \lambda_4)$. The result is shown in Tab. 1.1. The processes $I - II$ that are allowed by energy conservation are also illustrated in Fig. 1.3.

I	$(++, ++)$	particle and hole
	$(+-, +-)$	number separately
	$(+-, -+)$	conserved
II.1	$(++, +-)$	Auger recombination
	$(+-, --)$	
II.2	$(+-, ++)$	impact ionization
	$(--, +-)$	
III	$(++, --)$	not possible

Table 1.1: *The classification of the different scattering processes due to Coulomb interaction in graphene. Here we used the signature $(\lambda_1\lambda_3, \lambda_2\lambda_4)$ for the band indices of the initial, (λ_1, λ_3), and final states, (λ_2, λ_4), for a process according to Eq. (1.19).*

For the processes II.1 and II.2 in Tab. 1.1, one can further show that the constraint (1.20) can only be fulfilled for collinear scattering. Collinear scattering means that the initial and final momenta as well as

the momenta of the two scattering partners $\vec{p}_1$ and $\vec{p}_2$ are parallel. For example the scattering signature $(++;+-)$ implies $p_1 + p_3 = |\vec{p}_1 + \vec{q}| - |\vec{p}_3 - \vec{q}|$. With the triangle inequalities $|\vec{a} - \vec{b}| \leq |\vec{a} + \vec{b}| \leq |\vec{a}| + |\vec{b}|$, it follows that

$$|\vec{p}_1| + |\vec{p}_3| = |\vec{p}_1 + \vec{q}| - |\vec{p}_3 - \vec{q}| \leq |p_1 + p_3| \leq p_1 + p_3 \,. \tag{1.21}$$

Obviously, the inequalities in Eq. (1.21) must be equalities and we have that $\vec{p}_1$ and $\vec{p}_3$ need to point in the same direction. Furthermore $\vec{q}$ lies on the same line as $\vec{p}_1$ and $\vec{p}_3$.

We observe that the collinear scattering processes therefore have a negligible phase space. Mathematically speaking this means that the phase space of forward scattering is of zero measure. This statement only holds true for the clean graphene not taking into account additional perturbations. The latter manifests off-shell evolution of states thus the perfect quasiparticle picture is no longer valid. For perfect quasiparticles the conservation of energy (1.20) was a strict constraint. However, broadening of this energy constraint due to a finite quasiparticle lifetime would transform the strict δ-function expressing energy conservation into a Lorentzian to first approximation. The finite particle lifetime would thus open up the phase space for these forward scattering processes, namely Auger recombination and impact ionization. We will use the term Auger processes for both of them in the following. The associated phase space for Auger processes would in this case be controlled by the scattering rate which in turn defines the width of the quasiparticle peak.

In fact, the question regarding the relevance of Auger processes is an intricate problem since the scattering matrix elements for these processes usually diverge on the bare level. However, within the random phase approximation (RPA) (see Sec. 1.2.2) the forward scattering divergence in the bare matrix element of scattering is compensated by a similar divergence in the polarization operator [35] thus rendering the screened Coulomb interaction non-singular. Still, the forward scattering singularity leads to a logarithmic enhancement of certain relaxation rates [39, 57, 58].

In fact, it has been suggested that singular forward scattering might lead to the breakdown of Fermi liquid theory in 2D [59].[4] This is related to the fact that under strong collinear scattering the system is expected to behave rather like a Luttinger liquid than a Fermi liquid. For graphene this is confirmed to some extend by the fact that the RG analysis of graphene reveals some similarities between graphene and the Luttinger liquid. However, it appears that there is no breakdown of the quasiparticle picture in the sense that the quasiparticle weight remains finite. We will briefly touch upon this in Sec. 1.3. We will also talk about forward scattering in more detail in the context of relaxation dynamics of optically excited carriers due to Coulomb interaction in Chapt. 4 and in the context of hydrodynamics in Chapt. 5, where the dominant forward scattering can be employed to obtain solutions of the transport parameters analytically.

If we exclude Auger processes we observe that the number of conduction- and valence-band electrons is separately conserved under the scattering due to electron-electron interaction. We emphasize that this is only true to leading order in the graphene coupling constant α_g [60]. Higher order terms corresponding to three-particle collisions are expected to violate this conservation law [31, 60]. So does the interplay of disorder and phonons [61].

1.2.2 The random phase approximation (RPA)

The treatment of Coulomb interaction in graphene at zero chemical potential and zero temperature bears some difficulties. A prominent example is the calculation of the interaction corrections to the

---

[4]It was proposed that in the presence of a finite upper Hubbard band singular forward scattering leads to the breakdown of Fermi-liquid theory.
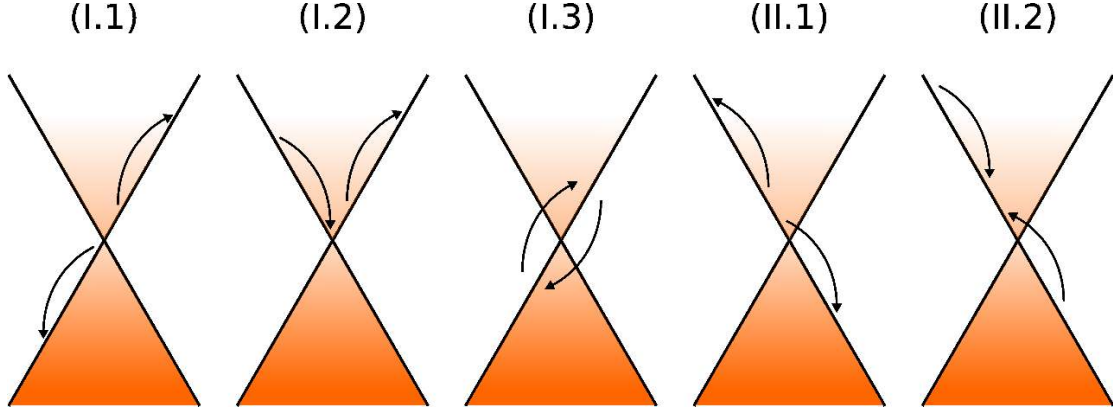
Figure 1.3: *Some of the scattering mechanisms as classified in Tab. 1.1 in the main text. The processes I conserve separately conduction and valence band densities. The processes II.1 describe Auger recombination, while II.2 is called impact ionization. Both violate the separate conservation of conduction and valence band electrons. However, they are constraint to be forward scattering.*

universal high frequency optical conductivity [62] in graphene [63–65]. The individual diagrams contributing to the optical conductivity need to be regularized since they cancel occurring divergences among each other. However, the result for the interaction corrections to the optical conductivity are depending on the regularization scheme. This issue was resolved by a proper tight-binding calculation of the optical conductivity on the honeycomb lattice [66].

Physically the reason for the complication is the fact that the electronic density vanishes at the Dirac point. Hence no screening can take place at zero temperature. This generally leads to logarithmic divergences in the first order self-energy corrections. These logarithmic divergences need to be cut-off by higher order self-energy contributions [39]. And this is in fact what happens in the regime of finite temperature by means of the random phase approximation, that is the summation of the electronic bubble diagram in Fig. 1.2(b) into an effective Coulomb interaction [50]. This resummation is formally an expansion in the number of flavors N, which in graphene is $N = 4$. From such a large-N RG analysis it furthermore follows that the RPA at small frequencies sums up the leading log contributions to the self-energy [67].

We have mentioned earlier that collinear scattering processes are suppressed due to a similar forward scattering resonance in the polarization operator. This can already be seen in the $T = 0$ case, where the polarization operator reads as [35, 58, 67]

$$\Pi(\omega, q) = \frac{q^2}{8\sqrt{q^2 - \omega^2}} \,. \tag{1.22}$$

In the general case of finite temperature and chemical potential the real and imaginary part of the

polarization operator are given by

$$\mathrm{Im}\Pi^R(\Omega, Q) = \frac{TQ}{8\pi}\left\{\frac{\Theta(1-|\beta|)}{\sqrt{1-\beta^2}}\int_1^\infty \mathrm{d}\xi \sum_{s=\pm 1}\sqrt{\xi^2-1}\frac{\sinh(\beta Q)}{\cosh(\beta Q)+\cosh(s\xi Q-\tilde{\mu})}\right.$$
$$\left. -\frac{\Theta(|\beta|-1)}{\sqrt{\beta^2-1}}\int_{-1}^1 \mathrm{d}\eta\sqrt{1-\eta^2}\frac{\sinh(\beta Q)}{\cosh(\beta Q)+\cosh(\mathrm{sign}(\beta)\eta Q+\tilde{\mu})}\right\}, \tag{1.23}$$

$$\mathrm{Re}\Pi^R(\Omega, Q) = -\frac{TQ}{8\pi^2}P\int_{-1}^1 \mathrm{d}\eta\int_1^\infty \mathrm{d}\xi\sum_{s=\pm 1}\left\{\frac{1}{\beta-s\eta}\sqrt{\frac{\xi^2-1}{1-\eta^2}}\frac{\sinh(s\eta Q)}{\cosh(s\eta Q)+\cosh(s\xi Q-\tilde{\mu})}\right.$$
$$\left. -\frac{1}{\beta-s\xi}\sqrt{\frac{1-\eta^2}{\xi^2-1}}\frac{\sinh(s\xi Q)}{\cosh(\xi Q)+\cosh(s\eta Q+\tilde{\mu})}\right\}. \tag{1.24}$$

Here we use the dimensionless momentum $Q = q/2T$ and frequency $\Omega = \omega/2T$, where T is the temperature. In Eq. (1.24) $P\int$ denotes the Cauchy principle value. The polarization operator has been studied in various regimes in Ref. [58]. We extended this work into the regime of finite chemical potential as we reported in Ref. [68]. The results are summarized in Tab. 1.2 where we introduce the dimensionless chemical potential $\tilde{\mu} = \mu/T$.

	$|\beta| < 1$		$|\beta| > 1$	
	$Q \ll \tilde{\mu}$	$Q \gg \tilde{\mu}$	$Q \ll \tilde{\mu}$	$Q \gg \tilde{\mu}$
$\mathrm{Re}\Pi^R$	$\frac{|\mu|}{2\pi}$	$\frac{TQ}{16\sqrt{1-\beta^2}}$	$-\frac{T}{8\pi}\frac{I_1(Q)}{\beta^2}\frac{\tilde{\mu}^2}{Q}$	$-\frac{T}{4\pi\beta^2 Q}$
$\mathrm{Im}\Pi^R$	$\frac{|\mu|}{2\pi}\frac{\Omega}{\sqrt{Q^2-\Omega^2}}$	$\frac{T}{4\sqrt{2\pi Q}}\,\mathrm{e}^{-(1-\beta)Q}$, for $(1-\beta)Q \gg 1$	$-\frac{T}{16}\frac{Q^2}{\sqrt{\Omega^2-Q^2}}\frac{\sinh(\Omega)}{\cosh(\Omega)+\cosh(\tilde{\mu})}$	$-\frac{T}{16}\frac{Q^2\tanh\Omega}{\sqrt{\Omega^2-Q^2}}$

Table 1.2: *The asymptotics of the polarization operator in graphene for $|\tilde{\mu}| \gg 1$ in the different regimes from Eqs. (1.23) and (1.24). Here $I_1(z)$ denotes the modified Bessel function of the first kind. Furthermore, we use the dimensionless momentum $Q = q/2T$ and frequency $\Omega = \omega/2T$, where T denotes the temperature. The parameter $\beta = \omega/q$, discriminates between inter- and intraband processes.*

1.2.3 Collinear scattering resonance in graphene

For the description of transport and relaxation processes in interacting systems the description by a kinetic equation is most suitable. The kinetic equation for weakly interacting gases or plasmas was pioneered by Landau [69]. The collision integral for Coulomb interaction contains the so-called Coulomb logarithm. The latter is a manifestation of the singular forward scattering in plasmas and contains the ratio of the average thermal energy of the particle and the screening length. A similar logarithmically divergent Coulomb scattering integral is encountered in graphene as will be discussed in further detail in Chapt. 4. Here we will briefly review how the singularity due to collinear scattering occurs in graphene simply due to kinematics in the Coulomb scattering. We will demonstrate this using the collision integral due to electron interactions in the semi-classical Boltzmann equation as discussed in detail in Sec. 3.2.4.

The linearized Coulomb collision integral $\mathcal{C}$ acts on the deviation δf from the equilibrium Fermi-Dirac distribution $f^{(0)}_{\nu,\vec{k}}$ and reads as

$$
\begin{aligned}
\mathcal{C}\delta f_{\lambda,\vec{p}} = \sum_{\nu,\nu',\lambda'} \int_{\vec{k},\vec{p}',\vec{k}'} & |M|^2 (2\pi)^3 \delta(\varepsilon_{\lambda p} + \varepsilon_{\nu k} - \varepsilon_{\lambda',p'} - \varepsilon_{\nu',k'}) \, \delta(\vec{p}+\vec{k}-\vec{p}'-\vec{k}) \\
& \times f^{(0)}_{\lambda,p} f^{(0)}_{\nu,k} (1-f^{(0)}_{\lambda',p'})(1-f^{(0)}_{\nu',k'}) \Big[\delta f_{\lambda,p} + \delta f_{\nu,k} - \delta f_{\lambda',p'} - \delta f_{\nu',k'} \Big] .
\end{aligned}
\tag{1.25}
$$

Here M is the matrix element of Coulomb interaction discussed in Chapt. 3.2.4 and Appendix B.2. As also discussed in Chapt. 5, the quantity to consider is the projected or integrated collision integral

$$
\int_p g(\vec{p}) \, \mathcal{C}\delta f_{\lambda,\vec{p}} ,
\tag{1.26}
$$

where g can be considered as some test function at this point. For simplicity let us set $g=1$.[5] We thus average the collision integral (1.25) over the momentum $\vec{p}$. Let us for simplicity assume only intraband processes in the upper band, corresponding to the process (I.2) in Fig. 1.3. Furthermore we introduce the transferred momentum $\vec{q} = \vec{k} - \vec{k}'$ and distinguish the longitudinal momenta $p_\parallel = \vec{p}\cdot\hat{q}$ and $k_\parallel = \vec{k}\cdot\hat{q}$ from the transverse momenta $p_\perp = \vec{p}\cdot(\hat{z}\times\hat{q})$ and $k_\perp = \vec{k}\cdot(\hat{z}\times\hat{q})$. We expand the collision kernel for small perpendicular momenta to study the vicinity of collinear scattering which yields

$$
\int_p \mathcal{C}\delta f_{\vec{p}} \sim \int_q \int_{k_\parallel,p_\parallel} \int_{p_\perp} V(q)^2 \frac{1}{q|p_\perp|} \sqrt{p_\parallel k_\parallel (p_\parallel + q)(k_\parallel - q)} \ldots .
\tag{1.27}
$$

Now it is apparent that the integration over the transverse momentum $p_\perp$ leads to a logarithmic divergence at small momenta that is for $\vec{k},\vec{p} \parallel \vec{q}$. For large transverse momenta the integral over $k_\perp$ will be cut off at k itself. The reason is that the divergences at large momenta only occur due to the fact that we approximated the collision kernel for small $p_\perp$. That means the upper cut off will be the average kinetic energy determined by temperature for $T \gg |\mu|$. The lower cut off will be due to screening effects that are contained in higher order self-energies. As a consequence the resulting logarithm contains the ratio of both quantities. This logarithm reappears in Chapt. 4. We refer to Fig. 4.2 in particular and the discussion in the main text of Sec. 4.3.2.

Note also that in graphene the divergence is more severe than in a system with a parabolic spectrum due to the linear dispersion relation. In fact the $1/|p_\perp|$ term stems from the δ-function of the energy constraint, which yields for small transverse momenta,

$$
\delta(\varepsilon_{\lambda p} + \varepsilon_{\nu k} - \varepsilon_{\lambda',p'} - \varepsilon_{\nu',k'}) \simeq \delta\Big(\frac{q}{2}\Big\{ \frac{p_\perp^2}{p_\parallel(p_\parallel+q)} - \frac{k_\perp^2}{k_\parallel|k_\parallel - q|} \Big\}\Big) .
\tag{1.28}
$$

A quadratic dispersion relation however yields

$$
\delta(\varepsilon_{\lambda p} + \varepsilon_{\nu k} - \varepsilon_{\lambda',p'} - \varepsilon_{\nu',k'}) \simeq \delta(2(k_\perp - p_\perp)q) .
\tag{1.29}
$$

We observe that compared to Eq. (1.28), there is only a divergence due to small q after evaluating the δ-function in Eq. (1.29), whereas in graphene we had the additional factor $\sim 1/|p_\perp|$.

---

[5] The projected collision integral can be understood as a scalar product of the linearized collision operator with the test function g in a functional space of all possible distribution functions. More specifically, the projection of the linearized collision integral on a particular set of basis functions in this function space leads to the matrix elements of the collision operator in the particular basis. See also Sec. 5.3.1 in Chapt. 5.

1.2.4 Plasmons in graphene

As we have already mentioned in the introduction graphene is also believed to be a promising platform for plasmonics since it hosts tunable 2D plasmons. Due to the truly 2D nature of graphene its plasmon excitations are sometimes referred to as surface plasmons. For two dimensional materials it is known that the plasmon dispersion is proportional to the square root of the momentum, i.e. $\omega(q) \propto \sqrt{q}$. Interestingly in pristine graphene at finite doping, thus in the Fermi liquid regime of $|\mu| \gg T$, the plasmon dispersion

$$\omega(q) = \omega_0 \sqrt{q}, \quad \omega_0 = (2e^2 \sqrt{\pi n})^{1/2}, \tag{1.30}$$

can be tuned by the gate voltage or in other words by the equilibrium charge density n in the graphene sheet. The square root dispersion relation forbids the excitation of plasmons by light in a broad spectral range and therefore also for most experimental frequencies. This is simply a consequence of the momentum mismatch between the electromagnetic field that is the photon and the plasmon. However, optical gratings, prisms and microantennas can be utilized to bridge the mentioned momentum mismatch and convert light into tightly confined plasmons [34]. Chapter 5 will largely be motivated by this prospect of creating and observing plasmon waves in graphene.

While to date most experiments focus on the Fermi liquid regime, plasmons in the regime $T \gg |\mu|$ have been proposed theoretically [58, 70]. In the Refs. [35, 58] the plasmon dispersion was derived from the RPA (see Sec. 1.2.2). The result is shown in Fig. 1.4 that we took from the same reference [35]. It is interesting to note that plasmons in graphene within the RPA do not cross into the intraband particle continuum. However they can decay by interband excitation above the energy $2\mu - q$ in the case of $\mu \gg T$. This fact is illustrated in Fig. 1.4 by the region denoted $\text{SPE}_{\text{inter}}$ (single particle excitation). The intraband particle-hole continuum is depicted by the region $\text{SPE}_{\text{intra}}$.
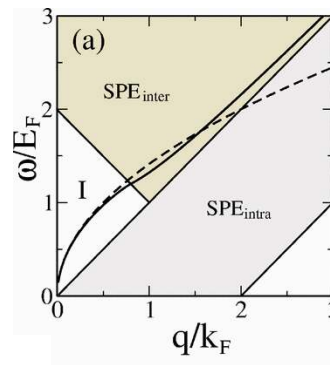
Figure 1.4: *The plasmon dispersion (solid line) calculated from RPA in graphene at finite Fermi energy E_F. The regions SPE_{inter} and SPE_{intra} show the range of energies and frequencies where inter- and intraband particle excitations are possible. The dashed line illustrates a generic 2D plasmon dispersion. Note that the plasmons in RPA do not cross into the intraband continuum. Reprinted figure with permission from: Hwang, Das Sarma, PRB 75, 205418 (2007).*

In Chapt. 5 we will consider a different limit compared to the RPA. In the hydrodynamic, thus collision-dominated regime the natural excitations close to the Dirac point become energy waves with linear dispersion relation. The latter are known as cosmic sound in the generic relativistic liquid when the pressure is the dominant contribution to the dispersion [71]. Upon doping away from the Dirac

point these energy waves quickly hybridize with the charge sector and develop into the 2D graphene plasmon with square-root dispersion (see Chapt. 5).

Furthermore different damping mechanisms of graphene plasmons have been discussed [32, 33, 36]. Among those are interactions with optical and polar surface phonon modes of the substrate. Intrinsic optical phonons in graphene and scattering from the edges have been identified as important scattering mechanisms in the mid-infrared regime [36]. In particular on SiO_2 hybridization of plasmons with phonons leads to a dramatic change in the plasmon dispersion. These hybridization effects usually become relevant at higher frequencies compared to the frequencies we are going to consider in the hydrodynamic theory in Chapt. 5 and we can therefore neglect them. We will add to the analysis of damping of graphene plasma waves a study of intrinsic effects due to electron-electron interaction in the collision-dominated hydrodynamic regime.

1.3 RG analysis and quantum criticality
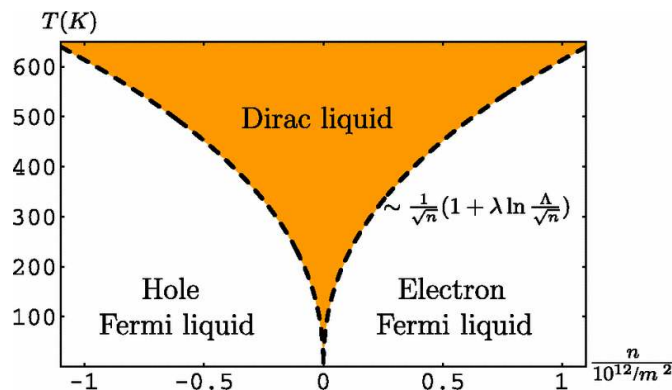
Figure 1.5: *The phase diagram of graphene close to the Dirac point as a function of density n and temperature T. The figure is calculated for the vacuum with $\epsilon = 1$. The dashed lines illustrate the crossover from the Fermi liquid into the Dirac liquid. The quantum critical point is situated at $T = n = 0$. Reprinted figure with permission from: Sheehy and Schmalian, PRL, 99, 226803 (2007).*

In this section we are going to review the Wilson renormalization group (RG) procedure of the interacting graphene described by the action (1.15). The calculation can be found in Ref. [47], whereas Refs. [48, 72, 73] pursue a more field-theoretical approach to RG. Generally speaking the RG is the tool of choice to sum up logarithmic self-energy corrections. It is therefore interesting for graphene at the Dirac point since the latter is exactly at its upper critical dimension $D = 3$. It exhibits at quantum critical point. The crossover behavior at finite temperatures in the vicinity of the quantum critical point has been studied in Ref. [47]. The result is illustrated in Fig. 1.5 from the same reference. For a system at criticality logarithmic corrections are expected, that we are going to discuss in the following. Moreover, the fact that graphene at the Dirac point exhibits only a Fermi point in contrast to a Fermi line simplifies the RG procedure.

In the condensed matter context of quantum field theory we usually have a natural cut-off in the theory through the band width of the model under consideration. In high energy field theory the situation is usually different since the microscopic theory is not known. There, it is of primary importance

to distinguish the renormalizable field theories. For the latter ultraviolet divergences can be absorbed into bare coupling constants. More specifically, a finite number of renormalized couplings suffices to cancel all of the ultraviolet divergences. For a renormalizable theory the renormalized theory should not depend on the intermediate regularization of those divergences which becomes merely a technical issue. However as pointed out above we anyway choose a simple high energy cutoff that is physically motivated. Still we can speak of a renormalizable theory in the condensed matter context, when no extra terms are generated under the RG or at least the extra terms are marginal.

Given a natural high energy cut-off Λ in graphene, as becomes apparent from Fig. 1.1(b), the general procedure of the Wilson RG is to divide the momentum space into high energy modes with momenta $k > \Lambda/b$ and low energy modes $k < \Lambda/b$, where $b > 1$ is the RG parameter usually written as $b = e^l$. Subsequently the high energy modes are integrated out so that we are left with a theory in terms of the low energy modes. Finally the momenta are rescaled in order to restore the connection to the initial theory albeit with renormalized parameters.

For graphene it follows from the action (1.15) that the engineering dimension of the field operators Ψ is $[\Psi] = -2$.[6] This is due the fact that we choose the non-interacting action to be invariant under the scale transformation. Using this scaling dimension in the emerging Coulomb interaction of the slow fields $\Psi_{\vec{k}}^<$ for momenta $k < \Lambda/b$ we see that the Coulomb interaction is marginal. Thus kinetic energy scales similarly as the Coulomb interaction. Therefore higher order corrections due to fast fields have to decide whether the interaction becomes relevant or irrelevant in the infrared. This is in contrast to the usual Fermi liquid scenario, where for spatial dimension $d \geq 2$, Coulomb interaction is irrelevant. The difference is due to the fact that for graphene with zero chemical potential we only have a Fermi point instead of an extended Fermi line or surface. As a consequence we have a simple scaling between energy and absolute value of momentum $\omega' = b\omega$ and $k' = bk$, whereas a finite Fermi surface will break this symmetry in scaling since only the momentum perpendicular to the Fermi surface will scale [74]. Interestingly the presence of only two Fermi points rather than lines is reminiscent of the Luttinger liquid state in one dimension. We already mentioned this similarity before and will come back to this fact below.

Taking into account the corrections due to integrating out the high energy modes we see that this amounts to taking into account the Fock self-energy diagram for the slow modes

$$\Sigma_{\mathrm{HF}}(\omega, \vec{k}) = \int_{\Lambda/b < |\vec{k}'| < \Lambda} \frac{\vec{k} \cdot \sigma}{\omega_n^2 + k'^2} \frac{2\pi e^2}{\epsilon|\vec{k} - \vec{k}'|} \,, \tag{1.31}$$

whereas the Hartree bubble does not contribute due to the overall charge neutrality of the system. For similar reasons there is no renormalization of the chemical potential $\mu = 0$ that is pinned to zero, thus total charge is conserved. Evaluating the integral in Eq. (1.31) for $b = e^l$ with $l \ll 1$ ($l > 0$) one obtains

$$\Sigma_{\mathrm{HF}}(\omega, \vec{k}) = \frac{e^2}{4\epsilon} \vec{k} \cdot \vec{\sigma} \,. \tag{1.32}$$

Thus one observes that after rescaling the fields and momenta as well as the temperature, the new action resembles the old one with a renormalized Fermi velocity

$$v_F \to v_F \left(1 + \frac{e^2}{4\epsilon v_F} \ln b \right) \,. \tag{1.33}$$

---

[6]Here we use the notation $[E] = 1$ for units of energy. Remember that we have set $\hbar = 1$.

We observe that the effective coupling of the theory is $\alpha_g/4$. The temperature is a relevant perturbation under the RG procedure and is rescaled as $T' = Z_T^{-1} T$, where

$$Z_T = b^{-1} \left(1 + \frac{\alpha_g l}{4} \right) . \tag{1.34}$$

We choose the rescaling of the fields according to $\Psi_k = Z_\Psi \Psi'_{k'}$ such that the free part of the action remains of the same form under the RG procedure but with a different Fermi velocity. This yields

$$Z_\Psi = b^2 \left(1 + \frac{\alpha_g l}{4} \right)^{-1} . \tag{1.35}$$

According to the general RG scheme the procedure outlined above is now repeated for infinitesimal l. Successive RG steps then lead to the flow equations

$$\frac{\mathrm{d}\alpha_g(b)}{\mathrm{d}\ln b} = -\alpha_g(b)^2/4 , \quad \frac{\mathrm{d}T(b)}{\mathrm{d}\ln b} = T(b)(1 - \alpha_g(b)/4) . \tag{1.36}$$

From Eq. (1.36) it again becomes apparent that the interaction flows to smaller values thus it is marginal irrelevant close to the Dirac point.

Finally we note that due to a Ward identity connected to the conservation of charge, the electric charge e is not renormalized in the model with a static Coulomb potential. Therefore the renormalization of the fine structure constants in graphene is only due to velocity renormalization in $\alpha_g = e^2/v_F$. We observe that lowering the energy leads to an increase in the Fermi velocity and thus a decrease in the coupling constant. While the engineering dimension of the interaction was marginal, we can say now that the electron interaction in graphene is marginal irrelevant. In this sense we can also say that at least starting from a weak coupling analysis valid for example for graphene on a substrate the system is infrared stable. There is no occurrence of a symmetry broken state. The latter has been predicted by some strong coupling theories. The most discussed candidate is the excitonic condensate leading to a charge density wave formation [75, 76]. However the excitonic gap has not been observed, even in suspended graphene.

One might be surprised what happens at very low temperatures when the renormalization of the Fermi velocity (1.33) will ultimately reach the speed of light c and thus relativistic scales. However, performing a truly relativistic RG calculation reveals a nontrivial infrared fix point for which $v_F = c$ and Lorentz invariance is restored [73].

Finally we comment on the presence of a quantum critical point in graphene and its marginal or strange Fermi liquid behavior. First of all the fact that highly electron doped graphene exhibits a circular Fermi surface and so does the highly hole doped case implies that in between a quantum critical region has to exist in which we go from an electron doped Fermi liquid to a hole doped one [15]. This conjecture is strengthened by the findings that the quasiparticle decay rates scale linear with particle energy [73, 77] or that relaxation rates at finite temperature scale linear in temperature in the intrinsic graphene of $T \gg |\mu|$ [58]. This is apparently due to the fact that temperature is the only scale close to the quantum critical point and the dominant perturbation away from criticality. In fact there is a quantum critical region close to the Dirac point for $|\mu|/T \ll 1$ for clean graphene [47]. The fact that relaxation rates are linear in energy suggest the similarity to the marginal Fermi liquid phase proposed for the cuprates [78]. However, this scenario also suggests that the quasiparticle weight goes to zero similar as in the case of the Luttinger liquid. This is however not the case in graphene, where

the quasiparticle weight goes to a finite fixed value [67]. Also the anomalous exponent of the correlation function η depends on the interaction strength [48] and is thus similar to the Luttinger liquid [79]. In this sense one might argue that graphene rather constitutes a strange Fermi liquid [48] showing some aspects of non-Fermi liquid behavior but not fitting in a general scheme of the Luttinger liquid for example.

In the presence of a quantum critical point and a quantum critical regime for $|\mu|/T \ll 1$, the low frequency response of the clean graphene is suggested to be described by hydrodynamics [15, 39]. More specifically by relativistic hydrodynamics. The latter bears some peculiarities in comparison to usual hydrodynamics. For example the 2nd or bulk viscosity is supposed to vanish [71]. The latter is true for all scale invariant systems [80]. We are going to derive the relativistic hydrodynamics for graphene from the microscopic Boltzmann equation in Chapt. 5. Our analysis yields explicit expressions for the equations of state of the relativistic liquid describing graphene. We will also give explicit expressions for the relevant transport parameters in terms of microscopic scattering rates. Furthermore the fact that we have the full set of equations including all equations of state allows us to simulate nonlinear effects in graphene in the collision-dominated hydrodynamic regime.

2 Chapter 2

Linear response within the Kubo formalism

This chapter is devoted to the theory of linear transport in graphene within the Kubo formalism. We will review results on the dc transport in disordered graphene and at finite frequency. In the end we will briefly discuss the results for finite frequency response in magnetic fields obtained in our work [81]. This includes Shubnikov-de Haas oscillation in the dc and optical conductivity as well as magnetoresponse in the regime of separated Landau levels. In particular the results for the universal conductivities will serve as a reference later on in this thesis.

2.1 Kubo formalism

The Kubo formula relates the linear response function of a certain observable to field theoretical correlation functions [49, 82]. More specifically, we are interested in the conductivity, that is the response of the electric current to an electric field. With the help of the response function

$$\chi^R_{\alpha\beta}(t - t', \vec{r} - \vec{r}') = -\mathrm{i}\,\Theta(t - t')\langle[j_\alpha(\vec{r}, t), j_\beta(\vec{r}', t')]\rangle\,, \tag{2.1}$$

we obtain the conductivity

$$\sigma_{\alpha\beta}(\omega, q) = -\frac{\chi^R(\omega, q)}{\mathrm{i}\omega}\,. \tag{2.2}$$

Here an in Eq. (2.1) the greek indices α and β take values among the Cartesian coordinates x, y. In Eq. (2.1) we introduced the current operator j that for graphene reads as

$$\vec{j} = e\Psi^\dagger(\vec{r})\vec{\sigma}\Psi(\vec{r})\,. \tag{2.3}$$

The current operator can either be obtained from the Heisenberg equation of motion of the density $n = \Psi^\dagger\Psi$, which must take the form of a continuity equation due to the correspondence principle. From the latter the form of the current density operator can be deduced. Alternatively one might employ Noether's theorem to obtain the current density from the action (1.15).

The retarded response function (2.1) is calculated most conveniently within the Matsubara technique [50, 83] and then obtained by analytical continuation. That means one calculates

$$\sigma^M_{\alpha\beta}(\mathrm{i}\Omega, q) = \frac{1}{\Omega}\int \mathrm{d}\tau\, \mathrm{e}^{+\mathrm{i}\Omega\tau}\langle j_\alpha(\tau, \vec{q})j_\beta(0, -\vec{q})\rangle\,, \tag{2.4}$$

and obtains $\sigma(\omega, q)$ from $\sigma(\omega, q) = \sigma^M(\omega + \mathrm{i}0, q)$. Here $\mathrm{i}\Omega$ is a bosonic Matsubara frequency. This procedure also yields the expression

$$\sigma(\omega) = \int \frac{\mathrm{d}\varepsilon}{4\pi} \frac{f_{\varepsilon+\omega}^{(0)} - f_{\varepsilon}^{(0)}}{\omega} \mathrm{tr} \left[\left(\hat{G}_{\varepsilon_1}^R - \hat{G}_{\varepsilon_1}^A \right) \hat{j}_x \left(\hat{G}_{\varepsilon_2}^R - \hat{G}_{\varepsilon_2}^A \right) \hat{j}_x \right] , \qquad (2.5)$$

where $f^{(0)}$ is the Fermi Dirac distribution and $\hat{G}^{R,A}(\varepsilon)$ is the retarded and advanced Green's function in graphene defined in Sec. 3.1. We see that the optical conductivity and thus also the transmission is an average of the microscopic state of the system encoded in the distribution function $f^{(0)}$ and the spectral Green's functions $G^{R,A}$. Therefore pump-probe transmission measurements are an indirect measurement on the state of the system.

2.2 Linear response in disordered and clean graphene

The conductivity in graphene shows a couple of peculiarities due to the linear dispersion relation that leads to the absence of scales in the high frequency interband response. Very early on in the graphene research following its discovery in 2004 [1] it was found that indeed the high frequency conductivity of graphene possesses a universal value[1]

$$\sigma_{\mathrm{opt}}(\omega) = \frac{e^2}{4\hbar} , \qquad (2.6)$$

due to this absence of any other scale given $\omega \gg T, |\mu|$. Small corrections to this universal value due to interaction effects have been discussed and different values have been under debate [63–65] until just recently [66].

Neglecting all corrections due to finite temperature, disorder and interaction, the universal value of the high frequency conductivity, Eq. (2.6), is a property of the intrinsic graphene and a result of the linear quasi-relativistic dispersion relation. On the other hand, the vicinity of a quantum critical regime close to the Dirac point leads to another universal limit of the dc conductivity, i.e. at small frequencies. More specifically, this universal value of the conductivity arises due to disorder in contrast to the high frequency result (2.6).[2] Here the model of disorder is crucial to determine the precise value [53]. The result for the conductivity in the self-consistent Born approximation and diagonal weak disorder [53] as well as weak chiral disorder at the Dirac point is given by

$$\sigma_0 = \frac{2e^2}{\pi^2 \hbar} . \qquad (2.7)$$

Furthermore finite size effects and the specific type of the infrared regulator influence the universal value significantly at the Dirac point. The hydrodynamic theory presented in Chapt. 5 is suited to explore the finite size effects to the conductivity in the collision dominated regime of $\alpha_g^2 T \gg \tau_d^{-1}$. Here τ_d is the characteristic scattering time due to disorder, T is the temperature and α_g denotes the graphene fine-structure constant. This is in particular interesting since Coulomb interaction can lead to a finite conductivity at the Dirac point [39, 57] in the collision-dominated regime. This fact can be understood in the following way. The conductivity is determined by the product $D\nu^{\mathrm{th}}$. Here the diffusion constant D is temperature-dependent through the scattering time due to Coulomb interaction

---

[1]We restore Planck's constant in this section for convenience.

[2]Another universal value of the conductivity close to the Dirac point due to Coulomb interaction will be discussed in Chap. 5.

$D \sim 1/T$. The thermodynamic density of states however scales as $\nu^{\text{th}} \sim T$. The product $D\nu^{\text{th}}$ is therefore temperature-independent. The fact that the scattering rate scales linear with temperature is precisely due to the presence of the quantum critical point as discussed in Chapt. 1, where temperature is the dominant perturbation away from the critical point in the interaction-dominated regime. This result will also be obtained within the hydrodynamic description of transport in graphene in Chapt. 5.

Interestingly, experimental measured values for the dc conductivity at the Dirac point are either $\sigma_0 = 4e^2/h$ or more recently in very clean samples a universal conductivity $\sigma_0 = 1.7 \times 4e^2/\pi h$ has been reported in Ref. [84]. However, the value of the conductivity might very well depend on the specific sample quality, the geometry and the substrate. Long and wide samples for example show qualitatively different behavior compared to short and long samples, see e.g. Ref. [42]. Here the length should be compared for example with the characteristic mean free paths of carriers.

2.3 Optical conductivity and transmission

In the context of optical experiments on graphene it is interesting that there is a direct relation between the optical conductivity and the transmission coefficient in linear response. The relation is obtained from solving the Maxwell equations in the presence of a graphene sheet with conductivity $\sigma(\omega)$ [85]. If the graphene is in vacuum and one considers normal incident light the transmission coefficient $\mathcal{T}$ reads as

$$\mathcal{T} = \frac{1}{(1 + 2\pi\sigma(\omega)/c)^2} \,. \tag{2.8}$$

Interestingly due to the universal value of the conductivity at high frequencies, Eq. (2.6), one observes that the transmission of the graphene is determined by the fine structure constant of real quantum electrodynamics $\alpha_{\text{QED}} \simeq 1/137$, more specifically it holds for weak absorption $\mathcal{T} \simeq 1 - \pi\alpha_{\text{QED}}$. This yields the familiar universal high frequency transmission of graphene for normal incident light $\mathcal{T} \simeq 0.977$. Likewise one obtains for the reflectivity the simple relation

$$\mathcal{R} = \frac{\pi^2 \alpha_{\text{QED}}^2}{4} \mathcal{T} \,. \tag{2.9}$$

The universal value of the transparency of the graphene and its connection to the fine structure constant has been measured in Ref. [62].

2.4 Linear magnetotransport in graphene

We also discuss the magnetotransport in graphene. The results can be found in our work reported in Ref. [81]. Furthermore a discussion of the magnetotransport can be found in Ref. [86]. Magnetotransport in graphene is interesting since Dirac fermions show unusual Landau quantization and quantum Hall effect [11] as pointed out in the introduction.

The Landau levels (LLs) in graphene are unconventional due to the Dirac nature of carriers. First of all LLs are not equidistant as in a usual two-dimensional electron gas with parabolic dispersion. Their energies are given by

$$\varepsilon_n = \text{sign}(n)\omega_c\sqrt{|n|} \,, \tag{2.10}$$

where $n \in \mathbb{Z}$ is the LL index. This means that we have Landau levels with negative energy from the hole band and Landau levels with positive energy from the electron band as well as a zeroth LL with

$\varepsilon_n = 0$. From Eq. (2.10) we see that the LL move closer together at higher energies. The cyclotron frequency in Eq. (2.10) is given by $\omega_c = 1/l_B$ with the magnetic length $l_B = 1/\sqrt{eB}$. Thus the cyclotron frequency of the zeroth LL $\omega_c \sim \sqrt{B}$. For higher LLs it is advantageous to introduce the local cyclotron frequency $\omega_{c,n} = |\varepsilon_{|n|+1} - \varepsilon_{|n|}|$, that goes like $\omega_{c,n} \simeq \omega_c/2\sqrt{|n|}$ for high LL index n. If one considers magnetotransport in the presence of disorder the LLs will first of all be broadened by disorder. The broadening within the self-consistent Born approximation is given by the scattering rate Γ due to disorder. Except for the zeroth LL which has the width $\sqrt{2}\Gamma$ in comparison to the other LLs, the scattering rate is independent of the LL index in the case of diagonal white-noise disorder [81]. As a consequence an energy independent scattering rate is expected in experiments with dominant short-range scattering. Due to the fact that the zeroth LL has a different width we will nevertheless retain the notation Γ_n for the scattering rate due to disorder. Taking into account that the LLs move closer together with higher LL index it is obvious that they have to overlap at a certain index or energy respectively. We will denote the energy scale where LLs start to overlap as $\varepsilon_{\mathrm{ov}}$.

2.4.1 Intra-Landau level transitions

We will give the results on the dc limit ($\omega \to 0$) of the magnetotransport in graphene. That means due to the limit $\omega \to 0$ only intra-LL transitions can take place.[3] We find two distinct temperature regimes set by the disorder scattering rate Γ: a) $T \ll \Gamma$ and b) $T \gg \Gamma$. We assume the chemical potential to lie within one LL which we denote by L_N, i.e. as the LL with index N and energy ε_N. We introduce the coefficient $c_n = 1$ for $n \neq 0$ and $c_n = 2$ for $n = 0$. This is necessary due to the peculiar role played by the zeroth LL.

a) When the temperature is the smallest scale, $T \ll \Gamma$, only the level L_N, determined by the position of the chemical potential, contributes. The conductivity becomes ($\sigma_0 = 2e^2/\pi^2$) [87]

$$\sigma = \sigma_0 \, \frac{c_N \omega_c^2}{2\omega_N^2} \left(1 - \frac{(\mu - E_N)^2}{\Gamma_N^2} \right) . \tag{2.11}$$

Note that one recovers the universal conductivity at the Dirac point for $\Gamma \to 0$ as discussed in the previous section.

b) In the limit of high temperature, i.e. $T \gg \Gamma$ the conductivity reads as

$$\sigma = \sigma_0 \sum_{n=-\infty}^{\infty} \frac{c_n \omega_c^2 \Gamma_n}{6\omega_n^2 T \cosh^2[(E_n - E_N)/2T]} . \tag{2.12}$$

Here the sum is over all LLs. The summation limits are sent to infinity since the contribution of large energies where LLs overlap is exponentially small. In Eq. (2.12) the zeroth LL is again special since its width is bigger by a factor of $\sqrt{2}$ and its oscillator strength is enhanced by a factor of two. However, its contribution is significant only for $N = 0$ and $T \lesssim \omega_c$. From Eq. (2.12) we obtain the following three high T regimes:

b.1) For $\Gamma \ll T \ll \omega_N$ only L_N contributes, while the contribution from the levels farther away from the chemical potential is exponentially suppressed. The conductivity in this limit is given by

$$\sigma = \sigma_0 \, \frac{c_N \omega_c^2 \Gamma_N}{6\omega_N^2 T} . \tag{2.13}$$

---

[3]The results for the optical conductivity at very small but finite frequencies $\omega < \Gamma$ in Landau quantized graphene can be found in Ref. [81].

The conductivity σ is determined by the phase space $\sim \Gamma_N / T$.

b.2) For the intermediate temperature regime $\omega_N \ll T \ll \mu < \varepsilon_{\text{ov}}$, the influence of zeroth LL can be neglected since $\mu \gg T$. Furthermore, due to $T \gg \omega_N$ the sum in Eq. (2.12) can be converted into an integral, which gives

$$\sigma = \sigma_0 \, \frac{64\Gamma |\mu|^3}{6\omega_c^4} \, . \tag{2.14}$$

The conductivity in this regime is T-independent.

b.3) For $\omega_N, \mu \ll T < \varepsilon_{\text{ov}}$ we obtain

$$\sigma = \sigma_0 \, \frac{48\zeta(3)\Gamma T^3}{\omega_c^4} \, , \tag{2.15}$$

where $\zeta(z)$ is the Riemann ζ-function. We observe that the temperature takes the role of the chemical potential in Eq. (2.14).

2.4.2 Inter-Landau level transitions

(a)

(b)
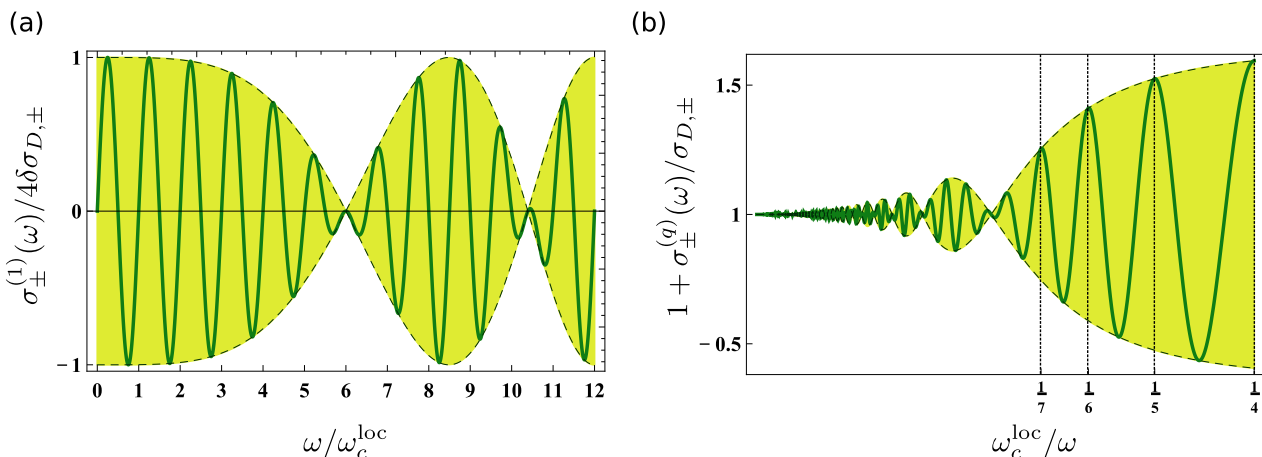
Figure 2.1: *(a) The SdH oscillations in the dynamic conductivity (solid line) and the envelope function showing slow modulation due to nonequidistant spectrum of LLs (dashed line) calculated according to Eq. (2.17) for $\varepsilon_F / \omega_c = 6$. (b) Magnetoconductivity $\sigma_{D,\pm}(\omega) + \sigma_\pm^{(q)}(\omega)$ of graphene at high temperatures normalized to the Drude value (2.16) and calculated according to (2.18) for $\varepsilon_F / \omega_c = 6$. Vertical lines mark the position of integer harmonics of the cyclotron resonance.*

In the limit of finite frequency the optical conductivity in graphene shows a rich pattern of resonances depending on the chemical potential and the frequency. This is primarily due to the fact that LLs in graphene are non-equidistant. Also remember that the regimes of overlapping and separated LLs are nearly always realized simultaneously. For realistic disorder strength and high magnetic fields LL start to overlap at higher energies ε_{ov}. The results are qualitatively different depending on whether the probed energy range is within the regime of separated or overlapping LL. In the latter simple analytical results can be obtained and the connection to the classical system with parabolic spectrum are possible. Additional quasiclassical and quantum correction due to the Landau quantized graphene are small in

the Dingle factor $\delta = \mathrm{e}^{-\pi/\omega_c^{\mathrm{loc}}\tau_q}$ where the quantum time due to disorder is $\tau_q = 1/\kappa\pi|\varepsilon|$ [81]. Here, the constant κ is the dimensionless disorder strength. Furthermore we introduced the local cyclotron frequency $\omega_c^{\mathrm{loc}} = \omega_c^2/2|\varepsilon|$, that is the continuous version of $\omega_{c,n}$ given above. Here for $T \ll |\mu|$ it follows that $\varepsilon \sim \mu$ in ω_c^{loc} is the local characteristic energy scale determining the cyclotron frequency.

For high chemical potentials and $\omega < ||\mu| - \varepsilon_{\mathrm{ov}}|$, the conductivity to leading order in δ indeed assumes the Drude value [81],

$$\sigma_{D,\pm}(\omega) = \frac{1}{\pi} \frac{\mathcal{D}/\tau_{\mathrm{tr}}}{(\omega \pm \omega_c^{\mathrm{loc}})^2 + \tau_{\mathrm{tr}}^{-2}}, \qquad \mathcal{D} = \frac{e^2|\varepsilon_F|}{2}. \tag{2.16}$$

Here we introduced the transport time in graphene $\tau_{\mathrm{tr}} = 2\tau_q$. In a conventional parabolic spectrum the transport time and the quantum time would be identical for white-noise disorder. However, due to the Dirac electron's Berry phase, the leading order Shubnikov-de Haas (SdH) oscillations are [81],

$$\sigma_{\pm}^{(1)}(\omega) = 4\sigma_{D,\pm}\delta\cos\left(\frac{2\pi(\varepsilon_F^2 + \omega^2)}{\omega_c^2}\right)\frac{\sin\frac{2\pi\omega}{\omega_c^{\mathrm{loc}}}}{2\pi\omega/\omega_c^{\mathrm{loc}}}. \tag{2.17}$$

In addition to the SdH oscillations we have higher order quantum corrections that read as [81]

$$\sigma_{\pm}^{(q)}(\omega) \simeq 2\,\sigma_{D,\pm}\,\delta^2\,\frac{\sin\frac{2\pi\omega^2}{\omega_c^2}}{2\pi\omega^2/\omega_c^2}\,\cos\frac{2\pi\omega}{\omega_c^{\mathrm{loc}}}. \tag{2.18}$$

The common feature of the magnetooscillations in the classically strong magnetic field is that due to the unusual Landau quantization the oscillations show a slow beating with increasing frequency ω [81]. The behavior of the first order quantum corrections (2.17) and second order quantum corrections (2.18) is illustrated in Fig. 2.1. We observe that indeed on top of the quantum oscillations with the local cyclotron frequency ω_c^{loc} a slow beating with a frequency given by the cyclotron frequency of the first Landau level ω_c is visible.

If the system is close to the Dirac point and the regime of separated LLs is explored by the finite frequency a complicated pattern of resonances is occurring that can be tuned quite strongly by the chemical potential. For a detailed discussion we refer to our work in Ref. [81] that extends the results from Ref. [86], and to the experimental works in Refs. [88–91]. Quite recently also interaction effects on the Landau level quantization in graphene have been studied in a joint experimental and theoretical work in Ref. [92]. This work is interesting since it is situated in between our work on linear magnetotransport presented here and in Ref. [81] and the theory for interaction effects in graphene that we will discuss in the Chapts. 4 and 5. We will discuss the mentioned experimental works in the following chapter including a comparison with our findings for the optical conductivity in the regime of separated LLs.

2.5 Comparison with experiments

Measurements of magnetotransport phenomena are a versatile tool to investigate transport coefficients and the interplay of different scattering mechanisms. For example optical spectroscopy of Landau levels in graphene gives access to the quantum times and other scattering times due to disorder [89, 91, 93]. As we have seen in Sec. 2.3 the optical conductivity is directly related to the transmission of graphene. Therefore, optical transmission experiments are able to measure for example the cyclotron resonance, Eq. (2.16), in the case of overlapping LLs. Similarly the cyclotron resonance in the regime of separated

LLs can be explored. Here the width of the cyclotron resonance is determined by the spectral width of the LLs. As a consequence two direct measurements of disorder-related parameters are possible. First, Dingle plots of the SdH oscillations, i.e. a finite temperature analysis of the conductivity in Eq. (2.17) in the limit $\omega \to 0$ yields the quantum time. At the same time, mobility measurements in the disorder-dominated regime access the transport scattering time τ_q. Second, Landau level spectroscopy yields the line width of the cyclotron resonance in the regime of well separated LLs. The latter is determined by the scattering rate Γ as introduced in the previous section. In the following we summarize typical values found in the literature. We also calculate the disorder strength for the measured values of τ_q and Γ within the model of diagonal white-noise disorder. These values are important to relate our findings to future experiments and to test the model of short-range scattering. The latter predicts in particular the relation $\tau_{\mathrm{tr}} = 2\tau_q$.

In Tab. 2.1 we give an overview of common quantum times τ_q and the corresponding scattering rate $\Gamma_q = 1/2\tau_q$. Both are obtained from Dingle plots of the temperature dependence of the Shubnikov-de Haas oscillations in graphene. The experiments are performed at finite doping leading to a finite charge density ρ. If available we also provide the ratio τ_{tr}/τ_q, where the transport time τ_{tr} is obtained from mobility measurements. For diagonal white-noise disorder a ratio of $\tau_{\mathrm{tr}}/\tau_q = 2$ is expected. We see that this is indeed the case for the samples in Ref. [93]. From the chemical potential μ corresponding to the charge density ρ and the relation $\tau_q = 1/\kappa\pi|\mu|$ we determine the disorder strength κ for the samples. The obtained disorder strength ranges from 0.01 to 0.05 in all samples.

ρ [1/cm^2]	τ_q	Γ_q	τ_{tr}/τ_q	κ	μ [cm^2/Vs]	Ref.
$3 \cdot 10^{12}$	34 fs	9.7 meV	−	0.03		[94]
$3 \cdot 10^{12}$	$25 - 74$ fs	$4.5 - 13$ meV	$2.2 - 5.1$	$0.01 - 0.04$		[94]
$2 \cdot 10^{12}$	20 fs	16.5 meV	2	0.06	$2000 - 4000$	[93]
$3.1 \cdot 10^{6}$	53.5 fs	6.15 meV	−	0.02	$4400 - 17000$	[95]

Table 2.1: *Typical values for the quantum time τ_q and the corresponding scattering rate Γ_q due to disorder obtained from Dingle plots of SdH oscillations as reported in the Refs. [93–95]. The experiments are performed at finite doping characterized by the charge density ρ. If available, we also show the ratio between the quantum time and the transport scattering time. The latter is obtained from the mobility which is also given for the last two experiments. Furthermore, from the charge density ρ and the values for the quantum time we determine the disorder strength κ with the help of the formula $\tau_q = 1/\kappa\pi|\varepsilon|$. Here $\varepsilon \simeq \mu$, where μ is the chemical potential derived from ρ.*

In the case of separated Landau levels only recently experiments were able to measure the actual width of the cyclotron resonance. We give values from experiments in Tab. 2.2. For the values in the second line of Tab. 2.2 the system is in the regime of overlapping Landau levels yielding an energy dependent width of the cyclotron resonance. Let us relate these findings to our theoretical predictions. The cyclotron resonance is given by Eq. (2.16). From this equation we see that the width of the cyclotron resonance is indeed characterized by the transport time τ_{tr}. Remember that for the model of diagonal white-noise disorder considered here, we have $\tau_{\mathrm{tr}} = 2\tau_q$. We also mentioned that $1/\tau_q$ depends linearly on energy. If we identify the measured width with our definition of the transport time we can determine the disorder strength κ from the relation $\tau_q = 1/\kappa\pi|\varepsilon|$. The obtained value is also listed in Tab. 2.2. For lower LLs the authors of Ref. [91] find that the width of the Landau levels becomes energy independent. This is in agreement with the scenario that the LLs at lower energies are well

separated. Using the obtained parameters and the given magnetic field strength, let us check for the condition that the Landau levels overlap. For the calculated disorder strength of $\kappa \simeq 0.017$ the zeroth and first Landau level should be separated [86]. In fact, we expect the Landau levels to overlap above the third Landau level. For comparison we also mention typical values that we extracted from other measurements of the cyclotron resonance in graphene [93, 94].

n [1/cm^2]	B	$1/\tau_q$	Γ	κ	Ref.
$1 \cdot 10^{12}$	16 T	$11 - 16.5 \, \text{meV}$	$20 - 30 \, \text{meV}$	$0.03 - 0.05$	[93, 94]
$\simeq 10^{10}$	4 T	$\tau_q^{-1} = \kappa\pi|\varepsilon|$	$\Gamma = \kappa\pi|\varepsilon|$	$2 \cdot 0.026/\pi \simeq 0.017$	[91]

Table 2.2: *The scattering rate due to disorder and the quantum time τ_q obtained from the measurements of the width of the cyclotron resonance. The first line is a measurement in the regime of separated LLs yielding an energy independent value of the width. The second line shows results for lower magnetic fields yielding an energy dependent scattering rate. The latter is an indication for the regime of overlapping LLs as explained in the main text.*

We compare our results on the conductivity in the regime of separated LLs qualitatively with the mentioned experimental spectroscopy studies. The regime of separated LLs is discussed in more detail in our work in Ref. [81]. In Fig. 2.2(a) we show the transmission spectrum of graphene in a magnetic field of 0.4 T. The experiment was performed at a temperature of $T = 1.9 \, \text{K}$. The transmission $\mathcal{T}$ is connected to the optical conductivity according to Eq. (2.3). The absorption of graphene is strongest for the cyclotron resonances corresponding to the selection rules of the clean graphene. The selection rules allow optical transitions from the LL with index n to the LL with index n' with a change in the LL index of $n - n' = \pm 1$. The relevant transitions for the given window of frequencies are shown in the inset of Fig. 2.2(a). We use the same nomenclature for the transitions between LLs in the Figs. 2.2(b)-(d). As a comparison to the experimental results in Fig. 2.2(a) we show in Figs. 2.2(b)-(d) results for the optical conductivity from our work, Ref. [81], for different chemical potentials. We see that the conductivity and hence the transmission varies significantly with the chemical potential. For example, comparing Fig. 2.2(c) with (d), we see that the transition A, i.e. the transition from the LL with $n = 1$ to the LL with $n' = 2$, only becomes visible as soon as the chemical potential jumps into the first LL. Similarly, we conclude from the comparison of Fig. 2.2(d) with Fig. 2.2(b) that the relative intensity of the transition (A) and (B) is an indication for the position of the chemical potential in the first LL. At the same time we can conclude that the experiment in Fig. 2.2(a) corresponds to the Fig. 2.2(b). The position of the chemical potential is illustrated in the insets of Figs. 2.2(b)-(d).

In closing this section on the linear transport and in particular the linear magnetotransport we would like to highlight the influence of interaction effects on the transport in magnetic fields. In particular the interplay of interaction and disorder leads to prominent corrections of the low-field transport in two-dimensional systems. For example, logarithmic corrections to the weak field magneto-resistance of graphene have been measured in Ref. [96]. As the origin of the logarithmic corrections weak localization, Kondo-physics as well as Altshuler-Aronov corrections have been proposed. A detailed analysis of the temperature dependence of the magnetoresistance in Ref. [96] revealed that the relevant mechanism is indeed electron-electron interaction. Furthermore the analysis allowed for the extraction of the interaction strength. In view of the spectroscopy measurements, just recently the influence of electron-electron interaction on the width of LLs has been investigated in Ref. [92]. This study is also interesting as it is situated in between the work presented in this chapter and the analysis of the subsequent chapters

of this thesis which are devoted to the effects of interaction on the relaxation dynamics of electrons in graphene. It appears promising to bring both topics together in the future.

2.6 Summary

This chapter was devoted to the linear transport in graphene within the Kubo formalism. We reviewed general results regarding the universal values of the conductivity at high frequencies as well as the universal dc conductivity due to disorder. In particular the universal high frequency conductivity yields the universal absorption of a single graphene sheet of 2.3%. The main results of this chapter concerned the conductivity of disordered graphene in quantizing magnetic fields. More specifically, we assumed the model of diagonal white-noise disorder and calculated the dynamic conductivity in the regime of overlapping as well as for separated Landau levels. The Landau levels in graphene are nonequidistant and as they become broadened by disorder the regime of separated and overlapping Landau levels can be realized simultaneously at different energies.

i) In the regime of overlapping Landau levels we find that the Shubnikov-de Haas oscillations in the dynamic conductivity as well as in the higher order quantum corrections reveal the nonequidistant Landau level spectrum. More specifically, the fact that transitions take place between Landau levels with different cyclotron frequency, leads to a beating in the magnetooscillations. We also extract relevant parameters as the quantum and scattering time as well as the disorder strength from experiments.

ii) The regime of separated Landau levels is characterized by a rich spectrum of resonances for finite frequencies. They can be tuned to a large extend by the chemical potential, i.e. the filling factor. We compared the results with experiments and extracted the disorder strength for our model similar as in the case of overlapping Landau levels. In particular in the dc limit where only intraband Landau level transitions can occur we make prediction for the temperature dependence of the conductivity: a) For $\Gamma \ll T \ll \omega_c^2/|\mu|$ we find $\sigma \sim 1/T$. b) For $\omega_c^2/|\mu| \ll T \ll |\mu|$ on the other hand $\sigma \sim$ const. c) Whereas in the case of $|\mu| \ll T \ll \varepsilon_{\mathrm{ov}}$, we have $\sigma \sim T^3$.
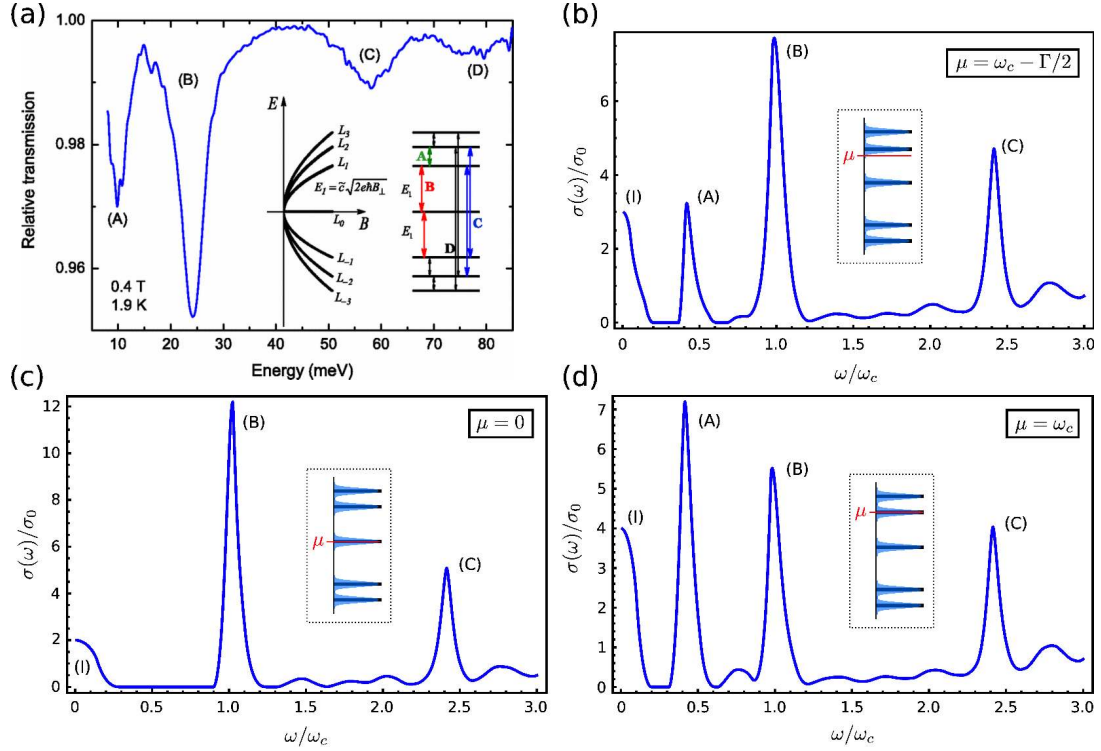
Figure 2.2: *(a) The transmission spectrum of Landau quantized graphene from Ref. [89]. The experiment was performed in a magnetic field of 0.4 T at a temperature of $T = 1.9$ K. The inset associates the absorption peaks to transitions in the Landau staircase. Here and in the following (A) denotes the transition $L_1 \leftrightarrow L_2$, (B) stands for the transition $L_0 \leftrightarrow L_{\pm 1}$ and (C) for the transitions $L_{-1} \leftrightarrow L_2$ and $L_{-2} \leftrightarrow L_1$. The transmission is connected to the optical conductivity according to Eq. (2.8). Reprinted figure with permission from: Sadowski et al, PRL, 97, 266405 (2006). (b) The predicted optical conductivity as a function of the frequency from our work [81]. The chemical potential is located in the lower half of the disorder broadened LL. (c) The optical conductivity from the same reference for the chemical potential located in the center of the zeroth LL; and (d) for the chemical potential situated in the center of the first LL. The transitions (A) − (C) in Fig. (b)-(d) are the same as in the inset of Fig. (a). In addition the transition (I) denotes the intra-LL transition which occurs for small frequencies. Furthermore the position of the chemical potential is illustrated in the insets of (b)-(d).*

3 Chapter 3
Quantum kinetic equation for graphene

While the previous section was devoted to the theoretical study of linear transport in graphene within the Kubo formalism, we are now going to develop the quantum kinetic equation for graphene which will give us an alternative and more versatile tool to study non-equilibrium setups and interaction effects in transport. Furthermore we will later derive the nonlinear hydrodynamics in graphene from the Boltzmann limit. The hydrodynamic theory also allows for the description of finite size effects.

3.1 Diagrammatic Keldysh formalism and Kadanoff-Baym ansatz

We begin our derivation of the quantum kinetic equation for graphene with a short introduction to the non-equilibrium field theory. The aim of the non-equilibrium field theory is to calculate real-time correlation functions, for example the two-point function

$$G(\vec{r}, t; \vec{r}', t') = -\mathrm{i}\langle \hat{T}\hat{\Psi}(\vec{r}, t)\hat{\Psi}^\dagger(\vec{r}', t')\rangle \,. \tag{3.1}$$

Here we have chosen the real space basis. Remember that the Green's function can be introduced independent of a basis. For example in the case of time-translation invariance one can define the retarded Green's function as the resolvent operator

$$\hat{G}^R(\varepsilon) = (\varepsilon - \hat{H} + \mathrm{i}0)^{-1} \,. \tag{3.2}$$

We will therefore and for a more compact notation sometimes omit the spatial arguments. In the zero temperature field theory the correlation functions are calculated using the adiabatic theorem. However, for finite temperatures the density matrix is no longer a projector on the ground state. Secondly, even if we were to restrict ourselves to the groundstate, in some situations we cannot rely on the adiabatic theorem. That means the final groundstate of the system, after switching on the interaction, might not be connected to the initial non-interacting groundstate. Therefore we would like to eliminate any reference to the state of the system after the perturbation has been switched on.

The Matsubara technique [50, 83] might as well fail in the sense that the density matrix need not be a simple exponential function. On the contrary there are situations where we rather want to compute the specific form of, for example, the reduced single-particle density matrix - the distribution function. It is known that under certain conditions the distribution function can be distinctly non-thermal [97, 98]. In this context the non-equilibrium field theory also represents a natural way to derive the Boltzmann equation and its quantum kinetic variants. The ultimate aim of this chapter is to derive the quantum

kinetic equation for graphene, taking into account the fact that we are dealing with Dirac fermions and thus effectively with a two band model.

The way to circumvent the above mentioned complications was first formulated by Schwinger [99] in a work on coupled oscillators in which he introduced a two-time contour, later named the Schwinger-Keldysh contour (see Fig. 3.1), and the concept of quantum and classical source fields. The theory was developed in the many-particle framework by Keldysh [100] and Craig [101]. An equivalent formulation, that is in principle a generalization of the Matsubara Green's function method [83] to the non-equilibrium situation, was developed by Kadanoff and Baym as well as Langreth and Wilkins [102, 103]. Our introduction to non-equilibrium field theory here is limited and merely serves as an introduction to our notations. A more detailed introduction to the non-equilibrium field theory, in particular the diagrammatic formulation can be found for example in Refs. [20, 56, 82, 102].

3.1.1 Keldysh contour and non-equilibrium Green's functions
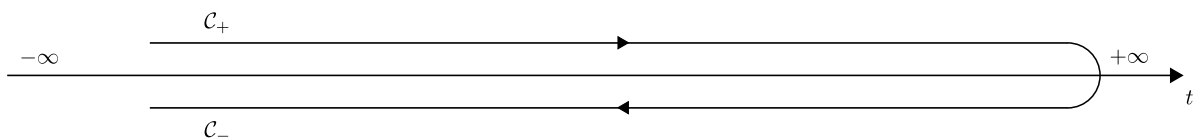
Figure 3.1: *The two-time Keldysh contour consisting of a forward $\mathcal{C}_+$ and backward time-contour $\mathcal{C}_-$.*

Suppose we want to calculate the two-point correlation function

$$\mathrm{i}G(\vec{r}, t; \vec{r}', t') = \langle \Phi(-\infty)|S(-\infty, +\infty)\hat{T}[S(+\infty, -\infty)\hat{\Psi}(\vec{r}, t)\hat{\Psi}^\dagger(\vec{r}', t')]|\Phi(-\infty)\rangle \,. \tag{3.3}$$

Here $\hat{T}$ is the usual time-ordering operator that arranges operators according to their time argument, the latest to the left. We also introduced the time-evolution operator in the interaction picture which we denoted $S(t, t')$. It is also called the S-matrix and is given by

$$S(t, t') = \hat{T} \exp\left(-\mathrm{i} \int_{t'}^{t} \mathrm{d}\tau \, H_{1,\mathrm{int}}(\tau)\right) \,, \tag{3.4}$$

where $H_{1,\mathrm{int}}$ is the perturbation in the interaction picture. At this point it is not possible to move the left S-matrix through the time ordering which is necessary to establish the perturbation theory with the help of Wick's theorem [50, 104]. This complication is overcome if we introduce a two-branch contour that is depicted in Fig. 3.1, and will be denoted $\mathcal{C}$ in the following. It consists of the forward $\mathcal{C}_+$ and backward branch $\mathcal{C}_-$. Furthermore we define time ordering along the contour arranged by a contour ordering operator $\hat{T}_c$. This procedure is sometimes referred to as the analytical continuation of time. The Green's function on the contour reads as

$$\mathrm{i}G(\vec{r}, \tau; \vec{r}', \tau') = \langle \hat{T}_c \hat{\Psi}(\vec{r}, \tau)\hat{\Psi}^\dagger(\vec{r}', \tau')\rangle \,. \tag{3.5}$$

Similarly we can define the Green's function (3.5) for finite temperatures,

$$\mathrm{i}G(\vec{r}, \tau; \vec{r}', \tau') = \mathrm{tr}\left[\rho(-\infty)\hat{T}_c\left\{S_c \, \hat{\Psi}(\vec{r}, \tau)\hat{\Psi}^\dagger(\vec{r}', \tau')\right\}\right] \,. \tag{3.6}$$

Here S_c is the S-matrix on the contour and will be given below in Eq. (3.8). It is now rather obvious that we have the following connections between the contour-time Green's function and the four possible real-time Green's functions,

$$G(\vec{r}, \tau; \vec{r}', \tau') = \begin{cases} G^T(\vec{r}, t; \vec{r}', t') & , \tau, \tau' \in \mathcal{C}_+ \, , \\ G^<(\vec{r}, t; \vec{r}', t') & , \tau \in \mathcal{C}_+, \tau' \in \mathcal{C}_- \, , \\ G^>(\vec{r}, t; \vec{r}', t') & , \tau \in \mathcal{C}_-, \tau' \in \mathcal{C}_+ \, , \\ G^{\tilde{T}}(\vec{r}, t; \vec{r}', t') & , \tau, \tau' \in \mathcal{C}_- \, . \end{cases} \tag{3.7}$$

Here, G^T and $G^{\tilde{T}}$ denote the time ordered and anti time ordered Green's functions. The four Green's function in (3.7) are not independent and usually a different set of linear combinations including the retarded and advanced correlation functions is more suitable. The latter describe the kinetics of the quasiparticles whereas the correlation functions $G^{\gtrless}$ encode the noise and statistics of the particles. For further properties and the rules for analytical continuation of products and convolutions of multiple Green's functions see Appendix A.

Contour Dyson equation

Similar to the equilibrium field-theory one can perform the perturbation theory in the Schwinger-Keldysh formalism by expanding the S-matrix

$$S = \hat{T}_c \exp\left(-i \oint_C d\tau \, H_{1,\text{int}}(\tau)\right) . \tag{3.8}$$

In passing, remember that the standard perturbation theory is based on Wick's theorem. However, application of Wick's theorem is only possible if either thermal averages are performed with respect to a non-interacting single-particle density matrix or a quadratic action in the zero temperature case. We did not touch upon the modifications that this requirement usually entails within the non-equilibrium formalism. Bear in mind however that for the decay of specially prepared initial correlations more care must be taken. We refer for example to the Refs. [14, 102, 105, 106]. For our later derivation of the kinetic equation in graphene it is of importance that one may introduce the self-energy Σ for the particles' Green's function in a similar manner as in the zero temperature case for example. Likewise it is possible to write a Dyson equation for the single-particle Green's function

$$\left[\mathcal{G}^{-1} - \Sigma\right] \circ G = \delta(\tau - \tau') . \tag{3.9}$$

Here we introduced the inverse Green's function

$$\mathcal{G}^{-1} = \left[i\frac{\partial}{\partial \tau_1} - \hat{H}(\tau_1)\right] \delta(\tau_1 - \tau_2) , \tag{3.10}$$

and wrote simply $\circ$ for the convolution in time and space here. The Dyson equation (3.9) can also be written in terms of the real-time Green's functions from Eq. (3.7). In this case it usually becomes a matrix equation in the space of Keldysh indices $\pm$, referring to the branches of the Keldysh contour. The equation of motion for the corresponding matrix Green's function

$$\mathcal{G}(\vec{r}_1, t_1; \vec{r}_2, t_2) = \begin{pmatrix} G^T(\vec{r}_1, t_1; \vec{r}_2, t_2) & G^<(\vec{r}_1, t_1; \vec{r}_2, t_2) \\ G^>(\vec{r}_1, t_1; \vec{r}_2, t_2) & G^{\tilde{T}}(\vec{r}_1, t_1; \vec{r}_2, t_2) \end{pmatrix} , \tag{3.11}$$

is given by

$$[i\partial_{t_1} - H_1]\mathcal{G}(\vec{r}_1, t_1; \vec{r}_2, t_2) - \int \Sigma(\vec{r}_1, t_1; \vec{r}_3, t_3)\tau_3\mathcal{G}(\vec{r}_3, t_3; \vec{r}_2, t_2)\mathrm{d}\vec{r}_3\mathrm{d}t_3 = \tau_3\delta(\vec{r}_1 - \vec{r}_2)\delta(t_1 - t_2) \,. \quad (3.12)$$

Here τ_3 is the third Pauli matrix acting in the space of forward and backward contour. From Eq. (3.12) follows the equation of motion for the Green's function $G^<$ as

$$\mathcal{G}^{-1}G^< - \Sigma^R \circ G^< - G^< \circ \Sigma^A = 0 \,. \quad (3.13)$$

This can easily be seen from the Langreth-Wilkins rules as explained in Appendix A.

Our subsequent goal is to write an equation of motion for the Green's function $G^<$ from Eq. (3.7). The reason is that the equal-time limit of the Green's function $G^<$ is connected to the single-particle distribution function. One can see this from the following considerations. Suppose the system is translational invariant. Then the Fourier transform of the single-particle density matrix $\rho(\vec{k}, t)$ of the momentum state $|\vec{k}\rangle$ is given by

$$G^<(\vec{k}; t_1, t_2)|_{t_1 \to t_2} = i\rho(\vec{k}, t_1) \,. \quad (3.14)$$

Here and in the following we are only dealing with fermions. The theory for bosons is similar. There have been developed several approaches to derive an equation of motion of the semi-classical single-particle distribution function. In the following we are going to pursue the strategy put forward by Kadanoff and Baym [105] and subsequently extended by Lipavsky et al [107]. In this procedure one performs the limit $t_1 \to t_2$ in the equation of motion (3.13). However the self-energy entering the resulting equation will still contain strictly two-time correlation functions. Thus the equation is not closed in the sense that it is an equation for the equal-time Green's function alone. The question is whether the two-time distribution function can be recovered from the equal-time or time-diagonal part and the spectral functions, i.e. the retarded and advanced Green's functions (see Appendix A). This very fundamental problem also touches the very question whether there is possible semiclassical distribution function that can follow from a quantum mechanical correlation function. It is usually referred to as the reconstruction problem.

3.1.2 The reconstruction problem - the generalized Kadanoff-Baym ansatz

In this section we are going to review the so-called reconstruction problem, that means the reconstruction of the two-time Green's function $G^<(t_1, t_2)$ from its time-diagonal part. There is a very general representation of the non-equilibrium Green's function $G^<$ in terms of the spectral functions G^R and G^A and another unknown function F,

$$G^<(t_1, t_2) = G^R(t_1, t_3) \circ F(t_3, t_2) - F(t_1, t_3) \circ G^A(t_3, t_2) \,. \quad (3.15)$$

This ansatz is simply motivated by the antihermitian character of the distribution function $G^<$. The function $F(t_1, t_2)$ can be regarded as a precursor to the semiclassical distribution function. More specifically for a homogeneous system in equilibrium, the Fourier transformed correlation function (3.15) reads as

$$G^<(\omega, \vec{p}) = F(\omega)[G^R(\omega, \vec{p}) - G^A(\omega, \vec{p})] \,. \quad (3.16)$$

As a consequence we identify the time-diagonal part of Eq. (3.15), in this case of thermal equilibrium, as the single-particle density matrix, that is given by the Fermi-Dirac distribution $F = f^{(0)}$ in equilibrium,

$$\rho^<(\vec{p}) = iG^<(t_1, t_2; \vec{p})|_{t_1=t_2} = i\int \frac{\mathrm{d}\omega}{2\pi} G^<(\omega; \vec{p}) = f^{(0)}(\varepsilon(\vec{p})) \,. \quad (3.17)$$

For a system away from equilibrium we assume that the relations (3.16) and (3.17) still give us access to the single-particle distribution function, which however need not be of Fermi-Dirac type.

For most practical purposes it is too complicated to calculate the two-time correlation function $F(t_1, t_2)$. However an approximate ansatz for the expression of the correlation function (3.15) in terms of the single-time distribution function (3.14) was put forward by Kadanoff and Baym and assumes that a similar relation to Eq. (3.16) also holds for the non-equilibrium situation [105], or at least close to equilibrium [107]. This ansatz reads as

$$G^{\gtrless}(t_1, t_2) = \mathrm{i}\left[G^R(t_1,t_2)G^{\gtrless}(t_2,t_2) - G^{\gtrless}(t_1,t_1)G^A(t_1,t_2)\right] . \tag{3.18}$$

This is called the generalized Kadanoff-Baym ansatz. It generalizes the somewhat simpler Kadanoff-Baym ansatz

$$G^{\gtrless}(t_1, t_2) = \mathrm{i}G^{\gtrless}(t)\left[G^R(t_1,t_2) - G^A(t_1,t_2)\right] . \tag{3.19}$$

However, the latter violates the causal structure of the Keldysh theory as it is incompatible with the Langreth-Wilkins rules (see Appendix A). Furthermore, corrections to the gradient expansion and renormalization effects are only taken into account incompletely [108, 109]. The difference however is of no importance in the quasiclassical Boltzmann limit of the kinetic equation, the equation of motion of the single-particle density matrix.

3.2 Multiband quantum kinetics in graphene

In the preceding section we have introduced the necessary concepts for deriving the quantum kinetic equation. We are now going to apply these concepts to the case of graphene. That means we are seeking the equation of motion for the equal-time correlation function (3.14), the single-particle density matrix. There are a couple of interesting specialties in graphene regarding its quantum kinetic equation. The most trivial one is due to the fact that we are effectively dealing with a two-band system. As a consequence the distribution function becomes a 2×2-matrix and similarly the quantum kinetic equation becomes a matrix equation. The latter furthermore contains intraband as well as interband driving terms in comparison to the semi-classical Boltzmann equation. A more exotic ingredient is the Dirac nature of the carriers in graphene. This for example leads to the appearance of the graphene specific Dirac factors.

3.2.1 Projected gauge-invariant Green's function

In order to derive a gauge invariant quantum kinetic equation we need to introduce a gauge invariant Green's function. This is necessary since otherwise the corrections to the Boltzmann equation will be ambiguous and depend on the way the field is introduced. But we rather seek a general expression, in which only the fields appear from the very beginning. As pointed out in Refs. [110, 111] as well as [112], the gauge invariant Green's function can be obtained as

$$g(\vec{r}_1, t_1; \vec{r}_2, t_2) = \mathrm{e}^{-\mathrm{i}\mathcal{W}(\vec{r}_1, \vec{r}_2, t_1, t_2)}\mathcal{G}(\vec{r}_1, t_1; \vec{r}_2, t_2) , \tag{3.20}$$

where

$$\begin{aligned} \mathcal{W}(\vec{r}_1, \vec{r}_2, t_1, t_2) = &(t_1 - t_2)\frac{e}{c}\int_{-1/2}^{1/2}\mathrm{d}\lambda\, \phi(\vec{R} + \lambda\vec{r}, T + \lambda\tau)\\ &- (\vec{r}_1 - \vec{r}_2)\cdot\frac{e}{c}\int_{-1/2}^{1/2}\mathrm{d}\lambda\, \vec{A}(\vec{R} + \lambda\vec{r}, T + \lambda\tau) . \end{aligned} \tag{3.21}$$

Here $\vec{A}(\vec{r}, t)$ is the vector potential and ϕ is the electrostatic potential describing the external field. In the case of homogeneous electric field $\vec{E} = -\partial_t \vec{A}$ we have $\vec{A} = -\vec{E}t$ and $\phi = 0$. The gauge invariant Green's function thus reads as

$$g(\vec{r}_1, t_1; \vec{r}_2, t_2) = \mathrm{e}^{+\mathrm{i}\frac{\vec{r}_1 - \vec{r}_2}{t_1 - t_2} \cdot \int_{t_2}^{t_1} \mathrm{d}t \vec{A}(t)} \mathcal{G}(\vec{r}_1, t_1; \vec{r}_2, t_2) \,. \tag{3.22}$$

Let us define the phase factor

$$I(\vec{r}, t_1, t_2) = \mathrm{i}\frac{\vec{r}_1}{t_1 - t_2} \cdot \int_{t_2}^{t_1} \mathrm{d}t \vec{A}(t) \,. \tag{3.23}$$

We already pointed out that for graphene the Green's function (3.20) is also a matrix in the sublattice space. In the following it is useful to chose a proper basis for the representation of this matrix. In the absence of a magnetic field the eigenstates of the free graphene are such a suitable basis. The kinetic equation and the Green's function (3.20) needs to be represented in this basis. Therefore we introduce the projected Green's function

$$g_{\nu_1 \nu_2}(t_1, t_2) = \int \mathrm{d}\vec{r}_1 \int \mathrm{d}\vec{r}_2 \phi_{\nu_1}^{\dagger}(\vec{r}_1) g(\vec{r}_1, t_1; \vec{r}_2, t_2) \phi_{\nu_2}(\vec{r}_2) \,. \tag{3.24}$$

Here ϕ_ν with $\nu = (\lambda, \vec{k})$ and $\lambda = \pm 1$, are the eigenstates of graphene, given in Eqs. (1.7) and (1.8). The inverse transformation of Eq. (3.24) is given by

$$g(\vec{r}_1, t_1; \vec{r}_2, t_2) = \sum_{\nu_1, \nu_2} \phi_{\nu_1}(\vec{r}_1) g_{\nu_1 \nu_2}(t_1, t_2) \phi_{\nu_2}^{\dagger}(\vec{r}_2) \,. \tag{3.25}$$

Shifting the phase factors $\mathrm{e}^{I(\vec{r}_{1,2}, t_1, t_2)}$ into the graphene states, we obtain the gauge-invariant eigenstates

$$\tilde{\phi}_\nu = \frac{\mathrm{e}^{\mathrm{i}\vec{k}\cdot\vec{r}}}{\sqrt{2}} \begin{pmatrix} \mathrm{e}^{-\mathrm{i}\varphi_k/2} \\ \lambda \mathrm{e}^{+\mathrm{i}\varphi_k/2} \end{pmatrix} \mathrm{e}^{\mathrm{i}I(\vec{r}_1, t_1, t_2)} \,. \tag{3.26}$$

In the following we are going to discuss a constant electrical field. The Hamiltonian is then given by

$$H = \vec{\sigma} \cdot \left(\vec{p} - \frac{e}{c}\vec{A} \right) \,. \tag{3.27}$$

Here the vector potential is $\vec{A} = -\vec{E}t$. In this case of a homogeneous electrical field the phase factor I is given by

$$I(\vec{r}, t_1, t_2) = +\frac{e}{c}\frac{(t_1 + t_2)}{2}\vec{r} \cdot \vec{E} \,. \tag{3.28}$$

And thus we obtain for the gauge-invariant Green's function,

$$g_{\nu_1 \nu_2}(t_1, t_2) = \int \mathrm{d}\vec{r}_1 \int \mathrm{d}\vec{r}_2 \tilde{\phi}_{\nu_1}^{\dagger}(\vec{r}_1) G(\vec{r}_1, t_1; \vec{r}_2, t_2) \tilde{\phi}_{\nu_2}(\vec{r}_2) \,. \tag{3.29}$$

3.2.2 Quantum kinetic equation

We are now going to derive the equation of motion (EOM) for the projected Green's function. This projected Green's function is a 2×2-matrix in the graphene band space. The single-particle Green's function is in general a function of two spatial coordinates $\vec{r}_1$ and $\vec{r}_2$ and needs not to be translational invariant. However if we introduce the relative coordinate $\vec{r} = \vec{r}_1 - \vec{r}_2$ and the center off mass coordinate $\vec{R} = (\vec{r}_1 + \vec{r}_2)/2$ and assume that the Green's function only varies slowly in $\vec{R}$, we can perform a gradient expansion in the variable $\vec{R}$. A parallel reasoning assures that the projected Green's function is diagonal in the momentum if the system is translational invariant. In this case we have to leading order in the gradient expansion for the equal-time limit of the Green's function (3.29) written as a 2×2-matrix in band space,

$$g_p^<(t) = \mathrm{i} \begin{pmatrix} \rho_{p,+}(t) & P_p(t) \\ P_p^*(t) & \rho_{p,-}(t) \end{pmatrix} , \qquad (3.30)$$

where the off-diagonal elements P are the interband polarization of the graphene while $\rho_{p,\pm}$ are the conduction and valence band populations. A macroscopic polarization P leads to a finite dipole moment in the system that can in turn couple to electromagnetic waves.

The projection of the equation of motion (3.12) onto the eigenstates of graphene leads us to the kinetic equation in the basis of the free graphene eigenstates,

$$[\mathrm{i}\partial_{t_1}\delta_{\nu_1\nu_3} - \xi_{\nu_1\nu_3}]g_{\nu_3\nu_2}(t_1, t_2) - [S_{\nu_1\nu_3}g_{\nu_3\nu_2} - g_{\nu_1\nu_3}S_{\nu_3\nu_2}] - K_{\nu_1\nu_2}[g] = \tau_3\delta_{\nu_1\nu_2}\delta(t_1 - t_2) . \qquad (3.31)$$

Here a convolution of the products is implied. We will now discuss the individual terms occurring the equation of motion (3.31). First, we introduced the kinetic part of the left-hand side of the EOM, the Liouvillian,

$$\xi_{\nu_1\nu_3} = \int \mathrm{d}\vec{r}\, \tilde{\phi}_{\nu_1}^\dagger(\vec{r}) H \tilde{\phi}_{\nu_3}(\vec{r}) . \qquad (3.32)$$

With the Hamiltonian (3.27) this evaluates to

$$\xi_{\nu_1\nu_3} = \delta_{\nu_1\nu_3}\varepsilon_{\nu_1} + \frac{e}{2c}\tau E_{\nu_1\nu_3} , \qquad (3.33)$$

where we abbreviated the relative time as $\tau = t_1 - t_2$. Note that the last term in Eq. (3.33) is purely quantum and vanishes in the limit of equal times $\tau \to 0$. It contains the matrix element of the electric field,

$$E_{\nu_1\nu_2} = (2\pi)^2\delta(\vec{k}_1 - \vec{k}_2)[\lambda_1\delta_{\lambda_1\lambda_2}\hat{k}_1 \cdot \vec{E} + \mathrm{i}\lambda_2\delta_{\lambda_1, -\lambda_2}\vec{E} \cdot (\hat{z} \times \hat{k}_1)] . \qquad (3.34)$$

The second term on the left-hand side of Eq. (3.31) describes the intraband as well as interband coupling of the electric field,

$$S_{\nu_1\nu_2} = \frac{e}{2c}(2\pi)^2\delta(\vec{k}_1 - \vec{k}_2)\left[\delta_{\lambda_1\lambda_2}\vec{E} \cdot \mathrm{i}\nabla_{k_2} - \delta_{\lambda_1, -\lambda_2}\frac{Ek_{2,\perp}}{k_2^2}\right] . \qquad (3.35)$$

The intraband term will lead to the usual driving term in the Boltzmann limit. More precisely the standard driving term is obtained if one performs the gradient expansion as described in the Appendix B. The interband term however is genuine for graphene. It is a major difference compared to the full Boltzmann limit where the polarization is neglected entirely. In the case of the constant electrical field it is responsible for the Landau-Zener physics [113, 114] taking place in the presence of strong electrical

fields. In other contexts the same effect is sometimes called Schwinger mechanism [115]. More details on the different driving terms can be found in the Sec. 3.2.3.

Let us introduce the decomposition of the driving terms in Eq. (3.35) due to the electrical field $S = S^{(1)} + S^{(2)}$, where the intraband driving is given by

$$S^{(1)}_{\nu_1\nu_2} = \frac{e}{2c}(2\pi)^2\delta(\vec{k}_1 - \vec{k}_2)\delta_{\lambda_1\lambda_2}\vec{E}\cdot\mathrm{i}\nabla_{k_2}\,. \tag{3.36}$$

The Schwinger mechanism manifests the interband coupling

$$S^{(2)}_{\nu_1\nu_2} = -\frac{\pi^2}{2c}(2\pi)^2\delta(\vec{k}_1 - \vec{k}_2)\delta_{\lambda_1,-\lambda_2}\frac{Ek_{2,\perp}}{k_2^2}\,, \tag{3.37}$$

which will couple polarization and population as we will see below in Sec. 3.2.3.

At last we introduced the following abbreviation for the self-energy that will later constitute the collision integral. We only consider the collision integral in the zero field limit, i.e. $E \to 0$. In principle the collision integral will also depend on the electrical field though the phase factors I in the gauge invariant formulation, see Sec. (3.2.1). We therefore neglect the intra-collisional field effect [20]. We arrive at the following expression for the projected self-energies that will make up the collision integral

$$K_{\nu_1\nu_2} = \sum_{\nu_3}\int \mathrm{d}t_3\sigma_{\nu_1\nu_3}(t_1,t_3)\tau_3 g_{\nu_3\nu_2}(t_3,t_2)\,. \tag{3.38}$$

In particular for $K^<$ we have according to the Langreth-Wilkins rules (see Appendix. A).

$$K^<_{\nu_1\nu_2} = \sum_{\nu_3}\int \mathrm{d}t_3\left[\sigma^R_{\nu_1\nu_3}(t_1,t_3)g^<_{\nu_3\nu_2}(t_3,t_2) + \sigma^<_{\nu_1\nu_3}(t_1,t_3)g^A_{\nu_3\nu_2}(t_3,t_2)\right]\,. \tag{3.39}$$

We denote the projected self-energies as $\sigma^{R,A}_{\nu_1\nu_2}$. Here and in Eq. (3.38) the self-energies $\sigma^{R,A}_{\nu_1\nu_2}$ are given explicitly in Appendix B for the Coulomb interaction in graphene. The collision integral has the diagrammatic representation shown in Fig. 3.2. Further discussion of the collision integral can be
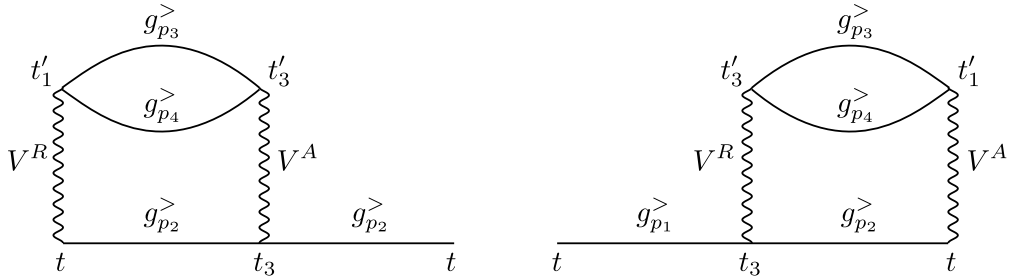
Figure 3.2: *The two diagrams contributing to the out-scattering term of the collision integral according to Eq. (B.23) from Appendix B.2. The in-scattering term is obtained by interchanging $g^< \leftrightarrow g^>$. Here the equal time limit of $t_1 = t_2$ has already been performed.*

found in Sec. 3.2.4. In order to obtain the final kinetic equation one considers the lesser component of Eq. (3.31) and its adjoint equation. One then subtracts the two equations from each other [56, 105]. This is done in order to remove explicit dependence on the relative time $t_1 - t_2$ on the left-hand side

of the resulting equation, at least to leading order in the gradient expansion. Finally the limit of equal times $t_1 = t_2 = t$ is taken and we later identify the equal time Green's function $-ig^<(t_1, t_1)$ with the distribution function. This procedure leads us to

$$i\partial_t g^<_{\nu_1 \nu_2}(t) - \frac{1}{2}[\xi, g^<(t)]_{\nu_1 \nu_2} - [S, g^<(t)]_{\nu_1 \nu_2} - \frac{1}{2}\Big([\sigma, g^<] - [\sigma^<, g]\Big)$$
$$= \frac{1}{4}\{\sigma^R - \sigma^A, g^<\} - \frac{1}{4}\{g^R - g^A, \sigma^<\} = -St[g] \,. \tag{3.40}$$

Again the convolution of products is implied and we introduced the matrix collision integral in graphene which is given by

$$St[g] = \frac{1}{4}\{\sigma^R - \sigma^A, g^<\} - \frac{1}{4}\{g^R - g^A, \sigma^<\} \,. \tag{3.41}$$

Furthermore, the last term on the left-hand side of the first line of Eq. (3.40) is a renormalization of the Liouvillian on the left-hand side. We will drop it in the following. We will now discuss the physical meaning of the remain terms individually.

3.2.3 Driving terms

We turn now to the intraband driving term, Eq. (3.36) occurring in the quantum kinetic equation (3.40). Furthermore we study the diagonal part of the matrix kinetic equation, that means we set $\nu_1 = \nu_2$ in Eq. (3.40), where $\nu = (\lambda, \vec{k})$. In this case we obtain for the commutator

$$[S^{(1)}, g^<]_{\nu\nu} = \Big(\overrightarrow{S}^{(1)}_{\nu\nu} g^<_{\nu\nu}(t) - g^<_{\nu\nu}(t)\overleftarrow{S}^{(1)}_{\nu\nu}\Big) \,. \tag{3.42}$$

Here no summation over the quantum numbers ν is performed and the arrows indicate that the derivative acts to the right or left. Taking into account that $-i\overrightarrow{\nabla}_k$ is hermitian with the adjoint operator $+i\overleftarrow{\nabla}_k$, we obtain

$$[S^{(1)}, g^<]_{\nu\nu} = -i\frac{e}{c}\vec{E} \cdot \nabla_k g^<_{k,\lambda}(t) \,. \tag{3.43}$$

and with the distribution function defined in Eq. (3.30) this becomes

$$[S^{(1)}, g^<]_{\nu\nu} = \frac{e}{c}\vec{E} \cdot \nabla_k \rho_{k,\lambda}(t) \,. \tag{3.44}$$

While the intraband term (3.37) leads to the usual driving term known from the Boltzmann equation, the interband term $S^{(2)}$ has no classical analog. It rather represents the coherent creation of particle hole pairs [113, 114, 116, 117]. Due to this it couples the diagonal elements of the single-particle density matrix (3.30) with the off-diagonal polarizations. From Eq. (3.37) and the kinetic equation (3.40), we obtain for the interband driving term in the diagonal equations that are obtained for $\nu_1 = \nu_2$ in Eq. (3.40) $[\nu = (\lambda, \vec{k})]$,

$$[S^{(2)}, g^<(t)]_{\nu\nu} = \frac{e}{c}\frac{Ek_\perp}{k^2}\lambda \operatorname{Im}P(t) \,. \tag{3.45}$$

Here we have abbreviated

$$k_\perp = (\hat{z} \times \vec{k}) \cdot \hat{E} \,. \tag{3.46}$$

Similarly in the off-diagonal equations of the matrix kinetic equation (3.40), which is obtained for $\nu_2 = \bar{\nu}_1$ in Eq. (3.40), where $\bar{\nu}_1 = (-\lambda, \vec{k})$, is given by

$$[S^{(2)}, g^<(t)]_{\nu\bar{\nu}} = \lambda\frac{e}{2c}\frac{Ek_\perp}{k^2}i\Big(\rho_{\lambda,k}(t) - \rho_{-\lambda,k}(t)\Big) \,. \tag{3.47}$$

We observe that the interband term couples the populations with the polarization P according to Eq. (3.45), and the polarization to the imbalance between conduction and valence band due to Eq. (3.47).

3.2.4 The collision integral

We introduced the collision integral previously in Eq. (3.41) in an implicit form expressed by the so far unspecified self-energies σ. We are interested in the collision integral due to Coulomb interactions. Explicit expression for the self-energies in Eq. (3.41) are given in Appendix B.2. There we also explain the Markov approximation necessary to derive the collision integral in the form presented below. In this approximation the collision integral has the diagrammatic representation in Fig. (3.2).

The collision integral is also a 2×2 matrix. The diagonal part yields the usual Boltzmann collision integral

$$
\begin{aligned}
St_{\lambda_1 \lambda_1}[\rho_{\lambda_1}(\vec{p}_1)] = & -\frac{N}{2} \int \frac{\mathrm{d}^2 q}{(2\pi)^2} \int \frac{\mathrm{d}\omega}{2\pi} \, |V(q,\omega)|^2 \\
& \times \sum_{\bar{\lambda}_1 = \pm 1} 2\pi \, \delta(\varepsilon_{\bar{\lambda}_1, \vec{p}_1 - \vec{q}} - \varepsilon_{\lambda_2, \vec{p}_1} - \omega) \, \Theta_{\lambda_1, \vec{p}_1; \bar{\lambda}_1, \vec{p}_1 - \vec{q}} \, \rho_{\lambda_1}(\vec{p}_1) \Big[1 - \rho_{\bar{\lambda}_1}(\vec{p}_1 - \vec{q}) \Big] \\
& \times \sum_{\lambda'_1, \bar{\lambda}'_1 = \pm 1} \int_{\vec{p}'_1} 2\pi \, \delta(\varepsilon_{\bar{\lambda}'_1, \vec{p}'_1 - \vec{q}} - \varepsilon_{\lambda'_1, \vec{p}'_1} + \omega) \, \Theta_{\lambda'_1, \vec{p}'_1; \bar{\lambda}'_1, \vec{p}'_1 - \vec{q}} \, \rho_{\bar{\lambda}'_1}(\vec{p}'_1 - \vec{q}) \Big[1 - \rho_{\lambda'_1}(\vec{p}'_1) \Big] \\
& - \{ \rho \leftrightarrow (1 - \rho) \} \,,
\end{aligned}
\tag{3.48}
$$

We observe that again the overlap elements of eigenstates in graphene, the Dirac factors, as introduced in Sec. 1.1 appear in the collision integral (3.48). They read as

$$
\Theta_{\lambda, \vec{k}; \lambda', \vec{k}'} = \frac{1}{2} \left(1 + \hat{v}_{\lambda, \vec{k}} \cdot \hat{v}_{\lambda', \vec{k}'} \right) \,,
\tag{3.49}
$$

where $\hat{v}_{\lambda, \vec{k}} = \lambda \vec{k} / |\vec{k}|$. They are given by the overlap of the graphene eigenstates and prohibit backscattering. We neglected corrections to the Boltzmann collision integral due to a finite interband polarization P. In doing so we obtain the Boltzmann limit of the kinetic equation if we further neglect the interband polarization in the driving terms in the diagonal parts (3.56), which then decouple entirely from the equation for P. In this case we write for the density matrix $\rho_\lambda(\vec{k})$ simply $f_\lambda(\vec{k})$. And we obtain the semiclassical Boltzmann equation for the distribution function f,

$$
\mathcal{L} f_\lambda(\vec{k}) = St[f] \,,
\tag{3.50}
$$

where the Liouvillian is given by

$$
\mathcal{L} = \partial_t + \hat{v} \cdot \nabla_r + \left[e\vec{E} + e(\hat{v} \times \vec{B}) \right] \cdot \nabla_k \,.
\tag{3.51}
$$

The collision integral is a complicated nonlinear operator acting on the distribution function ρ. For practical purposes it is advantageous to consider the linearized collision integral which is denoted $\mathcal{C}$. The latter is obtained by assuming that the system is close to equilibrium and the density matrix is given by $\rho = f^{(0)} + f^{(0)}(1 - f^{(0)})\delta f$, where $f^{(0)}$ is the Fermi Dirac distribution function that annihilates the collision integral. The function δf is a small deviation from this equilibrium. The linearized collision integral is a linear operator acting on the deviation δf. Linearizing the collision integral with respect to the small deviations one obtains,

$$
\begin{aligned}
\mathcal{C} \delta f_{\lambda, \vec{p}} = & \sum_{\nu, \nu', \lambda'} \int_{\vec{k}, \vec{p}', \vec{k}'} |M|^2 \, (2\pi)^3 \delta(\varepsilon_{\lambda p} + \varepsilon_{\nu k} - \varepsilon_{\lambda', p'} - \varepsilon_{\nu', k'}) \, \delta(\vec{p} + \vec{k} - \vec{p}' - \vec{k}') \\
& \times f^{(0)}_{\lambda, p} f^{(0)}_{\nu, k} \left(1 - f^{(0)}_{\lambda', p'} \right) \left(1 - f^{(0)}_{\nu', k'} \right) \Big[\delta f_{\lambda, \vec{p}} + \delta f_{\nu, \vec{k}} - \delta f_{\lambda', \vec{p}'} - \delta f_{\nu', \vec{k}'} \Big] \,.
\end{aligned}
\tag{3.52}
$$

Here the matrix element $|M|^2$ is given by

$$|M|^2 = N V(\omega, q) \Theta_{\lambda_1 \vec{p}_1; \bar{\lambda}_1, \vec{p}_1 - \vec{q}} \Theta_{\lambda'_1 \vec{p}'_1; \bar{\lambda}'_1, \vec{p}'_1 + \vec{q}} \,. \tag{3.53}$$

The Dirac factors Θ have been introduced in Sec. 1.1, see Eq. (1.12).

Similarly the off-diagonal part is responsible for the decay of the polarization due to Coulomb interaction. In principle it is also a complicated nonlinear operator, see Appendix B.2. However, assuming that the polarization is small we restrict it to the terms linear in the interband polarization which reads as

$$
\begin{aligned}
St_{\lambda_1, \lambda_2} = &-\frac{N}{2} \int \frac{\mathrm{d}^2 q}{(2\pi)^2} \int \frac{\mathrm{d}\omega}{2\pi} |V(q, \omega)|^2 \\
&\times \sum_{\bar{\lambda}_1 = \pm 1} 2\pi\, \delta(\varepsilon_{\bar{\lambda}_1, \vec{p}_1 - \vec{q}} - \varepsilon_{\lambda_2, \vec{p}_1} - \omega)\, \frac{1}{2}(1 - \lambda_2 \bar{\lambda}_1 \cos\varphi_{12})\, P_{\lambda_2}(\vec{p}_1)^* \left[1 - \rho_{\bar{\lambda}_1}(\vec{p}_1 - \vec{q})\right] \\
&\times \sum_{\lambda'_1, \bar{\lambda}'_1 = \pm 1} \int_{p'_1} 2\pi\, \delta(\varepsilon_{\bar{\lambda}'_1, \vec{p}'_1 - \vec{q}} - \varepsilon_{\lambda'_1, \vec{p}'_1} + \omega)\, \Theta_{\lambda'_1, \vec{p}'_1; \bar{\lambda}'_1, \vec{p}'_1 - \vec{q}}\, \rho_{\bar{\lambda}'_1}(\vec{p}'_1 - \vec{q}) \left[1 - \rho_{\lambda'_1}(\vec{p}'_1)\right] \\
&+ \{\rho \leftrightarrow (1 - \rho)\} \,.
\end{aligned}
\tag{3.54}
$$

Here φ_{12} is the angle between the momenta $\vec{p}_1$ and $\vec{p}_2 = \vec{p}_1 - \vec{q}$. We observe that in the off-diagonal collision integral the Dirac factors are of a different form. As a consequence the integral kernel for the decoherence time will be suppressed at the forward scattering resonance in contrast to the collision kernel for the diagonal collision integral.

3.2.5 Multiband quantum kinetic equation: Semiconductor Bloch equations

In this section we are going to combine the results from the previous sections and give the final quantum kinetic equations for graphene including the external field to leading order in the gradient expansion. In addition to the dc field discussed for example in Sec. 3.2.3 we will also take into account a classical time-dependent electric field. In this case we are able to study the response of graphene to an external laser pulse. We will briefly discuss the physics in Sec. 3.3, which will serve as a preparation for Chapt. 4, where we study the relaxation dynamics of optically excited carriers in graphene due to electron-electron interactions.

We also take into account a time dependent electric field

$$\vec{E}(t) = \vec{E}_0(t) \cos\omega t \,, \tag{3.55}$$

with a slowly varying envelope function $E_0(t)$ in addition to the dc electrical field E_{dc}. The envelope $E_0(t)$ will be specified in Sec. (3.3), where we consider the specific problem of a Gaussian laser pulse. For the time dependent field we performed the rotating wave approximation. Thus we neglect in the following the off-resonant intraband-driving due to the time-dependent electrical field.

We write the matrix quantum kinetic equation component-wise. The diagonal part is obtained for $\nu_1 = \nu_2 = \nu$ in Eq. (3.40), where $\nu = (\lambda, \vec{k})$ and $\lambda = \pm 1$. Let us introduce the interband dipole moment $\vec{d} = e(\hat{z} \times \vec{k})/k^2$, where $\hat{z}$ is the unit vector in z-direction. In the notation of the previous section the diagonal equations read as

$$\partial_t \rho_{\lambda, k}(t) + \frac{1}{2}[\xi, g^<]_{\nu\nu} + \frac{e}{c} \vec{E}_{\mathrm{dc}} \cdot \nabla_k \rho_{\lambda, k} + \frac{e}{c} \frac{E_{\mathrm{dc}} k_\perp}{k^2} \lambda \mathrm{Im}[P_k(t)] - \lambda \vec{E}(t) \cdot \vec{d}_k \mathrm{Im}[P_k(t)] = St_{\nu\nu}[g] \,. \tag{3.56}$$

The single-particle density matrix $\rho_{\lambda,k}(t)$ was defined in Eq. (3.30). Furthermore $k_\perp$ was defined in Eq. (3.46). On the other hand the equation for the complex polarization is obtained from the kinetic equation (3.40) for $\nu_2 = \bar{\nu}_1$ with $\nu_1 = (\lambda, \vec{k})$ and $\bar{\nu}_1 = (-\lambda, \vec{k})$ and it reads as

$$\partial_t P_k(t) + \mathrm{i}\delta_k P_k + \frac{e}{c}\vec{E}_{\mathrm{dc}} \cdot \nabla_k P_k + \mathrm{i}\frac{e}{2c}\frac{E_{\mathrm{dc}}k_\perp}{k^2}[\rho_{-,k} - \rho_{+,k}] - \mathrm{i}\vec{E}(t) \cdot \frac{\vec{d}_k}{2}[\rho_{-,k} - \rho_{+,k}] = St_{\nu\bar{\nu}}[g] \, . \quad (3.57)$$

Here we introduced the level spacing $\delta_k = \varepsilon_{+,k} - \varepsilon_{-,k} = 2\varepsilon_{+,k} = 2k$. Thus the imaginary part of P obeys

$$\partial_t\mathrm{Im}[P_k](t) + \delta_k\mathrm{Re}[P_k] + \frac{e}{c}\vec{E}_{\mathrm{dc}} \cdot \nabla_k\mathrm{Im}[P_k] + \frac{e}{2c}\frac{E_{\mathrm{dc}}k_\perp}{k^2}[\rho_{-,k} - \rho_{+,k}] - \vec{E}(t) \cdot \frac{\vec{d}_k}{2}[\rho_{-,k} - \rho_{+,k}] = St_{\mathrm{ImP}} \, . \quad (3.58)$$

Semiconductor Bloch equations

We now assume that only a time-dependent electric field is present. Furthermore we introduce the slowly varying polarization

$$p_k(t) = \mathrm{e}^{+\mathrm{i}\omega t}\, P_k(t) \, . \tag{3.59}$$

We then observe that the total population $\rho = \rho_- + \rho_+$ is conserved. Thus only the inversion

$$\Delta\rho = (\rho_- - \rho_+)/2 \, , \tag{3.60}$$

and the complex polarization p_k are dynamical variables. If we assume linearly polarized light, i.e. $\vec{E}_0(t) = \hat{x}E_0(t)$, we can write the quantum kinetic equations (3.56) and (3.57) into the standard form of the optical Bloch equations [20]

$$\partial_t\vec{S} = \begin{pmatrix} 0 & \Delta_k & 0 \\ -\Delta_k & 0 & -\frac{ek_y}{k^2}E_0(t) \\ 0 & +\frac{ek_y}{k^2}E_0(t) & 0 \end{pmatrix} \vec{S} \, . \tag{3.61}$$

Here the Bloch vector is

$$\vec{S} = \begin{pmatrix} \mathrm{Re}(p) & \mathrm{Im}(p) & \Delta\rho \end{pmatrix}^T \, . \tag{3.62}$$

We also introduced the detuning

$$\Delta_k = 2\varepsilon_k - \omega \, . \tag{3.63}$$

Note that only slowly varying functions $p_k(t)$ and $E_0(t)$ enter this equation. In Sec. (3.3) we are going to discuss the simple problem of a Gaussian laser pulse impinging on graphene and study the short-time coherent dynamics directly after the laser quench.

Schwinger mechanism

In this section we briefly discuss the graphene Bloch equations (3.61) in the presence of a constant electric field that is switched on at time $t = 0$. The system is assumed to be in equilibrium before the time $t = 0$. In general we can understand the interaction of the graphene with an optical or constant electric field in terms of spins or equivalently - two level systems. Here a conduction and a valence band state with the same momentum form the two-level system. As a consequence the weak field result (3.66) below resembles the Rabi formula for spin flips in spectroscopy of spin systems.

We start out from the Bloch equations

$$\partial_t \vec{S}(t) = \begin{pmatrix} 0 & -\delta_{\tilde{k}} & 0 \\ +\delta_{\tilde{k}} & 0 & -\frac{eEk_y}{\tilde{k}^2} \\ 0 & +\frac{eEk_y}{\tilde{k}^2} & 0 \end{pmatrix} \vec{S}(t) . \tag{3.64}$$

Here we have $\Delta = \delta = 2\varepsilon_k$ for $\omega = 0$ and we introduced the shifted momentum $\tilde{\vec{k}} = \vec{k} + e\vec{E}t$. The Bloch vector is given in Eq. (3.62).

We seek the solution of Eq. (3.64) for weak electrical field. In this case we neglect the shift of the energy dispersion by the electric field. As a result we obtain

$$\text{Im}[p(t)] = \Delta\rho(-\infty)\frac{eEk_y}{k^2}\frac{\sin(\delta_k t)}{\delta_k} . \tag{3.65}$$

From this we get the inversion

$$\frac{\Delta\rho(t) - \Delta\rho(-\infty)}{\Delta\rho(-\infty)} = \frac{(eEk_y)^2}{2k^6}\sin^2(kt) . \tag{3.66}$$

This formula resembles the exact Rabi result for Rabi flops in spin systems. It has also been obtained in Ref. [118] within a first quantization scheme, directly from the Dirac equation.

3.3 Ultrashort laser pulses in graphene

We apply the semiconductor Bloch equations to the graphene excited by a Gaussian laser pulse and we study the possibility of inversion. The main aim is however to obtain an effective rate equation that is used in Chapt. 4 to describe pump-probe experiments in graphene.

Let us assume that a graphene sheet is exposed to a short laser pulse described by the electrical field $\vec{E}(t)$ with central frequency ω, polarization in $\hat{x}$-direction and envelope function

$$E_0(t) \sim \frac{\bar{E}}{\sqrt{2\pi}\tau}\exp[-(t - t_0)^2/2\tau^2] . \tag{3.67}$$

Here we can chose without loss of generality $t_0 = 0$. The amplitude $\bar{E}$ is connected to the fluence of the pulse. From the Bloch equations (3.61) we immediately see that the change in the inversion after the laser pulse is given by

$$\Delta\rho(+\infty) - \Delta\rho(-\infty) = \frac{ek_y}{k^2}\int_{-\infty}^{+\infty}dt E_0(t)\text{Im}[p(t)] . \tag{3.68}$$

Interestingly, for a short laser quench, i.e. in the regime of energies for which $\Delta_k\tau \ll 1$ one can obtain an explicit expression for the change in the inversion. The calculation is given in Appendix C. The result reads as

$$\frac{\Delta\rho(+\infty) - \Delta\rho(-\infty)}{\Delta\rho(-\infty)} = -\frac{ek_y\bar{E}}{k^2}\sin\left(\frac{ek_y\bar{E}}{k^2}\right) . \tag{3.69}$$

From Eq. (3.69) it is now obvious that we only have a population inversion if

$$x\sin(x) > 1 , \quad x = \frac{ek_y\bar{E}}{k^2} . \tag{3.70}$$

From Eq. (3.70) we obtain the phase diagram for population inversion. Along the direction of strongest light matter coupling, i.e. for $\vec{k} \parallel \hat{x}$, it is depicted in Fig. 3.3(a). We plot the regions where Eq. (3.70) is fulfilled in the plane spanned by the amplitude $\bar{E}$ and the energy k. Those shaded regions indicate population inversion. We observe that for a given field strength the regions of population inversion organize into stripes. This is indicated by the red line in Fig. 3.3(a). The red line also indicates that there is a maximal energy where population inversion can occur. In Fig. 3.3(b) the regions of possible
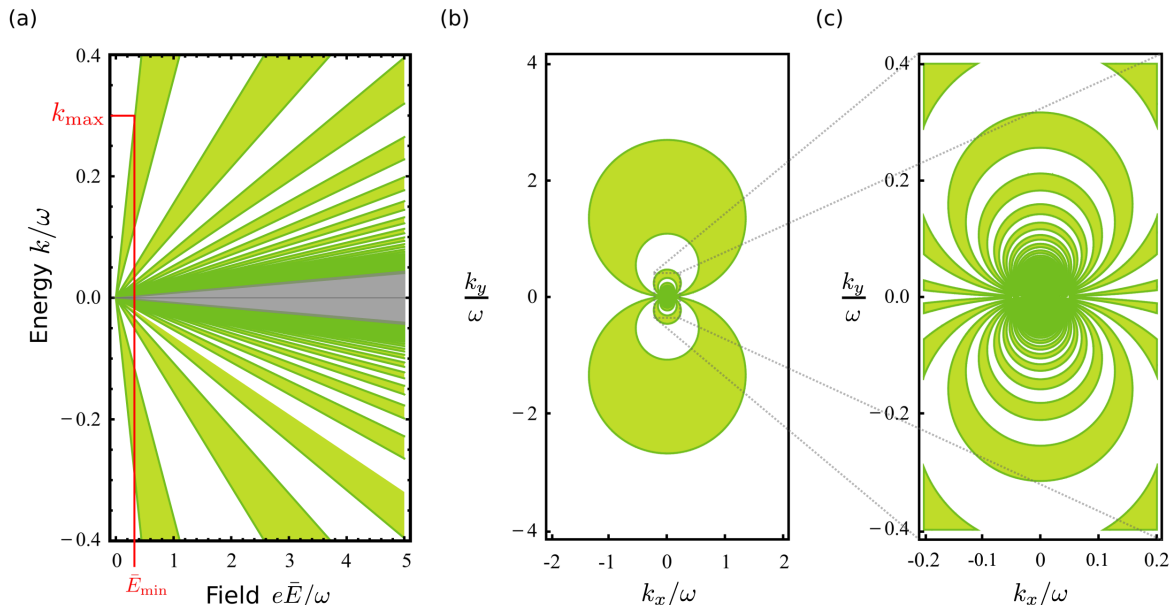

Figure 3.3: *The possible regions for population inversion (green areas) in momentum space. Figure (a) shows the phase diagram along the direction of strongest coupling. For a given energy k_y, we can extract the minimal field strength $\bar{E}_{min}$ at which population inversion is possible. Conversely, at a fixed field strength there is a certain maximal energy k_{max} at which population inversion can occur. Figure (b) illustrates the phase diagram in the 2D momentum space for a fixed field strength $e\bar{E} = \sqrt{2\pi}\omega$. The phase diagram of population inversion clearly shows a self similar structure as can be seen in Fig. (c).*

population inversion are shown in the 2D momentum space for a given field strength $\bar{E} = \sqrt{2\pi}\omega$. We observe that due to the electrons' Berry phase the coupling is the strongest perpendicular to the polarization of the field.

The occurrence of the regions where population inversion is obtained at short times can be understood in the following way. As pointed out already in Sec. 3.2.3 we can indeed interpret the combination of an electronic valence and conduction band state with the same momentum in graphene as a two level system. The argument of the sine in Eq. (3.69) can be understood as the pulse area of the pump pulse [119]. The regions where population inversion occurs are those states for which the given pulse area in combination with the momentum dependence of the dipole matrix element fulfills the condition for a π-pulse [119]. From Fig. 3.3(c) it becomes even more apparent that the pattern of population inversion in principle shows a self-similar structure. In fact, without interactions the graphene is scale invariant and a fractal structure like the pattern in Fig. 3.3(c) might have been expected. However, we must bear in mind that the slow envelope approximation for E_0 means that $\omega\tau > 1$, which means that there

is a finite strip around the resonance $\Delta = 0$ for which this simple picture expressed in Fig. 3.3 holds.

From Fig. 3.3(a), we infer that at a given energy there exists a minimal field strength at which population inversion can occur. On the other hand, for a fixed field strength there is a maximal energy at which population inversion can occur. If we express $\bar{E}$ in terms of the pump fluence density I_p of the laser pulse, we obtain for the maximal energy at which population inversion can be observed

$$\varepsilon_{\max} = \frac{4\pi^{3/4}ev_F\tau}{x_{\min}} \left(\frac{I_p}{\tau c}\right)^{1/2} , \qquad (3.71)$$

which depends on the square root of the pump fluence I_p as well as the pulse length τ. In Eq. (3.71) we have restored the Fermi velocity v_F for convenience and c is the speed of light. The constant $x_{\min}$ in Eq. (3.71) is the smallest solution of Eq. (3.70) for x. We obtain $x_{\min} \sim 1.114$. It is interesting to note that the maximal energy (3.71) depends of the square root of the pump fluence and thus is linear in the amplitude of the laser field. The square root is also confirmed in numerical studies [see discussion below and Fig. 3.5].

The analytical result for short laser pulse agrees well with numerical solutions to the Bloch equations (3.61). The numerical solution of the Bloch equations is shown as a density plot in Fig. 3.4. Here the inversion after the laser pulse, i.e. for $t \gg \tau$ is depicted. The regions of population inversion obtained from the analytical result, Eq. (3.70) are indicated by the dashed black lines.
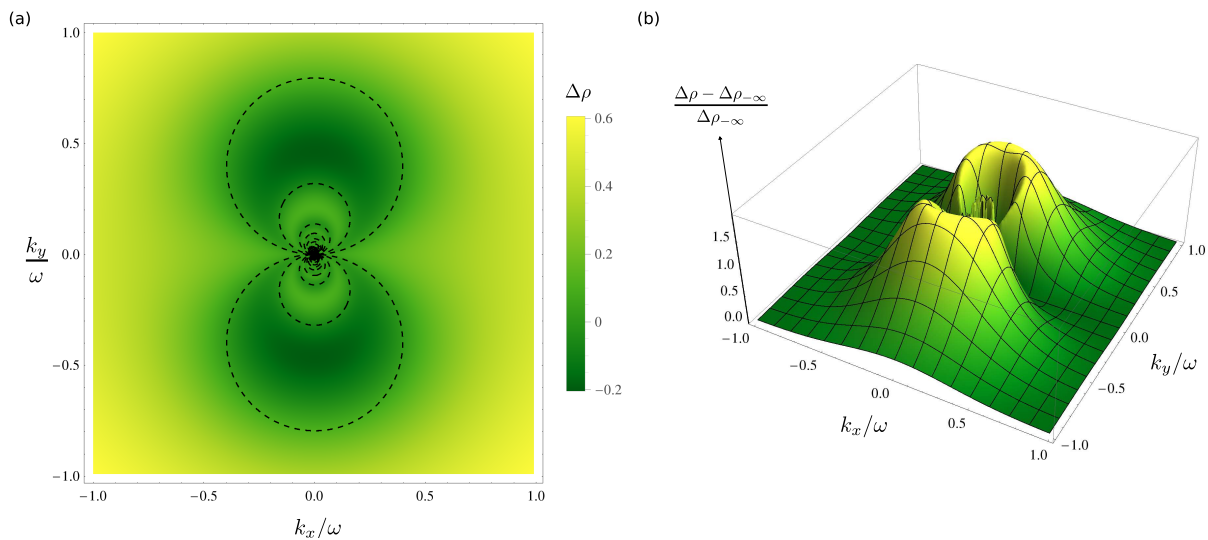
Figure 3.4: *(a) The inversion $\Delta\rho$ for long time, i.e. $t \gg t_0$ and $t - t_0 \gg \tau$. The inversion is obtained from the numerical integration of the non-interacting Bloch equations for a Gaussian quench with $e\bar{E} = \sqrt{2\pi}\omega$ and $\omega\tau = 1$. The regions of population inversion, i.e. $\Delta\rho(+\infty) < 0$ agree with the predicted fractal structure in Fig. 3.3. The black dashes lines denote the analytical result (3.70). (b) The absolute value of the relative inversion $(\Delta\rho(+\infty) - \Delta\rho(-\infty))/\Delta\rho(-\infty)$ from the same simulation as in (a). Values larger than 1 indicate population inversion, i.e. $\Delta\rho(+\infty) < 0$.*

We stress that we do not take into account any relaxation mechanism here. In a realistic setup the inversion will quickly decay due to super-diffusive relaxation by electron-electron interaction (see Chapt. 4) and also due to electron-phonon interaction. However, there is evidence for short-time

population inversion in non-degenerate pump-probe measurements [25, 120]. We will briefly discuss the possibility of population inversion. We already mentioned two major relaxation mechanisms. The relaxation due to optical phonons alone is quenched for energies below the optical phonon frequency [24, 121]. Below the optical phonon frequencies only intervalley acoustic phonons relax electrons [122]. These processes are generally slow and of minor importance at small time scales. Although it should be said that combined scattering of electrons off phonons and disorder leads to very fast energy relaxation, the so-called supercollisional cooling mechanism [61]. Another pathway of relaxation is due to electron-electron interaction where the energy remains in the electronic system. The inverted regions, depicted in Figs 3.3 and 3.4 will be redistributed in momentum space due to electron-electron interaction (see Chapt. 4). More specifically, the excited carriers at higher energies that make up the inverted regions will move quasi-diffusively towards the Dirac-point to thermalize [68]. The rate of thermalization is of the order $\sim \alpha_g^2 T$ if the graphene is close to the Dirac point. It is also known that to leading order in the coupling constant electron-electron interaction conserves the number of particles in the valence- and conduction-band separately [60]. Therefore interaction cannot alter the total inversion, i.e. the inversion integrated over the momentum. All this said, we can conclude that the upper bound (3.71) on the highest energy at which inversion occurs remains valid. In fact the square root dependence agrees qualitatively well with numerical simulations of carriers dynamics by Malic et al, reported in Ref. [28]. Their result is depicted in Fig. 3.5, where the result from the numerical simulation from Ref. [28] is shown. The figure shows the maximal energy at which population inversion is observed at very short times in a numerical integration of the semiconductor Bloch equations. The findings should be compared with our formula (3.71). Indeed they find a square root dependence of the minimal energy as a function of the pump fluence as depicted in Fig. 3.5. Furthermore, if we take into account the relaxation of the inversion in the relaxation time approximation (see Appendix C) the condition in Eq. (3.70) is altered to $x \sin(x) > e^{\Gamma_1 \tau}$. Here Γ_1 is the energy relaxation rate. The expression contains the pulse length τ since in the presence of relaxation the condition for inversion necessarily depends on time. We thus evaluate the condition for inversion right after the pulse has passed.
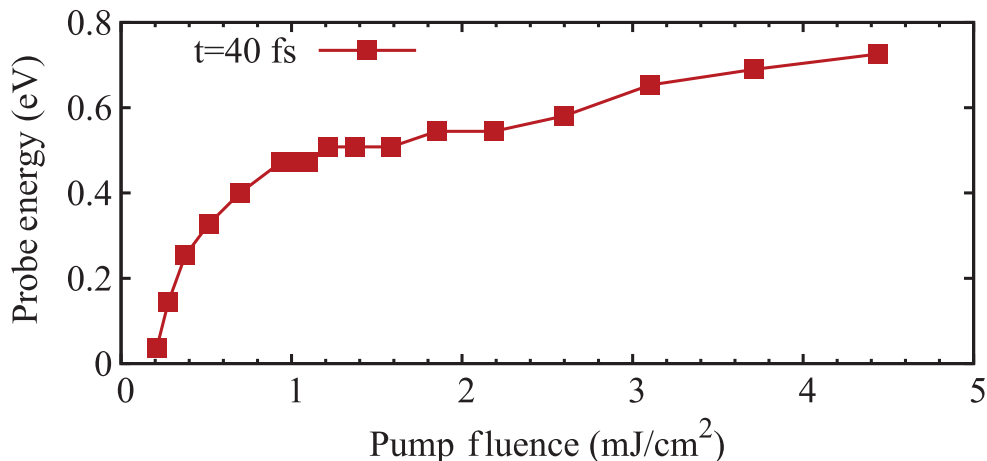

Figure 3.5: *The maximal probe energy at which population inversion is observed 40 fs after the excitation by the pump pulse as a function of the pump fluence I_p. The values were obtained in numerical simulations of the semi-conductor Bloch equations of Ref. [28]. Reprinted figure with permission from: Winzer et al, PRB, 87, 165413 (2013).*

Effective rate equation

Along the calculation that leads us to the result (3.69) for the inversion we also obtain the polarization as a function of time (see Appendix C). In general this relation is implicit. To leading order in the field envelope $E_0(t)$ this relation reads as

$$\text{Im}[p_{\vec{k}}(t)] = -\Delta\rho_{\vec{k}}(-\infty) \, \frac{ek_y}{k^2} \int_{-\infty}^{t} \mathrm{d}t_1 \, E(t_1) \, \cos[\Delta(t-t_1)] \,. \tag{3.72}$$

For the Gaussian pulse (3.67), one can evaluate the integral in Eq. (3.72), which yields
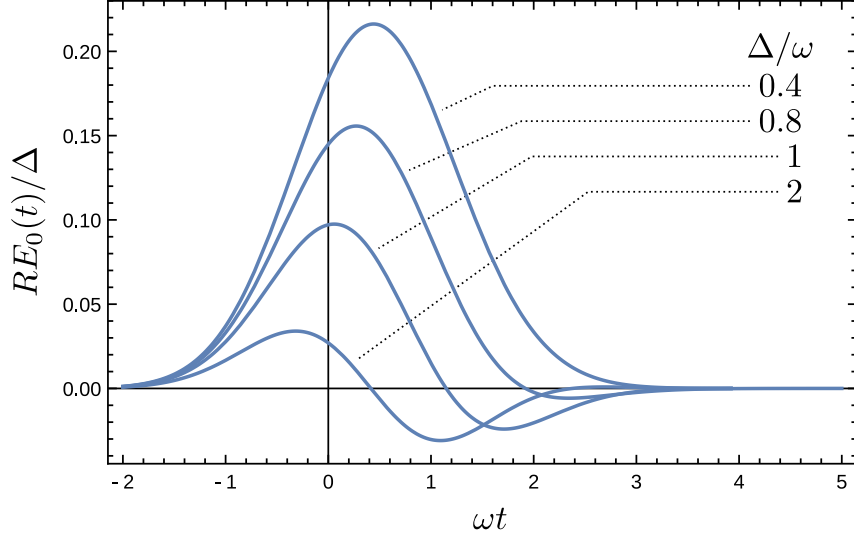
Figure 3.6: *The figure shows the product $E_0(t)R(\Delta t, \Delta\tau)$ for different values of $\Delta\tau$ as indicated in the figure. The function R is given in Eq. (3.74). The Gaussian pulse E_0 is given in Eq. (3.67). We have set $t_0 = 0$.*

$$\partial_t \Delta\rho_{\vec{k}}(t) = -\Delta\rho_{\vec{k}}(-\infty) \left(\frac{ek_y}{k^2}\right)^2 \bar{E} \, E_0(t) \, R(\Delta(t-t_0), \Delta\tau) \,. \tag{3.73}$$

Here the function $R(x, y)$ is given by

$$R(x, y) = \frac{1}{2} \, e^{-y^2/2} \, \text{Re}\left\{ e^{-ix} \left[1 + \text{Erf}\left(\frac{x - iy^2}{\sqrt{2}y} \right) \right] \right\} \,. \tag{3.74}$$

Given the frequency ω we can also compare Δ/ω with $\omega\tau$ to discriminate between short and long pulses. Using this normalization the behavior of the product $E_0(t)R(\Delta(t-t_0), \Delta\tau)$ is depicted in Fig. 3.6. One observes that the generation rate in Eq. (3.73) decreases for large Δ/ω. The product $E_0(t)R(\Delta(t-t_0), \Delta\tau)$ also starts to oscillate and even becomes negative for increasing Δ/ω. As a consequence of this oscillations around zero, as for example in the case of $\Delta/\omega = 2$ in Fig. 3.6, the excitation of electron hole pairs off-resonance becomes less efficient. The characteristic quantity determining the deviation from resonance is the dimensionless product $\Delta\tau$. This variation of the generation rate with detuning Δ is an expression for the uncertainty relation. Short pulses have a

broadband optical spectrum and excite electron hole pairs also off-resonance, whereas for longer pulses effectively only $\Delta = 0$ is relevant. Interestingly the product of the field envelope $E_0(t)$ and the function $R(\Delta(t - t_0), \Delta\tau)$ entering the generation rate on the right-hand side of Eq. (3.73) yields simply

$$\int_{-\infty}^{+\infty} dt\, E_0(t) R(\Delta(t - t_0), \Delta\tau) = \frac{1}{2}\, e^{-\Delta^2\tau^2}\,, \qquad (3.75)$$

when integrated over time t.

Finally, in the very extreme case $\Delta\tau \to 0$ we obtain from the equation (3.73),

$$\partial_t \Delta\rho_{\vec{k}}(t) = -\Delta\rho_{\vec{k}}(-\infty) \left(\frac{ek_y}{k^2}\right)^2 \Theta(t - t_0)\, \bar{E}\, E_0(t)\,. \qquad (3.76)$$

Here we used that from $\Delta\tau \ll 1$ follows $\Delta(t - t_0) \ll 1$ and Θ is the Heaviside Theta function with $\Theta(0) = 1/2$. Finally one can rewrite the kinetic equation again for $\rho_{\lambda,\vec{k}}$ using the relation $\rho_{\lambda,\vec{k}} = \rho_{\vec{k}}/2 - \lambda\Delta\rho_{\vec{k}}$. This yields the effective rate equation for the distribution function for $t_0 = 0$,

$$\partial_t \Delta\rho_{\lambda\vec{k}}(t) = +\lambda\Delta\rho_{\vec{k}}(-\infty) \left(\frac{ek_y}{k^2}\right)^2 \bar{E}E_0(t)R(\Delta t, \Delta\tau)\,. \qquad (3.77)$$

We end up with a single equation for the distribution function $\rho_{\lambda,\vec{k}}$, that does not contain the polarization explicitly anymore. The rate equation (3.77) is used later in Chapt. 4.

3.4 Discussion and comparison with other theoretical works

We comment on the relation of the semiconductor Bloch equations derived so far for the description of optical pump-probe experiments with other theoretical approaches in the literature. The Bloch equations have been used extensively in the context of semiconductor pump-probe experiments, see for example Ref. [20]. In the equations derived here in particular the interband matrix element is characteristic for graphene. As a side remark, the overlap $\langle u_{+,\vec{k}}|\nabla_k|u_{-\vec{k}}\rangle$ that determines the interband matrix element is also called the Berry connection. Interestingly these matrix elements, the Berry connection, appear to be divergent for small energies and we comment on that below.

In the context of graphene similar equations have been employed in Refs. [123, 124] and Refs. [21, 22, 28, 29]. Here, the Refs. [21, 22, 28, 29] performed numerical simulation of the semiconductor Bloch equations in the presences of collisions in contrast to the analytical analysis presented here. Here the works reported on in Refs. [123, 124] employed a phenomenological approach to dephasing without further collisions and performed perturbative solution of the Bloch equations. Interestingly the perturbative solutions including a momentum independent phenomenological dephasing lead to a divergent nonlinear response at the Dirac point [124]. Since we also obtain an expression for the off-diagonal collision integral due to Coulomb interaction we can estimate the dephasing due to electron-electron interaction. The calculation (see Appendix B.2) yields that in fact the dephasing also diverges approaching the Dirac point. Therefore it is expected to compensate the divergence in the optical interband matrix element.

3.5 Summary

In this chapter we present the derivation of the quantum kinetic equation for graphene. Since graphene is a two-band system the resulting quantum kinetic equation is a 2×2 matrix equation in band space. More importantly the distribution function exhibits the same matrix structure. Here the off-diagonal elements represent the microscopic interband polarization also called interband coherence. In particular a classical light field couples the diagonal populations with the off-diagonal interband coherence. This coupling is mediated by the matrix element of the optical interband transition. The latter is the Berry connection of the two-band system. The matrix element also yields the angular dependence of the coupling to the electric field. We find that the coupling is the strongest perpendicular to the polarization of the external light field. This fact is a consequence of the pseudospin conservation along the direction of the polarization of the electromagnetic field.

Finally we derive expression for the collision integral due to electron-electron interaction which contains the graphene specific Dirac factors. The latter are again a manifestation of the multiband character of the system. It is a direct consequence of the two bands being gapless and therefore representing massless Dirac particles. Apart from the diagonal part of the collision integral due to Coulomb interaction we also derive the out-scattering part to leading order in the polarization. The latter describes for example dephasing of the interband decoherence due to Coulomb scattering.

The resulting system of equations makes up the semiconductor Bloch equations for graphene including Coulomb interaction. These equations represent a versatile formalism, in particular suitable to study pump-probe setups. The formalism also represents the basis of our following discussion of the relaxation of high-energy electrons due to Coulomb interaction that is important for optical pump-probe experiments.

We apply the equations to the problem of laser pulses impinging on a graphene sample. Here we include the relaxation in terms of a phenomenological relaxation time. For very short pulses we obtain an analytical expression for the population inversion after the pulse. This result is strictly nonlinear in the fields as there is no population inversion to leading order in the electric field. From the analytical result for the population inversion in the nonlinear regime and short pulses we derive the central result of this part. We find that there is a maximal energy at which population inversion can occur after the pulse has passed the system. More specifically, we find that the threshold scales with the square root of the pump fluence and also with the square root of the pulse length. If we turn the above statement around, we can also say that for any given energy there exists a minimal pump fluence to achieve population inversion after the pulse. This result is in accordance with numerical calculations including the relaxation.

While the semiconductor Bloch equations include the field to all orders we also derive an effective rate equation for the populations in the conduction and valence band alone. In this effective equations the interband polarization disappears. Still the resulting equation contains the energy and angular dependence of the optical matrix element. Furthermore it contains the full time dependence of the generation rate of particle-hole pairs due to the laser pulse. This result is distinctly different from the often encountered time integrated generation rate. The latter is proportional to the Fouriertransform of the laser pulse. In particular in the analysis of experimental data this simplification has been used before.

4

Chapter 4

Pump-probe measurements in graphene

This chapter is devoted to the relaxation of optically excited carriers as they are created in pump-probe experiments. In this section we are going to utilize the techniques developed in the previous chapter to explore the early stage of the relaxation of high-energy electrons after laser excitation. We are going to analyze the relaxation of electrons due to Coulomb interaction and finally make connection to the experiments on the basis of the effective rate equation derived in Chapt. 3.

4.1 Pump-probe experiments

This section serves as a brief overview of the recent experimental activity on pump-probe experiments in graphene in various regimes of parameters.

Pump-probe experiments are a powerful tool to investigate short-time dynamics in various types of systems. Advances in pump-probe measurements over the recent years have given access to femtosecond time-scales. And those techniques have become the predominant tool to study transient non-equilibrium dynamics.

The basic idea is as follows. First, the system is excited by the pump pulse. The pump creates an initial non-equilibrium state. This can be an excited state of an atom. Or in the case of semiconductors, and in particular in the case of graphene, the pump excites electron-hole pairs. The pump pulse is usually of high intensity. In experiments on graphene the pump fluence ranges between $I \simeq 300 - 3800 \, \mu\text{J}/\text{cm}^2$ [17, 21, 22, 25, 30]. Above fluences of $I_p \simeq 1800 \, \mu\text{J}/\text{cm}^2$ the experiment shows nonlinear pump fluence dependence in the probe signal [25]. Apart from the fluence a desired frequency can be chosen among the available laser sources. The temporal resolution is naturally limited by the pulse length of the initial pump as well as the length of the probe pulse following the pump after a certain delay time. The variation of the time delay between the pump and the probe enables the observation of the time-evolution of the system. The probe is usually a second laser pulse that measures the change in transmission of the sample. However it is also possible to use ARPES, Raman or fluorescence spectroscopy as a probe. In general direct and indirect measurements of the system's state must be distinguished. We discuss two different techniques for pump probe measurements that are important for our theoretical study.

First, the probe can simply measure the transmission or reflectivity of the graphene after the excitation by the pump. More specifically the most common observables are the differential change in transmission $\Delta\mathcal{T}/\mathcal{T}_0$ or the differential change in reflectivity $\Delta\mathcal{R}/\mathcal{R}_0$. Here $\Delta\mathcal{R} = \mathcal{R}(t) - \mathcal{R}_0$ and $\Delta\mathcal{T} = \mathcal{T}(t) - \mathcal{T}_0$ are the change in reflectivity and transmission, where $\mathcal{R}(t)$ and $\mathcal{T}(t)$ are the total

reflectivity or transmission at time t. On the other hand $\mathcal{R}_0$ and $\mathcal{T}_0$ are the equilibrium values as given in Sec. 2.3 for high frequencies in graphene. These kind of experiments are an indirect measurement of the state of the system since the macroscopic transmission is already an average of all microscopic states. We have also seen this in Sec. (2.3), where the connection between the transmission and the optical conductivity has been established. Furthermore, the probe can measure the transmission of the sample at the same frequency as the pump, in which case the setup is called a degenerate pump-probe measurement, or the probe pulse measures the transmission at a different frequency. In a common setup for graphene the system is excited in the ultraviolet and probed in the THz region. This basically implies a measurement of the effective electron temperature by the probe pulse as in Ref. [30]. This work also established the cascade picture that we will discuss in the following section.

Other experiments at higher pump fluences, see for example Ref. [25], investigated the possibility of population inversion in graphene, a topic we have briefly touched upon in Sec. 3.3. Here the system was pumped with a source exhibiting the frequency $\omega = 1.55\,\mathrm{eV}$ and probed in the degenerate setup as well as with low energy probes with frequencies $\omega = 1.16\,\mathrm{eV}$ and $\omega = 1.33\,\mathrm{eV}$. At the highest fluence of $I = 3.9\,\mathrm{mJ/cm^2}$ the system shows a population inversion at the low-energy probe frequency whereas the threshold for population inversion at the pump frequency has not been reached. The result is qualitatively consistent with our findings in Sec. 3.3. There we have seen that indeed at a given field strength a maximal energy where population inversion can occur exists.

A third group of experiments we want to discuss within the group of indirect pump-probe measurements is devoted to the study of possible Auger processes in graphene, as for example in Ref. [22]. However, there seems no unambiguous evidence for the presence of Auger processes. As we have mentioned in Chapt. 1, there are severe restrictions for Auger processes. We will again comment on the possibility of Auger processes later in this chapter (see Sec. 4.3.2). However, we will disregard them in the following analysis, again for reasons stated in Sec. 1.2.1.

Another more recent avenue of research for graphene is a direct measurement of the electronic state of the graphene after the pump pulse by means of ARPES measurements. Here the ARPES laser pulse constitutes the probe and the technique directly measures the electronic distribution function. A prominent example is the work in Ref. [125]. With down to femtosecond time resolution the very early stage of electronic relaxation has been measured directly from the distribution function. We will come back to this experiment at the end of this chapter.

4.2 Previous theoretical work

Since the first pump-probe experiments on graphene [17, 18] there has been intensive theoretical work on the description of the relaxation mechanisms in graphene. Those works of course follow the experimental trends and questions that we have briefly reviewed in the preceding section. Initial theoretical work focused on pump-probe transmission spectroscopy while numerical studies also accessed the time-evolution of the distribution function. Several theoretical works explored the possibility of population inversion [28, 126, 127]. Regarding the calculation of the relaxation rates the theoretical studies so far focused on the relaxation rates of thermal electrons using static or dynamical screening in the random phase approximation as in Refs. [35, 39, 57, 58, 73, 128].

Specifically for the pump probe experiments comprehensive numerical studies elucidated the interplay of the electron-electron interactions and phonon interactions [22, 129] as well as the importance of different scattering channels in particular in the context of carrier multiplication via Auger processes [130]. The relaxation of optically excited carriers in doped graphene was theoretically studied [31] at

zero temperature. Here, the cascade picture was developed that we will explain below. The latter was experimentally confirmed in Ref. [30].

This chapter extends the calculation of relaxation rates to high energies $\varepsilon \gg \max(|\mu|, T)$. Therefore we are also considering finite temperature in contrast to previous works. Furthermore we develop an analytical theory to describe the electronic relaxation of high-energy electrons due to Coulomb scattering in pump-probe experiments. As we have seen in Sec. 3.3 the semiconductor Bloch equations developed in Sec. 3.2.5 are also suitable to study the nonlinear response as for example in Ref. [131].

4.3 The relaxation of high-energy electrons - anomalous diffusion and Lévy flights

In this section we will present the results of our findings on the relaxation of high-energy carriers as they arise in the optical pump-probe experiments described in the beginning of this chapter. More specifically, we are going to explore the relaxation of high-energy electrons due to electron-electron interaction. Experiments [30] and numerical simulations [22, 28] suggest that electron-electron interaction is the fastest scattering process and is responsible for the relaxation cascade of optically excited carriers after laser excitation.

4.3.1 The relaxation cascade

Among the experiments mentioned in the previous section the work reported in Ref. [30] established the concept of the cascade picture describing the relaxation processes of the optically excited carriers in graphene. We briefly explain the relevant ideas.

In the above mentioned work, Ref. [30], the authors studied the relaxation of optically excited carriers in a pump-probe setup. They considered the graphene at finite chemical potential μ. The main goal was to find evidence for carrier multiplication. While they did not see any evidence for interband carrier multiplication due to Auger processes (see Sec. 1.2.1), they could conclude that during the relaxation process the high-energy electrons successively excite particle-hole pairs within the conduction band. In order words the high-energy electrons scatter with thermalized electrons at low energies and promote them above the Fermi surface. The characteristic energy transfer in a single scattering event could be shown to be of the order of the Fermi energy. The latter finding was supported by a theoretical analysis of the scattering process where an average transferred energy of the order of the Fermi energy was confirmed [31]. The fact that the high-energy electrons relax in successive steps of the size of the Fermi energy is exactly what is meant by the term relaxation cascade. The evidence for a fixed step width is the following. The temperature after thermalization is a measure of the number of excited electrons above the Fermi energy. The latter in turn is proportional to the number of steps in the cascade. A simple approximately linear scaling between the temperature and the frequency of the light that sets the length of the cascade thus implies an on average constant step size.

Within the cascade picture, the frequency of the pump sets the length scale of the relaxation cascade. The temperature after thermalization is a measure for the number of hot electrons that have been promoted above the Fermi surface. The approximately linear scaling again implies that the electrons relax on average in successive steps. Very importantly, the interpretation above also implies that the cascade is due to electron-electron collisions [30]. Phonon-processes are much slower and become important at a later stage to reduce the electronic temperature [24, 121]. In contrast, during the cascade the energy of the pump-pulse stays nearly entirely in the electronic system.

The question we are now concerned with is first what is the detailed statistics of the cascade for finite temperatures. More specifically, what is the character of a single scattering event in the limit $|\mu| \gg T$ and $T \gg |\mu|$ respectively. With respect to the entire cascade the fluctuations of the average step size are also important.

4.3.2 A single cascade step

Our aim is to understand the relaxation cascade (see Sec. 4.3.1) in terms of a random walk. To this end we are first going to study a single cascade step. We are going to study the relaxation step by means of the semi-classical Boltzmann equation for a homogeneous graphene sheet. Therefore the occupation of a given state will be given by the distribution function measuring the local probability or phase space density. For moderate pump fluence the phase space density of the excited electrons is much lower then the one of thermal electrons. Scattering and energy relaxation of a high-energy excited electron is therefore predominantly due to interaction with thermal electrons. We neglect the mutual scattering of high-energy electrons and assume that the low energy electrons remain thermal with temperature T. For small fluences we also neglect the change in T due to illumination. We are also not going to ask for the generation of the excited electrons by the initial laser pulse at this stage of the analysis. The quantum kinetic equation in the form of the Bloch equations is suitable to study this broader question. In this limit the diagonal part of the optical Bloch equations assumes the Boltzmann form and we will therefore use the notation $\rho_{\lambda,\vec{k}} \to f_\lambda(\vec{k})$ for the distribution function in the following. Since our aim is first to understand the relaxation dynamics we simply look at an initially prepared disturbance to the thermal distribution $f^{(0)}(\varepsilon) = 1/[1 + \exp((\varepsilon - \mu)/T)]$, of the form

$$f_\lambda(\vec{k}) = f^{(0)}(\lambda k) + \delta f_\lambda(\vec{k}) \,, \quad \delta f_\lambda(\vec{k}) = \delta_{\lambda,+1} \delta_{\vec{k},\vec{p}} \,. \tag{4.1}$$

Based on the approximations mentioned above we now follow the evolution of a single electron added due to the correction $\delta f_\lambda(\vec{k})$. The excited electron starts its relaxation process at momentum $\vec{p}$ as it relaxes due to scattering with the thermal electrons with energies $\varepsilon \ll \varepsilon_p$. Since we focus here on the dynamics of the high-energy electrons rather than the questions associated with the equilibration of the low energy thermal electrons we do not consider changes to the distribution function at low energies. Remember that strictly speaking, we also restrict our analysis to the earliest stage dominated by electron-electron interactions as explained previously, in which the energy remains entirely in the electronic system. Therefore, within the cascade picture the excited electrons with an energy of the order $\omega_{\text{pump}}/2$ are relaxing in consecutive steps due to the interaction with a thermal bath of low energy electrons at equilibrium. The time-evolution of the perturbation δf in Eq. (4.1) is governed by the semi-classical Boltzmann equation. The relaxation rate for the high-energy electron is therefore defined via the Boltzmann equation according to

$$\partial_t \delta f_\lambda(\vec{k}) = St[f_\lambda(\vec{k})] \,. \tag{4.2}$$

The collision integral $St[f]$ describes the electron-electron scattering and is explicitly given in Sec. 3.2.4. We emphasize again that we are considering an electronic state with momentum $\vec{p}$ in the conduction band and energy $\varepsilon_p = |\vec{p}|$, see also Eq. (4.1).

With the ansatz (4.1) inserted into Eq. (4.2), we observe that the relaxation rate of the high-energy electron is determined by the out-scattering rate in the collision integral. The latter reads as

$$St[f_{+1}(\vec{p})] = -\sum_{2,3,4} W_{12,34} f_3 (1 - f_4)(1 - f_2) \,. \tag{4.3}$$

In Eq. (4.3) we used the short-hand notation $i = (\varepsilon_i, \vec{k}_i)$. The transition rate of Coulomb scattering $W_{12,34}$ is given in Appendix D. Here, we remind the reader that in the case of Dirac particles it contains the overlap of the eigenstates $\langle \lambda_j, \vec{k}_j | \lambda_i, \vec{k}_i \rangle$, that leads to a suppression of backscattering, in addition to the semiclassical matrix element of Coulomb scattering. We have also seen this in Chapt. 3 where we derived the quantum kinetic equation. In the following analysis of the random walk in energy space that will describe the cascade it is advantageous to express the rate in terms of the transferred energy ω and momentum q. For the energies ε_i of the scattering states in the transition rate W in the Boltzmann equation (4.2) we have, $\varepsilon_1 = \varepsilon_p$, $\varepsilon_2 = \varepsilon_p - \omega$, $\varepsilon_3 = \varepsilon_4 - \omega$ and $\vec{k}_2 = \vec{p} - \vec{q}$, $\vec{k}_3 = \vec{k}_4 - \vec{q}$, due to the conservation of energy and momentum.

According to the discussion of the kinematics of the electron-electron interaction in graphene in Sec. 1.2.1 we can classify the possible scattering processes in terms of interband, $|\omega| > q$, and intraband scattering, $|\omega| < q$. Collinear scattering occurs exactly at $|\omega| = q$. But as we have also discussed in Sec. 1.2.2, the phase space is not only negligible, dynamical screening in the random phase approximation also leads to an additional suppression of collinear scattering, though the presence of additional scattering mechanisms may invalidate this statement.

We now make progress on the scattering rate. Combining Eqs. (4.2) and (4.3) we obtain an expression for the relaxation rate Γ_p of the photoexcited electron, defined by the Boltzmann equation

$$\partial_t \delta f_{+1}(\vec{p}) = -\Gamma(p) = St[f_{+1}(\vec{p})] \,. \tag{4.4}$$

Interestingly the scattering rate Γ can be written in terms of the following integral over all transferred energies ω,

$$\Gamma = \int_{-\infty}^{+\infty} d\omega \, P(\omega) \,. \tag{4.5}$$

Here $P(\omega)$ is the scattering rate per frequency interval $(\omega, \omega + d\omega)$. On the other hand it defines the distribution of the transferred energy in a single scattering event or cascade step. We thus refer to $P(\omega)$ as the jump-size distribution (JSD) of the relaxation cascade. This is exactly the probability distribution we are seeking for to describe the relaxation process as a random work. And all its characteristics will be derived from the JSD $P(\omega)$.
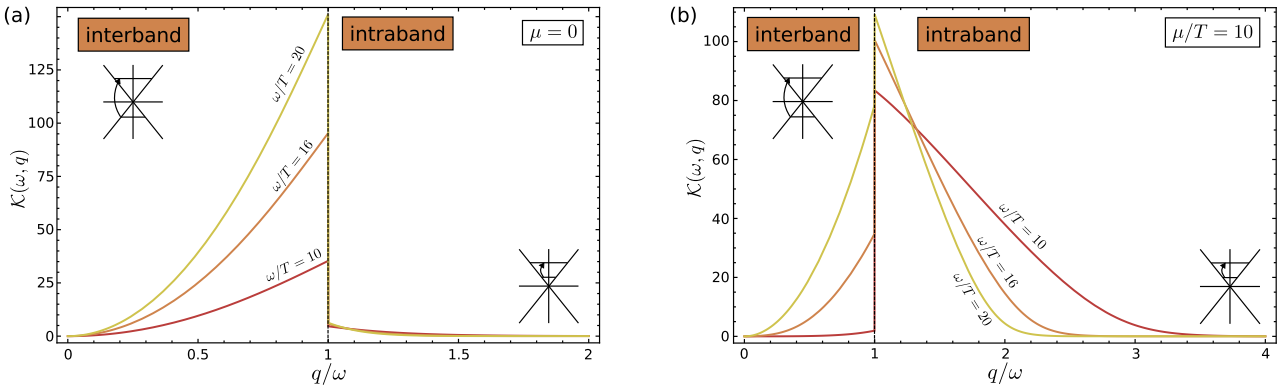

Figure 4.1: *The kernel $\mathcal{K}(\omega, q)$, Eq. (4.9), determining the phase space of scattering for thermal electrons for different frequencies ω and (a) $\mu = 0$, (b) $\mu/T = 10$. The regions of intraband ($q > |\omega|$) and interband ($q < |\omega|$) scattering are separated by the dashed line.*

As long as $\omega < \varepsilon_p$ the excited electron is scattered within the conduction band, which implies $q > |\omega|$. Since the particle number in the conduction and valence band are separately conserved in pair collisions, the thermal electron that scatters with the high-energy electron also performs an intraband transition [60]. We find that the contribution for $\omega > \varepsilon_p$ corresponding to interband transitions is negligible for the relaxation rate Γ, Eqs. (4.4) and (4.5), as well as for the statistics of the entire cascade (see Sec. 4.3.1). Moreover, calculation shows that the relevant transferred energies satisfy $|\omega| \ll \varepsilon_p$. Scattering in this case is predominantly in forward direction, which simplifies the overlap functions

$$|\langle \lambda_2, \vec{k}_2| + 1, \vec{p}\rangle|^2 = \frac{1 + \lambda_2(\vec{p} \cdot \vec{k}_2)/pk_2}{2} \simeq 1 \,. \tag{4.6}$$

Taking into account that $f_2 \simeq 0$ for $|\varepsilon_p - \omega| \gg \max(|\mu|, T)$ in Eq. (4.3), we obtain the compact expression for the JSD,

$$P(\omega) = \int_{|\omega|}^{\infty} \mathrm{d}q \, q \, \frac{N|V(\omega, q)|^2}{|q^2 - \omega^2|} \mathcal{K}(\omega, q) \,. \tag{4.7}$$

Here we assumed $\varepsilon_p \gg \max(|\mu|, T)$ and as a consequence $P(\omega)$ is independent of the particle energy ε_p. In Eq. (4.7) the RPA-screened matrix element of Coulomb scattering

$$V(\omega, q) = V_0(q)/\varepsilon(\omega, q) \,, \tag{4.8}$$

where the dielectric function $\varepsilon(\omega, q) = 1 + V_0(q)N\Pi(\omega, q)$. The RPA polarization operator $\Pi(\omega, q)$ is given in Sec. 1.2.2. The bare Coulomb interaction $V_0(q) = 2\pi\alpha_g/q$ has also been introduced in a broader discussion in Sec. 1.1. The number of flavors $N = 4$ and the coupling constant in graphene $\alpha_g = e^2/\epsilon\hbar v_F$ in our notations is $\alpha_g = e^2/\epsilon$. Remember that in the presence of a dielectric environment with dielectric constant $\epsilon \gg 1$ the coupling constant can be small, $\alpha_g \ll 1$, which we assume in the following. Therefore we adopt the weak coupling assumption already employed in the RG analysis in Sec. 1.3. Finally the integral kernel $\mathcal{K}$ in Eq. (4.7) describes the phase space of the thermalized electrons that scatter with the photo-excited electron under consideration. It is defined according to

$$\mathcal{K}(\omega, q) = \int_{-\infty}^{+\infty} \mathrm{d}\varepsilon_4 \, \sqrt{(\omega - 2\varepsilon_4)^2 - q^2} \, f_T(\varepsilon_4 - \omega)[1 - f_T(\varepsilon_4)] \,. \tag{4.9}$$

We will call the kernel $\mathcal{K}$ in the following the kinetic kernel. The asymptotics can be found in Appendix D. It is furthermore related to the vertex function $\Gamma^{(0)}$ introduced in Appendix. E.3. The relation reads as

$$\mathcal{K}(\omega, q) = \frac{T\sqrt{|q^2 - \omega^2|}}{1 + \mathrm{e}^{-\omega/T}} \Gamma^{(0)}(\omega, q) \,. \tag{4.10}$$

The latter naturally arises when solving the linearized Boltzmann equation. It has a simple diagrammatic correspondence in the high temperature Boltzmann limit as will also be explained in Appendix E. This diagrammatic correspondence agrees with the interpretation as a phase space weight as adopted here. The kinetic kernel is illustrated in Fig. 4.1.

At this point we briefly need to comment on the validity of the RPA. We refer mainly to our review in Sec. 1.2.2. We have mentioned in Chapt. 1.2.2 that the RPA is also logarithmically accurate for small frequencies $|\omega| < \max(|\mu|, T)$. This follows from the RG calculation justified in the large N limit. That means for $|\omega| > \max(T, |\mu|)$ the RPA as well as the results derived on the basis of the RPA screening here are correct in the large N limit. The RPA screening is important for the following analysis since we immediately realize that the denominator of the integrand in Eq. (4.7) is singular in the

case of collinear scattering $|\omega| = q$, which in the absence of screening would lead to the logarithmically divergent Coulomb scattering integral [39, 69, 132]. However the polarization operator in RPA is also divergent in the case of collinear scattering, thus the total scattering amplitude remains finite. We refer to Sec. 1.2.2 for more details and a discussion thereof. In passing we remark that the singular nature of the scattering of Dirac particles with linear dispersion also manifests itself in the phase space kernel (4.9). Figure 4.1 shows $\mathcal{K}$ for intrinsic graphene ($|\mu| \ll T$) as well as for $|\mu| \gg T$. In either case $\mathcal{K}$ exhibits a jump at collinear scattering. One observes that for $\mu = 0$ [Fig. 4.1(a)] the phase space of intraband processes is strongly suppressed and controlled by T. On the contrary, for $|\mu| \gg T$ [Fig. 4.1(b)] $\mathcal{K}$ is dominated by intraband processes.

We now have derived the definition of the probability density of the random walk – the jump-size distribution (JSD). Let us now discuss the JSD separately for $T \gg |\mu|$ and $|\mu| \gg T$, before we move on to reformulate the relaxation cascade finally as a random walk in Sec. 4.4.

The quantum critical region in the limit $T \gg |\mu|$

Close to the Dirac point or in other words in the quantum critical regime of $T \gg |\mu|$, we expect anomalous relaxation rates as we have discussed in Chapt. 1 and as it is known in literature [58, 73]. For the regime $T \gg |\mu|$, the JSD is depicted in Fig. 4.2. For $T \gg |\mu|$, there are two important scattering processes. The first one is intraband scattering with small momentum transfer $q < 2T$, which leads to a logarithmic divergence in the JSD for frequencies $|\omega| < \alpha_g T$, depicted as the dash-dotted line in Fig. 4.2(b). The logarithmic divergence is a characteristic feature of the Coulomb collision integral in particular in two dimensions. As we discussed in Chapt. 1 a similar logarithmically divergent electron-electron collision integral is known as the Landau collision integral in plasma theory. Here, that means in the JSD as depicted in Fig. 4.2(b), the logarithm occurs due to the failure of screening at small frequencies and momenta which enables resonant forward scattering. The logarithmic divergence is however integrable since it is cut off by screening effects at larger momenta.

The contribution of scattering with $q < 2T$, that is responsible for the logarithmic divergence decreases monotonically with increasing frequency and vanishes for $|\omega| \geq 2T$ since $|\omega| > q$ forbids intraband scattering.

The second kind of process is intraband scattering with large momentum transfer $q > 2T$. This contribution increases with increasing frequency up to $\omega = 2T$. It dominates over scattering with small momentum transfer for $\omega \sim 2T$ and higher frequencies. For frequencies $\omega > 2T$ it decreases monotonically. Specifically, we find that at large ω the JSD falls of as $\omega^{-5/2}$, shown in Fig. 4.2(a).

There is a finite probability for the excited electron to gain energy from the bath of thermal electrons. However negative frequencies are exponentially suppressed as shown in Fig. 4.2(a). This fact is simply an expression of the irreversible and dissipative character of the interaction of the high-energy electron with the thermal electrons. In principle one can also view the ratio between gain and loss $P(-|\omega|)/P(+|\omega|) \sim \exp(-|\omega|/2T)$ as a manifestation of fluctuation relations that are well established in equilibrium thermodynamics however under debate in the generic non-equilibrium situation [133].

The slow decay of the JSD for large frequencies has important implications for the fluctuations of ω as discussed in Sec. 4.3.1. In particular it is different from the JSD of a Fermi liquid which is flat in the range $0 < \omega < \varepsilon_p$. Thus an electron in a Fermi liquid would lose most of its energy by a single jump. The Fermi liquid regime is realized under the conditions $|\mu| \gg T$ and $\varepsilon_p \ll |\mu|$.

Important for the cascade is also the characteristic timescale associated with a single scattering event. Therefore we calculate the total scattering rate Γ, given by Eq. (4.5). It turns out that for the scattering
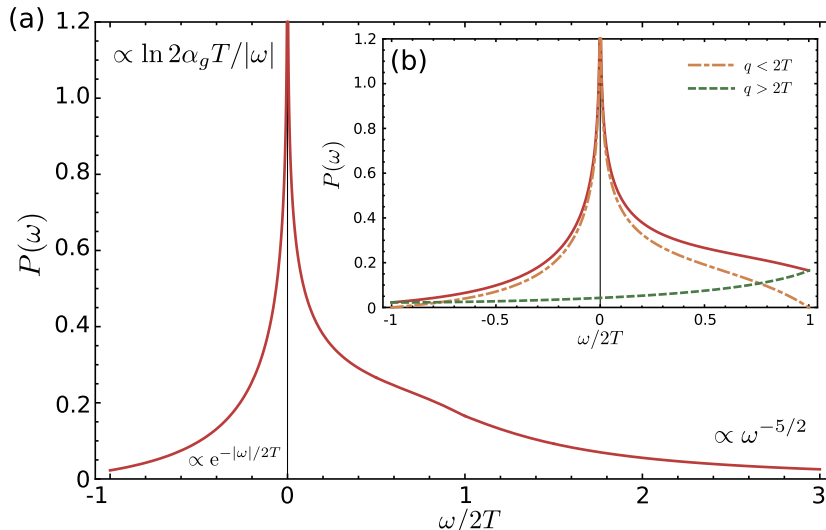
Figure 4.2: *The jump-size distribution (4.7) for $T \gg |\mu|$. The inset (b) shows the contributions of $q > 2T$ (dashed line) and $q < 2T$ (dash-dotted line) to $P(\omega)$ (solid line) for $|\omega| < 2T$. Both curves are calculated for $\alpha_g = 0.75$. For details of the calculation, see App. D.*

rate (4.5) the region $|\omega| < 2T$ is most important and

$$\Gamma = \kappa \alpha_g T, \qquad |\mu| \ll T, \, \alpha_g \ll 1, \qquad (4.11)$$

where $\kappa = 4\pi^2(1 + \ln 2 + G/2) \simeq 84.92$ and $G \simeq 0.916$ is the Catalan constant. We remind the reader that the linear dependence on T is a characteristic feature of intrinsic graphene that distinguishes it from the Fermi liquid [73]. It is a manifestation of the quantum critical point and temperature as the dominant perturbation away from criticality is the only important scale determining the relaxation rate. Furthermore, due to screening the rate (4.11) is independent of the number of flavors N and linear in α_g contrary to the Golden rule result $\Gamma \propto \alpha_g^2 T$ [58]. The rate (4.11) is also independent of the particle energy $\varepsilon_p \gg \max(|\mu|, T)$.

The Fermi liquid limit of $|\mu| \gg T$

For $|\mu| \gg T$ the JSD is dominated by the region $|\omega| < 2|\mu|$ as can be seen in Fig. 4.3(a) while the weight of the tail is strongly reduced. In particular the mean jump-size will be of the order $|\mu|$. At the lowest frequencies $|\omega| < \alpha_g T$, the JSD $P(\omega)$ shows a logarithmic divergence due to unscreened collinear scattering. Here the JSD recovers the Fermi liquid form $P(\omega) \propto (T/|\mu|) \ln |\mu/\omega|$ (see Ref. [128]) in contrast to the result for $T \gg |\mu|$, where we obtain $P(\omega) \propto \ln(\alpha_g T/|\omega|)$. Furthermore in the $T = 0$ limit the logarithmic divergence at small energies vanishes, see Fig. 4.3(b). In this case $P(\omega)$ reproduces qualitatively the result of Ref. [31].

The dominant process for $|\omega| < 2|\mu|$ is the intraband scattering with small momentum transfer, $q < 2|\mu|$. Similar to the case $T \gg |\mu|$, such small-momentum scattering is not possible for $\omega > 2|\mu|$ where scattering with $q > 2|\mu|$ leads to the fat tail $\propto \omega^{-5/2}$. The contribution of negative frequencies $P(\omega < 0) \propto \exp(-|\omega|/2T)$ is again exponentially small just as in the quantum critical regime of $T \gg |\mu|$.
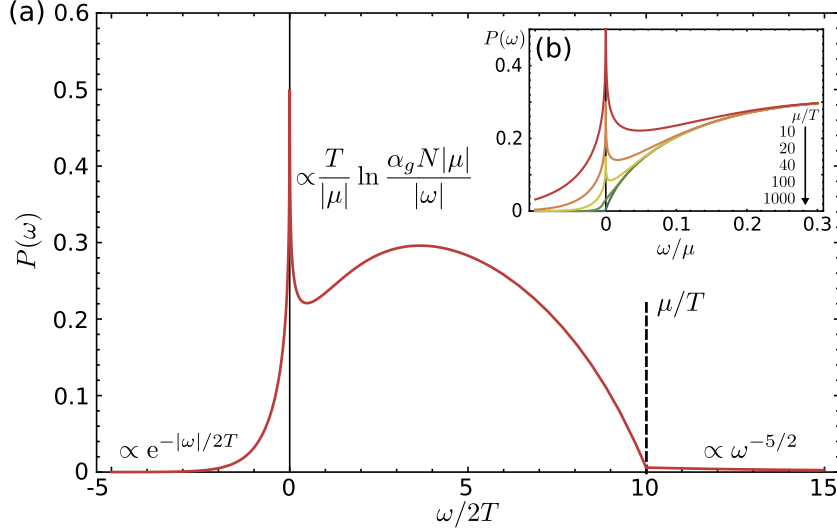
Figure 4.3: *The JSD (4.7) for $\mu/T = 10$. In the region $|\omega| < 2|\mu|$ processes with $q < 2|\mu|$ are dominant. For $|\omega| > 2|\mu|$ processes with $q > 2|\mu|$ determine the fat tail of the JSD. The inset (b) illustrates the evolution of the forward scattering resonance with lowering temperature. Both curves are calculated for $\alpha_g = 0.75$. For details of the calculation, see Appendix D.*

In the case $T \gg |\mu|$, the relaxation rate was determined by $|\omega| < 2T$. The total rate for $|\mu| \gg T$, is dominated by $0 < \omega < 2|\mu|$ and is given by

$$\Gamma = 8\alpha_g\pi^2|\mu|, \qquad |\mu| \gg T, \ \alpha_g \ll 1 . \tag{4.12}$$

Remember that the rate Γ determines the characteristic time scale associated to a single scattering event as in the case of $T \gg |\mu|$.

Additional comments

At this point a brief remark regarding the stability of the results in the presence of other scattering mechanism is in order. The rates (4.12) and (4.11) are calculated in the ballistic regime $T\tau_{\mathrm{dis}} \gg 1$, where we neglect the influence of disorder with the characteristic scattering time τ_{dis}. In the FL case it is known that the presence of disorder has strong influence on the inelastic relaxation of particles in the diffusive regime $T\tau_{\mathrm{dis}} \ll 1$ [134–136]. However, even in the diffusive regime the tails of the JSD $\propto \omega^{-5/2}$ are preserved for $\omega\tau_{\mathrm{dis}} \gg 1$, since they emerge due to scattering with large momentum transfer.

We finish this section with a short discussion of corrections to the results above due to the possibility of Auger processes. We have ruled out Auger processes primarily due to the restriction of the phase space as discussed in Sec. 1.2.1. We here discuss one mechanisms to open up phase space for Auger processes. More specifically we consider the nonlinearity of the spectrum at high energies $\varepsilon^* \lesssim \Lambda$, where Λ is the cutoff energy. The nonlinear correction to the dispersion relation reads $\varepsilon_\lambda(p) - \lambda k \propto k^2 \sin\varphi_k/\Lambda$, where φ_k is the angle of the direction of $\vec{k}$. The parameter that controls violations of the linear dispersion relation is therefore ε^*/Λ. Here $\varepsilon^* \sim \omega_{\mathrm{pump}}$ is a characteristic energy. A positive curvature of the spectrum opens a phase space for Auger processes. Auger processes thus also contribute to the tail of the JSD. From a simple estimate we obtain that Auger processes dominate over intraband processes for

$\omega \gtrsim T(T^{1/3}\Lambda^{2/3}/\varepsilon^*)^2$. This region is irrelevant if $\varepsilon^* \lesssim \Lambda(T/\Lambda)^{5/9}$. Under this condition the nonlinearity does not modify the tail of $P(\omega)$. For room temperature and the cutoff $\Lambda = 1$ eV, even near-infrared to visible light is within the range of validity of the results of this section. Since positive curvature only occurs in certain directions, Auger processes should be even weaker than in the simple estimate above. We furthermore want to stress that a negative curvature prevents Auger processes. Negative curvature appears due to intrinsic band curvature in certain directions of the reciprocal space and due to renormalization of the electronic spectrum due to interactions (see Sec. 1.3).

4.3.3 Stable distributions and Lévy flights

In view of the findings on the jump-size distribution in the last section and also in view of our final goal to describe the relaxation process of electrons in graphene as a random walk we need to discuss the notion of Lévy processes also called Lévy flights and stable distributions. The reason is primarily the fat tail of the JSD as found in Sec. 4.3.2. We return to the discussion of the relaxation cascade in Sec. 4.3.4.

Stable distributions occur in the context of a generalized limiting theorem for sums of identical and independently distributed random variables. Suppose we have such independently distributed random variables l_n, which have the probability density $p(l)$. We then ask whether the sum

$$S_n = \frac{1}{B_n}\sum_{k=1}^{} l_k - A_n \,, \tag{4.13}$$

has a limiting distribution for $n \to \infty$, i.e. $G_n(x) = \mathrm{prob}(x < S_n < x + dx)$. Furthermore one is interested in the general properties of the limiting distribution if it exists and under which conditions imposed on the distribution $p(l)$ does the sum converge towards a specific limiting distribution. Mathematically speaking one is interested in the domain of attraction of the distribution $G_n(x) = G(x)$.

The central limit theorem for distributions with finite first and second moments, i.e. finite mean and variance, is well known. In this case the limiting distribution of the sum (4.13) will be the Gaussian distribution, determined solely by the first two moments mentioned above. However the more general case seems to be less known and we will therefore give a brief introduction into the theory of stable distributions and Lévy processes in the following.

We start out with the notion of a stable distribution. A stable distribution is defined by the following property, expressing a certain linearity in the argument of the probability density. Suppose we have two independent identical copies x_1 and x_2 of the random variable x distributed according to the probability density $G(x)$. The variable x and its distribution are called stable if the linear combination $a_1 x_1 + a_2 x_2$ has the same distribution as the variable $cx + d$ for a given $c, d \in \mathbb{R}$ with $c, d > 0$ in our case. The above stated property is equivalent to the invariance under convolution of the distribution $G(x)$ which reads as

$$G(cz + d) = \int_{-\infty}^{+\infty} \mathrm{d}x \, G(a_1(z - x) + b_1)G(a_2 x + b_2) \,. \tag{4.14}$$

For example the Gaussian as well as the Cauchy distribution belong to the class of stable distributions. Besides these two examples stable distributions include many more. Interestingly there exists a full parametrization of all stable distributions due to Lévy and Khintchine [137]. They showed that the characteristic function of a stable distribution $G_n(x)$, i.e. the expectation value $\Phi_n = \langle e^{ikx} \rangle$ can be specified fully in terms of the four real parameters μ, α, β and c. Here the brackets $\langle \ldots \rangle$ denote the

average with respect to the distribution $G(x)$. For an observable $\mathcal{O}(x)$ this reads as

$$\langle \mathcal{O}(x) \rangle = \int \mathrm{d}x \, \mathcal{O}(x) G(x) \, . \tag{4.15}$$

We have furthermore the restrictions $0 < \alpha \leq 2$ and $-1 < \beta < +1$. The parameter μ is related to the mean of the stable distribution and referred to as the location parameter, whereas the parameter c is called scale parameter. They determine the overall position of the stable distribution and can be adjusted by means of a scale transformation. The shape parameters β and α determine the skewness and the asymptotics of the distribution. The parameter α is called the characteristic exponent. Although β is referred to as the skewness, note that the second moment need not exist for a generic stable distribution. The latter is reproduced by $\alpha = 2$. In the following we exclude $\alpha = 1$, which is not important for our subsequent application of Lévy flights to the physics in graphene. The characteristic function of a stable or also called α-stable distribution reads as

$$\Phi_n(\alpha, \delta, \beta, c; z) = \mathrm{e}^{\mathrm{i}zn\delta - nc|z|^\alpha(1 - \mathrm{i}\beta\mathrm{sign}(z)\tan(\alpha\pi/2))} \, , \tag{4.16}$$

where n labels the number of terms in the sum (4.13). From the Lévy-Khintchine representation follows that indeed the characteristic exponent α determines the asymptotics of the stable distribution at large values of x. If for example we have $\beta = 0$, an α-stable distribution $G(x)$ has the asymptotic behavior

$$G(x) \simeq \frac{1}{|x|^{\alpha+1}} \, , \tag{4.17}$$

for $x \to \pm\infty$. In the case of $\beta = 1$ the distribution furthermore becomes single-sided. That means the distribution shows the power law tail according to Eq. (4.17) for $x \to +\infty$ and is exponentially small for $x \to -\infty$.

In the beginning of this section we were also asking for the criterion for the convergence of the sum (4.13) towards a stable distribution. It was found that the initial distribution exactly lies in the domain of attraction of a stable distribution with scale parameters c and α if it possesses the asymptotics [137],

$$p(x) \simeq \frac{c^\alpha(1 + \mathrm{sign}(x)\beta)\sin(\alpha\pi/2)\Gamma(\alpha+1)/\pi}{|x|^{\alpha+1}} \, . \tag{4.18}$$

Interestingly Lévy processes also show scaling behavior. This is not surprising in view of the power law tail that indicates scale invariance. The scaling relation for Lévy flights reads as

$$G_n(S_n) = n^{-1/\alpha} G_1(Y/n^{1/\alpha})|_{\delta=0} \, , \tag{4.19}$$

where the variable $Y = S_n - n\delta$ describes the fluctuations of the cascade after the constant drift has been subtracted.

Lévy process

Having defined the notion of the stable distributions we now sketch how they naturally arise in random walks. A very general class of random walks is the Lévy process. The latter is a random process of the random variable $X(t)$, that means the variable $X(t)$ changes randomly over the course of time. For the Lévy process one demands that the increments of the random process $X(t_2) - X(t_1)$, $X(t_3) - X(t_2)$,

..., up to $X(t_n) - X(t_{n-1})$ are independent random variables. Furthermore it is demanded that the increments are stationary, which means

$$X(t_1 + h) - X(t_1) \sim X(t_2 + h) - X(t_2) \,, \tag{4.20}$$

for arbitrary times t_1 and t_2 and $h \in \mathbb{R}$. The equivalence in Eq. (4.20) means that $X(t_1 + h) - X(t_1)$ is equivalent in probability to $X(t_2 + h) - X(t_2)$, i.e. both increments in Eq. (4.20) have the same probability distribution.

Important for our case is the discrete Lévy process. Here the time steps separating t_n are of fixed length Δt, i.e. $t_n = n\Delta t$ and the Lévy process X_n is given by

$$X_n = \sum_{k=0}^{n} l_k \,, \tag{4.21}$$

where the l_k are distributed according to the same distribution function. The Lévy process thus constitutes a random walk with so far arbitrary distribution for the increments l_n.

It now becomes clear that the relaxation cascade can be understood as a random walk in the following sense. We are considering a discrete Lévy process or random walk where the length of one time-step is given by the characteristic scattering time of the high-energy electron. This will be the total scattering rate Γ and the time step will therefore be $\Delta t \sim \Gamma^{-1}$, where Γ is determined by Eq. (4.4). The distribution of increments is the jump-size distribution calculated in the previous section 4.3.2 in the quantum critical regime as well as in the Fermi liquid regime. Bear in mind that the electron loses energy, except for a negligible probability to actually gain energy from the bath of thermal electrons. Therefore whenever we are talking about increments we mean increments in the cascade which means decrease in the electrons energy. The cascade of course stops when the high-energy electron reaches energies of the order of the chemical potential or temperature.

The truncated Lévy flight

The unique behavior of Lévy α-stable distributions originates from the fat tails of the distributions. These tails lead to a divergence in the second moment of the distribution as we mentioned above. However, in the real world the divergence of the second moment is cut-off by some scale. The latter can be system size, measurement time or in our case the initial energy of the particle that is determined by the frequency of the pump pulse. It is therefore interesting to study the truncated Lévy flight. The latter exhibits all characteristics of the canonical Lévy flight up to a certain scale Λ beyond which the power law tail is suppressed. Truncated Lévy flights have been studied in the literature both numerically [138] as well as analytically [139]. Both studies reveal the following picture. By increasing n in the sum (4.13), the distribution of S_n first converges to a Lévy distribution and finally for very large n crosses over into the normal distribution. The convergence to the Gaussian was however found to be very slow. The analytical theory predicts that the crossover to the normal distribution happens at large values of $n > \Lambda^\alpha$, where α is the characteristic exponent of the Lévy flight that emerges before the transition to the normal distribution. This slow convergence of the truncated Lévy flights to the Gaussian is confirmed by our numerical sampling in Sec. 4.3.4, a result that is important for our later discussion of the relaxation cascade in the following sections.

4.3.4 The relaxation cascade revisited

We are now ready to continue our analysis of the relaxation cascade of photoexcited electrons in graphene. In particular we will apply the concepts of stable distributions and Lévy processes from

Sec. 4.3.3. in the following to the cascade. More specifically, we will review the cascade picture proposed in Ref. [30] in terms of the fluctuations of the number of cascade steps and the first passage time of the underlying Lévy process.

We have seen that the JSD of a high-energy electron with energy $\varepsilon_p \gg \max(|\mu|, T)$ in graphene implies an average jump size of the order of either temperature or chemical potential. This is in contrast to the FL result where the JSD is flat up to the particle's energy. In graphene, the excited carriers relax in a cascade, with on average $\langle n \rangle \sim \varepsilon_p/\langle \omega \rangle$ jumps, where $\langle \ldots \rangle$ is the average according to the JSD as defined in Eq. (4.15). The time scale of the cascade is then $t \sim n/\Gamma$ [30, 31] and the time scale of a single scattering event is naturally given by $1/\Gamma$ and constitutes the time increment of the Lévy process that describes the relaxation cascade (see Sec. 4.3.3). The above conclusion concerns the mean number of steps in the cascade as well as the average cascade time. We now discuss the statistics of the random walk modeling the relaxation cascade in more detail with an emphasis on the fluctuations of the number of cascade steps.

Due to the fact that the JSD exhibits the fat tail $P(\omega) \propto \omega^{-5/2}$, it does not possess a second moment. Therefore, the fluctuations of the number of cascade steps should show an unusual behavior. The particle energy provides a natural cutoff for the JSD, rendering its variance finite. But on an intermediate scale, before the electron energy reaches $\max(|\mu|, T)$, the distribution behaves as if it possessed no finite variance. This is also demonstrated in Fig. 4.4(a)-(b) where we conducted an analysis of the relaxation cascade in the presence of a finite cut off by numerically sampling the random walk from the JSD in the regime $T \gg |\mu|$.

According to the concepts presented in the previous section in particular in the context of the Lévy process the relaxation cascade is given by

$$S_n = \omega_1 + \cdots + \omega_n \,. \tag{4.22}$$

Here the ω_i are the jump lengths of the successive scattering events in which the electron loses the energy ω_i. The steps ω_i are independent and identically distributed. The statistics of the cascade following from the simulation of the random walk is illustrated in Fig. 4.4(b). For not too large n, a finite cutoff in the JSD does not change the distribution of S_n in Fig. 4.4(b). It fits nicely to the Lévy distribution with the characteristics drawn from the results of Sec. 4.3.2, that means in particular an index of stability of $\alpha = 3/2$ and $\beta = 1$. Further details on the simulation of the cascade is given below.

As a consequence of the fat tail of the JSD, the large-n limit of the distribution of the cascade S_n does not approach the normal distribution. It rather lies in the domain of attraction of an α-stable law $G_n(S_n)$. We introduced these as generalized limiting distributions for random processes with stationary and independent jumps [137] including fat-tailed distributions as well as the normal distribution ($\alpha = 2$) in Sec. 4.3.3. Their characteristic function as given in Eq. (4.16) of Sec. 4.3.3, is fully parameterized by four parameters. The index of stability $\alpha = 3/2$ follows from the condition that $G_n(S_n)$ lies in the domain of attraction of an α-stable law formulated in Eq. (4.18). Since the large-ω asymptotic of the JSD, $P(\omega)$, is given by

$$P(\omega)T/\Gamma \simeq c \,(\omega/2T)^{-5/2} \,. \tag{4.23}$$

The scale parameter c is obtained from Eqs. (D.16) and (D.19). It will be related to the anomalous diffusion constant in Sec. 4.4, Eq. (4.32). The skewness $\beta = 1$ in the case of graphene, rendering the distribution single sided - the electron loses energy in the cascade. The location parameter $\delta = \langle \omega \rangle$. For $|\mu| \gg T$ we have $\delta \sim \alpha_g |\mu|$ whereas $\delta \sim \alpha_g T$ for $T \gg |\mu|$.
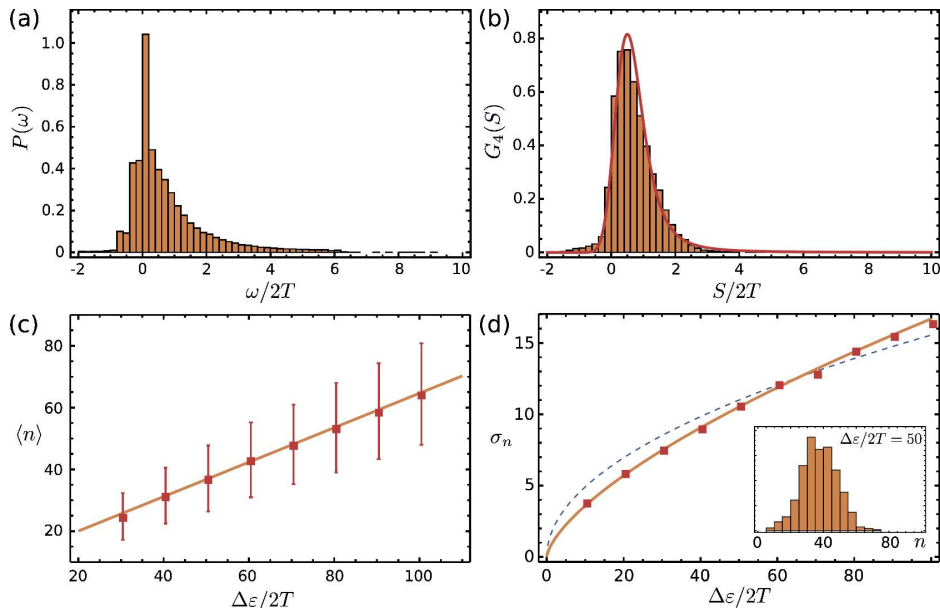
Figure 4.4: *(a) Sample of the JSD for $T \gg |\mu|$ (see Fig. 4.2). (b) Sample of the cascade variable $S_n = \omega_1 + \cdots + \omega_n$ from the JSD for $n = 4$ with a high energy cutoff for the JSD given by the particle energy $\varepsilon_p/T = 100$. The solid line is the stable distribution with $\alpha = 3/2$ and $\beta = 1$. (c) The average number of steps sampled from the JSD as a function of the cascade length $\Delta\varepsilon$. The error bars show the typical fluctuations σ_n of the number of cascade steps. (d) The fluctuation σ_n as a function of the cascade length $\Delta\varepsilon$. The solid line is the $\Delta\varepsilon^{2/3}$ law (4.28). The dashed line illustrates Gaussian fluctuations for comparison. The inset shows a typical distribution of cascade steps for $\Delta\varepsilon/2T = 50$.*

The random variable $Y = S_n - n\delta$, describing the fluctuations of the cascade, obeys a strictly stable distribution. The random motion on top of the drift during the relaxation processes is thus not the standard Brownian motion that would be described by a Gaussian distribution. It is rather superdiffusive and contains long jumps. We discuss three important consequences for the statistics of the cascade. These concern, first the relaxation rate of the entire cascade. Second, we discuss the secondary electrons excited above by the high-energy electrons since they take over a portion of its energy. And finally we take a look at the fluctuations in the cascade time.

The relaxation rate γ_c of the entire cascade is given by the rate Γ divided by the average number of steps. The latter is given by $\varepsilon_p/\langle\omega\rangle$. Thus we obtain

$$\gamma_c \sim \alpha_g^2 \begin{cases} \mu^2/\varepsilon_p, & |\mu| \gg T \\ T^2/\varepsilon_p, & T \gg |\mu| \end{cases}. \tag{4.24}$$

Regarding the second consequence, we ask whether we can say anything about the distribution of the secondary electrons excited to higher energies by scattering with the primary high-energy electron. The high-energy tail of the JSD $P(\omega^*)$, $\omega^* \gg \max(|\mu|, T)$, gives also the probability density for a secondary electron or hole to be created in the energy interval $\omega^* \lesssim |\varepsilon| \lesssim \omega^* + \max(|\mu|, T)$. More precisely, in the case $\mu \gg T$ ($-\mu \gg T$) only hot electrons (holes) are created with probability density

$P(\omega^*)$, while in the case $T \gg |\mu|$ electrons and holes are created with equal probability $P(\omega^*)/2$. Using $P(\omega^*) \ll P(\langle\omega\rangle)$, the probability to create a secondary electron at energy $\varepsilon \sim \omega^*$ during the entire cascade is then given (up to the factor $1/2$) by $P(\omega^*)\varepsilon_p/\langle\omega\rangle$. We conclude that the energy scale

$$\omega_0 \sim \begin{cases} T(\varepsilon_p/\alpha_g|\mu|)^{2/5}, & |\mu| \gg T \\ T(\varepsilon_p/\alpha_g T)^{2/5}, & T \gg |\mu| \end{cases}, \tag{4.25}$$

separates the regions where the density of downstream particles is smaller ($\omega^* < \omega_0$) and larger ($\omega^* > \omega_0$) than the density of secondary particles. In the former region the distribution function should show traces of the tail of the JSD accordingly. However secondary electrons generated during the cascade will also relax. The account for this relaxation requires the full solution of the kinetic equation.

The third consequence concerns the scaling behavior of fluctuations of the cascade time - the first passage time of the Lévy process on the finite distance $\Delta\varepsilon$ in the energy space - which is directly related to the random variable Y. The distance $\Delta\varepsilon$ can be for instance given by $\Delta\varepsilon = (\omega_{\text{pump}} - \omega_{\text{probe}})/2$, the difference between the excitation and probing frequency. We use the scaling of Lévy stable distributions,

$$G_n(S_n) = n^{-1/\alpha} G_1(Y/n^{1/\alpha})|_{\delta=0}, \tag{4.26}$$

that follows from Eq. (4.16) and obtain

$$\langle Y^2 \rangle \sim \Delta\varepsilon^{2/\alpha} T^{2(\alpha-1)/\alpha}. \tag{4.27}$$

The mean square fluctuation of the number of steps is then given by $\sigma_n^2 = \langle n^2 \rangle - \langle n \rangle^2 = \delta^{-2}\langle Y^2 \rangle$ while the fluctuation of the cascade time

$$\sigma_t = \Gamma^{-1}\sigma_n = T^{(\alpha-1)/\alpha}\Delta\varepsilon^{1/\alpha}/\Gamma\langle\omega\rangle. \tag{4.28}$$

Using Eq. (4.11) and (4.12) in Eq. (4.28) we obtain,

$$\sigma_t \sim \left(\frac{\Delta\varepsilon}{T}\right)^{1/\alpha} \begin{cases} T/\mu^2, & |\mu| \gg T \\ T^{-1}, & T \gg |\mu| \end{cases}. \tag{4.29}$$

Both for $|\mu| \gg T$ and for $T \gg |\mu|$ we find a nontrivial dependence on $\sigma_t(T)$ determined by the index of stability α. Since $\alpha = 3/2$ in our case, the fluctuations increase $\propto T^{1/3}$ at $T \ll |\mu|$ and decrease $\propto T^{-5/3}$ at $T \gg |\mu|$.

The dependence of the fluctuations in the number of cascade steps n on the length of the cascade $\Delta\varepsilon$ is demonstrated in Figs. 4.4(c)-(d). Here the cascade is simulated by generating a sequence of steps from the JSD until the cascade length $\Delta\varepsilon$ is reached. The average number of steps $\langle n \rangle$ in Fig. 4.4(c) scales linearly with the cascade length $\Delta\varepsilon$. On the other hand, the fluctuations of the number of steps σ_n in Fig. 4.4(d) obey the relation (4.28).

At last we would like to comment on the relation between the Lévy flight and the fractal dimension of the random walk. The exponent of $\Delta\varepsilon$ in the fluctuations σ_t, Eq. (4.28), is known as the Hurst exponent $H = 1/\alpha$ [140, 141]. There are different ways to define the fractal dimension of the random walk [142]. One way is to associate the characteristic exponent with the fractal dimension [142] such that we would have $D_f = 3/2$. Sometimes the fractal dimension of the random walk is related to the Hurst exponent $D_f = 2 - H = 4/3$ [143]. In any case the fractal dimension is between the one

and two dimensional random walk. The fractal nature of the relaxation cascade in graphene can be understood in terms of a fast one-dimensional backbone of forward scattering as discussed in Sec. 1.2.3, augmented by other less efficient channels in the 2D momentum space. If the scattering was purely collinear scattering, the random walk would also be one dimensional. However the fact that electrons in fact exist in two-dimensional space and scatter into a small cone around the collinear case intuitively leads to the fractional dimension.

Sampling of the Lévy flights

We conducted a numerical simulation of the relaxation cascade on the basis of the JSD as calculated in Sec. 4.3.2. The main goal here was to investigate the convergence of the statistics of the cascade towards a stable distribution. In particular in the presence of a finite cut off in the fat tail of the JSD we tested the convergence of the thus truncated Lévy flight (see Sec. 4.3.3) towards a stable distribution.

We use a numerical implementation of the inversion method to sample random numbers from the JSD in the quantum critical regime of $T \gg |\mu|$ as depicted in Fig. 4.4(a). When sampling from the analytical result shown in Fig. 4.4, we enforce a finite cut off in the JSD that is of the order of the particle energy itself which also defines the length of the cascade. The random walk that is the cascade is then simulated by successively reducing the particle energy by the random number until it reaches the scale of temperature that means its energy is zero. In doing so we obtain nearly all interesting statistics of the cascade for a truncated Lévy flight that we can then check against our analytical formulas.

First, we checked that the cascade variable, more specifically the distribution of sum (4.22) does still converge to the α-stable distribution in the presence of a finite cut off. This is true for not too large cascade length as is illustrated in Fig. 4.4(b). Here the distribution of S_4 is shown. It agrees well with an α-stable distribution with the expected parameters $\alpha = 3/2$, $\beta = 1$ and c extracted from Eqs. (D.16) and (D.19). Also all other characteristics of the cascade agree well with our findings from the previous section. For example in Fig. 4.4(c) the average number of steps is depicted as a function of the cascade length. We observe that the average number of steps is indeed in good agreement with an average step length of the size T thus the average number of steps $\langle n \rangle$ is indeed given by $\langle n \rangle \sim \varepsilon_p / \langle \omega \rangle$. Similarly the fluctuations in the number of steps show good agreement with the analytical result (4.29) as is apparent from Fig. 4.4(d). Here the fluctuation in the number of steps is shown as a function of the length of the cascade $\Delta \varepsilon$ and reveals the Lévy flight specific scaling $\sim \Delta \varepsilon^{2/3}$. Note that the fluctuations are distinct from the usual Gaussian statistics which are indicated as the dashed line in Fig. 4.4(d).

4.4 Fractional kinetics and effective rate equation

In the following we reformulate the random walk, that is the relaxation cascade, in the continuum limit using a fractional Fokker-Planck equation. Since the fractional kinetics is based on the calculation of the JSD from Sec. 4.3.2, the same approximations as before apply here. Furthermore we want to extend the description towards the effective rate equation for the distribution function. To this end we employ the generation rate as calculated in Sec. 3.3 and look at the isotropic part of the distribution function that only depends on the particle energy and is obtained after angular average of the full distribution. The photo-emission measurements directly measure the distribution function that follows the effective rate equation. The transmission spectroscopy however measures the state of the graphene indirectly. We therefore also make the connection to the differential change in transmission.

4.4.1 Fractional kinetics

In the previous section we showed that the statistics of the relaxation dynamics is given by Lévy flights. The continuum description of the Lévy flight is by means of the fractional Fokker-Planck equation. The latter generalizes the known Fokker-Planck approximation of the collision integral to scattering kernels, i.e. the JSD $P(\omega)$, with power law tail. The dynamics of the distribution function is then given by the fractional Fokker-Planck equation (FFPE) [144], which reads as

$$\partial_t W(\varepsilon, t) = \Gamma \langle \omega \rangle \, \partial_\varepsilon W(\varepsilon, t) + D \nabla^\alpha_{(\beta)} W(\varepsilon, t) \,. \tag{4.30}$$

Here $W(\varepsilon, t)$ with $W(\varepsilon, t = 0) = \delta(\varepsilon)$ is the propagator of the FFPE which will be given below. We also introduced the Riesz-Feller fractional derivative [145], which is defined by its Fourier transform,

$$\nabla^\alpha_{(\beta)} f(\varepsilon) = \int \frac{\mathrm{d}z}{2\pi} \, \ln[\Phi_1(\alpha, 0, \beta, 1; z)] f(z) \mathrm{e}^{iz\varepsilon} \,, \tag{4.31}$$

where Φ_1 is the characteristic function of the underlying stochastic process. In our case it is a Lévy α-stable law with $\alpha = 3/2$ and $\beta = 1$, see Eq. (4.16). In the FFPE (4.30) we also introduced the average energy loss rate $\Gamma \langle \omega \rangle$ and the anomalous diffusion constant $D = \Gamma c$, where c is the scale parameter of the Lévy process, see Eqs. (4.16) and (4.23). From these formulas we obtain for the anomalous diffusion constant

$$D = \frac{2^\alpha 128 \sqrt{2\pi}}{N/4} \, T^{\alpha+1} \,. \tag{4.32}$$

In contrast to the conventional diffusion constant it has the anomalous dimension $[D] \sim \mathrm{Energy}^\alpha/s$.

Usually the Fokker-Planck equation follows from an underlying Langevin equation. The emergence of the fractional kinetics expressed by the FFPE (4.30) can be understood on the basis of a Langevin-type rate equation for the electron energy,

$$\partial_t \varepsilon(t) = -\Gamma \langle \omega \rangle + \eta(t) \,, \tag{4.33}$$

where $\eta(t)$ is a random variable which is distributed according to an α-stable law and describes the noise in the relaxation process due to the interaction of the high-energy electron with the bath of thermal electrons.

The general solution $F(\varepsilon, t)$ of the FFPE with initial conditions $F(\varepsilon, t = 0) = f(\varepsilon)$ is obtained with the propagator according to

$$F(\varepsilon, t) = \int \mathrm{d}\varepsilon' \, W(\varepsilon - \varepsilon', t) f(\varepsilon') \,. \tag{4.34}$$

In our case we choose the initial probability density to be

$$f(\varepsilon) = n_0 \delta(\varepsilon - \omega_{\mathrm{pump}}/2) \,. \tag{4.35}$$

Here n_0 is the integrated flux density of the pump pulse. We have $F(\varepsilon, t) = n_0 W(\varepsilon_t, t)$, where

$$\varepsilon_t = \varepsilon - \omega_{\mathrm{pump}}/2 + \Gamma \langle \omega \rangle t \,, \tag{4.36}$$

is the running energy. The propagator $W(\varepsilon, t)$ and thus the solution $F(\varepsilon, t)$ in our case of $\alpha = 3/2$ and $\beta = 1$ can be calculated explicitly. We obtain

$$W(\varepsilon, t) = \frac{\pi T}{\alpha} (Dt)^{-1/\alpha} K(s) \tag{4.37}$$

for the propagator in terms of the dimensionless variable

$$s = \varepsilon_t / (Dt)^{1/\alpha} . \tag{4.38}$$

In Eq. (4.37) the function $K(s)$ is given by,

$$K(s) = -e^{\frac{s^3}{27}} \left[\sqrt[3]{2/3}\, s\mathrm{Ai}\left(\frac{s^2}{\sqrt[3]{486}} \right) + \sqrt[3]{12}\, \mathrm{Ai}'\left(\frac{s^2}{\sqrt[3]{486}} \right) \right] . \tag{4.39}$$

Here $\mathrm{Ai}(z)$ is the Airy function and $\mathrm{Ai}'(z)$ its derivative. In particular, W has the following asymptotics for large times,

$$W(\varepsilon, t) \simeq \frac{TDt}{\sqrt{2\pi}\alpha} \, |\varepsilon - \varepsilon_0 + \Gamma\langle\omega\rangle t|^{-(\alpha+1)} . \tag{4.40}$$

Using Eq. (4.32) and the results from Sec. 4.3.2 we obtain,

$$W(\varepsilon, t) \sim t^{-\alpha} \begin{cases} T(T/\mu^2)^{\alpha+1} , & |\mu| \gg T \\ T^{-\alpha} , & T \gg |\mu| \end{cases} . \tag{4.41}$$

We see that the tail of F for large times but fixed ε is proportional to $t^{-3/2}$ and scales as $T^{-3/2}$ for $T \gg |\mu|$ and as $T(T/\mu^2)^{5/2}$ for $|\mu| \gg T$.

The evolution of the probability distribution $W(\varepsilon, t)$ due to the fractional kinetics is illustrated in Fig. 4.5. The solid line depicts the solution of the FFPE (4.30), given by the Eqs. (4.37)-(4.39), while the dashed lines show the Gaussian solution of the usual Fokker-Planck equation. The fractional kinetics leads to a strong asymmetry, compared to the Gaussian drift-diffusion, since the fluctuations in the underlying Lévy process are single-sided, i.e. $\beta = 1$ in Eq. (4.16) and (4.30).
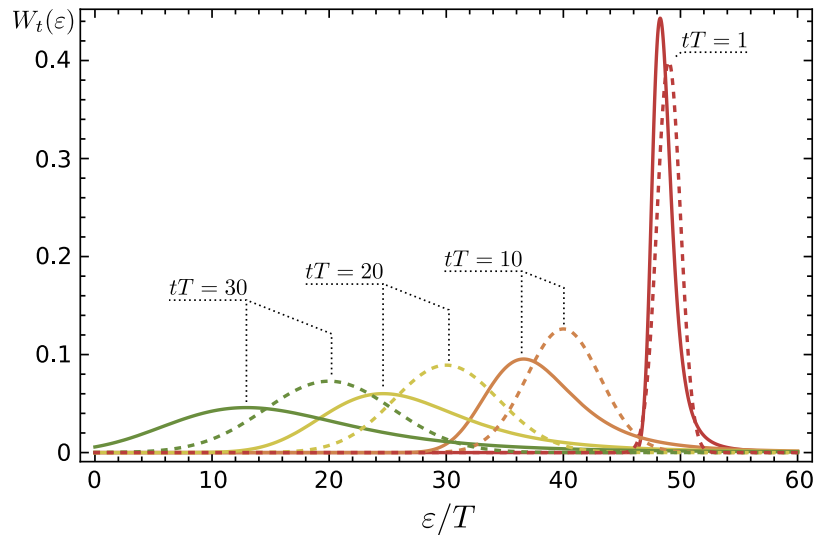

Figure 4.5: *The solution [see Eqs. (4.37)-(4.39)] of the FFPE (4.30) (solid line) as a function of energy in comparison to the result obtained for Gaussian diffusion (dashed line) for different times.*

4.4.2 The effective rate equation

We will now merge the findings of the previous section with the effective rate equation (see Sec. 3.3) obtained from the quantum kinetic equation derived in Chapt. 3. More specifically we will incorporate the fact that the relaxation of high-energy electrons due to electron-electron interactions is given by Lévy flights and shows fractional kinetics into the effective rate equation. We will then compare the results obtained from the most simple rate equation usually employed to fit experiments with the one containing the fractional kinetics.

As we pointed out in the preceding section the FFPE (4.30) is an equation for the homogeneous part of the distribution function. In order to include also the generation of carriers by the laser pulse we use the effective rate equation (3.76) from Sec. 3.3, for the isotropic part of the distribution function. We denote the isotropic part of the distribution function

$$f_\lambda(k) = \langle \rho_{\lambda \vec{k}} \rangle_\varphi = f^{(0)} + N(\varepsilon, t) \,. \tag{4.42}$$

Here ρ is the single-particle density matrix introduced in Sec. 3 and $\langle ... \rangle_\varphi$ denotes the angular average. Moreover $f^{(0)}$ is the Fermi-Dirac distribution function. We denote the correction to the Fermi-Dirac distribution function $N(\varepsilon, t)$ and it describes the distribution of photoexcited electrons in the following. Averaging the rate equation

$$\partial_t \rho_{\lambda, \vec{k}}(t) = \lambda \Delta \rho_{\vec{k}}(-\infty) \left(\frac{e k_y}{k^2} \right)^2 \bar{E} \, E_0(t) \, R(\Delta t, \Delta \tau) \,, \tag{4.43}$$

over all angle of the momentum $\vec{k}$ yields

$$\partial_t N(\varepsilon, t) = \lambda \, \Delta \rho(\varepsilon, -\infty) \frac{e^2}{2k^2} \bar{E} \, E_0(t) \, R(\Delta t, \Delta \tau) = \lambda P(\varepsilon, t) \,. \tag{4.44}$$

Here and in Eq. (4.43) $\Delta \rho(\varepsilon, -\infty) = [f^{(0)}_-(k) - f^{(0)}_+(k)]/2$ with $k = |\varepsilon|$ is the initial equilibrium inversion of the population. All functions in Eq. (4.44) only depend on the energy $\varepsilon = \lambda |\vec{k}|$ now. Here we introduced $P(\varepsilon, t)$ for the generation rate in the rate equation. Now let us add on the right-hand side of Eq. (4.44) the relaxation term from the FFPE (4.30) and we obtain

$$\partial_t N(\varepsilon, t) = -\frac{N(\varepsilon, t)}{\tau_1} + \Gamma \langle \omega \rangle N(\varepsilon, t) + D \nabla^\alpha_{(\beta)} N(\varepsilon, t) + P(\varepsilon, t) \,. \tag{4.45}$$

Here we also added another decay channel in the relaxation time approximation described by the time τ_1. From the previous section we know the Green's function $G(\varepsilon, t)$ of the FFPE which obeys

$$\left[\partial_t + \Gamma \langle \omega \rangle \partial_\varepsilon - D \nabla^\alpha_{(\beta)} \right] G(\varepsilon - \varepsilon', t - t') = \delta(t - t') \delta(\varepsilon - \varepsilon') \,. \tag{4.46}$$

Namely $G(\varepsilon, t)$ is given by

$$G(\varepsilon, t) = \Theta(t) W(\varepsilon_t, t) \,, \tag{4.47}$$

where $\Theta(t)$ is the Heaviside Theta function and $W(\varepsilon, t)$ is the solution of the FFPE (4.30) with initial condition $W(\varepsilon, 0) = \delta(\varepsilon)$. The latter is given by Eq. (4.37) and in the definition of the Green's function, Eq. (4.47), the energy argument is the running energy $\varepsilon_t = \varepsilon + \Gamma \langle \omega \rangle t$, also given in Eq. (4.36).

From Eqs. (4.45) and (4.46) we see according to the standard approach that the solution of the rate equation is given by

$$N(\varepsilon, t) = \int_{-\infty}^t \mathrm{d}t' \int_0^{+\infty} \mathrm{d}\varepsilon' \, \mathrm{e}^{-(t-t')/\tau_1} \, W(\varepsilon_{t-t'} - \varepsilon', t - t') P(\varepsilon', t') \,. \tag{4.48}$$

4.5 Discussion and connection to experiments

In order to draw the connection to experiments we show results for two observables. First, the differential change in transmission in the interaction-dominated regime. Second, the evolution of the distribution function according to the solution (4.48). The latter is measured in time resolved ARPES measurements as explained in Sec. 4.1.

First, we discuss the differential change in transmission for pump-probe experiments. As we have seen in Sec. 2.2, the transmission of the graphene is connected to the change in the optical conductivity. The latter can be related to the change in the distribution function f. We are mainly interested in the evolution of the transmission after the pulse has passed. Therefore we assume that the correction to the distribution function is simply given by Eq. (4.35) at time $t_0 = 0$. We also consider the isotropic part of the distribution function only, as we have already done in the previous section. Then the change in the conductivity is given by

$$\Delta\sigma(t)/\sigma_0 = -\left[F(\omega_{\text{probe}}/2, t) - F(-\omega_{\text{probe}}/2, t) \right] . \tag{4.49}$$

Here the universal conductivity at high frequencies σ_0 was introduced in Sec. 2.2. Given the particle hole symmetry of the correction to the distribution function at high energies, i.e. $F(-\varepsilon, t) = -F(\varepsilon, t)$, we finally have for the relative differential transmission

$$\frac{\Delta\mathcal{T}(t)}{\mathcal{T}_0} = 2n_0 W(\omega_{\text{probe}}/2, t) . \tag{4.50}$$

Here $\mathcal{T}_0$ is the transmission due to σ_0 (see Sec. 2.2). We remind the reader n_0 is the integrated flux density of the pump pulse. The behavior of $\Delta\mathcal{T}$ as a function of time, Eq. (4.50), is illustrated in Fig. 4.6. The solid line depicts the result (4.37) due to the fractional kinetics in graphene, while the dashed line is the expected result for conventional Gaussian drift-diffusion. We see that the diffusion in the case of Lévy flights (solid line) is stronger due to the fact that the α-stable law is single sided, i.e. $\beta = 1$. Therefore fluctuations enhance the drift in energy space, see also Fig. 4.5. Furthermore the transient differential transmission shows power law behavior with time and temperature according to Eq. (4.41), instead of exponential decay in the case of usual diffusion [see Fig. 4.6(b)]. We stress that Eq. (4.50) does not take into account the initial rise of the transmission. This is due to the fact that we approximated the initial correction to the distribution function by Eq. (4.35). This initial regime will be included in the following where we illustrate the evolution of the distribution function taking into account the generation of carriers, see Eq. (4.48).

Second, we investigate the evolution of the distribution function itself. This study is relevant for photo-emission measurements. We have mentioned the work from Ref. [125] in Sec. 4.1 that pioneered the photo-emission studies in graphene on picosecond time scales. More recent experiments [146] explored even shorter time scales of the order of a few femtoseconds. Those experiments reveal nonthermal carriers for the first time as depicted in Fig. 4.7. In figure 4.7 the number of electrons emitted in photo-emission experiments is plotted as a function of energy. The energy resolution yields a snapshot of the transient carrier distribution function. The dashed lines are fits of Fermi-Dirac functions to the data. We observe that at very short times the distribution shown in Fig. 4.7 is nonthermal. The difference between the data and the Fermi-Dirac fit is an estimate for the density of nonthermal electrons. The latter is depicted in blue in Fig. 4.7. The density of nonthermal carriers is described by the solution of the effective rate equation (4.45). Their relaxation is in particular discussed in the previous section.

(a)

$\Delta\mathcal{T}/\Delta\mathcal{T}_{\mathrm{max}}$

(b)

$\Delta\mathcal{T}/\Delta\mathcal{T}_{\mathrm{max}}$
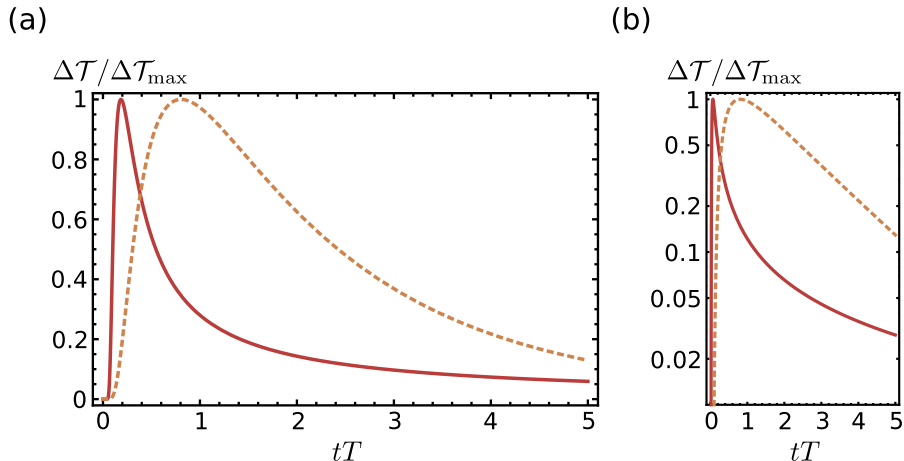
Figure 4.6: *The normalized differential transmission $\Delta\mathcal{T}/\Delta\mathcal{T}_{max}$ as a function of the dimension-less time tT. Here $\Delta\mathcal{T}_{max}$ denotes the maximum value of $\Delta\mathcal{T}$. Figure (b) shows the results on a logarithmic scale. The solid curves are calculated according to Eq. (4.50) and Eqs. (4.37) and (4.39), for $\Delta\varepsilon/T = (\omega_{pump} - \omega_{probe})/T = 25$ and $\Gamma\langle\omega\rangle/T^2 = 20$ as well as $D/T^{\alpha+1}$ from Eq. (4.32). The dashed lines in (a) and (b) illustrate the result for usual diffusion in comparison to the fractional kinetics (solid line).*

There we found that the high-energy electrons relax by anomalous diffusion. The corresponding theo-retical prediction to the experimentally measured density depicted in blue in Fig. 4.7, is illustrated in Fig. 4.5.

The analysis of the experimental data in Ref. [146] included the time evolution of the temperature obtained from the Fermi-Dirac fits. The latter is shown in Fig. 4.8(a) together with the time evolution of the number of nonthermal carriers (NTC). The experiment was analyzed with a simple model of relaxation of nonthermal carriers. More specifically, a relaxation time ansatz was used to fit the red and blue curves in Fig. 4.8(a). The relaxation time ansatz yields the simplified rate equation

$$\partial_t N(\varepsilon,t) = -\frac{N(\varepsilon,t)}{\tau_1} + P^*(\varepsilon,t)\,, \tag{4.51}$$

for the distribution of nonthermal carriers. In contrast to Eq. (4.45) the superdiffusive relaxation due to electron-electron interaction is not included here. Moreover, a simpler generation rate P^* than the one from Eq. (4.45), is used in the analysis of the experimental data in Ref. [146]. For simplicity an energy-independent matrix element was assumed. Furthermore, the function R in Eq. (4.45) was replaced by the time integrated generation rate.

The result that one obtains from Eq. (4.48) is compared to the result we get from Eq. (4.51) in Fig. 4.8 for the nondegenerate case. We observe that indeed a difference between the two models exists at short times. Further analysis on more refined data is therefore interesting to analyze whether the decay follows the power law decay suggested by Eq. (4.41).

4.6 Summary

This chapter presents a theoretical description of pump-probe experiments with emphasis on the role of electron-electron interaction in the relaxation dynamics. We also reviewed the experimental status
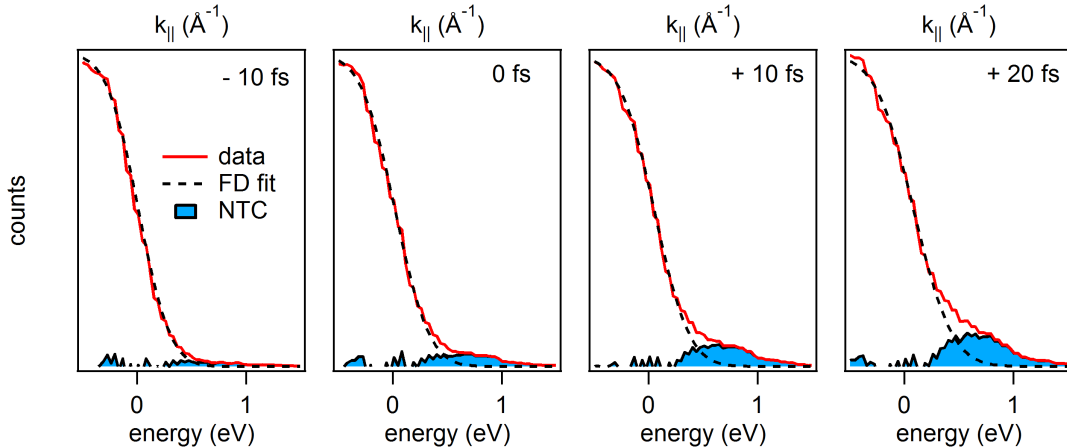
Figure 4.7: *The number of electrons emitted in ARPES. The energy resolution yields a snapshot of the carrier distribution in the graphene sample. The dashed lines are fits of Fermi-Dirac functions to the data. The density of nonthermal electrons is illustrated as the blue area. Reprinted figure from Ref. [146].*

of pump-probe measurements on graphene. Most important in this context is the cascade picture of the relaxation in graphene which was introduced in Ref. [30].

Motivated by these early works we ask the question whether the cascade can be described in terms of diffusive relaxation in energy space. The central ingredient of a possible description in terms of diffusion is the distribution of the jump-size in the relaxation process, i.e. the probability distribution of the transferred energy in a single scattering event. Therefore we performed a detailed analysis of the energy resolved scattering probability for high-energy electrons due to Coulomb interaction. The latter is exactly the desired jump-size distribution since the transferred energy is the length of a single relaxation step in the cascade.

We obtain results for finite temperature in the quantum critical regime of $T \gg |\mu|$ as well as in the Fermi liquid regime at finite chemical potential where $|\mu| \gg T$. There are two important features of the obtained results in the case of $T \gg |\mu|$ as well as $|\mu| \gg T$. First, the jump-size distribution shows a logarithmic divergence at small transferred energies. This logarithmic divergence is the known Coulomb logarithm that we discussed in Sec. 1.2.3. It contains the ratio of the average kinetic energy of the low energy thermal electrons and the transferred energy in the cascade step. However, we find that the main contribution of the relaxation process of high-energy electrons comes from larger energy transfers ω. Most importantly at large step sizes the jump-size distribution shows a power law tail. In both cases of $T \gg |\mu|$ as well as $|\mu| \gg T$, the power law is $\sim \omega^{-5/2}$. From the energy resolved scattering probability we also obtain the total scattering rate Γ for a single cascade step. The latter sets the characteristic time scale Γ^{-1} for the cascade. We find that the scattering rate is linear in the coupling strength $\Gamma \sim \alpha_g$. This deviates from the expectation based on the Golden rule but can be explained due to the peculiar screening in graphene. Furthermore, the relaxation rate scales as $\Gamma \sim \max(T, |\mu|)$. The Coulomb logarithm is of little importance for the relaxation rate as the high-energy electrons have a large phase space of final states. As a consequence the rate is determined by large energy transfer whereas the Coulomb logarithm occurred for small energy transfer compared to the temperature.

We apply our findings to the relaxation cascade. Due to the fat tail of the jump-size distribution the cascade can not be described by ordinary diffusive motion. The underlying random walk rather

(a)

(b)
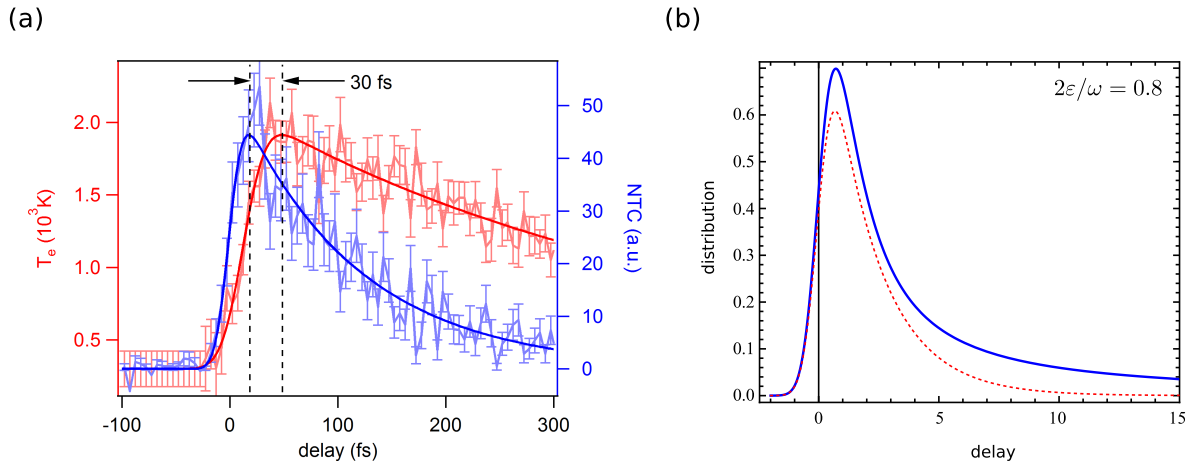
Figure 4.8: *(a) The time-evolution of the temperature (red curve) that is obtained from the fit of the Fermi Dirac function to the data shown in Fig. 4.7. Furthermore the time-evolution of the number of nonthermal carriers (NTC) is shown in blue. The number of NTC is the grey area in Fig. 4.7. Reprinted figure from Ref. [146]. (b) The qualitative comparison between the solution of the relaxation time ansatz formulated in equation (4.51) and the FFPE (4.48). The energy at which the density of photoexcited electrons $N(\varepsilon, t)$ is evaluated is given by $2\varepsilon/\omega = 0.8$.*

represents Lévy flights and leads to anomalous diffusion. In particular, the Lévy flight is characterized completely by the results regarding a single scattering event, i.e. the energy resolved scattering probability mentioned above. The anomalous character of the relaxation process has important consequences for the statistics of the entire cascade. First, the fluctuations σ_t of the time it takes the electron to complete the entire relaxation cascade, scale anomalous with the length of the cascade and with temperature. Regarding the length $\Delta\varepsilon$ of the cascade, we find that $\sigma_t \sim \Delta\varepsilon^{2/3}$. Moreover, we have for $T \gg |\mu|$ that $\sigma_t \sim T^{-5/3}$ while for $|\mu| \gg T$ it holds that $\sigma_t \sim T^{-5/3}(T/\mu)^2$. We found that the relaxation rate for a single cascade step is linear in the coupling strength α_g. Interestingly, the rate γ_c for the entire cascade is proportional to α_g^2. At the same time it depends on the length $\Delta\varepsilon$ of the cascade according to $\gamma_c \sim \max(T, |\mu|)/\Delta\varepsilon$.

Finally, we formulate the relaxation cascade in the continuum limit. In this limit usual diffusive relaxation was described by a Fokker-Planck equation. The fact that in the case of graphene the relaxation due to electron-electron interaction is characterized by Lévy flights is captured by a fractional Fokker-Planck equation. This formulation allows us to include the relaxation due to electron-electron interaction in the effective rate equation derived in Chap. 3.

We calculate two observables relevant for pump-probe experiments. First, the time dependent differential change in transmission. Second, the time evolution of the density of nonthermal carriers. We compare the resulting model qualitatively with recent experiments which performed pump-probe experiments on graphene at ultra short time scales. These works revealed the existence of nonthermal electrons for the first time. A further quantitative comparison of both works is promising.

5 Chapter 5
Hydrodynamics in graphene

In this section we will construct an effective macroscopic model of transport in terms of hydrodynamic currents and densities. The hydrodynamic theory is derived from the microscopic description of graphene in terms of the kinetic equation in the Boltzmann limit. The emergent hydrodynamics will be due to the presence of electron-electron interaction.

5.1 Introduction to hydrodynamics

Hydrodynamics is a classical field theory for the description of fluids, where the fields are the relevant densities and hydrodynamic velocities. Both of them depend on the position $\vec{r}$ in space. Our aim is to describe the electronic transport in graphene by a suitable classical hydrodynamic field theory. The hydrodynamic theory is mainly motivated by two experimental trends. First, the fabrication of very clean samples on boron nitride [147, 148] yields very homogeneous charge densities. Second, experimental techniques to directly image the local charge density [32, 33] are suitable to image hydrodynamics in graphene. These techniques have been applied in particular to the study of plasmons.

So far we have mostly dealt with a microscopic description of the electronic properties of graphene. In particular Chapt. 4 was devoted to the distribution function of graphene after laser excitation. The quantum kinetic equation from Chapt. 3 is able to describe the nonlinear response of the system. For example in the simple case of graphene without any interactions we obtained the relation (3.69) for the inversion of the population after excitation by a laser pulse. However the inclusion of interactions and the coupling to a bath render many questions regarding the nonlinear response a formidable task. Furthermore, in finite size samples boundary condition are important. They create inhomogeneities of the densities such as particle number or energy density. These inhomogeneities add an additional degree of complexity. Luckily, in some situations the distribution function contains more information than needed to describe the transport in the system. This idea is at the heart of the hydrodynamic description. The distribution function that in general also depends on the position in space is a complicated function of the single-particle states, more specifically the single-particle energies ε. It contains information on all moments[1] that can be generated by averages with respect to the distribution function $f(\varepsilon, \vec{r})$. A hydrodynamic description is possible if only a finite number of these local moments is important. Whether this is indeed the case can be ensured by the presence of interactions that want to thermalize the system locally.

---

[1] A definition of the local moments can be found in Sec. 5.4.

We will focus on this limit of collision-dominated hydrodynamics due to Coulomb interaction. There are two consequences of the Coulomb scattering. First, it drives the system towards local equilibrium with a specific temperature and chemical potential. As a consequence both temperature and chemical potential are functions of position $\vec{r}$. Second, Coulomb interaction leads to dissipation in the system. In the case of graphene in the quantum critical regime of $T \gg |\mu|$ electron-electron interaction leads to a finite conductivity at the Dirac point and also causes diffusion of the particle density as well as thermal diffusion.

Interestingly, there are also systems that can be described by dissipationless quantum hydrodynamics. Examples are the Luttinger liquid [43] and the Calogero-Sutherland model. The latter describing fractional quantum Hall edge states. Here hydrodynamics mainly emerge due to the fact that those systems are genuinely correlated. Furthermore, in the one-dimensional case they are naturally described by densities and velocities.[2] The dissipationless hydrodynamics in those systems shows instabilities towards the formation of shock waves and the subsequent formation of solitons [43, 44]. The dissipationless or Euler limit of the hydrodynamics in graphene will be studied numerically in Sec. 5.7. Although dissipative systems are less prone to develop shock waves there are other interesting phenomena occurring specifically in diffusive systems. The easiest and most interesting ones are coupled two-component systems. Commonly known as reaction-diffusion systems. Graphene close to the Dirac point is such a two-component system since the number of electrons and holes is separately conserved as we discussed in Sec. 1.2.1 and in Chapt. 4.

Moreover we mentioned in Sec. 1.3 that the graphene exhibits a quantum critical point at $T = 0$ and $\mu = 0$. Therefore, in the critical region of $T \gg |\mu|$ the system is described by relativistic fermions and the emergent hydrodynamics will be a relativistic theory. The dissipative corrections mentioned above are determined by the transport rates in the critical regime that scale as $\alpha_g^2 T$. Here α_g is the graphene fine structure constant and T is the temperature. We observe that for high temperatures scattering rates due to interaction can therefore become dominant. In experiments under high bias as for example in Ref. [12] temperatures as high as 1200K are achieved. Therefore the collision-dominated hydrodynamics will be an adequate description of transport. Furthermore it is usually more convenient to incorporate boundary effects in the hydrodynamic theory than in the case of the microscopic Boltzmann equation. Finally we mention three possible applications of the hydrodynamic theory.

First, the graphene has been found to exhibit a remarkably small viscosity [40] which yields a low threshold for turbulent flow. In the collision-dominated hydrodynamics the viscosity is one of the transport parameters generated by electron-electron interactions. In view of the remarkably small value of viscosity it is also interesting to find experimental ways to measure it. In fact, the hydrodynamic theory yields the low-frequency optical response of the system and the latter also contains the viscosity in graphene as shown in Sec. 5.5. Therefore, nonlocal optical measurements might give access to this transport parameter.

Second, the excitation of the graphene by a laser pulse will naturally lead to the formation of hotspots. The latter arise after local thermalization. The early stage of the thermalization of high energy electrons was studied in Chapt. 4. Subsequently the system thermalizes globally. This process is described by hydrodynamics. In view of this we will also study the relaxation of a hot spot in Sec. 5.7.

At last we note that recently experimental techniques have been developed that can give access to the hydrodynamics in graphene. Among those are the SNOM technique mentioned in the introduction to this thesis [32, 33]. But very recently also nanoantennas directly fabricated on the graphene enable the excitation of plasma waves in the graphene [149]. Specific shapes of the antenna can be used to focus

---

[2]Note that for example in the Luttinger liquid there is in fact no strict distinction between densities and currents.

plasma waves in those experiments. For the intensities in current experiments, the systems are in the linear regime but it appears promising to investigate the nonlinear hydrodynamics also experimentally in the future.

5.2 Previous theoretical works on the hydrodynamics in graphene

The hydrodynamic description of graphene was pioneered by Sachdev et al in Refs. [38] and [39]. There it was realized that the vicinity of the quantum critical point (see Sec. 1.3) in graphene gives rise to relativistic hydrodynamics. The authors of Ref. [39] reasoned that due to criticality there is a single transport parameter determined by the graphene fine structure constant α_g and temperature T. There are in fact additional transport parameters. However, except for the viscosity they become irrelevant at the Dirac point as we will see later in Sec. 5.4. The viscosity η in graphene close to the Dirac point shows similar behavior as the other transport parameter and scales as $\eta \sim T^2/v_F^2 \alpha_g^2$ [40]. Note that the viscosity does not change under the renormalization group flow since the product $\alpha_g v_F$ does not change [40].[3] In fact, it was found that the ratio of viscosity and entropy[4]

$$\frac{\eta(T)}{s(T)} \sim [\ln(T_\Lambda/T)]^2 \,, \tag{5.1}$$

grows only logarithmically with lowering temperature and for relevant temperatures graphene is a more perfect liquid than helium. More specifically its viscosity to entropy ratio is smaller than the one for liquid helium. It even comes close to the lower bound of the ratio in Eq. (5.1) for strongly correlated systems [150]. A perfect liquid would be realized for $\eta = 0$.

The hydrodynamic theories in Refs. [38, 39] and [40] have been adapted from standard relativistic hydrodynamics. Furthermore the fact that there is only a single transport parameter apart from viscosity is now understood as the two-mode ansatz as we will explain in the following Sec. 5.3. The linear hydrodynamic theory was extended to the three-mode ansatz in Ref. [42]. In the latter reference the hydrodynamics is also derived from the Boltzmann equation and analyzed in linear response also for finite samples and in the presence of a magnetic field.

The hydrodynamics is in particular suitable to study the nonlinear transport regime. The nonlinear hydrodynamics in graphene has been studied for homogeneous systems in Ref. [151]. The possibility of soliton formation has been explored in Ref. [41]. The latter work does not include dissipative corrections due to electron-electron interactions that is however intrinsic to the graphene and has important consequences on nonlinear waves as we will see in Sec. 5.7.

5.3 Microscopic description

The hydrodynamic theory is a coarse grained prescription of the system with local fluid elements of the size l_{hydro}^2. Since we assume $l_{\mathrm{hydro}} \gg 1/T$, the electrons in a given fluid element are characterized by the local distribution function. We want to develop an effective macroscopic theory that is capable to describe transport in graphene in the collision-dominated regime at large length scales. More specifically on length scales larger than l_{hydro}. We assume that the Coulomb interaction is the dominant scattering mechanism. In this case electron-electron interaction has the tendency to thermalize the system locally.

---

[3] Remember that the renormalization of the coupling constant α_g was caused by the flow of v_F alone as we have seen in Sec. 1.3.

[4] Here T_Λ is the temperature determined by the high energy cut-off.

This thermalization is the necessary mechanism to reduce the number of independent dynamic moments of the Boltzmann equation that we have to take into account as we will explain later. The rate of thermalization is of the order $\sim \alpha_g^2 T$ if the graphene is close to the Dirac point. More precisely the rate of isotropization is of the order $\alpha_g^2 T$. The latter is the rate at which different momentum directions equilibrate among each other. In contrast, energy relaxation is logarithmically enhanced and the rate is proportional to $\alpha_g^2 \ln \alpha_g$ [58]. In the end electron-electron interactions determine the mentioned microscopic scale l_{hydro} above which we expect that hydrodynamic behavior emerges. The scale is of the order of the mean free path that is given by $l_{\mathrm{hydro}} \sim 1/\alpha_g^2 T$ in the quantum critical regime close to the Dirac point, i.e. for $T \gg |\mu|$. This length scale is assumed to be much shorter than the scattering length due to disorder. While at the Dirac point Coulomb interaction alone leads to a finite dc conductivity, for finite charge density the dc-conductivity is divergent for $\omega \to 0$. We therefore keep disorder as an infrared regulator. However, the optical response of graphene in the frequency window $\alpha_g^2 T > \omega > \tau_{\mathrm{dis}}^{-1}$ will be given by the hydrodynamic response of the system and the relevant transport coefficients are determined by electron-electron scattering alone. For most results in this frequency window we can thus safely assume $\omega \tau_{\mathrm{dis}} \gg 1$.

The final theory will be formulated in terms of a finite number of macroscopic densities and currents that constitute the effective fluid which describes the transport in the low frequency limit as outlined in the introduction.

The distribution function of electrons is given by $f = f_{\lambda,\vec{k}}(\vec{r})$ and is governed by the Boltzmann equation

$$\mathcal{L}f = St_{ee}[f] - \tau_{\mathrm{dis}}^{-1}(f - \langle f \rangle_\varphi) \,. \tag{5.2}$$

Here $St_{ee}[f]$ is the electron-electron collision integral which was discussed in Sec. 3.2.4. We emphasize that the distribution function f might explicitly depend on the coordinate $\vec{r}$ now. This inhomogeneity of the microscopic state is due to finite gradients in the Liouvillian $\mathcal{L}$ in Eq. (5.2). The latter reads as

$$\mathcal{L} = \partial_t + \hat{v} \cdot \nabla_r + \left[e\vec{E} + e(\hat{v} \times \vec{B}) \right] \cdot \nabla_k \,. \tag{5.3}$$

Furthermore Eq. (5.2) contains the average

$$\langle f \rangle_\varphi = \int_\varphi f = \int_{-\pi}^{+\pi} \frac{\mathrm{d}\varphi}{2\pi} \, f_\varphi \,, \tag{5.4}$$

over the angle φ of $\vec{k}$ in Eq. (5.2). The last term on the right-hand side of Eq. (5.2) takes into account disorder in the relaxation time ansatz, where τ_{dis} is the characteristic relaxation time due to disorder.

In accordance with the standard approach to hydrodynamics [71] as outlined in the introduction to this chapter, we assume that the system is close to equilibrium in the local fluid element. To a first approximation the distribution function $f_{\lambda,\vec{k}}(\vec{r})$, is given by the local equilibrium function [41, 152]

$$f_{\lambda,\vec{k}}^{(0)}(\vec{r}) = \left\{ 1 + \exp\left[\beta(\varepsilon_{\lambda,\vec{k}} - \mu_\lambda(\vec{r}) - \vec{u}(\vec{r}) \cdot \vec{k}) \right] \right\}^{-1} \,. \tag{5.5}$$

Here the coefficient $\beta = 1/T(\vec{r})$ with the local temperature $T(\vec{r})$. Furthermore we have the local chemical potential $\mu_\lambda(\vec{r})$ for conduction ($\lambda = +1$) and valence band electrons ($\lambda = -1$). Finally the quantity $\vec{u}(\vec{r})$ is the hydrodynamic velocity field as will become apparent later. This form of the distribution function is chosen for two reasons. First, the function annihilates the collision integral. On the other hand it maximizes the entropy in the local fluid element under the constraints of a fixed local density of conduction and valence band electrons as well as energy and momentum density.

The inhomogeneity of the system, i.e. the spatial variation of the parameters T, μ_λ and $\vec{u}$ in Eq. (5.5), lead to deviations δf of the distribution function $f = f^{(0)} + \delta f$ from its equilibrium value, Eq. (5.5). However, the fast thermalization allows us to treat the corrections to Eq. (5.5) as a weak perturbation away from local equilibrium. More specifically, they are small corrections as long as the thermodynamic parameters μ_λ, T and $\vec{u}$ vary slowly on the scale l_{hydro}, set by interactions. In this case, the corrections δf will be proportional to the gradients of the parameters T, μ_λ and $\vec{u}$ and additional forces. The latter include for example the self-consistent electric field. Therefore, if the gradients have the characteristic scale l_∇, the corrections δf will be controlled by the Knudsen number $\mathrm{Kn} = l_{\mathrm{hydro}}/l_\nabla$. We can thus reformulate the condition for the validity of the hydrodynamic theory in the following way. The dissipative corrections to the hydrodynamic flow, that originate from the corrections δf, need to be small in the Knudsen number. We will come back to this issue in the next section were we sketch a common strategy to solve the Boltzmann equation. We will see there that we ultimately have to invert the linearized collision integral which is possible perturbatively in the coupling α_g.

We parametrize the corrections δf to the local equilibrium distribution function, Eq. (5.5), in the local fluid rest frame, i.e. the reference frame in which $\vec{u} = 0$ holds. As a consequence of the fast thermalization, the deviations δf are small in the Knudsen number. In general, they are still complicated functions of energy. However, due to the fast collinear scattering, this additional degree of complexity can be reduced. We have seen in Sec. 1.2.3 that the collision integral in graphene exhibits a severe logarithmic divergence originating from collinear scattering. It has been shown that this divergence enables one to solve the Boltzmann equation to logarithmic accuracy analytically [39, 57]. We explain this in more detail in Sec. 5.3.1 below. To leading logarithmic accuracy in the coupling constant α_g, the corrections δf to the distribution function $f^{(0)}$ can be parametrized in the following way:

$$\delta f = \left(-\frac{\partial f^{(0)}}{\partial \varepsilon_k} \right) \left[\delta f^{(1)} + \delta f^{(2)} \right] , \tag{5.6}$$

where the first term in Eq. (5.6) is proportional to the velocity and reads as

$$\delta f^{(1)} = \frac{v_\alpha}{T} \sum_{j=1}^{3} \phi_j h_\alpha^{(j)} . \tag{5.7}$$

The second part is given by

$$\delta f^{(2)} = \frac{v_\alpha v_\beta}{T^2} \sum_{j=1}^{3} \phi_j \, g_{\alpha\beta}^{(j)} . \tag{5.8}$$

In both cases, Eqs. (5.7) and (5.8), we introduced the modes ϕ_j corresponding to the conserved quantities under electron-electron collisions, which are

$$\phi_j = \begin{cases} 1, \ j = 1 \\ \lambda, \ j = 2 \\ \varepsilon/T, \ j = 3 \end{cases} , \tag{5.9}$$

where $\lambda = \pm 1$ is the band index. Furthermore, as a consequence of the collinear scattering, the coefficients $h_\alpha^{(j)}$ in Eq. (5.7) as well as $g_{\alpha\beta}^{(j)}$ in Eq. (5.8) are independent of the energy. Moreover, we do not consider perturbations of the form

$$\delta f^{(0)} \sim \sum_{j=1}^{3} \phi_j l^{(j)} , \tag{5.10}$$

with some coefficients $l^{(j)}$. The reason is, corrections of the form (5.10) correspond to changes in the local parameters $T(\vec{r})$ and $\mu(\vec{r})$. Therefore, they would also change the densities of electrons and holes as well as the energy density. However, we assume that the local equilibrium already contains the right densities. The conditions that any correction to the densities vanish are usually called the Landau Lifshitz conditions in hydrodynamics [71].

We stress that to leading logarithmic accuracy we only need to take into account the modes (5.9) that correspond to the conserved quantities under electron-electron scattering. Other coefficients are suppressed by a factor $\sim 1/\ln(\alpha_g)$. If one only takes into account the modes ϕ_1 and ϕ_3 one obtains the two-mode ansatz mentioned in Sec. 5.2. It is accurate exactly at the Dirac point however neglects the coupling between the densities of conduction and valence band electrons. Note that the coefficient $h^{(3)}$ in Eq. (5.7) can be understood as a shift of the velocity $\vec{u}$. This mode is related to an overall change in the momentum density of the fluid element. Since it is connected to a conservation law of the electron-electron interaction, the momentum conservation, it cannot be damped by Coulomb interaction. At the Dirac point it leads to a divergent heat conductivity in the dc limit, whereas away from the Dirac point it also entails an infinite dc conductivity [57]. In this context disorder is again needed as a regulator in the limit $\omega\tau_{\text{dis}} \ll 1$. Furthermore, we demand the coefficients $g^{(k)}_{\alpha\beta}$ to be traceless in order to leave the densities unchanged by the local collision integral. We have the additional constraint that the fluctuations of the energy current $\delta\vec{j}_E$ are zero in the local fluid rest frame. Since the densities are also conserved this translates into $\delta\vec{u} = 0$.

Generally speaking, the coefficients $h^{(i)}_\alpha$ and $g^{(i)}_{\alpha\beta}$ are determined from the Boltzmann equation [39, 153] which becomes a matrix equation in the restricted subspace of modes ϕ_j. Inverting the matrix collision integral yields the coefficients $h^{(i)}_\alpha$ and $g^{(i)}_{\alpha\beta}$. The following chapter is devoted to the general framework that leads to the matrix collision integral and subsequently to the solution of the Boltzmann equation.

5.3.1 The functional formulation of the Boltzmann equation

We will briefly present the functional formulation of the Boltzmann equation. Within this functional formalism the solution of the Boltzmann equation is represented in a suitable basis. This functional basis naturally leads to the representation of the collision integral as a matrix. This section follows the work presented in Ref. [153] and introduces the notation that becomes useful in the development of the hydrodynamic theory.

We consider a linearized ansatz for the distribution function

$$f_{\lambda,\vec{p}} = f^{(0)}_{\lambda,\vec{p}} + f^{(1)}_{\lambda,\vec{p}} = f^{(0)}_{\lambda,\vec{p}} + f^{(0)}_{\lambda,\vec{p}}\Big[1 - f^{(0)}_{\lambda,\vec{p}}\Big]\delta f_{\lambda,\vec{k}}\,, \tag{5.11}$$

where $f^{(0)}_{\lambda,\vec{p}}$ shall be the local equilibrium distribution function (5.5). The equilibrium distribution is selected by the symmetries of the collision integral and remember that it fulfills $St[f^{(0)}] = 0$ and it maximizes the local entropy density. We start from the linearized Boltzmann equation

$$\mathcal{L}f_{\lambda,\vec{p}}(\vec{r},t) = -\mathcal{C}\delta f\,, \tag{5.12}$$

where the linearized collision operator $\mathcal{C}$ is given in Sec. 3.2.4 and the Liouvillian $\mathcal{L}$ was introduced in Eq. (5.3).

The driving terms

We illustrate the concepts of the functional formulation with the calculation of the viscous response of a system. Therefore we only consider gradients in the velocity $\vec{u}(\vec{r})$ here. Using the derivative of the

Fermi Dirac function

$$\mathrm{d}f^{(0)}_{\lambda,\vec{p}}(\vec{r}) = f^{(0)}\left[1 - f^{(0)}\right]\mathrm{d}\left[\beta\vec{u}\cdot\vec{p} - \beta\varepsilon_{\lambda,p} + \beta\mu_\lambda\right] , \qquad (5.13)$$

we obtain for the left-hand side of the Boltzmann equation (5.12) in the static limit

$$\mathcal{L}f = \beta f^{(0)}_\lambda\left(1 - f^{(0)}_\lambda\right)\lambda|\vec{p}|\left[\frac{p_i p_j}{p^2}\nabla_{r,i}u_j\right] . \qquad (5.14)$$

We rewrite the expression in the brackets as

$$\frac{p_i p_j}{p^2}\nabla_i u_j = \sqrt{2}\left(\frac{p_i p_j}{p^2} - \frac{1}{2}\delta_{ij}\right)\frac{1}{2^{3/2}}\left(\nabla_i u_j + \nabla_j u_i - \delta_{ij}\nabla\cdot\vec{u}\right) + \frac{1}{2}\nabla\cdot\vec{u} . \qquad (5.15)$$

Let us for now consider a divergence free velocity field, for which

$$\frac{p_i p_j}{p^2}\nabla_i u_j = I_{ij}X_{ij} . \qquad (5.16)$$

Here we introduced the following tensors for convenience

$$I_{ij} = \sqrt{2}\left(\frac{p_i p_j}{p^2} - \frac{1}{2}\delta_{ij}\right) , \qquad (5.17)$$

$$X_{ij} = \frac{1}{2^{3/2}}\left[\nabla_i u_j + \nabla_j u_i - \delta_{ij}\nabla\cdot\vec{u}\right] . \qquad (5.18)$$

We have chosen the normalization such that $I^2 = 1$ and both tensors are traceless. The tensor X_{ij} is proportional to the viscous part of the energy stress tensor and it couples to the I_{ij} that can be understood as the corresponding charge in this situation. In this notation the driving term on the left-hand side of Eq. (5.12) assumes the form,

$$\mathcal{L}f = \beta f^{(0)}_\lambda\left(1 - f^{(0)}_\lambda\right)\lambda|\vec{p}|I_{ij}X_{ij} . \qquad (5.19)$$

In the local fluid rest frame it holds $\vec{u} = 0$. Note that in Eq. (5.19) we only considered the leading contribution in the gradients of the velocity field. These sources are described by the tensor X_{ij} from Eq. (5.18). From Eq. (5.12) it becomes clear that, within this linear analysis, the corrections δf on the right-hand side of Eq. (5.12) must also be proportional to the driving X_{ij}. Moreover, since the collision operator is invariant under rotation in the local fluid rest frame, the angular dependence in δf must be proportional to the product $I_{ij}X_{ij}$. Therefore, the solution must be given by

$$\delta f_{\lambda,\vec{p}}(\vec{r},t) = \beta^2 X_{ij}I_{ij}\chi(\lambda,|\vec{p}|) = \beta^2 X_{ij}\chi_{ij}(\lambda,|\vec{p}|) . \qquad (5.20)$$

The linearized Boltzmann equation in the basis of the X_{ij} therefore assumes the form

$$S^\lambda_{ij}(\vec{p}) = (\mathcal{C}\chi_{ij})(\lambda,\vec{p}) . \qquad (5.21)$$

Where we introduced the abbreviation S_{ij} for the driving term,

$$S^\lambda_{ij} = -T\lambda|\vec{p}|f^{(0)}_\lambda\left(1 - f^{(0)}_\lambda\right)I_{ij}(\hat{p}) . \qquad (5.22)$$

The functional for the Boltzmann equation

The Boltzmann equation (5.21) can in principle be solved by discretizing the momentum and solving a large matrix equation. However, it is usually more efficient to consider the following variational approach, which is equivalent to the Boltzmann equation (5.21). Let us first define the inner product

$$(f, g) = N \sum_{\lambda} \int_{\vec{p}} f_\lambda(\vec{p}) g_\lambda(\vec{p}) , \qquad (5.23)$$

where as usual $\int_{\vec{p}} = \int \frac{\mathrm{d}^2 p}{(2\pi)^2}$ and $N = 4$ is the degeneracy. Note that the linearized collision operator $\mathcal{C}$ is hermitian with respect to the above defined inner product (5.23). This allows us to obtain the Boltzmann equation (5.21) as a minimal solution of the following functional

$$Q[\chi] = (\chi_{ij}, S_{ij}) - \frac{1}{2}(\chi_{ij}, \mathcal{C}\chi_{ij}) . \qquad (5.24)$$

The functional $Q[\chi]$ is minimal if $\chi(\lambda, |\vec{p}|)$ satisfies the linear equation (5.21). More explicitly, the two terms in Eq. (5.24) are

$$(\chi_{ij}, S_{ij}) = -\beta^{-1} N \sum_{\lambda} \int_{\vec{p}} f_\lambda^{(0)} \left(1 - f_\lambda^{(0)}\right) \lambda |\vec{p}| \, (\vec{p}) \chi(\lambda, |\vec{p}|) , \qquad (5.25)$$

$$(\chi_{ij}, \mathcal{C}\chi_{ij}) = \frac{N}{4} \sum_{\lambda ...} \int_{\vec{p}...} |M|^2 (2\pi)^3 \delta(\vec{p} + \vec{k} - \vec{p}' - \vec{k}') \delta(\varepsilon_p + \varepsilon_k - \varepsilon_{p'} - \varepsilon_{k'})$$

$$\times f_\lambda^{(0)} f_\nu^{(0)} \left(1 - f_{\lambda'}^{(0)}\right) \left(1 - f_{\nu'}^{(0)}\right) \left[\chi_{ij}^\lambda(\vec{p}) + \chi_{ij}^\nu(\vec{k}) - \chi_{ij}^{\lambda'}(\vec{p}') - \chi_{ij}^{\nu'}(\vec{k}') \right]^2 . \qquad (5.26)$$

The factor $1/4$ takes care of the double counting under symmetrization of the functional.

If one uses an approximation for the function χ, only a restricted subspace of the full functional space containing all possible functions χ is explored. For example one can consider the Taylor expansion of $\chi_{ij}(\varepsilon)$ as a function of ε. This means that in particular an approximation for the function χ that minimizes the functional in the restricted subspace also has to satisfy the linear equation (5.21). Let us assume we perform a Taylor expansion of the functions $\chi(\varepsilon)$ and terminate the series after a finite number of terms. Then the linearized equation (5.21) becomes a finite dimensional matrix equation for the coefficients of the Taylor expansion. Then the task of minimizing the functional (5.24) is reformulated into inverting the matrix collision integral in the linearized equation (5.21). When inverting the collision integral the eigenmodes with the smallest eigenvalue contribute the most. This is the basic idea to solve the Boltzmann equation to leading logarithmic accuracy. More specifically, we only have to take into account the modes or coefficients in the sense of a suitable expansion that do not lead to a logarithmic eigenvalue. Those modes are exactly those that are zero modes in the collinear limit of the collision integral. We will briefly touch upon this in the next section before we continue with the hydrodynamic description for graphene in Sec. 5.4. The hydrodynamic description can be easily formulated in the language we have introduced in this section.

5.3.2 The collinear scattering resonance

We have seen in Sec. 1.2.3 that the electron-electron collision integral possesses a singularity for forward scattering. This forward singularity can also be employed to minimize the functional (5.24) to logarithmic accuracy [39, 57]. It can be used to reduce the dimension of the functional space we have

to consider. In order to see this, we expand the kernel of the collision integral for small perpendicular momenta as was done in Sec. 1.2.3. The perpendicular momenta $k_\perp$ and $p_\perp$ are defined according to $k_\perp = (\hat{z} \times \hat{q}) \cdot \vec{k}$ and $p_\perp = (\hat{z} \times \hat{q}) \cdot \vec{p}$ where $\hat{q} = \vec{q}/q$ and $\vec{q} = \vec{p} - \vec{p}'$ is the transferred momentum due to Coulomb interaction. The vector $\hat{z}$ is the unit vector in z-direction. In this limit the tensor I_{ij} reads as

$$I_{ij} \simeq \frac{1}{\sqrt{2}} \left(2\hat{q}_i\hat{q}_j - \frac{\delta_{ij}}{2} \right) , \tag{5.27}$$

to leading order in the perpendicular momenta. With this representation we obtain

$$(\chi_{ij}, \mathcal{C}\chi_{ij}) \sim \frac{N}{4} \int_q \int_{k_\parallel, p_\parallel} \int_{p_\perp} |M|^2 \frac{1}{q|p_\perp|} \sqrt{p_\parallel k_\parallel (p_\parallel + q)|k_\parallel - q|}$$
$$\times f_\lambda^{(0)} f_\lambda^{(0)} \left(1 - f_\lambda^{(0)} \right) \left(1 - f_\lambda^{(0)} \right) \left\{ I_{ij}(\hat{q}) \left[\chi^\lambda(p) + \chi^\lambda(k) - \chi^\lambda(p+q) - \chi^\lambda(k-q) \right] \right\}^2 . \tag{5.28}$$

Here we only consider intraband scattering since the interband scattering has reduced phase space and from $\lambda = \lambda'$ follows also $\nu = \nu'$ in the collinear limit. In the collinear limit expressed by Eq. (5.28) there are three zero modes that do not lead to the collinear scattering resonance. Namely the functions χ of the form

$$\chi = g^{(1)} + \lambda g^{(2)} + \varepsilon g^{(3)} , \tag{5.29}$$

annihilate the collision integral in the collinear limit. Therefore the ansatz $\chi_{ij} = \chi I_{ij}$ with χ from Eq. (5.29) will not lead to a logarithmically large value of the matrix collision integral as discussed in the previous section. The ansatz (5.29) is exactly the parametrization we have chosen in Eq. (5.8). The parametrization (5.29) is a zero mode of the collinear limit because the three coefficient $g^{(i)}$ are multiplied by conserved quantities of the Coulomb interaction. More specifically, in Eq. (5.28), the bracket

$$\left[\chi^\lambda(p) + \chi^\lambda(k) - \chi^\lambda(p+q) - \chi^\lambda(k-q) \right] , \tag{5.30}$$

vanishes for the ansatz (5.29) due to the conservation laws of Coulomb interaction.

5.4 Macroscopic description - collision-dominated hydrodynamics

The aim of this section is to discuss the emergent macroscopic hydrodynamics. The theory will be formulated in terms of a finite number of hydrodynamic densities and currents. On large scales the relevant densities and currents are selected by the symmetries of the electron-electron interaction and are precisely the locally conserved quantities. For the Coulomb interaction those conserved quantities are the densities of conduction- and valence band electrons, $n_\pm$, the energy density n_E and the energy current $\vec{j}_E$. This means that in local equilibrium they do not mix with other macroscopic densities and currents due to collisions and can thus be understood as the hydrodynamic normal modes. Only gradients and fields will establish a coupling between them. Furthermore all macroscopic observables must be expressed in terms of the hydrodynamic normal modes.

As before we use the following short-hand notation for the integration measure,

$$\int_{\vec{k}} \rightarrow N \int \frac{d^2k}{(2\pi)^2} , \quad \int_{\lambda, \vec{k}} \rightarrow \sum_{\lambda = \pm 1} \int_{\vec{k}} , \tag{5.31}$$

where $N = 4$ accounts for the spin and valley degeneracy in graphene. As a side remark we note that for explicit calculations one has to introduce a high energy cut-off Δ in the integral in Eq. (5.31). Such that for example the energy density at half filling and zero temperature is given by

$$n_{E0} = \int_{\vec{k}} \varepsilon_{-1,k} \to \int_{|\vec{k}|<\Delta} \varepsilon_{-1,k} \, . \tag{5.32}$$

For the coarse grained hydrodynamic description we assume that within a local fluid element of the size $l_{\mathrm{hydro}}^2 > 1/T^2$ the system is described by the distribution function $f_{\lambda,\vec{k}}(\vec{r})$. Guided by the principles outlined in the introduction we then define the local densities according to

$$n_+ = \int_{\vec{k}} f_{+1,\vec{k}} \, , \tag{5.33}$$

$$n_- = \int_{\vec{k}} \left(1 - f_{-1,\vec{k}}\right) , \tag{5.34}$$

$$n_E = \int_{\lambda,\vec{k}} \varepsilon_{\lambda,k} f_{\lambda,\vec{k}} - n_{E0} \, . \tag{5.35}$$

Here we measure the energy density relative to the energy density at charge neutrality and zero temperature (5.32). From the conduction-, Eq. (5.33), and valence band densities, Eq. (5.34), we form the linear combinations

$$n = n_+ - n_- \, , \tag{5.36}$$

$$n_I = n_+ + n_- \, , \tag{5.37}$$

which are the total charge density in units of the electric charge e, Eq. (5.36), and total quasiparticle number density or imbalance density, Eq. (5.37). All densities are conserved quantities with respect to the electron-electron collisions. However, remember that the separate conservation of conduction- and valence-band electron numbers only holds to leading order in the coupling strength α_g [60]. If three particle collisions are taken into account only the net particle number n is conserved as we already mentioned in Sec. 1.2.1.

Apart from the densities we define the hydrodynamic currents which are given by

$$\vec{j}_+ = \int_{\vec{k}} \hat{v}_{+1,\vec{k}} \, f_{+1,\vec{k}} \, , \tag{5.38}$$

$$\vec{j}_- = \int_{\vec{k}} \hat{v}_{-1,\vec{k}} \left(1 - f_{-1,\vec{k}}\right) , \tag{5.39}$$

$$\vec{j}_E = \int_{\lambda,\vec{k}} \varepsilon_{\lambda,k} \hat{v}_{\lambda,\vec{k}} \, f_{\lambda,\vec{k}} \, . \tag{5.40}$$

These are the particle current due to electrons, Eq. (5.38); and holes, Eq. (5.39); as well as the energy current, Eq. (5.40). As in the case of the densities it is more convenient to introduce the linear combinations:

$$\vec{j} = \vec{j}_+ + \vec{j}_- \, , \tag{5.41}$$

$$\vec{j}_I = \vec{j}_+ - \vec{j}_- \, . \tag{5.42}$$

Here $\vec{j}$ is the electric current and $\vec{j}_I$ is the imbalance current . The latter is related to the quasiparticle current. Note that the electric as well as the imbalance current or their counterparts, Eqs. (5.38)

and (5.39), are not hydrodynamic in the sense that they do mix with other densities by collisions. In contrast the energy current (5.40) is the only hydrodynamic current density. This means that ultimately the dynamic quantities of the theory will be the densities from Eqs. (5.33)-(5.37) and the energy current. The electric and imbalance currents however will be related to the latter by their equations of state (5.53) below.

The hydrodynamic densities, Eqs. (5.35)-(5.37), and currents, Eqs. (5.40)-(5.42), can be understood as averages of the microscopic modes from Eq. (5.9) with respect to the distribution function $f_{\lambda,\vec{k}}$. In the following we write this using the the short-hand notation (f, g) for the average of a test function g with respect to the distribution function and related integrals. The scalar product $(\cdot, \cdot)$ was defined in the context of the functional formulation of the Boltzmann equation in Eq. (5.23). The hydrodynamic equations of motion for the densities and currents are now obtained by averaging the Boltzmann equation (5.2) with respect to the modes (5.9). Explicitly this is done by means of

$$(\phi_j, \mathcal{L}f) = -(\phi_j, \mathcal{C}\delta f) = 0 \,. \tag{5.43}$$

Note that the hydrodynamic modes (5.9) do not generate a finite collision integral since they are conserved. Equation (5.43) immediately leads us to the continuity equations for the hydrodynamic densities,

$$\partial_t n + \nabla \cdot \vec{j} = 0 \,, \tag{5.44}$$

$$\partial_t n_I + \nabla \cdot \vec{j}_I = 0 \,, \tag{5.45}$$

$$\partial_t n_E + \nabla \cdot \vec{j}_E = e\vec{E} \cdot \vec{j} \,. \tag{5.46}$$

Only the energy current is a current in the hydrodynamic sense. It can also be interpreted as the momentum density of the system. This is connected to the quasi-relativistic character of the theory such that the electric and energy current, or more precisely the momentum density which is equal to the energy current in graphene, are different. Only in the Fermi liquid limit of high chemical potential the Galilean invariance is restored. In this limit, momentum density as well as particle current become proportional to each other again. The corresponding equation of motion for the energy current $\vec{j}_E$, which will ultimately be the Navier-Stokes equation in our theory, is then obtained from $(\varepsilon\hat{v}, \mathcal{L}f) = 0$ and given by

$$\partial_t \vec{j}_{E,\alpha} + \nabla_\beta \Pi^E_{\beta\alpha} - enE_\alpha - en(\vec{u} \times \vec{B})_\alpha = -\vec{j}_{E,\alpha}/\tau_{\text{dis}} \,. \tag{5.47}$$

Here we introduced the energy-stress tensor

$$\Pi^E_{\alpha\beta} = \int_{\lambda\vec{k}} \varepsilon_{\lambda,\vec{k}} \hat{v}_\alpha \hat{v}_\beta f_{\lambda,\vec{k}} \,. \tag{5.48}$$

Furthermore the electric field in Eq. (5.47) and (5.46) is the effective field and thus also includes the Vlasov field $\vec{E}_V$ generated self-consistently by the charge fluctuations $\delta n(\vec{r}) = n(\vec{r}) - n_0$, where n_0 is the background charge density,

$$\vec{E}_V(\vec{r}) = -\nabla_r \int_{r'} V(\vec{r} - \vec{r}')\delta n(\vec{r}') \,. \tag{5.49}$$

Here $V(\vec{r}) = e^2/r$ is the 3D Coulomb potential. We observe that Eq. (5.40), the equation for the energy current, couples to the yet unknown energy-stress tensor (5.48). Similarly the yet unknown electric and imbalance current appear in the continuity equations for the densities, Eqs. (5.44)-(5.46).

The occurrence of the energy stress tensor in Eq. (5.47) leads in general to an infinite hierarchy of equations which is the main difficulty in the hydrodynamic formulation. However, the presence of electron-electron interaction allows us to truncate the hierarchy of equations arising in the so far generic hydrodynamic formulation. More specifically, the local equilibrium ansatz (5.5), with the deviations from local equilibrium (5.7), leads to the desired equations of state that express the electric current, the imbalance current as well as the energy-stress tensor in terms of the hydrodynamic quantities given in Eqs. (5.33)-(5.37) and (5.40).

First of all we obtain from the definition of the energy current, Eq. (5.40), and the distribution function according to Eqs. (5.6)-(5.8), the following equation of state for the energy current:

$$\vec{j}_E = \frac{3n_E \vec{u}}{2 + u^2} \ . \tag{5.50}$$

The relation (5.50) allows us to replace the energy current by the velocity field $\vec{u}(\vec{r})$. The equations of state for the electric and imbalance current are obtained from their equations of motion which in contrast to the energy current, Eq. (5.47), generate a finite collision integral. The latter even mixes the two currents which results in the matrix equation

$$\partial_t \begin{pmatrix} \vec{j} \\ \vec{j}_I \end{pmatrix} + \frac{1}{2} \begin{pmatrix} \nabla n - e\vec{E}\partial_\mu n \\ \nabla n_I - e\vec{E}\partial_\mu n_I \end{pmatrix} = -\underline{\mathcal{C}}_J \begin{pmatrix} \vec{j} - n\vec{u} \\ \vec{j}_I - n_I \vec{u} \end{pmatrix} \ . \tag{5.51}$$

Here the matrix collision integral of the currents $\underline{C}_J$ contains the scattering times

$$\underline{\mathcal{C}}_J = \begin{pmatrix} \tau_{11}^{-1} & \tau_{12}^{-1} \\ \tau_{21}^{-1} & \tau_{22}^{-1} \end{pmatrix} \ , \quad \underline{\mathcal{C}}_J^{-1} = \begin{pmatrix} \tau_1 & \tau_2 \\ \tau_3 & \tau_4 \end{pmatrix} \ . \tag{5.52}$$

The energy current however decouples from the other two currents since the fluctuations (5.6) cannot decay into a conserved mode. After inversion of the collision integral $\underline{C}_J$ in Eq. (5.51) we obtain the equations of state for the electric and imbalance currents,

$$\begin{pmatrix} \vec{j} \\ \vec{j}_I \end{pmatrix} = \begin{pmatrix} n\vec{u} \\ n_I \vec{u} \end{pmatrix} + \underline{\mathcal{C}}_J^{-1} \begin{pmatrix} \frac{n}{3n_E}\nabla n_E - \frac{1}{2}\nabla n - \left(\frac{2en^2}{3n_E} - \frac{e}{2}\partial_\mu n\right)\vec{E} \\ \frac{n_I}{3n_E}\nabla n_E - \frac{1}{2}\nabla n_I - \left(\frac{2enn_I}{3n_E} - \frac{e}{2}\partial_\mu n_I\right)\vec{E} \end{pmatrix} \ . \tag{5.53}$$

Explicit expressions for the scattering time τ_i that occur in the matrix C_J^{-1} can be found in Appendix E. Strictly speaking they depend on the charge density and energy density, i.e. the local chemical potentials and temperature. In the following simulations of the hydrodynamic equations we assume that the scattering rates are given by their constant equilibrium value. In particular the scattering times τ_2 and τ_3 vanish at the Dirac point.

A similar procedure as in the case of the electric and imbalance current densities leads to the expression of the energy-stress tensor in terms of the hydrodynamic modes which reads as

$$\Pi_{\alpha\beta}^E = \frac{n_E}{2 + u^2}\left[\delta_{\alpha\beta}(1 - u^2) + 3u_\alpha u_\beta\right] - \eta\left[\nabla_\alpha u_\beta + \nabla_\beta u_\alpha - \delta_{\alpha\beta}\nabla \cdot \vec{u}\right] \ , \tag{5.54}$$

Here we assumed that the viscosity η is determined by the equilibrium background densities and thus does not vary in space. Details on the calculation of the viscosity can be found in Appendix E. We note here that the second or bulk viscosity is zero in graphene due to the Landau Lifshitz conditions that we

have formulated in Sec. 5.3. Technically the trace of the energy stress tensor does not acquire corrections due to deviations from local equilibrium (5.5) since the coefficients $g_{\alpha\beta}$ are traceless. The bulk viscosity is however connected to corrections to the trace of the energy stress tensor. In order to generate a finite bulk viscosity one therefore needs to relax the condition that the coefficients $g_{\alpha\beta}$ are traceless. This can only be done when one of the densities n, n_E and n_I is not conserved under electron-electron interactions. In fact, this is true for the imbalance density to higher order in the coupling constant α_g as we mentioned earlier. Three-particle collision indeed lead to a violation of separate conservation of conduction and valence band electrons [60]. As a consequence, to higher orders in the coupling constant α_g the bulk viscosity is finite. These corrections are however beyond the study presented in this thesis.

If we introduce the dissipative corrections to the electric current $\delta\vec{j} = \vec{j} - n\vec{u}$, we can rewrite the equation of the energy current in the standard form of relativistic hydrodynamics

$$W\partial_t u_\alpha + W(\vec{u}\cdot\nabla)u_\alpha + \nabla_\alpha P + u_\alpha\partial_t P + u_\alpha\, e\vec{E}\cdot\delta\vec{j} = en[\vec{E} - \vec{u}(\vec{u}\cdot\vec{E})] + \eta\nabla^2 u_\alpha\,. \tag{5.55}$$

Here we introduced the nonlinear enthalpy W and pressure P,

$$W = \frac{3n_E}{2+u^2}\,, \qquad P = \frac{(1-u^2)n_E}{2+u^2}\,. \tag{5.56}$$

There are several features of the graphene Navier-Stokes equation (5.55) that distinguish it from the standard case. First, we are dealing with relativistic hydrodynamics which manifests in the term $\partial_t P$ in Eq. (5.55). Second, the relations of pressure and enthalpy (5.56) contain the velocity explicitly. If the enthalpy and the pressure are not chosen as in Eq. (5.56) the equations do not assume the standard form as in Ref. [41]. However both relations (5.56) follow immediately from the local equilibrium ansatz (5.5). One observes that the pressure vanishes in the ultrarelativistic limit of $u \to 1$. Furthermore, the electric field does only change the direction of the velocity in the limit $u \to 1$, the absolute value is limited by the Fermi velocity.

5.5 Linear analysis

We will briefly discuss certain features of the hydrodynamic equations in graphene presented in the previous section.

First we consider the linear response conductivity of an infinite sample. After linearizing the hydrodynamic equations (see Appendix E.2) one obtains for the conductivity

$$\sigma(\omega, q) = \sigma_0 + \frac{2\mathrm{i}e^2 n^2}{3n_E\omega}\left[1 + \frac{\mathrm{i}q^2}{\omega^2}\left(\frac{1}{2} - \frac{2\mathrm{i}\eta\omega}{3n_E}\right)\right]$$
$$+ \frac{\mathrm{i}q^2}{\omega}\left\{\frac{\tau_1^2 + \tau_2\tau_3}{2}\left(\frac{2e^2 n^2}{3n_E} + e^2\partial_\mu n\right) + \frac{\tau_2(\tau_1 + \tau_4)}{2}\left(\frac{2e^2 n n_I}{3n_E} + e^2\partial_\mu n_I\right)\right\}\,. \tag{5.57}$$

Here the finite dc conductivity at the Dirac point due to electron-interactions [57] is given by

$$\sigma_0 = e^2\left[\tau_1\left(\frac{\partial_\mu n}{2} - \frac{2n^2}{3n_E}\right) + \tau_2\left(\frac{\partial_\mu n_I}{2} - \frac{2n n_I}{3n_E}\right)\right]\,. \tag{5.58}$$

Related results have been found in Ref. [38], where the authors calculate the conductivity for finite frequency and momentum also from a hydrodynamic description. However only a single transport

parameter τ_1 has been taken into account in contrast to the work presented here which also includes the coupling between imbalance and the charge densities by the scattering times τ_2 and τ_3 through the 3-mode ansatz (5.6). Furthermore Ref. [38] calculates the reducible conductivity. The latter is the response to the external electric field and includes a linear in q term due to screening. The result (5.57) is the irreducible conductivity. Compared to Ref. [38] we do not only calculate the irreducible conductivity but also consider the corrections of order q^2 and take into account a finite background charge density $n^{(0)}$. The latter leads to the fact that the coupling of the charge and imbalance densities becomes apparent in the nonlocal conductivity (5.57). Moreover we observe that the viscosity directly enters the nonlocal conductivity away from the Dirac point, i.e. for finite charge density $n^{(0)}$ in Eq. (5.57). As a consequence nonlocal optical measurements in the graphene can give access to the shear viscosity. The fact that the influence of the shear viscosity on the nonlocal conductivity vanishes at the Dirac point can be understood as follows. The viscosity is connected to gradients in the energy current or momentum density. The conductivity however is the response of the particle current. Right at the Dirac point both currents decouple and therefore the effect due to viscosity vanishes for $n^{(0)} \to 0$.

Second, let us consider the graphene at the Dirac point in the absence of any dissipative terms. It follows from Eqs. (5.55) and (5.46) that the system at the Dirac point supports energy waves with linear dispersion $\omega_q = v_s q$, where the sound velocity is $v_s = v_F/\sqrt{2}$. The latter are sometimes denoted cosmic sound and known for cosmic plasmas [71]. Thus the system shows ballistic energy transfer at the Dirac point which results in an infinite thermal conductivity. On the other hand the charge density or the particle density is transported diffusively close to the Dirac point. This is in contrast to the Galilean invariant system where the energy is transported diffusively and the mass density travels ballistically. It must be stressed that close to the Dirac point the diffusive motion is only due to the Coulomb interaction and present without any disorder. However, for finite charge density the Vlasov field also establishes coupling between the energy density and the charge density and leads to a hybridization of the energy waves with charge oscillations leading to the formation of standard 2D plasmons with square root dispersion. From the linear analysis of the hydrodynamic equations (5.44)-(5.46) and (5.55) we obtain the real part of the plasmon dispersion

$$\omega(q) = \left\{ \frac{q^2}{2} \left(1 + \frac{4\alpha_g n^2}{3 n_E q} \right) - \frac{q^4}{9} \left(\frac{\eta}{n_E} - \frac{3\sigma_0}{2e^2} \frac{\alpha_g}{q} + \frac{3(\tau_1 + \tau_4)}{4} + \frac{3}{2\tau_d q^2} \right)^2 \right\}^{1/2}. \tag{5.59}$$

The dispersion (5.59) is illustrated in Fig. 5.1. The evolution from the linear dispersion towards the 2D plasmon behavior $\omega \simeq \sqrt{q}$ is apparent. Furthermore we observe that the dissipative corrections lead to a modification of the plasmon dispersion. The hydrodynamic theory can cover small momenta and agrees with the RPA (see Sec. 1.2.4) in this limit. And as depicted in Fig. 5.1(b) the presence of disorder affects the hydrodynamic plasmon dispersion at small momenta.

5.6 Hydrodynamic simulation techniques

In this section we are going to explain some of the techniques employed in the simulation of the nonlinear hydrodynamics in graphene formulated in the previous section.

We will briefly explain the implementation of the semi-implicit scheme, also called implicit-explicit scheme (IMEX) [131, 154], for the numerical computations. We will also mention how we calculate the Vlasov field for the evolution of the hot spot shown in Sec. 5.7.
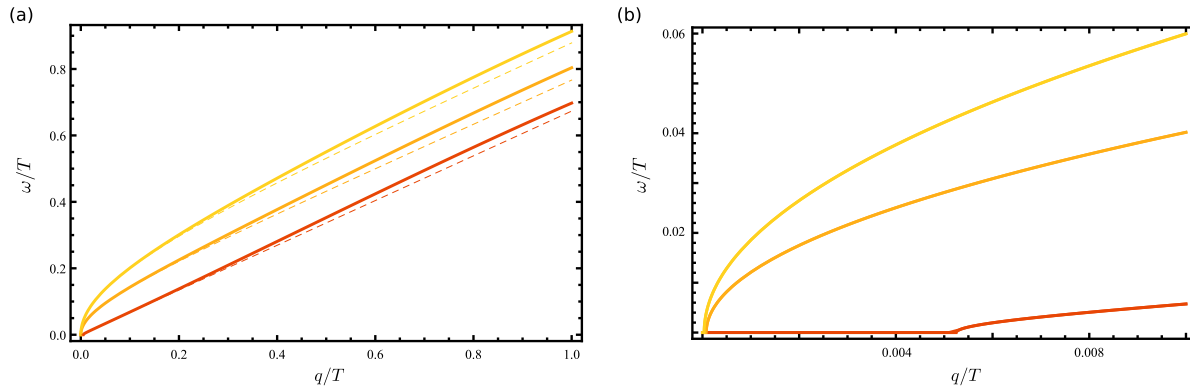
Figure 5.1: *(a) The plasmon dispersion, Eq. (5.59), for different chemical potentials. The dashed lines are the dispersion relations without dissipative terms. The solid lines are the dispersions including corrections due to finite viscosity and conductivity. (b) The dispersion of plasmons for small momenta where the disorder scattering $1/T\tau_{dis} = 0.001$ affects the plasmons strongly.*

5.6.1 The semi-implicit solver

A variety of methods have been developed for the simulation of hydrodynamic flow in the field of computational fluid dynamics. Among those are the finite-difference time-domain, the finite element and spectral methods to name only a few. For the nonlinear hydrodynamics in graphene we developed a finite-difference time-domain simulation code for the system of equations constituted by the continuity equations (5.44)-(5.46) and the graphene Navier-Stokes equation (5.55). Those have to be solved in conjunction with the equations of state (5.53) for the electric and imbalance current and the equation for the Vlasov field, Eq. (5.49).

The Navier-Stokes equation (5.55) in the presence of finite dissipative corrections, Eq. (5.53), belongs to the class of convection-diffusion systems. The convective term is a major nonlinearity of the Navier-Stokes equation (5.55), while diffusion due to electron-interaction close to the Dirac point is contained in the dissipative corrections in Eq. (5.53). Structurally the viscous terms are of similar type. It is known that for convection-diffusion systems an explicit discretization of the differential equations in time and space leads to a stiff system. This can be seen from a straightforward application of the finite-difference scheme to the diffusion equation

$$\partial_t n = D\nabla^2 n \,, \tag{5.60}$$

which reads as

$$n_{t+1}^k = n_t(1 - 2D\Delta t)n_t^k + \dots \,. \tag{5.61}$$

Here Δt is the time step and n_t^k denotes the density at time t and space point k. The explicit Euler scheme expressed by Eq. (5.61) only yields reliable results for small $D\Delta t$. That means that for a finite diffusion constant very small time steps have to be chosen to reach convergence. Mixed implicit and explicit discretization have been successfully employed to circumvent this problem [154]. More specifically, the convective terms are discretized explicitly on a staggered grid that is explained in the next section. We use an Euler scheme for these parts of the hydrodynamic equations. A generalization to multi-step methods is however possible [154]. Here convective terms denote the Euler limit of the nonlinear hydrodynamic equations that is obtained when the viscosity and all dissipative corrections
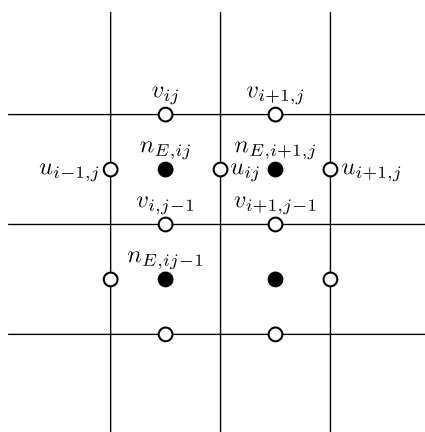
Figure 5.2: *The staggered grid consists of two grids for the velocities and the pressure shifted by half a lattice constant. As a result the two components of the velocity vector u and v are given on the sidewalls of the cells shown in the picture while the densities and thus the pressure are calculated in the middle of the cell.*

are neglected. The dissipative terms are then discretized by a backward Euler scheme. This implicit formulation leads to a sparse, positive-definite and symmetric matrix equation that can be solved in a reasonable amount of time fore each time step.

In each of these time steps we also have to solve for the Vlasov field. The integral representation is equivalent to the Poisson equation with suitable boundary conditions at infinity. We also use an implicit scheme for the Poisson equation. The linear system is solved at each time step. For the evolution of the energy density bump in Sec. 5.7 we can furthermore eliminate the boundary conditions by the following procedure. In each time step we solve the Poisson equation twice. First for the homogeneous initial charge density. Then we solve the Poisson equation for the total charge density profile. Since the Poisson equation is linear we can subtract the solution for the homogeneous background from the second solution. The result is the desired electric field of the localized charge bump alone without any influence of the boundaries. In a more general case a volume large enough to remove effects due to boundary conditions has to be simulated.

Technically the implicit scheme as well as the discretization of the Poisson equation lead us to sparse linear systems that need to be solved. As we have mentioned before they are symmetric and positive-definite. We therefore use the LDLT decomposition of the Eigen libraries for C++ to accomplish this task.

5.6.2 The staggered grid

The analog of the Navier-Stokes equation in graphene shows a couple of similarities to its classical analog and of course certain differences discussed in the previous chapter. Many of the numerical difficulties encountered in the treatment of the Navier-Stokes equation therefore also occur in our problem.

When discretizing the Navier-Stokes equation special care must be taken in the study of nonlinear effects, e.g. in the regime of dominant convective terms. In general it might happen that the discretized version possesses solutions and properties not shared with the continuous equations.

It is known that for large convective terms for example the method of central differences for the
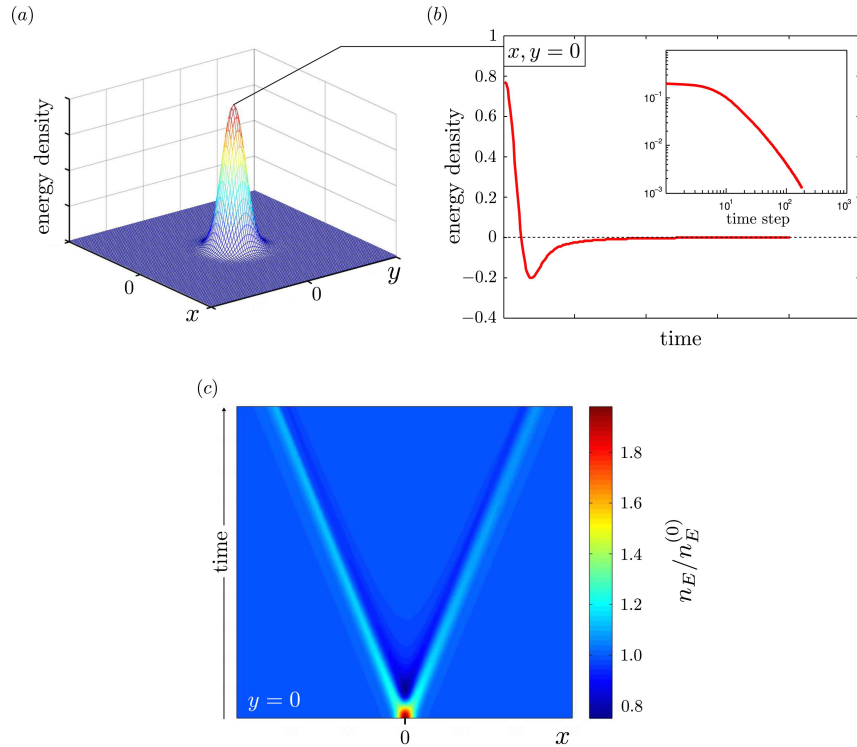
Figure 5.3: *(a) The initial energy density n_E normalized to the equilibrium background energy density $n_E^{(0)}$. The maximum height of the initial energy perturbation is $\hat{n}_E = 0.8\, n_E^{(0)}$. The width is given by $5a$, where a is the high energy cut off $a \sim 1/T$. (b) The time evolution of the energy density at the origin. The inset shows the energy density on a double logarithmic plot. (c) The time evolution of the energy density in the absence of the Vlasov field and dissipative corrections. The plot depicts a cut through the energy density profile at $y = 0$ for different time steps.*

spatial derivatives can lead to unnatural oscillations in the solution if the discretization in space is chosen too small [131]. However, in terms of convergence central differences are favorable over forward or backward difference schemes [131].

Another problem that also leads to unphysical oscillations is associated with the fact that we need not only solve for the velocities but also for the pressure. If we use a single grid for all of the quantities u, v and the pressure p, that means we evaluate all three quantities on the same grid point, then the discretized version of the Navier-Stokes equation for zero velocities allows for arbitrary oscillations in the pressure profile. To avoid this the velocities and the pressure are specified on different grids that are shifted by half a lattice spacing [131]. The resulting arrangement is shown in Fig. 5.2. Here the two-component vector velocity $\vec{u}$, i.e. the hydrodynamic velocity field from Sec. 5.4, is rewritten in terms of

$$\vec{u}(\vec{r}) = \begin{pmatrix} u(\vec{r}) \\ v(\vec{r}) \end{pmatrix}, \tag{5.62}$$

which is then evaluated on the finite-difference grid as depicted in Fig. 5.2. In our case, the pressure is associated to the densities. The latter are given in the center of the cells shown in Fig. 5.2, whereas

the velocities are given on the boundaries. When velocities are now needed on the pressure grid or vice versa then appropriate averages of the surrounding grid points are chosen to compute velocities on the pressure grid and the pressure in the Navier-Stokes equation. We give explicit expressions for the discretization of the derivatives in the Appendix F.

5.6.3 Dimensionless variables

In the numerical scheme we introduce a high energy cut off in the theory, due to the finite-differences on the staggered grid. We denote this cut off as $a \sim v_F \hbar / T_0$ and chose it of the order of the inverse equilibrium background temperature T_0 as it corresponds to the validity of the hydrodynamics. The system is initially prepared in equilibrium with a background energy density $n_E^{(0)}$. We therefore normalize the energy density in the following with respect to the background energy density $n_E^{(0)}$. The charge density is normalized as $a^2 n \sim n/T^2$. The latter is the particle density in one plaquette of the staggered grid as depicted in Fig. 5.2. Note furthermore that $a^2 n$ also measures the deviation from the Dirac point. From the inspection of the Poisson equation one obtains the dimensionless Vlasov coupling constant

$$g = \frac{4\pi\alpha_g}{\epsilon} \frac{v_F \hbar}{a^3 n_E^{(0)}} , \tag{5.63}$$

where we restored $\hbar$ and v_F for convenience. In equation (5.63) we introduced the dielectric constant ϵ of the surrounding.

5.7 Nonlinear hydrodynamics: Relaxation of hot spots

This section presents a first application of the nonlinear hydrodynamics developed in Sec. 5.4. We conduct a numerical study of the time evolution of a hot spot and investigate its relaxation. This specific initial perturbation was partly motivated by the theoretical studies of hydrodynamics in 1D systems as described in Refs. [43, 44]. On the other hand, as was mentioned in the introduction to this thesis, a number of experimental techniques have been developed to create and detect plasmon waves in graphene. Moreover, the study of the relaxation dynamics of a hot spot continues our work from Chapt. 4. The hydrodynamic theory describes the spatial relaxation of the system after it has been heated locally, for example by a laser pulse.

The initial perturbation studied here is the following. Suppose the graphene is initially in equilibrium with energy density $n_E^{(0)}$ and particle number $n^{(0)}$ as well as imbalance density $n_I^{(0)}$. The initial hydrodynamic flow is zero. The latter conditions can be translated into the initial temperature of the graphene and chemical potentials for electrons and holes. The system is then driven out of equilibrium by adding a localized energy density. We assume a Gaussian profile for the perturbation in the energy density as depicted in Fig. 5.3(a). We consider a system at temperature $T = 300\,\mathrm{K}$. The dimensionless initial particle density is $n^{(0)} = 0.5$, which translates into a charge density of $1.7 \cdot 10^9 \,\mathrm{cm}^{-2}$. The corresponding Vlasov coupling is given by $g = 5$.

5.7.1 Dissipationless limit

We start the discussion of the nonlinear hydrodynamics with the dissipationless limit of the hydrodynamic equations. At first we neglect all corrections due to Coulomb interaction.[5] More specifically,

---

[5]Note however that for stability in the implicit scheme we chose the dissipative terms negligible small.
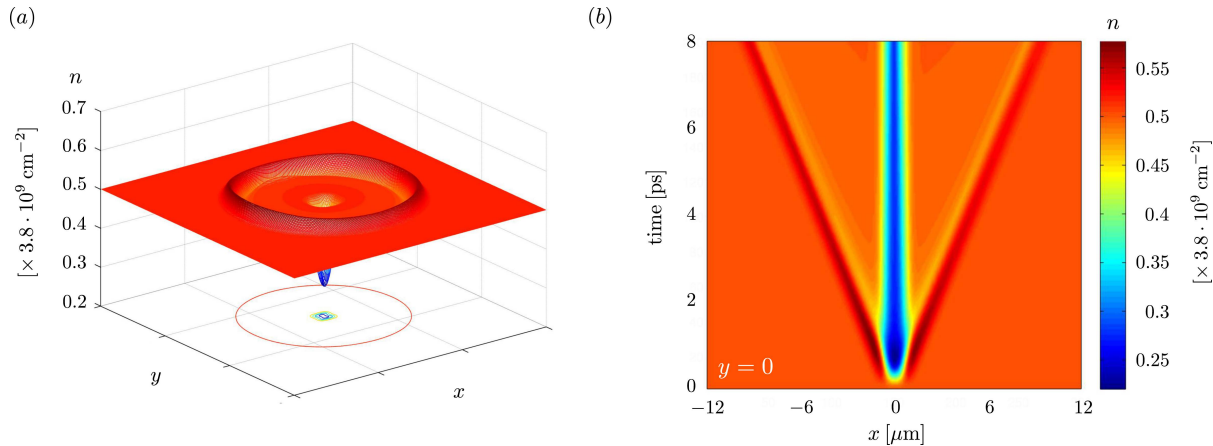
Figure 5.4: *(a) A snapshot of the dimensionless hydrodynamic particle density n at time $t = 0.15\,ps$ after preparation of the disturbance away from equilibrium given in Fig. 5.3(a). The evolution is due to the hydrodynamic equations without Vlasov field and dissipative corrections. (b) The time evolution of the particle density in the absence of the Vlasov field and dissipative corrections. The plot depicts a cut through the particle density profile at $y = 0$ for different times.*

we neglect the Vlasov field for now and neglect the terms proportional to the scattering times τ_i in Eq. (5.52) as well as the viscosity.

For this limit of free propagation, the evolution of the energy density is illustrated in Fig. 5.3. Figure 5.3(a) depicts the initial perturbation at time $t = 0$. The system is rotational symmetric at all times we therefore plot the cut of the energy density at $y = 0$ and different times in Fig. 5.3(c). We observe that the initial energy bump evolves into an energy wave emitted from the origin. This energy wave carries a finite hydrodynamic velocity. Moreover we observe that behind the wave front the energy density becomes depleted again. However, due to the fact that we are considering two-dimensional hydrodynamics the density at the origin does not vanish immediately as is shown in Fig. 5.3(b). It rather shows an after glow which is typical for two-dimensional hydrodynamics. The inset of Fig. 5.3(b) reveals the after glow in a double logarithmic plot at long times. The power law decay that manifests this effect is due to the t^{-1} asymptotics of the Green's function of the two-dimensional wave equation. Later, we will find that the density at the origin is strongly affected by interactions, in particular by the Vlasov field at short times. The power law decay is then changed. The energy wave emitted by the hot spot at the origin carries a finite hydrodynamic velocity $\vec{u}$. Since we also have a finite background charge density $n^{(0)} = 0.5$ this entails the emergence of a similar hydrodynamic wave in the particle density that follows the wave in the energy density according to Eq. (5.44). At the Dirac point this effect vanishes since $n\vec{u} = 0$ everywhere and as a consequence only an energy wave propagates in the system. Interestingly, in contrast to the energy density that is depleted behind the wave front in the situation of Fig. 5.3(c), the particle density develops a dip at the origin, see Fig. 5.4. This can be understood in the following way. The wave front in the energy density is generated by the additional energy in the hot spot. More specifically the gradient in the pressure is the source for the velocity field $\vec{u}$. However as the energy wave drags the particle density along due to the finite velocity $\vec{u}$ it creates a dip at the position of the initial hot spot. Without dissipative terms and without the presence of a Vlasov field this dip can not relax, simply because the gradient of the pressure has already vanished and
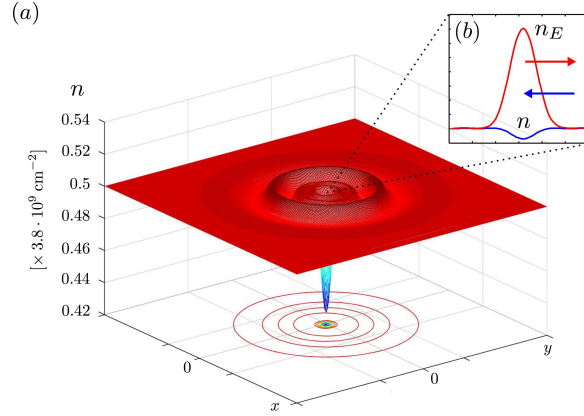
Figure 5.5: *(a) A snapshot of the dimensionless hydrodynamic particle density n after prepara-tion of the disturbance away from equilibrium given in Fig. 5.3(a) The evolution is due to the hydrodynamic equations including the Vlasov field but without dissipative corrections. (b) The inset shows the energy density as well as the charge density at the initial location of the hot spot. Both are plotted along the line y = 0 for the time t = 0.05 ps. The arrows indicate the direction of the forces due to the pressure (red arrow) and the Vlasov field (blue arrow).*

the local velocity is zero. Therefore a charge dip remains at the origin as one can see in Fig. 5.4(b). We come back to the fate of this structure in the presence of a finite Vlasov term in the following paragraph. Moreover, we discuss the effects of finite dissipative corrections in the following section 5.7.2.

Let us now consider the same initial condition as in the previous paragraph [see Fig. 5.3(a)] but including a finite Vlasov field. A snapshot of the evolution of the particle density in the presence of a finite Vlasov field is shown in Fig. 5.5. The Vlasov term leads to a hybridization of the charge density and the energy density and the energy waves turn into a plasmonic wave showing rapid oscillations. The latter are emitted by the hot spot. Interestingly the dip in the charge density at the origin remains even in the presence of the Vlasov field. In general the self-consistent electric field favors a homogeneous background charge density profile. However, here the dip in the charge density is accompanied by a positive bump in the energy density at the origin. This positive energy bump creates a pressure gradient that compensates the Vlasov field of the charge inhomogeneity. This interplay is depicted in the inset (c) in Fig. 5.5. Here, the energy density (red curve) as well as the charge density (blue curve) are shown in the vicinity of the origin. We observe that the charge density (blue curve) forms an oppositely directed dip with respect to the bump in the energy. The direction of the pressure is indicated by the red arrow, whereas the action of the Vlasov field is illustrated by the blue line. We will see in the next section that this complex becomes metastable in the presence of dissipative corrections.

5.7.2 Relaxation dynamics including dissipation

Finally we leave the dissipationless limit and consider the relaxation of the same initial condition as before in the presence of the Vlasov field and, moreover, including dissipative corrections. For simplicity we set the scattering times τ_i $(i = 1, ..., 4)$, which describe the dissipative corrections defined in Eq. (5.52), all equal to $\tau_i = 1$ fs. The resulting time evolution of the charge density is depicted in
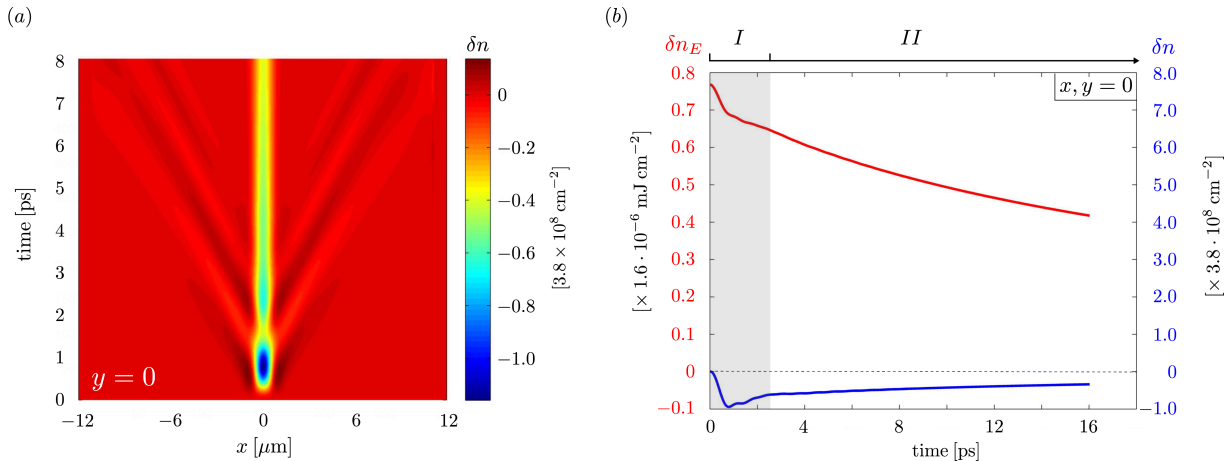
Figure 5.6: *(a) The time evolution of the corrections to the particle density $\delta n = n - n^{(0)}$, in the presence of the Vlasov field including dissipative corrections due to the following values of the scattering times from Eq. (5.52): $\tau_i = 1\,fs$ $(i = 1, ..., 4)$. The plot depicts a cut through the particle density profile at $y = 0$ for different times. The initial condition is depicted in Fig. 5.3(a). (b) The time evolution of the corrections of particle density, $\delta n = n - n^{(0)}$, (blue line) and the energy density, $\delta n_E = n_E - n_E^{(0)}$, (red line) at the origin, i.e. the initial position of the hot spot.*

Fig. 5.6.

The time evolution of the particle density is shown in Fig. 5.6(a) along the line $y = 0$. We observe that in contrast to the previous case the hot spot emits a short train of charge oscillations. More specifically we observe that there is a short time after the simulation has started, in which the energy density starts to collapse. This is illustrated in Fig. 5.6(b). Here the deviations of the energy density as well as the charge density at the origin are plotted as a function of time. The gray region I demarks the mentioned initial stage of the collapse of the hot spot characterized by a sudden drop in the energy density. At the same time the charge density starts to drop as well. This collapse remains incomplete as the hot spot stabilizes in a metastable state. The latter is based on the same mechanisms as in the previous section and depends on a compensation between pressure and Vlasov field, which we illustrated in Fig. 5.5(c). In the regime I the system also emits waves as shown in Fig. 5.6(a).

After the regime I, the train of waves has left the hot spot and the system enters the regime II. This second regime is characterized by a slow decay of the densities at the origin [see Fig. 5.6(b)], while the wave train propagates away from the hot spot. In contrast to the dissipationless propagation the emitted waves have a finite propagation length within the regime II. This can be seen in Fig. 5.6(a) if one follows the trajectory of a wave maximum. The decay of the wave is due to the finite viscosity and dissipative terms which lead to a finite life time of the hydrodynamic plasmons.

5.7.3 Discussion

We see that the decay of a hot spot in the hydrodynamic regime contains an interesting interplay between different mechanisms. We find that the Vlasov term is essential to describe the correct relaxation dynamics. Moreover we find two distinct time regimes. The first one is characterized by the onset of collapse of the hot spot and excitation of waves in the charge density which are emitted by the hot
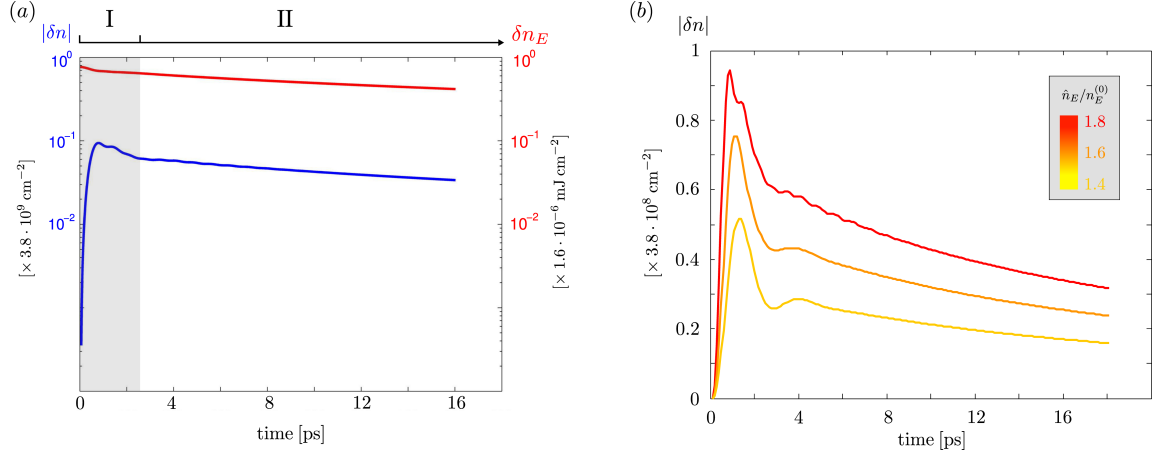
Figure 5.7: *(a) The time evolution of the corrections of particle density, $\delta n = n - n^{(0)}$, (blue line) and the energy density, $\delta n_E = n_E - n_E^{(0)}$, (red line) to the equilibrium background values at the origin, i.e. the initial position of the hot spot. The evolution is plotted on a logarithmic scale. The latter reveals the exponential decay of the hot spot at long times. (b) The time evolution of δn for different initial heights $\hat{n}_E$ of the hot spot.*

spot. More importantly the collapse of the hot spot remains incomplete. It rather forms a metastable state as discussed in the previous sections and illustrated in Fig. 5.5(c). Following this initial short time regime that leads to the formation of this metastable state accompanied by the emission of plasmons, the second regime II is characterized by a slow decay of the hot spot while the emitted waves propagate away from the origin. More specifically, the quasi-equilibrium between the energy and charge density means a compensation of pressure and electrostatic forces in the hot spot. This is illustrated in the inset, Fig. 5.5(c). The relaxation is then only due to dissipative correction and slow compared to the initial stage I. These two regimes are illustrated in Fig. 5.7(a), where we show the densities at the origin on a logarithmic plot. From Fig. 5.7(a) we conclude that the regime II is characterized by an exponential decay of the hot spot. We emphasize that the decay is solely due to the Coulomb inter-action close to the Dirac point. In Fig. 5.7(b) the evolution of the density fluctuations at the origin is depicted for different initial heights $n_{E,\max}$ of the hot spot. We observe that the regime I is increasing with decreasing height of the hot spot.

We discuss the emergence of the exponential decay in more detail. In the regime II the velocity at the hot spot is negligible. We neglect the coupling fo the imbalance density and the charge density due to Coulomb scattering. Finally, we neglect the Vlasov field in the dissipative corrections (5.53) for simplicity. In this case we have

$$\partial_t n \simeq \tau_1 \left(\frac{n}{3 n_E} \nabla n_E - \frac{1}{2} \nabla n \right) . \tag{5.64}$$

Let us assume that the deviations δn_E of the energy density as well as the charge density, δn, on top of their respective equilibrium values, $n_E^{(0)}$ and $n^{(0)}$, are given by Gaussians,

$$\delta n_E = B \mathrm{e}^{-r^2/L^2} , \tag{5.65}$$

$$\delta n = -A \mathrm{e}^{-r^2/L^2} . \tag{5.66}$$
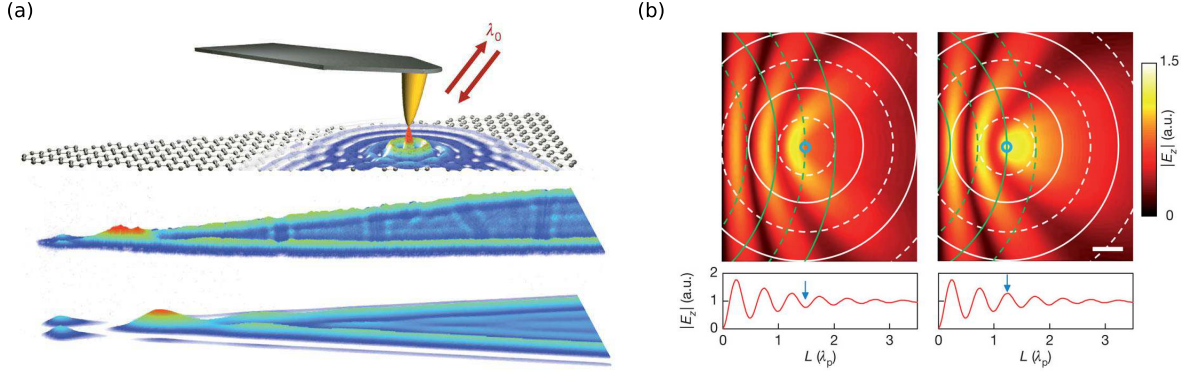
Figure 5.8: *(a) Schematic of the excitation of plasmons within the SNOM technique (upper image) and the resulting standing wave patter in a tapered graphene ribbon (lower images). The image of the standing wave pattern is also obtained by means of SNOM as reported in Ref. [33]. The lower image shows a magnified view of the ribbon tip. Reprinted figure with permission from: Chen et al, Nature 487, 77–81 (2012). (b) Measured standing wave pattern of plasmon waves from Ref. [32]. The data is also obtained from SNOM and the figure shows the optical near-field intensity. Reprinted figure with permission from: Fei et al, Nature 487, 82–85 (2012).*

The amplitudes A and B are related since in the metastable state the pressure as well as the Vlasov field must compensate. We assume in the following a simlified model for the self-consistent Vlasov field. Assuming we had a nearby gate that screens the Coulomb potential, the Vlasov field is proportional to the local density gradients and we have $\vec{E}_V = -G\nabla n$. Here G is the effective coupling. In this model $B/A \simeq 2Gn^{(0)}$. With this we obtain within the linear analysis for the slowly varying amplitude $A(t)$,

$$\partial_t A(t) = -\frac{2\tau_1}{L^2}\left(\frac{2G[n^{(0)}]^2}{3n_E^{(0)}} + \frac{1}{2}\right)A(t) \, . \tag{5.67}$$

We see that the amplitude is always decaying due to the dissipative term that is proportional to τ_1. The decay is however slowest close to the Dirac point. Although we should mention that in contrast to the simulation the simple analysis here is restricted to the linear regime. Close to the Dirac point however we eventually have $n^{(0)} \sim \delta n$.

5.8 Relation to experiments

At the end of this chapter we review the relevant experiments which are related to the theory of nonlinear hydrodynamics as developed in this thesis. We have already mentioned several experimental works in the introduction to this thesis and the current chapter. We describe their relation and importance to our work in more detail now.

In the two seminal works of Ref. [33] and [32] the SNOM techniques was first applied to study graphene plasmons. In Fig. 5.8 we illustrate results from both works. Figure 5.8(a) depicts a schematic of the experimental technique performed on a tapered graphene ribbon. The image is taken from Ref. [33]. An AFM tip, shown in yellow, is used to launch plasmons when illuminated by the far-field radiation. At the same time the scattered light is used to detect the optical near-field, which allows

monitoring the subsequent propagation of the plasmons. The reflection of plasmons at the boundaries gives rise to standing waves. The resulting pattern of standing waves is also illustrated in Fig. 5.8(a). Similar results from Ref. [32] are shown in Fig. 5.8(b). Here the standing wave pattern due to reflection at the boundary is used in order to determine the plasmon wavelength and the plasmon life time. From Fig. 5.8(a) the similarity between the problem of a hot spot that we considered before and the excitation of plasmons within the SNOM is apparent. In the experiments depicted in Fig. 5.8 the AFM tip is a source that excites the charge density whereas we studied the evolution of a initially prepared energy bump. The developed formalism can be extended to the experimental situation. In summary, we stress two important aspects. First, the precited evolution of the charge density in the previous section can be measured by means of SNOM. Second, what is measured in current experiments can be simulated by means of the developed hydrodynamics. In this regard, both the experimental as well as the theoretical techniques are complementary in testing future graphene device concepts, in particular graphene based plasmonic devices. We have also seen that the plasmonic waves, for example in Fig. 5.6(a), acquire a finite life time due to interactions. It is therefore interesting to compare quantitatively the experimentally obtained plasmon life times and with thoses which we obtain in the simulations.

One such plasmonic device concept is the fabrication of nanoantennas on the graphene as reported in Ref. [149]. The experiment is shows in Fig. 5.9 along with the measured plasmon wavelength and the near-field amplitudes from Ref. [149]. The fabrication of the nanoantenna on top of the graphene sheet enables the creation and the detection with two different experimental techniques. Furthermore specifically shaped antennas can be used to focus plasmon waves. In view of this experiments it is also possible to study hydrodynamics in the nonlinear regime in the future. Here, the hydrodynamic theory is in particular suitable to test the upcoming design concepts.

5.9 Summary

On the one hand this chapter was devoted to the development of collision-dominated hydrodynamics in graphene. Apart from the theoretical formalism we also developed a numerical hydrodynamic solver designed for the description of transport in graphene. The numerical tool incorporates dissipative corrections due to Coulomb intercation as well as the self-consistent Vlasov field. On the other hand, we applied the developed formalism to the specific problem of the relaxation of hot spots in graphene. This numerical study is a first application of the developed formalism and simulation tools.

We investigated the interaction-dominated regime for which the emergent hydrodynamics has been proposed theoretically before in Refs. [16, 38]. In view of these previous works, we developed a formalism to treat nonlinear hydrodynamics in graphene taking consistently into account dissipative corrections due to electron-electron interaction. Close to the Dirac point the theory assumes the form of relativistic hydrodynamics. As a consequence, the dynamical densities in the hydrodynamic sense are the energy, particle and imbalance density. In contrast to conventional systems the energy current is the only hydrodynamic current. The electric as well as the imbalance, i.e. the neutral quasiparticle current, are obtained through their equations of state and fully determined by the hydrodynamic densities.

The resulting macroscopic description includes:

i) The Navier-Stokes equation for graphene including the nonlinear equations of state for the pressure and enthalpy,

ii) equations of state for the macroscopic electric and imbalance current that include dissipative terms due to Coulomb scattering,
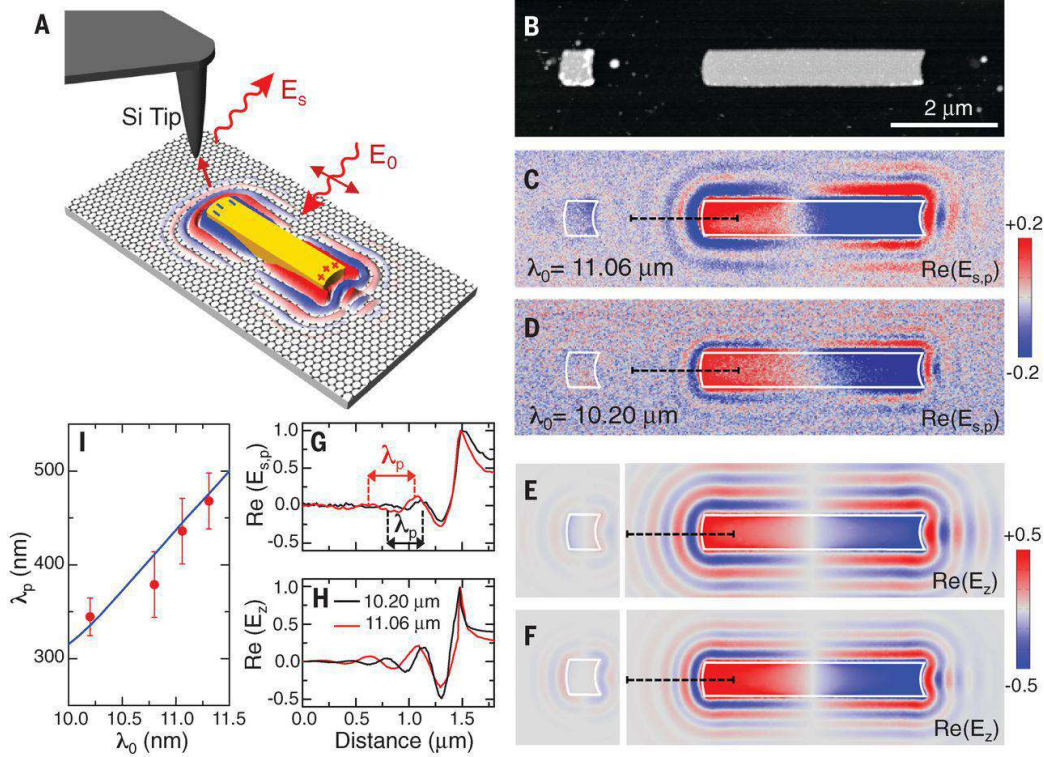
Figure 5.9: *(a) The experimental setup of Ref. [149]. (b) Topography of the sample. (c)-(d) The measured near-field intensity. (e)-(f) Simulated field amplitude. (g)-(h) Cut through the measured field amplitude. (i) Plasmon wavelength as a function of the wavelength of the incident radiation. Reprinted figure with permission from: Alonso-González et al, Science 344 ,6190, 1369-1373 (2014).*

iii) an explicit formalism to calculate the relevant scattering times entering the macroscopic hydrodynamic equations from the microscopic collision integral. The scattering times determine the dissipative terms which describe various interaction-induced phenomena. In particular, interactions affect the transport in graphene in the critical regime of $T/|\mu| \gtrsim 1$ strongly in contrast to Galilean invariant systems. Most prominently, the Coulomb interaction leads to a finite dc-conductivity at the Dirac point, see e.g. Refs. [39, 57, 153]. This is due to the interplay between the anomalous scaling of relaxation times close to the QCP and the linear density of states. Since the relaxation time τ scales as $1/T$ and the thermodynamic density of states reads as $\nu_{\text{th}} \sim T$ the product $\tau\nu_{\text{th}}$ is independent of the temperature. Beyond that, Coulomb interaction gives rise to diffusion close to the Dirac point and a thermoelectric effect. In addition, interactions lead to a finite viscosity in graphene that assumes a remarkably small value for graphene as reported elsewhere [40].

iv) Finally our theoretical formalism is complemented by a numerical solver for two-dimensional hydrodynamics in graphene. The tool includes dissipative corrections due to electron-electron interaction and the self-consistent Vlasov field.

Using the developed framework we obtain the following physical results:

First, in view of the small value of the viscosity to entropy ratio in graphene, that comes close to the universal bound for interacting systems, it is interesting to find observables that are sensitive to

the viscous damping. We find that the nonlocal conductivity reveals effects due to the viscosity in graphene. Within linear response the effect only appears if the system is doped away from the Dirac point. Otherwise the viscous corrections decouple from the electric current. At the same time the viscosity affects the dispersion of plasmons in the hydrodynamic regime giving another access to the viscosity in graphene.

Second, the nonlinear hydrodynamics is suitable to describe a broad class of physical setups. As a first example we performed a numerical analysis of the relaxation dynamics of a hot spot close to the Dirac point. This analysis takes into account the convective nonlinearities and the Coulomb interaction. In the macroscopic equations, the latter manifests the self-consistent electric field due to charge fluctuations and the dissipative corrections.

Although the system exhibits ballistic energy modes, due to the presence of electron interactions the relaxation of the hot spot is not fully ballistic. The presence of Coulomb interactions rather lead to a slow relaxation in contrast to the non-interacting case, where the hot spot decays into fully ballistic energy waves. Moreover, we find that the relaxation dynamics of the hot spot due to electron-electron interactions can be separated into two time regimes:

i) The first regime is characterized by the onset of the collapse of the hot spot. If the system is away from charge neutrality this collapse excites fluctuations in the charge density and the hot spot emits plasmonic waves. In this sense the initial stage is similar to the non-interacting limit. However the Vlasov field represents additional dispersive terms that lead to a modulation of the emitted waves and the formation of plasmons. Interestingly, due to interactions, the collapse of the hot spot is not complete. The hot spot rather evolves into a metastable state. The latter is reached after the wave has left the hot spot where a finite excess energy remains which is stabilized by a local charge at the origin.

ii) In the following second stage of the relaxation, the Vlasov field and the dissipative terms are the most important mechanisms for the subsequent relaxation of the hot spot. While the interaction between the outgoing wave and the hot spot is negligible, the latter decays due to the dissipative corrections in the second regime. This longer time scale compared to the first one is of the order of picoseconds. At the same time the plasmonic waves experience damping due the Coulomb interaction, more specifically, due to viscous and diffusive damping.

Conclusion

This thesis is devoted to the study of non-equilibrium phenomena in graphene and the influence of Coulomb interaction on the relaxation towards equilibrium. Thanks to advances in experimental techniques the physics of non-equilibrium phenomena is a rapidly growing field of research. In general nonlinear response and out of equilibrium phenomena enable a deeper look into microscopic parameters and mechanisms.

In particular optical experiments are suitable to explore the dynamics of such transient non-equilibrium states. For example pump-probe experiments yield time-resolved snapshots of the system's state and allow the detailed investigation of the relaxation process. Recently, this kind of measurements have been conducted on graphene. In particular it was found that the relaxation of high-energy electrons takes place in successive steps, a fact that led to the concept of the relaxation cascade [30, 31]. This cascade is entirely due to electron-electron interaction and determines the initial stage of the relaxation. In view of these findings we asked the question whether one can understand the relaxation cascade in terms of a diffusive motion in energy space. Such a description would be similar to the description of relaxation cascades in plasmas. However the peculiar forward scattering resonance in graphene (see Sec. 1.2.3), that is more severe than in massive systems, leads to a qualitatively different result as we will explain below.

Apart from short-time dynamics investigated in pump-probe experiments graphene also promises new ways to tailor optical near-fields due to its tunable plasmons. Those have been studied recently by optical near-field techniques [32, 33]. Motivated by the possibility to image the optical near-field we extended our study of relaxation dynamics due to Coulomb interaction to the macroscopic regime. Here the time evolution in the low frequency regime is given by relativistic hydrodynamics. Close to the Dirac point the Coulomb interaction alone gives rise to diffusion and additional dissipative terms in the hydrodynamic equations. Those dissipative terms are important for the relaxation dynamics of hot spots in graphene.

Before we review our findings in detail let us summarize the most important results of this work. The key results of the theoretical work presented in this thesis are the following:

- We derive the quantum kinetic equation for graphene in the presence of classical electromagnetic fields including Coulomb scattering. The kinetic equation takes the form of the semiconductor Bloch equations. The formalism is reduced to an effective rate equation for the distribution of photoexcited electrons.

- We perform a detailed analysis of the distribution of transferred energies ω in a single scattering event of high-energy electrons due to Coulomb interaction. The central result is that the distribution of transferred energies has a power law tail with $\omega^{-5/2}$.

- This analysis yields the average transferred energy $\langle \omega \rangle$ as well as the total scattering rate for one scattering event Γ. We find that $\Gamma \sim \alpha_g \max(T, |\mu|)$. Due to screening the scattering rate is only linear in the graphene coupling constant α_g.

- We furthermore analyze the statistics of the entire relaxation process which is given by Lévy flights. We obtain expressions for the average time t of the relaxation process as well as the fluctuations σ_t of this quantity. We find in particular that $\sigma_t \sim T^{1/3}$ for $|\mu| \gg T$ and $\sigma_t \sim T^{-5/3}$ in the case of $T \gg |\mu|$. The analysis also yields the relaxation rate γ_c of the entire cascade which reads as $\gamma_c \sim \alpha_g^2 \max(T, |\mu|)/\Delta\varepsilon$, where $\Delta\varepsilon$ is the length of the relaxation cascade and of the order of the optical frequency of the pump, i.e. $\Delta\varepsilon \sim \omega_{\text{pump}}/2$. We perform numerical calculations to confirm our analytical results.

- We devise a continuum description of the relaxation process by means of a fractional Fokker-Planck equation. The latter contains the anomalous diffusion constant D, due to electron-electron interaction which captures the Lévy flights in the relaxation process. We obtain for the temperature dependence of the anomalous diffusion constant $D \sim T^{5/2}$.

- The fractional Fokker-Planck equation yields two interesting observables: i) the time evolution of the differential change in transmission in the interaction-dominated regime, ii) the time evolution of the distribution of high-energy electrons at very short times when Coulomb interaction dominates the relaxation process. Both cases show power law decay due to the underlying Lévy flight in the relaxation process.

- We obtain an effective macroscopic hydrodynamic theory from the Boltzmann limit of the kinetic equation. At the Dirac point the normal modes of the theory are ballistic energy waves.

- We implemented the theoretical formalism in a semi-implicit numerical solver for nonlinear hydrodynamics in graphene. The simulation tool includes dissipative corrections as well as the calculation of the self-consistent electric field.

- Within linear response we obtain expression for the plasmon dispersion and the conductivity at finite frequency and wave vector. Both results take into account effects due to Coulomb scattering. In particular we predict the influence of the viscosity on the conductivity.

- We applied the framework for nonlinear hydrodynamics to the relaxation of hot spots. We find that the relaxation process is divided into two stages. The first one is characterized by the emission of plasmonic waves and the formation of a metastable state at the hot spot. During the second much longer stage, the plasmonic waves as well as the hot spot decay due to viscous and diffusive damping.

In the following we review our findings regarding the relaxation dynamics due to Coulomb interaction in graphene in more detail and put them in perspective. First we discuss the microscopic analysis of relaxation of electrons in energy space due to Coulomb scattering. Second, we comment on our results regarding the nonlinear hydrodynamics in graphene. In particular we discuss the application of the framework to the spatial relaxation in the hydrodynamic regime. This analysis extends the investigation of the microscopic relaxation to the macroscopic domain and the relaxation of inhomogeneities as they occur due to local heating.

We begin with the microscopic relaxation of graphene in the context of optical pump-probe measurements. For the description of pump-probe experiments we developed a theory capturing the short-time dynamics of high-energy electrons in the presence of external laser fields and Coulomb interaction. A detailed analysis of the scattering processes due to electron-electron scattering revealed that the probability distribution of the transferred energy in a single scattering event shows a power law tail. This

result is in contrast to the result for a low-energy electron in the Fermi liquid regime. Contrary to the naive expectation the fluctuations $\langle \omega^2 \rangle$ of the transferred energy are of the same order as the average $\langle \omega \rangle$. As a consequence one should query whether the average $\langle \omega \rangle$ has much meaning.

The emergence of the power law can be attributed to the dominant collinear scattering. The collinear scattering singularity is present in many systems interacting via long range interaction, in particular in systems with Coulomb interaction. In graphene though, the singular collinear scattering is not only present for small momentum transfer but due to the linear dispersion relation it also occurs for scattering with large momentum transfer. The latter gives rise to the power law tail in the distribution of the transferred energy.

Due to the fat tail, i.e. the power law mentioned above, it is not possible to understand the relaxation of high-energy electrons in terms of a simple diffusive motion in energy space. In this sense we have to negate the initial question regarding the character of the relaxation cascade. There is no usual Fokker-Planck type description of the Coulomb scattering for high-energy electrons in graphene. Such a description meant usual Gaussian diffusion. This would neglect the rare scattering events with large energy transfer. Interestingly those rare events are actually present in many physical systems. Usually they are difficult to describe theoretically and even more difficult to predict. Underestimating them or neglecting them can however lead to dramatic mispredictions. Fat tailed distributions arise for example in the statistics of environmental catastrophes and financial market crashes as well as in the movements of albatrosses or sharks. A special kind of random processes with power law probability distributions that are relevant for us and describe rare but large scale events are referred to as Lévy flights. They are discussed in Chapt. 4.

Being unable to describe the relaxation cascade in terms of Gaussian diffusion there is still an alternative to the usual Fokker-Planck description of the Coulomb scattering. The fact that the relaxation is described by Lévy flights gives rise to anomalous diffusion. In the continuum limit this anomalous diffusion can be formulated in terms of a fractional Fokker-Planck equation. The latter employs fractional derivatives to capture the fat tail of the distribution of the step size in the underlying random walk. All characteristics of the anomalous diffusion derive from the statistics of a single scattering event. They were therefore obtained in our initial analysis of the distribution of the transferred energy. As a consequence, we have to reconsider the preliminary negative answer to the question whether the relaxation cascade can be described by diffusion. Indeed, we cannot describe it in terms of ordinary diffusion. It is rather given by a superdiffusive motion containing rare but long jumps. This anomalous diffusion is due to Lévy flights in the relaxation cascade.

The emergence of the fractional kinetics is caused by the power law of the distribution of the step size in the random walk constituting the relaxation cascade. Both the power law and therefore also the anomalous diffusion arise due to the strong collinear scattering in graphene. Qualitatively we understand the anomalous diffusion in the following way. The relaxation is dominated by fast collinear scattering. If the scattering was strictly collinear, the diffusive motion was one-dimensional. However, due to the fact that the Dirac electrons in graphene do scatter in two-dimensional space the effective dimensionality of the relaxation process is neither truly one-dimensional nor really two-dimensional. This fact is indeed captured by the anomalous diffusion. As an example, anomalous diffusion has also been found on self-similar networks. Here the fractal dimension of the random walk on the network gives rise to Lévy flights.

Our findings on the character of the relaxation cascade of high-energy electrons in graphene are important for the interpretation of experimental data in pump-probe experiments. One fundamental objective is to separate the influence of Coulomb scattering and phonon scattering on the relaxation of high-energy electrons. In order to do so one has to take into account that the fast relaxation due

to Coulomb scattering leads to power law decay in the distribution of high-energy electrons and the differential transmission. Regarding numerical simulations of carrier dynamics in the context of pump-probe experiments we stress that rare events in the Coulomb scattering are crucial. This is in particular important for Monte Carlo simulations.

In order to facilitate this analysis of experimental data, we make specific predictions for the time-dependence of two important observables. First, we determine the differential change in transmission and, second, we calculate the density of photoexcited electrons. In both cases we give expressions for the temperature dependence of the relevant quantities describing the relaxation cascade as for example the anomalous diffusion constant.

We studied the microscopic relaxation of photoexcited electrons in the first part of this thesis. The second part was devoted to the nonlinear hydrodynamics in graphene. On the one hand, it presents a framework to describe transport in graphene in the interaction-dominated regime. This includes the theoretical formalism as well as the necessary computational tools. On the other hand, the second part extends our study of relaxation processes to the relaxation of inhomogeneities in space. More specifically, we investigate the relaxation of hot spots using the developed framework.

We develop an effective description of nonlinear transport by hydrodynamics. This formalism is in particular interesting for graphene device simulations. This emergent hydrodynamics shows unusual properties close to the Dirac point. First of all it is formulated in terms of relativistic hydrodynamics. Second, graphene close to the Dirac point is a generic two-component system. It is described by the densities of electrons and holes as well as the energy density. Interestingly, the only hydrodynamic current is the energy current. In graphene this is related to the momentum density due to the linear spectrum. Moreover there is a clear distinction between the electric and the energy current at the Dirac point. The decoupling of the electric current from the momentum density also leads to the unusual result that the Coulomb interaction causes a finite dc conductivity at the Dirac point. On the other hand the system exhibits ballistic energy modes. The latter entails an infinite heat conductivity at the Dirac point.

In contrast to previous works we performed a microscopic derivation of the nonlinear hydrodynamics in the presence of Coulomb interaction. This construction also yields dissipative corrections that describe the finite conductivity at the Dirac point as well as the thermoelectric effect and diffusion caused by Coulomb interaction. In contrast to the conventional situation the diffusion is due to interactions alone. No disorder needs to be present. Another dissipative correction caused by Coulomb interaction is a finite viscosity. From a fundamental point of view the viscosity in graphene is an interesting quantity. While a perfect liquid is characterized by a vanishing viscosity, real liquids always include interactions that lead to a finite viscosity. One might ask how perfect a real liquid can be. For strongly correlated systems there indeed exists a lower bound for the ratio of viscosity and entropy [150]. For graphene it was found that the viscosity to entropy ratio is remarkably small. In view of these findings we asked for the influence of the viscosity on the nonlocal optical response at the beginning of this thesis. As it turns out the optical response at finite wave vector indeed reveals the viscosity if the system is not strictly at the Dirac point. Right at the Dirac point, i.e. for $\mu = 0$, the energy current decouples from the charge current. However, the optical conductivity is the response of the electric current and the viscosity is connected to the dissipation for the energy current. Therefore if both currents decouple the influence of the viscosity on the optical conductivity must vanish in linear response.

We continued the study of relaxation dynamics in the hydrodynamic regime. One of the main questions raised in the introduction concerned the relaxation of hot spots in graphene due to Coulomb interaction. While we investigated the relaxation in energy space in the first part of our work, we

now turn to the spatial relaxation of a hot spot. Here, the influence of the Coulomb interaction is twofold. First, the Coulomb interaction generates a self-consistent electric field. If the system is away from charge neutrality this electric field couples the charge density and the energy density. This hybridization eventually leads to the formation of generic two-dimensional plasmons. Second, the Coulomb interaction leads to diffusion and viscous damping of waves. Both mechanisms are important for the relaxation and determine the dynamics of the hot spot at different times. More specifically, we identify two different regimes. During the first stage the hot spot excites plasmon waves. The second longer time scale is characterized by diffusive relaxation of the hot spot while the emitted waves are spatially separated from the hot spot.

In conclusion, the second part of this thesis presents a derivation of the collision-dominated hydrodynamics that includes a consistent description of dissipative corrections due to Coulomb scattering. We emphasize that Coulomb scattering is an intrinsic property of the graphene and thus a limiting factor even for ultra clean samples. The hydrodynamic theory represents an effective method to understand and predict transport properties of devices in the nonlinear regime. In view of this agenda we also developed a hydrodynamic solver for the simulation of nonlinear hydrodynamics in graphene. As a first application we applied this tool to the relaxation dynamics of hot spots. However, we believe that the hydrodynamic theory has the potential to describe even more complicated transport setups.

This prospect of future applications also brings us to the limitations of the theory presented in this thesis as well as an outlook regarding future studies.

We have emphasized the fact that the hydrodynamics is due to Coulomb interaction. We did include disorder on the level of the relaxation time approximation. Phonons can be added in a similar fashion. In contrast to disorder phonons would affect the local energy density. Future studies should therefore elucidate the interplay between the diffusive relaxation by Coulomb interaction and the cooling due to the interaction with the lattice. Moreover, the simulations should be extended towards finite system sizes including proper boundary conditions. Finally, an extension to systems with finite magnetic fields promises new effects. In particular in view of the possible neutral currents $\vec{j}_I$. The latter did not play an important role in the setups discussed here, but becomes relevant in the presence of magnetic fields.

Regarding the microscopic theory devoted to the study of relaxation in the context of pump-probe measurements we stress the following two important limitations of the theory. First, the results from Chapt. 4 are limited to the linear regime. We did not consider the scattering among photoexcited electrons themselves as it should occur for high pump fluences. Second, we did not include phonons in the analysis. We focused on the very early stage where Coulomb interaction dominates. However, the result (4.48) can be extended to include phonons in the relaxation time approximation. Studies of the nonlinear regime are a promising topic for future studies. The coupling to an external bath is also important to answer the question how the system at criticality, i.e. for $\mu = T = 0$, relaxes towards equilibrium. We have seen that our results yield that the high-energy electrons do not relax at all. In this limit one should also reconsider the importance of Auger processes. Furthermore, it is interesting to extend the analysis of relaxation dynamics to the regime of quantizing magnetic fields. In view of the findings of Refs. [123, 124], as discussed in Sec. 3.4, it is also interesting to include dephasing of the interband polarization. As a first step we calculated the dephasing time (see Appendix B.3). Those preliminary results indicate that the divergences occurring in the phenomenological approach towards dephasing (see e.g. Ref. [124]), are mitigated due to decoherence by Coulomb scattering.

At the end of this thesis let us reconsider the initial objective of this work. We set out to theoretically study non-equilibrium situations in graphene. In particular we wanted to investigate the relaxation

dynamics due to Coulomb interaction. More specifically we asked two major questions.

First, can one understand the relaxation of high-energy electrons in terms of a diffusive motion? The simple answer is no. However sometimes a negative answer reveals even more interesting physics. In this case it turns out that the relaxation is described by anomalous diffusion and the underlying random walk describes Lévy flights. As a consequence one obtains power law decay of deviations from the equilibrium distribution function at high energies.

Second, this anomalous diffusion is in particular in contrast to the result we obtain for the relaxation of a hot spot in the hydrodynamic regime. Within the effective macroscopic description in terms of hydrodynamics we find that the relaxation of a spatially localized hot spot close to the Dirac point follows an exponential decay. The latter is due to dissipative corrections caused by Coulomb scattering.

We see from these two examples that Coulomb scattering in graphene manifests in many different ways. We searched for diffusion in the relaxation of electrons in energy space but found anomalous diffusion, recovered however the usual diffusion in the spatial relaxation of hot spots due to Coulomb interaction. In both cases the interaction is the driving force for equilibration but the character of the time evolution is completely different. These results also underline a paradigm that has grown strong over the past years in condensed matter physics. Systems far away from equilibrium can reveal completely novel effects and give deeper insight into the character of specific scattering mechanisms.

Acknowledgments

List of publications

Some parts of this thesis are based on the following publications by the author.

Ref. [86]   U. Briskot, „Optoelectronics of disordered graphene in quantizing magnetic fields", Diploma thesis, 2012.

Ref. [81]   U. Briskot, I. A. Dmitriev, and A. D. Mirlin, Quantum magneto-oscillations in the ac conductivity of disordered graphene, Phys. Rev. B 87, 195432, 2013.

Ref. [68]   U. Briskot, I. A. Dmitriev, and A. D. Mirlin, Relaxation of optically excited carriers in graphene: Anomalous diffusion and Lévy flights, Phys. Rev. B 89, 075414, 2014.

–   U. Briskot, M. Schütt, I. V. Gornyi, B. N. Narozhny, M. Titov, and A. D. Mirlin, Nonlinear collision-dominated hydrodynamics in graphene, to be published.

Bibliography

[1] K. S. Novoselov, A. K. Geim, S. V. Morozov, D. Jiang, Y. Zhang, S. V. Dubonos, I. V. Grigorieva, and A. A. Firsov. Electric field effect in atomically thin carbon films. *Science*, 306(5696):666–669, 2004. doi: 10.1126/science.1102896. URL `http://www.sciencemag.org/content/306/5696/666.abstract`.
(Cited on pages vii, 1, and 18.)

[2] A. K. Geim and K. S. Novoselov. The rise of graphene. *Nature Materials*, (6):183 − 191, 2007. doi: doi:10.1038/nmat1849.
(Cited on pages vii, 1, and 5.)

[3] A. H. Castro Neto, F. Guinea, N. M. R. Peres, K. S. Novoselov, and A. K. Geim. The electronic properties of graphene. *Rev. Mod. Phys.*, 81:109–162, Jan 2009. doi: 10.1103/RevModPhys.81.109. URL `http://link.aps.org/doi/10.1103/RevModPhys.81.109`.
(Cited on pages vii, 1, 3, and 4.)

[4] Changgu Lee, Xiaoding Wei, Jeffrey W. Kysar, and James Hone. Measurement of the elastic properties and intrinsic strength of monolayer graphene. *Science*, 321(5887):385–388, 2008. doi: 10.1126/science.1157996. URL `http://www.sciencemag.org/content/321/5887/385.abstract`.
(Cited on page vii.)

[5] Weiwei Cai, Arden L. Moore, Yanwu Zhu, Xuesong Li, Shanshan Chen, Li Shi, and Rodney S. Ruoff. Thermal transport in suspended and supported monolayer graphene grown by chemical vapor deposition. *Nano Letters*, 10(5):1645–1651, 2010. doi: 10.1021/nl9041966. URL `http://dx.doi.org/10.1021/nl9041966`. PMID: 20405895.
(Cited on page vii.)

[6] C. Faugeras, B. Faugeras, M. Orlita, M. Potemski, R. R. Nair, and A. K. Geim. Thermal conductivity of graphene in Corbino membrane geometry. *ACS Nano*, 4(4):1889–1892, 2010. doi: 10.1021/nn9016229. URL `http://dx.doi.org/10.1021/nn9016229`. PMID: 20218666.
(Not cited.)

[7] Jae-Ung Lee, Duhee Yoon, Hakseong Kim, Sang Wook Lee, and Hyeonsik Cheong. Thermal conductivity of suspended pristine graphene measured by raman spectroscopy. *Phys. Rev. B*, 83:081419, Feb 2011. doi: 10.1103/PhysRevB.83.081419. URL `http://link.aps.org/doi/10.1103/PhysRevB.83.081419`.
(Cited on page vii.)

[8] K. I. Bolotin, K. J. Sikes, Z. Jiang, M. Klima, G. Fudenberg, J. Hone, P. Kim, and H. L. Stormer. Ultrahigh electron mobility in suspended graphene. *Solid State Communications*, 146: 351 − 355, 2008. ISSN 0038-1098. doi: http://dx.doi.org/10.1016/j.ssc.2008.02.024. URL `http://www.sciencedirect.com/science/article/pii/S0038109808001178`.
(Cited on page vii.)

[9] P. R. Wallace. The band theory of graphite. *Phys. Rev.*, 71:622–634, 1947.
(Cited on pages vii, 1, and 2.)

[10] Gordon W. Semenoff. Condensed-matter simulation of a three-dimensional anomaly. *Phys. Rev. Lett.*, 53:2449–2452, 1984.
(Cited on pages vii, 1, and 2.)

[11] K. S. Novoselov, Z. Jiang, Y. Zhang, S. V. Morozov, H. L. Stormer, U. Zeitler, J. C. Maan, G. S. Boebinger, P. Kim, and A. K. Geim. Room-temperature quantum hall effect in graphene. *Science*, 315(5817):1379, 2007. doi: 10.1126/science.1137201. URL `http://www.sciencemag.org/content/315/5817/1379.abstract`.
(Cited on pages vii and 19.)

[12] Michael Engel, Mathias Steiner, Antonio Lombardo, Andrea C. Ferrari, Hilbert v. Löhneysen, Phaedon Avouris, and Ralph Krupke. Light-matter interaction in a microcavity-controlled graphene transistor. *Nat Commun*, 3:906, Jun 2012. doi: 10.1038/ncomms1911. URL `http://dx.doi.org/10.1038/ncomms1911`.
(Cited on pages viii, x, and 72.)

[13] Zhipei Sun, Tawfique Hasan, Felice Torrisi, Daniel Popa, Giulia Privitera, Fengqiu Wang, Francesco Bonaccorso, Denis M. Basko, and Andrea C. Ferrari. Graphene mode-locked ultrafast laser. *ACS Nano*, 4(2):803–810, 2010. doi: 10.1021/nn901703e. URL `http://dx.doi.org/10.1021/nn901703e`. PMID: 20099874.
(Cited on page viii.)

[14] Pia Gagel, Peter P. Orth, and Jörg Schmalian. Universal postquench prethermalization at a quantum critical point. *Phys. Rev. Lett.*, 113:220401, Nov 2014. doi: 10.1103/PhysRevLett.113.220401. URL `http://link.aps.org/doi/10.1103/PhysRevLett.113.220401`.
(Cited on pages viii and 29.)

[15] Subir Sachdev and Markus Müller. Quantum criticality and black holes. *J. Phys.: Condens. Matter*, 21(16):164216, 2009. doi: 10.1088/0953-8984/21/16/164216.
(Cited on pages viii, 15, and 16.)

[16] Kedar Damle and Subir Sachdev. Nonzero-temperature transport near quantum critical points. *Phys. Rev. B*, 56:8714–8733, Oct 1997. doi: 10.1103/PhysRevB.56.8714. URL `http://link.aps.org/doi/10.1103/PhysRevB.56.8714`.
(Cited on pages viii and 94.)

[17] J. M. Dawlaty, S. Shivaraman, M. Chandrashekhar, F. Rana, and M. G. Spencer. Measurement of ultrafast carrier dynamics in epitaxial graphene. *Appl. Phys. Lett.*, 92:042116, 2008. doi: 10.1063/1.2837539. URL `http://apl.aip.org/resource/1/applab/v92/i4/p042116_s1`.
(Cited on pages ix, 47, and 48.)

[18] Dong Sun, Zong-Kwei Wu, Charles Divin, Xuebin Li, Claire Berger, Walt A. de Heer, Phillip N. First, and Theodore B. Norris. Ultrafast relaxation of excited dirac fermions in epitaxial graphene using optical differential transmission spectroscopy. *Phys. Rev. Lett.*, 101:157402, Oct 2008. doi: 10.1103/PhysRevLett.101.157402. URL `http://link.aps.org/doi/10.1103/PhysRevLett.101.157402`.
(Cited on pages ix and 48.)

[19] M. Lindberg and S. W. Koch. Theory of coherent transients in semiconductor pump–probe spectroscopy. *J. Opt. Soc. Am. B*, 5(1):139–146, Jan 1988. doi: 10.1364/JOSAB.5.000139. URL http://josab.osa.org/abstract.cfm?URI=josab-5-1-139.
(Cited on page ix.)

[20] H. Haug and A.-P. Jauho. *Quantum Kinetics in Transport and Optics of Semiconductors*. Springer, 1996.
(Cited on pages ix, 28, 34, 38, 44, and 131.)

[21] S. Winnerl, F. Göttfert, M. Mittendorff, H. Schneider, M. Helm, T. Winzer, E. Malic, A. Knorr, M. Orlita, M. Potemski, M. Sprinkle, C. Berger, and W. A. de Heer. Time-resolved spectroscopy on epitaxial graphene in the infrared spectral range: relaxation dynamics and saturation behavior. *Journal of Physics: Condensed Matter*, 25(5):054202, 2013. doi: 10.1088/0953-8984/25/5/054202. URL http://stacks.iop.org/0953-8984/25/i=5/a=054202.
(Cited on pages ix, 44, and 47.)

[22] M. Breusing, S. Kuehn, T. Winzer, E. Malić, F. Milde, N. Severin, J. P. Rabe, C. Ropers, A. Knorr, and T. Elsaesser. Ultrafast nonequilibrium carrier dynamics in a single graphene layer. *Phys. Rev. B*, 83:153410, Apr 2011. doi: 10.1103/PhysRevB.83.153410. URL http://link.aps.org/doi/10.1103/PhysRevB.83.153410.
(Cited on pages ix, 44, 47, 48, and 49.)

[23] J. Shang, Z. Luo, C. Cong, J. Lin, T. Yu, and G. G. Gurzadyan. Femtosecond uv-pump/visible-probe measurements of carrier dynamics in stacked graphene films. *Appl. Phys. Lett.*, 97: 163103, 2010. doi: 10.1063/1.3504704. URL http://apl.aip.org/resource/1/applab/v97/i16/p163103_s1.
(Cited on page ix.)

[24] Raseong Kim, Vasili Perebeinos, and Phaedon Avouris. Relaxation of optically excited carriers in graphene. *Phys. Rev. B*, 84:075449, Aug 2011. doi: 10.1103/PhysRevB.84.075449. URL http://link.aps.org/doi/10.1103/PhysRevB.84.075449.
(Cited on pages 42 and 49.)

[25] T. Li, L. Luo, M. Hupalo, J. Zhang, M. C. Tringides, J. Schmalian, and J. Wang. Femtosecond population inversion and stimulated emission of dense Dirac fermions in graphene. *Phys. Rev. Lett.*, 108:167401, Apr 2012. doi: 10.1103/PhysRevLett.108.167401. URL http://link.aps.org/doi/10.1103/PhysRevLett.108.167401.
(Cited on pages 42, 47, and 48.)

[26] D. Brida, A. Tomadin, C. Manzoni, Y. J. Kim, A. Lombardo, S. Milana, R. R. Nair, K. S. Novoselov, A. C. Ferrari, G. Cerullo, and M. Polini. Ultrafast collinear scattering and carrier multiplication in graphene. *Nat Commun*, 4:1987, June 2013. URL http://dx.doi.org/10.1038/ncomms2987.
(Cited on page ix.)

[27] T Winzer and E Malic. The impact of pump fluence on carrier relaxation dynamics in optically excited graphene. *Journal of Physics: Condensed Matter*, 25(5):054201, 2013. URL http://stacks.iop.org/0953-8984/25/i=5/a=054201.
(Cited on page ix.)

[28] Torben Winzer, Ermin Malić, and Andreas Knorr. Microscopic mechanism for transient population inversion and optical gain in graphene. *Phys. Rev. B*, 87:165413, Apr 2013. doi: 10.1103/ PhysRevB.87.165413. URL `http://link.aps.org/doi/10.1103/PhysRevB.87.165413`. (Cited on pages 42, 44, 48, and 49.)

[29] Martin Mittendorff, Torben Winzer, Ermin Malic, Andreas Knorr, Claire Berger, Walter A. de Heer, Harald Schneider, Manfred Helm, and Stephan Winnerl. Anisotropy of excitation and relaxation of photogenerated charge carriers in graphene. *Nano Letters*, 14(3):1504–1507, 2014. doi: 10.1021/nl404730y. URL `http://dx.doi.org/10.1021/nl404730y`. PMID: 24559191. (Cited on pages ix and 44.)

[30] K. J. Tielrooij, J. C. W. Song, S. A. Jensen, A. Centeno, A. Pesquera, A. Zurutuza Elorza, M. Bonn, L. S. Levitov, and F. H. L. Koppens. Photoexcitation cascade and multiple hot-carrier generation in graphene. *Nat Phys*, 9(4):248–252, Apr 2013. ISSN 1745-2473. doi: 10.1038/ nphys2564. URL `http://dx.doi.org/10.1038/nphys2564`. (Cited on pages ix, 47, 48, 49, 59, 68, and 97.)

[31] Justin C. W. Song, Klaas J. Tielrooij, Frank H. L. Koppens, and Leonid S. Levitov. Photoexcited carrier dynamics and impact-excitation cascade in graphene. *Phys. Rev. B*, 87:155429, Apr 2013. doi: 10.1103/PhysRevB.87.155429. URL `http://link.aps.org/doi/10.1103/PhysRevB.87.155429`. (Cited on pages ix, 8, 48, 49, 54, 59, and 97.)

[32] Z. Fei, A. S. Rodin, G. O. Andreev, W. Bao, A. S. McLeod, M. Wagner, L. M. Zhang, Z. Zhao, M. Thiemens, G. Dominguez, M. M. Fogler, A. H. Castro Neto, C. N. Lau, F. Keilmann, and D. N. Basov. Gate-tuning of graphene plasmons revealed by infrared nano-imaging. *Nature*, 487(7405): 82–85, 2012. doi: 10.1038/nature11253. URL `http://dx.doi.org/10.1038/nature11253`. (Cited on pages x, 13, 71, 72, 93, 94, and 97.)

[33] Jianing Chen, Michela Badioli, Pablo Alonso-Gonzalez, Sukosin Thongrattanasiri, Florian Huth, Johann Osmond, Marko Spasenovic, Alba Centeno, Amaia Pesquera, Philippe Godignon, Amaia Zurutuza Elorza, Nicolas Camara, F. Javier Garcia de Abajo, Rainer Hillenbrand, and Frank H. L. Koppens. Optical nano-imaging of gate-tunable graphene plasmons. *Nature*, 487(7405): 77–81, 2012. (Cited on pages x, 13, 71, 72, 93, and 97.)

[34] Frank H. L. Koppens, Darrick E. Chang, and F. Javier García de Abajo. Graphene plasmonics: A platform for strong light–matter interactions. *Nano Letters*, 11(8):3370–3377, 2011. doi: 10. 1021/nl201771h. URL `http://dx.doi.org/10.1021/nl201771h`. PMID: 21766812. (Cited on pages x and 12.)

[35] E. H. Hwang and S. Das Sarma. Dielectric function, screening, and plasmons in two-dimensional graphene. *Phys. Rev. B*, 75:205418, May 2007. doi: 10.1103/PhysRevB.75.205418. URL `http://link.aps.org/doi/10.1103/PhysRevB.75.205418`. (Cited on pages 8, 9, 12, and 48.)

[36] Hugen Yan, Tony Low, Wenjuan Zhu, Yanqing Wu, Marcus Freitag, Xuesong Li, Francisco Guinea, Phaedon Avouris, and Fengnian Xia. Damping pathways of mid-infrared plasmons in

graphene nanostructures. *Nature Photonics*, 7(5):394–399, 2013.
(Cited on pages x and 13.)

[37] H. Marinchio, G. Sabatini, C. Palermo, J. Pousset, J. Torres, L. Chusseau, L. Varani, P. Shiktorov, E. Starikov, and V. Gružinskis. Hydrodynamic modeling of optically excited terahertz plasma oscillations in nanometric field effect transistors. *Applied Physics Letters*, 94(19):192109, 2009. doi: http://dx.doi.org/10.1063/1.3137189. URL `http://scitation.aip.org/content/aip/journal/apl/94/19/10.1063/1.3137189`.
(Cited on page x.)

[38] Markus Müller and Subir Sachdev. Collective cyclotron motion of the relativistic plasma in graphene. *Phys. Rev. B*, 78:115419, Sep 2008. doi: 10.1103/PhysRevB.78.115419. URL `http://link.aps.org/doi/10.1103/PhysRevB.78.115419`.
(Cited on pages x, 73, 83, 84, and 94.)

[39] Lars Fritz, Jörg Schmalian, Markus Müller, and Subir Sachdev. Quantum critical transport in clean graphene. *Phys. Rev. B*, 78:085416, Aug 2008. doi: 10.1103/PhysRevB.78.085416. URL `http://link.aps.org/doi/10.1103/PhysRevB.78.085416`.
(Cited on pages 8, 9, 16, 18, 48, 53, 73, 75, 76, 78, and 95.)

[40] Markus Müller, Jörg Schmalian, and Lars Fritz. Graphene: A nearly perfect fluid. *Phys. Rev. Lett.*, 103:025301, Jul 2009. doi: 10.1103/PhysRevLett.103.025301. URL `http://link.aps.org/doi/10.1103/PhysRevLett.103.025301`.
(Cited on pages x, 72, 73, and 95.)

[41] D. Svintsov, V. Vyurkov, V. Ryzhii, and T. Otsuji. Hydrodynamic electron transport and nonlinear waves in graphene. *Phys. Rev. B*, 88:245444, Dec 2013. doi: 10.1103/PhysRevB.88.245444. URL `http://link.aps.org/doi/10.1103/PhysRevB.88.245444`.
(Cited on pages x, 73, 74, and 83.)

[42] B. N. Narozhny, I. V. Gornyi, M. Titov, M. Schütt, and A. D. Mirlin. Hydrodynamics in graphene: Linear-response transport. *Phys. Rev. B*, 91:035414, Jan 2015. doi: 10.1103/PhysRevB.91.035414. URL `http://link.aps.org/doi/10.1103/PhysRevB.91.035414`.
(Cited on pages x, 19, 73, 151, and 152.)

[43] I. V. Protopopov, D. B. Gutman, P. Schmitteckert, and A. D. Mirlin. Dynamics of waves in one-dimensional electron systems: Density oscillations driven by population inversion. *Phys. Rev. B*, 87:045112, Jan 2013. doi: 10.1103/PhysRevB.87.045112. URL `http://link.aps.org/doi/10.1103/PhysRevB.87.045112`.
(Cited on pages x, 72, and 88.)

[44] I. V. Protopopov, D. B. Gutman, M. Oldenburg, and A. D. Mirlin. Dissipationless kinetics of one-dimensional interacting fermions. *Phys. Rev. B*, 89:161104, Apr 2014. doi: 10.1103/PhysRevB.89.161104. URL `http://link.aps.org/doi/10.1103/PhysRevB.89.161104`.
(Cited on pages x, 72, and 88.)

[45] Simon M. Sze and Kwok K. Ng. *Physics of Semiconductor Devices*. John Wiley & Sons, 2006.
(Cited on pages 1 and 6.)

[46] A. K. Geim and I. V. Grigorieva. Van der Waals heterostructures. *Nature*, 499:419–425, 2013. doi: doi:10.1038/nature12385.
(Cited on page 1.)

[47] Daniel E. Sheehy and Jörg Schmalian. Quantum critical scaling in graphene. *Phys. Rev. Lett.*, 99:226803, Nov 2007. doi: 10.1103/PhysRevLett.99.226803. URL http://link.aps.org/doi/10.1103/PhysRevLett.99.226803.
(Cited on pages 2, 13, and 15.)

[48] María A. H. Vozmediano. Renormalization group aspects of graphene. *Phil. Trans .Roy. Soc. Lond. A*, (369):2625–2642, 2011. doi: 10.1098/rsta.2010.0383.
(Cited on pages 2, 13, and 16.)

[49] Alexandre Zagoskin. *Quantum Theory of Many-Body Systems*. Springer, 1998.
(Cited on pages 2 and 17.)

[50] V. Abrikosov, L. P. Gorkov, and I. E. Dzyaloshinski. *Methods of quantum field theory in statistical physics*. Dover Publications, Inc. New York, 1975.
(Cited on pages 2, 9, 17, 27, and 28.)

[51] J. C. Slonczewski and P. R. Weiss. Band structure of graphite. *Phys. Rev.*, 109:272–279, 1957.
(Cited on page 2.)

[52] H.B. Nielsen and M. Ninomiya. Absence of neutrinos on a lattice: (i). Proof by homotopy theory. *Nuclear Physics B*, 185(1):20 – 40, 1981. ISSN 0550-3213. doi: http://dx.doi.org/10.1016/0550-3213(81)90361-8. URL http://www.sciencedirect.com/science/article/pii/0550321381903618.
(Cited on page 2.)

[53] P. M. Ostrovsky, I. V. Gornyi, and A. D. Mirlin. Electron transport in disordered graphene. *Phys. Rev. B*, 74:235443, Dec 2006. doi: 10.1103/PhysRevB.74.235443. URL http://link.aps.org/doi/10.1103/PhysRevB.74.235443.
(Cited on pages 2 and 18.)

[54] V. P. Gusynin, S. G. Sharapov, and J. P. Carbotte. Ac conductivity of graphene: From thight-binding to 2+1-dimensional quantum electrodynamics. *Int J Mod Phys B*, 21:4611–4658, 2007.
(Cited on pages 3 and 4.)

[55] Lyle Patrick and W. J. Choyke. Static Dielectric Constant of SiC. *Phys. Rev. B*, 2:2255–2256, Sep 1970. doi: 10.1103/PhysRevB.2.2255. URL http://link.aps.org/doi/10.1103/PhysRevB.2.2255.
(Cited on page 6.)

[56] J. Rammer and H. Smith. Quantum field-theoretical methods in transport theory of metals. *Rev. Mod. Phys.*, 58:323–359, Apr 1986. doi: 10.1103/RevModPhys.58.323. URL http://link.aps.org/doi/10.1103/RevModPhys.58.323.
(Cited on pages 6, 28, and 34.)

[57] Alexander B. Kashuba. Conductivity of defectless graphene. *Phys. Rev. B*, 78:085415, Aug 2008. doi: 10.1103/PhysRevB.78.085415. URL http://link.aps.org/doi/10.1103/PhysRevB.

78.085415.
(Cited on pages 8, 18, 48, 75, 76, 78, 83, and 95.)

[58] M. Schütt, P. M. Ostrovsky, I. V. Gornyi, and A. D. Mirlin. Coulomb interaction in graphene: Relaxation rates and transport. *Phys. Rev. B*, 83:155441, Apr 2011. doi: 10.1103/PhysRevB.83. 155441. URL `http://link.aps.org/doi/10.1103/PhysRevB.83.155441`.
(Cited on pages 8, 9, 10, 12, 15, 48, 53, 54, and 74.)

[59] P. W. Anderson. "Luttinger-liquid" behavior of the normal metallic state of the 2D Hubbard model. *Phys. Rev. Lett.*, 64:1839–1841, Apr 1990. doi: 10.1103/PhysRevLett.64.1839. URL `http://link.aps.org/doi/10.1103/PhysRevLett.64.1839`.
(Cited on page 8.)

[60] Matthew S. Foster and Igor L. Aleiner. Slow imbalance relaxation and thermoelectric transport in graphene. *Phys. Rev. B*, 79:085415, Feb 2009. doi: 10.1103/PhysRevB.79.085415. URL `http://link.aps.org/doi/10.1103/PhysRevB.79.085415`.
(Cited on pages 8, 42, 52, 80, and 83.)

[61] Justin C. W. Song, Michael Y. Reizer, and Leonid S. Levitov. Disorder-assisted electron-phonon scattering and cooling pathways in graphene. *Phys. Rev. Lett.*, 109:106602, Sep 2012. doi: 10. 1103/PhysRevLett.109.106602. URL `http://link.aps.org/doi/10.1103/PhysRevLett.109.106602`.
(Cited on pages 8 and 42.)

[62] R. R. Nair, P. Blake, A. N. Grigorenko, K. S. Novoselov, T. J. Booth, T. Stauber, N. M. R. Peres, and A. K. Geim. Fine structure constant defines visual transparency of graphene. *Science*, 320 (5881):1308, 2008. doi: 10.1126/science.1156965. URL `http://www.sciencemag.org/content/320/5881/1308.abstract`.
(Cited on pages 9 and 19.)

[63] E. G. Mishchenko. Minimal conductivity in graphene: interaction corrections and ultraviolet anomaly. *EPL (Europhysics Letters)*, 83(1):17005, 2008. URL `http://stacks.iop.org/0295-5075/83/i=1/a=17005`.
(Cited on pages 9 and 18.)

[64] Igor F. Herbut, Vladimir Juričić, and Oskar Vafek. Coulomb interaction, ripples, and the minimal conductivity of graphene. *Phys. Rev. Lett.*, 100:046403, Jan 2008. doi: 10.1103/PhysRevLett. 100.046403. URL `http://link.aps.org/doi/10.1103/PhysRevLett.100.046403`.
(Not cited.)

[65] Daniel E. Sheehy and Jörg Schmalian. Optical transparency of graphene as determined by the fine-structure constant. *Phys. Rev. B*, 80:193411, Nov 2009. doi: 10.1103/PhysRevB.80.193411. URL `http://link.aps.org/doi/10.1103/PhysRevB.80.193411`.
(Cited on pages 9 and 18.)

[66] J. Link, P. Orth, D. E. Sheehy, and J. Schmalian. Universal collisionless transport of graphene. to be published, 2015.
(Cited on pages 9 and 18.)

[67] J. González, F. Guinea, and M. A. H. Vozmediano. Marginal-Fermi-liquid behavior from two-dimensional Coulomb interaction. *Phys. Rev. B*, 59:R2474–R2477, Jan 1999. doi: 10.1103/PhysRevB.59.R2474. URL `http://link.aps.org/doi/10.1103/PhysRevB.59.R2474`. (Cited on pages 9 and 16.)

[68] U. Briskot, I. A. Dmitriev, and A. D. Mirlin. Relaxation of optically excited carriers in graphene: Anomalous diffusion and Lévy flights. *Phys. Rev. B*, 89:075414, Feb 2014. doi: 10.1103/PhysRevB.89.075414. URL `http://link.aps.org/doi/10.1103/PhysRevB.89.075414`. (Cited on pages 10, 42, and 107.)

[69] E. M. Lifshitz and L. P. Pitaevskii. *Course of Theoretical Physics: Physical Kinetics*. Butterworth Heinemann, 2002. (Cited on pages 10 and 53.)

[70] Oskar Vafek. Thermoplasma polariton within scaling theory of single-layer graphene. *Phys. Rev. Lett.*, 97:266406, Dec 2006. doi: 10.1103/PhysRevLett.97.266406. URL `http://link.aps.org/doi/10.1103/PhysRevLett.97.266406`. (Cited on page 12.)

[71] L. D. Landau and E. M. Lifshitz. *Course of Theoretical Physics: Fluid Mechanics*. Butterworth Heinemann, 2000. (Cited on pages 12, 16, 74, 76, and 84.)

[72] J. González, F. Guinea, and M.A.H. Vozmediano. Non-Fermi liquid behavior of electrons in the half-filled honeycomb lattice (a renormalization group approach). *Nuclear Physics B*, 424(3): 595 – 618, 1994. ISSN 0550-3213. doi: http://dx.doi.org/10.1016/0550-3213(94)90410-3. URL `http://www.sciencedirect.com/science/article/pii/0550321394904103`. (Cited on page 13.)

[73] J. González, F. Guinea, and M. A. H. Vozmediano. Unconventional quasiparticle lifetime in graphite. *Phys. Rev. Lett.*, 77:3589–3592, Oct 1996. doi: 10.1103/PhysRevLett.77.3589. URL `http://link.aps.org/doi/10.1103/PhysRevLett.77.3589`. (Cited on pages 13, 15, 48, 53, and 54.)

[74] R. Shankar. Renormalization-group approach to interacting fermions. *Rev. Mod. Phys.*, 66:129–192, Jan 1994. doi: 10.1103/RevModPhys.66.129. URL `http://link.aps.org/doi/10.1103/RevModPhys.66.129`. (Cited on page 14.)

[75] D.V. Khveshchenko and H. Leal. Excitonic instability in layered degenerate semimetals. *Nuclear Physics B*, 687(3):323 – 331, 2004. ISSN 0550-3213. doi: http://dx.doi.org/10.1016/j.nuclphysb.2004.03.020. URL `http://www.sciencedirect.com/science/article/pii/S0550321304002032`. (Cited on page 15.)

[76] Joaquín E. Drut and Timo A. Lähde. Is graphene in vacuum an insulator? *Phys. Rev. Lett.*, 102: 026802, Jan 2009. doi: 10.1103/PhysRevLett.102.026802. URL `http://link.aps.org/doi/10.1103/PhysRevLett.102.026802`. (Cited on page 15.)

[77] Guohong Li, Adina Luican, and Eva Y. Andrei. Scanning tunneling spectroscopy of graphene on graphite. *Phys. Rev. Lett.*, 102:176804, Apr 2009. doi: 10.1103/PhysRevLett.102.176804. URL `http://link.aps.org/doi/10.1103/PhysRevLett.102.176804`.
(Cited on page 15.)

[78] C. M. Varma, P. B. Littlewood, S. Schmitt-Rink, E. Abrahams, and A. E. Ruckenstein. Phenomenology of the normal state of Cu-O high-temperature superconductors. *Phys. Rev. Lett.*, 63: 1996–1999, Oct 1989. doi: 10.1103/PhysRevLett.63.1996. URL `http://link.aps.org/doi/10.1103/PhysRevLett.63.1996`.
(Cited on page 15.)

[79] F D M Haldane. 'Luttinger liquid theory' of one-dimensional quantum fluids. I. properties of the luttinger model and their extension to the general 1D interacting spinless Fermi gas. *Journal of Physics C: Solid State Physics*, 14(19):2585, 1981. URL `http://stacks.iop.org/0022-3719/14/i=19/a=010`.
(Cited on page 16.)

[80] Tilman Enss, Rudolf Haussmann, and Wilhelm Zwerger. Viscosity and scale invariance in the unitary Fermi gas. *Annals of Physics*, 326(3):770 – 796, 2011. ISSN 0003-4916. doi: http://dx.doi.org/10.1016/j.aop.2010.10.002. URL `http://www.sciencedirect.com/science/article/pii/S000349161000179X`.
(Cited on page 16.)

[81] U. Briskot, I. A. Dmitriev, and A. D. Mirlin. Quantum magneto-oscillations in the ac conductivity of disordered graphene. *Phys. Rev. B*, 87:195432, May 2013. doi: 10.1103/PhysRevB.87.195432. URL `http://link.aps.org/doi/10.1103/PhysRevB.87.195432`.
(Cited on pages 17, 19, 20, 22, 24, 26, and 107.)

[82] Jørgen Rammer. *Quantum Field Theory of Non-equilibrium States*. Cambridge University Press, 2011.
(Cited on pages 17 and 28.)

[83] Takeo Matsubara. A new approach to quantum-statistical mechanics. *Progress of Theoretical Physics*, 14(4):351–378, 1955. doi: 10.1143/PTP.14.351. URL `http://ptp.oxfordjournals.org/content/14/4/351.abstract`.
(Cited on pages 17, 27, and 28.)

[84] Xu Du, Ivan Skachko, Anthony Barker, and Eva Y. Andrei. Approaching ballistic transport in suspended graphene. *Nat Nano*, 3(8):491–495, Aug 2008. ISSN 1748-3387. doi: 10.1038/nnano.2008.199. URL `http://dx.doi.org/10.1038/nnano.2008.199`.
(Cited on page 19.)

[85] T. Stauber, N. M. R. Peres, and A. K. Geim. Optical conductivity of graphene in the visible region of the spectrum. *Phys. Rev. B*, 78:085432, Aug 2008. doi: 10.1103/PhysRevB.78.085432. URL `http://link.aps.org/doi/10.1103/PhysRevB.78.085432`.
(Cited on page 19.)

[86] U. Briskot. Optoelectronics of disordered graphene in quantizing magnetic fields. Master's thesis, Karlsruhe Institute of Technology, 2012.
(Cited on pages 19, 22, 24, and 107.)

[87] Nguyen Hong Shon and Tsuneya Ando. Quantum transport in two-dimensional graphite system. *Journal of the Physical Society of Japan*, 67(7):2421–2429, 1998. doi: 10.1143/JPSJ.67.2421. URL `http://dx.doi.org/10.1143/JPSJ.67.2421`. (Cited on page 20.)

[88] Zhenbing Tan, Changling Tan, Li Ma, G. T. Liu, L. Lu, and C. L. Yang. Shubnikov-de Haas oscillations of a single layer graphene under dc current bias. *Phys. Rev. B*, 84:115429, Sep 2011. doi: 10.1103/PhysRevB.84.115429. URL `http://link.aps.org/doi/10.1103/PhysRevB.84.115429`. (Cited on page 22.)

[89] M. L. Sadowski, G. Martinez, M. Potemski, C. Berger, and W. A. de Heer. Landau level spectroscopy of ultrathin graphite layers. *Phys. Rev. Lett.*, 97:266405, Dec 2006. doi: 10.1103/PhysRevLett.97.266405. URL `http://link.aps.org/doi/10.1103/PhysRevLett.97.266405`. (Cited on pages 22 and 26.)

[90] M. Orlita and M. Potemski. Dirac electronic states in graphene systems: optical spectroscopy studies. *Semiconductor Science and Technology*, 25(6):063001, 2010. URL `http://stacks.iop.org/0268-1242/25/i=6/a=063001`. (Not cited.)

[91] M. Orlita, C. Faugeras, R. Grill, A. Wysmolek, W. Strupinski, C. Berger, W. A. de Heer, G. Martinez, and M. Potemski. Carrier scattering from dynamical magnetoconductivity in quasineutral epitaxial graphene. *Phys. Rev. Lett.*, 107:216603, Nov 2011. doi: 10.1103/PhysRevLett.107.216603. URL `http://link.aps.org/doi/10.1103/PhysRevLett.107.216603`. (Cited on pages 22, 23, and 24.)

[92] C. Faugeras, S. Berciaud, P. Leszczynski, Y. Henni, K. Nogajewski, M. Orlita, T. Taniguchi, K. Watanabe, C. Forsythe, P. Kim, R. Jalil, K. Geim, A. M. Basko, D. and M. Potemski. Landau level spectroscopy of electron-electron interactions in graphene. *Phys. Rev. Lett.*, 114:126804, Mar 2015. doi: 10.1103/PhysRevLett.114.126804. URL `http://link.aps.org/doi/10.1103/PhysRevLett.114.126804`. (Cited on pages 22 and 24.)

[93] Z. Jiang, E. A. Henriksen, L. C. Tung, Y.-J. Wang, M. E. Schwartz, M. Y. Han, P. Kim, and H. L. Stormer. Infrared spectroscopy of Landau levels of graphene. *Phys. Rev. Lett.*, 98:197403, May 2007. doi: 10.1103/PhysRevLett.98.197403. (Cited on pages 22, 23, and 24.)

[94] X. Hong, K. Zou, and J. Zhu. Quantum scattering time and its implications on scattering sources in graphene. *Phys. Rev. B*, 80:241415, Dec 2009. doi: 10.1103/PhysRevB.80.241415. (Cited on pages 23 and 24.)

[95] Zhenbing Tan, Changling Tan, Li Ma, G. T. Liu, L. Lu, and C. L. Yang. Shubnikov-de Haas oscillations of a single layer graphene under dc current bias. *Phys. Rev. B*, 84:115429, Sep 2011. doi: 10.1103/PhysRevB.84.115429. (Cited on page 23.)

[96] Johannes Jobst, Daniel Waldmann, Igor V. Gornyi, Alexander D. Mirlin, and Heiko B. Weber. Electron-electron interaction in the magnetoresistance of graphene. *Phys. Rev. Lett.*, 108:106601, Mar 2012. doi: 10.1103/PhysRevLett.108.106601. URL http://link.aps.org/doi/10.1103/PhysRevLett.108.106601.
(Cited on page 24.)

[97] H. Pothier, S. Guéron, Norman O. Birge, D. Esteve, and M. H. Devoret. Energy distribution function of quasiparticles in mesoscopic wires. *Phys. Rev. Lett.*, 79:3490–3493, Nov 1997. doi: 10.1103/PhysRevLett.79.3490. URL http://link.aps.org/doi/10.1103/PhysRevLett.79.3490.
(Cited on page 27.)

[98] I. A. Dmitriev, A. D. Mirlin, D. G. Polyakov, and M. A. Zudov. Nonequilibrium phenomena in high Landau levels. *Rev. Mod. Phys.*, 84:1709–1763, Nov 2012. doi: 10.1103/RevModPhys.84.1709. URL http://link.aps.org/doi/10.1103/RevModPhys.84.1709.
(Cited on page 27.)

[99] Julian Schwinger. Brownian motion of a quantum oscillator. *J. Math Phys.*, 2(3):407–432, 1961. doi: http://dx.doi.org/10.1063/1.1703727. URL http://scitation.aip.org/content/aip/journal/jmp/2/3/10.1063/1.1703727.
(Cited on page 28.)

[100] L.V. Keldysh. Diagram technique for nonequilibrium processes. *JETP*, 20(4):1018, 1965.
(Cited on page 28.)

[101] R. A. Craig. Perturbation expansion for real-time Green's functions. *J. Math. Phys.*, 9(4):605–611, 1968.
(Cited on page 28.)

[102] L. P. Kadanoff and G. Baym. *Quantum Statistical Mechanics*. W. A. Benjamin, Inc., New York, 1962.
(Cited on pages 28, 29, 127, and 131.)

[103] David C. Langreth and John W. Wilkins. Theory of spin resonance in dilute magnetic alloys. *Phys. Rev. B*, 6:3189–3227, Nov 1972. doi: 10.1103/PhysRevB.6.3189. URL http://link.aps.org/doi/10.1103/PhysRevB.6.3189.
(Cited on pages 28 and 127.)

[104] G. C. Wick. The evaluation of the collision matrix. *Phys. Rev.*, 80:268–272, Oct 1950. doi: 10.1103/PhysRev.80.268. URL http://link.aps.org/doi/10.1103/PhysRev.80.268.
(Cited on page 28.)

[105] Gordon Baym and Leo P. Kadanoff. Conservation laws and correlation functions. *Phys. Rev.*, 124:287–299, Oct 1961. doi: 10.1103/PhysRev.124.287. URL http://link.aps.org/doi/10.1103/PhysRev.124.287.
(Cited on pages 29, 30, 31, and 34.)

[106] Adrian Stan, Nils Erik Dahlen, and Robert van Leeuwen. Time propagation of the Kadanoff–Baym equations for inhomogeneous systems. *The Journal of Chemical Physics*, 130 (22):224101, 2009. doi: http://dx.doi.org/10.1063/1.3127247. URL http://scitation.aip.

`org/content/aip/journal/jcp/130/22/10.1063/1.3127247`.
(Cited on page 29.)

[107] P. Lipavský, V. Špička, and B. Velický. Generalized Kadanoff-Baym ansatz for deriving quantum transport equations. *Phys. Rev. B*, 34:6933–6942, Nov 1986. doi: 10.1103/PhysRevB.34.6933. URL `http://link.aps.org/doi/10.1103/PhysRevB.34.6933`.
(Cited on pages 30, 31, and 131.)

[108] W. Hänsch and G. D. Mahan. Transport equations for many-particle systems. *Phys. Rev. B*, 28: 1902–1922, Aug 1983. doi: 10.1103/PhysRevB.28.1902. URL `http://link.aps.org/doi/10.1103/PhysRevB.28.1902`.
(Cited on page 31.)

[109] Sanjoy K. Sarker. Quantum transport theory for high electric fields. *Phys. Rev. B*, 32:743–749, Jul 1985. doi: 10.1103/PhysRevB.32.743. URL `http://link.aps.org/doi/10.1103/PhysRevB.32.743`.
(Cited on page 31.)

[110] B.L. Al'tshuler. Temperature dependence of impurity conductivity of metals at low temperatures. *JETP*, 48(4):670, 1978.
(Cited on page 31.)

[111] F. A. Buot and K. L. Jensen. Lattice Weyl-Wigner formulation of exact many-body quantum-transport theory and applications to novel solid-state quantum-based devices. *Phys. Rev. B*, 42: 9429–9457, Nov 1990. doi: 10.1103/PhysRevB.42.9429. URL `http://link.aps.org/doi/10.1103/PhysRevB.42.9429`.
(Cited on page 31.)

[112] Takafumi Kita and Hiromasa Yamashita. Quantum transport equation for Bloch electrons in electromagnetic fields. *Journal of the Physical Society of Japan*, 77(2):024711, 2008. doi: 10.1143/JPSJ.77.024711. URL `http://dx.doi.org/10.1143/JPSJ.77.024711`.
(Cited on page 31.)

[113] C. Zener. Non-adiabatic crossing of energy levels. *Proceedings of the Royal Society of London*, 137(6):696–702, 1932.
(Cited on pages 33 and 35.)

[114] L. Landau. Zur Theorie der Energieubertragung. II. *Physikalische Zeitschrift der Sowjetunion*, 2:46–51, 1932.
(Cited on pages 33 and 35.)

[115] Julian Schwinger. On gauge invariance and vacuum polarization. *Phys. Rev.*, 82:664–679, Jun 1951. doi: 10.1103/PhysRev.82.664. URL `http://link.aps.org/doi/10.1103/PhysRev.82.664`.
(Cited on page 34.)

[116] Ettore Majorana. Atomi orientati in campo magnetico variabile. *Il Nuovo Cimento*, 9(2):43–50, 1932.
(Cited on page 35.)

[117] E. C. G. Stueckelberg. Theorie der unelastischen Stösse zwischen Atomen. *Helvetica Physica Acta*, 5:369, 1932. doi: 10.5169/seals-110177. URL `http://retro.seals.ch/digbib/view?pid=hpa-001:1932:5::490`.
(Cited on page 35.)

[118] Balázs Dóra and Roderich Moessner. Nonlinear electric transport in graphene: Quantum quench dynamics and the Schwinger mechanism. *Phys. Rev. B*, 81:165431, Apr 2010. doi: 10.1103/PhysRevB.81.165431. URL `http://link.aps.org/doi/10.1103/PhysRevB.81.165431`.
(Cited on page 39.)

[119] Murray Sargent, Marlan Orvil Scully, and Willis E. Lamb. *Laser Physics*. Addison-Wesley Publishing Company, Inc., 1987.
(Cited on page 40.)

[120] J. Zhang, T. Li, J. Wang, and J. Schmalian. Post-transient relaxation in graphene after an intense laser pulse. *The European Physical Journal Special Topics*, 222(5):1263–1270, 2013. ISSN 1951-6355. doi: 10.1140/epjst/e2013-01920-2. URL `http://dx.doi.org/10.1140/epjst/e2013-01920-2`.
(Cited on page 42.)

[121] Haining Wang, Jared H. Strait, Paul A. George, Shriram Shivaraman, Virgil B. Shields, Mvs Chandrashekhar, Jeonghyun Hwang, Farhan Rana, Michael G. Spencer, Carlos S. Ruiz-Vargas, and Jiwoong Park. Ultrafast relaxation dynamics of hot optical phonons in graphene. *Applied Physics Letters*, 96(8):081917, 2010. doi: http://dx.doi.org/10.1063/1.3291615. URL `http://scitation.aip.org/content/aip/journal/apl/96/8/10.1063/1.3291615`.
(Cited on pages 42 and 49.)

[122] F. Bonaccorso, Z. Sun, T. Hasan, and A. C. Ferrari. Graphene photonics and optoelectronics. *Nat Photon*, 4(9):611–622, Sep 2010. ISSN 1749-4885. doi: 10.1038/nphoton.2010.186. URL `http://dx.doi.org/10.1038/nphoton.2010.186`.
(Cited on page 42.)

[123] J L Cheng, N Vermeulen, and J E Sipe. Third order optical nonlinearity of graphene. *New Journal of Physics*, 16(5):053014, 2014. URL `http://stacks.iop.org/1367-2630/16/i=5/a=053014`.
(Cited on pages 44 and 101.)

[124] J. L. Cheng, N. Vermeulen, and J. E. Sipe. Dc current induced second order optical nonlinearity in graphene. *Opt. Express.*, 22:15868–76, 2014. doi: 10.1364/OE.22.015868.
(Cited on pages 44 and 101.)

[125] Isabella Gierz, Jesse C. Petersen, Matteo Mitrano, Cephise Cacho, I. C. Edmond Turcu, Emma Springate, Alexander Stöhr, Axel Köhler, Ulrich Starke, and Andrea Cavalleri. Snapshots of non-equilibrium dirac carrier distributions in graphene. *Nat Mater*, 12(12):1119–1124, Dec 2013. ISSN 1476-1122. URL `http://dx.doi.org/10.1038/nmat3757`. Article.
(Cited on pages 48 and 66.)

[126] Akira Satou, Taiichi Otsuji, and Victor Ryzhii. Theoretical study of population inversion in graphene under pulse excitation. *Japanese Journal of Applied Physics*, 50(7R):070116, 2011. URL `http://stacks.iop.org/1347-4065/50/i=7R/a=070116`.
(Cited on page 48.)

[127] A. Satou, V. Ryzhii, Y. Kurita, and T. Otsuji. Threshold of terahertz population inversion and negative dynamic conductivity in graphene under pulse photoexcitation. *Journal of Applied Physics*, 113(14):143108, 2013. doi: http://dx.doi.org/10.1063/1.4801916. URL http://scitation.aip.org/content/aip/journal/jap/113/14/10.1063/1.4801916. (Cited on page 48.)

[128] S. Das Sarma, E. H. Hwang, and Wang-Kong Tse. Many-body interaction effects in doped and undoped graphene: Fermi liquid versus non-Fermi liquid. *Phys. Rev. B*, 75:121406, 2007. doi: 10.1103/PhysRevB.75.121406. URL http://link.aps.org/doi/10.1103/PhysRevB.75.121406. (Cited on pages 48 and 54.)

[129] Raseong Kim, Vasili Perebeinos, and Phaedon Avouris. Relaxation of optically excited carriers in graphene. *Phys. Rev. B*, 84:075449, Aug 2011. doi: 10.1103/PhysRevB.84.075449. URL http://link.aps.org/doi/10.1103/PhysRevB.84.075449. (Cited on page 48.)

[130] Andrea Tomadin, Daniele Brida, Giulio Cerullo, Andrea C. Ferrari, and Marco Polini. Nonequilibrium dynamics of photoexcited electrons in graphene: Collinear scattering, Auger processes, and the impact of screening. *Phys. Rev. B*, 88:035430, Jul 2013. doi: 10.1103/PhysRevB.88.035430. URL http://link.aps.org/doi/10.1103/PhysRevB.88.035430. (Cited on page 48.)

[131] Michael Griebel, Thomas Dornsheifer, and Tilman Neunhoeffer. *Numerical Simulation in Fluid Dynamics*. Society for Industrial and Applied Mathematics, 1997. (Cited on pages 49, 84, 87, 157, and 160.)

[132] Subir Sachdev. Nonzero-temperature transport near fractional quantum hall critical points. *Phys. Rev. B*, 57:7157–7173, Mar 1998. doi: 10.1103/PhysRevB.57.7157. URL http://link.aps.org/doi/10.1103/PhysRevB.57.7157. (Cited on page 53.)

[133] Massimiliano Esposito, Upendra Harbola, and Shaul Mukamel. Nonequilibrium fluctuations, fluctuation theorems, and counting statistics in quantum systems. *Rev. Mod. Phys.*, 81:1665–1702, Dec 2009. doi: 10.1103/RevModPhys.81.1665. URL http://link.aps.org/doi/10.1103/RevModPhys.81.1665. (Cited on page 53.)

[134] A. Schmid. On the dynamics of electrons in an impure metal. *Z. Phys.*, 271:251, 1974. doi: 10.1007/BF01677931. URL http://link.springer.com/article/10.10072FBF01677931. (Cited on page 55.)

[135] B. L. Al'tshuler and G. Aronov. Damping of one-electron excitations in metals. *JETP Lett.*, 30:482, 1979. URL http://www.jetpletters.ac.ru/ps/1367/article_20683.shtml. (Not cited.)

[136] Elihu Abrahams, P. W. Anderson, P. A. Lee, and T. V. Ramakrishnan. Quasiparticle lifetime in disordered two-dimensional metals. *Phys. Rev. B*, 24:6783–6789, Dec 1981. doi: 10.1103/PhysRevB.24.6783. URL http://link.aps.org/doi/10.1103/PhysRevB.24.6783. (Cited on page 55.)

[137] William Feller. *An introduction to probability theory and its applications*, volume 2:. Wiley, New York, NY, 2. ed. edition, 1971. ISBN 0-471-25709-5.
(Cited on pages 56, 57, and 59.)

[138] Rosario N. Mantegna and H. Eugene Stanley. Stochastic process with ultraslow convergence to a Gaussian: The truncated Lévy flight. *Phys. Rev. Lett.*, 73:2946–2949, Nov 1994. doi: 10.1103/PhysRevLett.73.2946. URL http://link.aps.org/doi/10.1103/PhysRevLett.73.2946.
(Cited on page 58.)

[139] Ismo Koponen. Analytic approach to the problem of convergence of truncated Lévy flights towards the Gaussian stochastic process. *Phys. Rev. E*, 52:1197–1199, Jul 1995. doi: 10.1103/PhysRevE.52.1197. URL http://link.aps.org/doi/10.1103/PhysRevE.52.1197.
(Cited on page 58.)

[140] H. E. Hurst. Long-term storage capacity of reservoirs. *Trans. Am. Soc. Civ. Eng.*, 116:770–808, 1951.
(Cited on page 61.)

[141] H. C. Fogedby, T. Bohr, and H. J. Jensen. Fluctuations in a Lévy flight gas. *Journal of Stat. Phys.*, 66:583, 1992.
(Cited on page 61.)

[142] Wolfgang Paul and Jörg Baschnagel. *Stochastic Processes: From Physics to Finance*. Springer, 1999.
(Cited on page 61.)

[143] Jens Feder. *Fractals*. Physics of solids and liquids. Plenum Pr., New York, 1988. ISBN 0-306-42851-2.
(Cited on page 61.)

[144] Sune Jespersen, Ralf Metzler, and Hans C. Fogedby. Lévy flights in external force fields: Langevin and fractional Fokker-Planck equations and their solutions. *Phys. Rev. E*, 59:2736–2745, Mar 1999. doi: 10.1103/PhysRevE.59.2736. URL http://link.aps.org/doi/10.1103/PhysRevE.59.2736.
(Cited on page 63.)

[145] Francesco Mainardi, Gianni Pagnini, and R.K. Saxena. Fox functions in fractional diffusion. *Journal of Computational and Applied Mathematics*, 178:321 – 331, 2005. ISSN 0377-0427. doi: http://dx.doi.org/10.1016/j.cam.2004.08.006. URL http://www.sciencedirect.com/science/article/pii/S0377042704003826.
(Cited on page 63.)

[146] I. Gierz, F. Calegari, S. Aeschlimann, M. Chavez Cervantes, C. Cacho, R. T. Chapman, E. Springate, S. Link, U. Starke, C. R. Ast, and A. Cavalleri. Tracking primary thermalization events in graphene with photoemission at extreme timescales. *arXiv:1506.00120*, 2015.
(Cited on pages 66, 67, 68, and 69.)

[147] Rëgis Decker, Yang Wang, Victor W. Brar, William Regan, Hsin-Zon Tsai, Qiong Wu, William Gannett, Alex Zettl, and Michael F. Crommie. Local electronic properties of graphene on a

bn substrate via scanning tunneling microscopy. *Nano Letters*, 11(6):2291–2295, 2011. doi: 10.1021/nl2005115. URL http://dx.doi.org/10.1021/nl2005115. PMID: 21553853.
(Cited on page 71.)

[148] Jiamin Xue, Javier Sanchez-Yamagishi, Danny Bulmash, Philippe Jacquod, Aparna Deshpande, K. Watanabe, T. Taniguchi, Pablo Jarillo-Herrero, and Brian J. LeRoy. Scanning tunnelling microscopy and spectroscopy of ultra-flat graphene on hexagonal boron nitride. *Nat Mater*, 10 (4):282–285, Apr 2011. ISSN 1476-1122. doi: 10.1038/nmat2968. URL http://dx.doi.org/10.1038/nmat2968.
(Cited on page 71.)

[149] P. Alonso-González, A. Y. Nikitin, F. Golmar, A. Centeno, A. Pesquera, S. Vélez, J. Chen, G. Navickaite, F. Koppens, A. Zurutuza, F. Casanova, L. E. Hueso, and R. Hillenbrand. Controlling graphene plasmons with resonant metal antennas and spatial conductivity patterns. *Science*, 344(6190):1369–1373, 2014. doi: 10.1126/science.1253202. URL http://www.sciencemag.org/content/344/6190/1369.abstract.
(Cited on pages 72, 94, and 95.)

[150] K. Kovtun, P. D. T. Son, and A. O. Starinets. Viscosity in strongly interacting quantum field theories from black hole physics. *Phys. Rev. Lett.*, 94:111601, Mar 2005. doi: 10.1103/PhysRevLett.94.111601. URL http://link.aps.org/doi/10.1103/PhysRevLett.94.111601.
(Cited on pages 73 and 100.)

[151] R. Bistritzer and A. H. MacDonald. Hydrodynamic theory of transport in doped graphene. *Phys. Rev. B*, 80:085109, Aug 2009. doi: 10.1103/PhysRevB.80.085109. URL http://link.aps.org/doi/10.1103/PhysRevB.80.085109.
(Cited on page 73.)

[152] D. Svintsov, V. Vyurkov, S. Yurchenko, T. Otsuji, and V. Ryzhii. Hydrodynamic model for electron-hole plasma in graphene. *Journal of Applied Physics*, 111(8):083715, 2012. doi: http://dx.doi.org/10.1063/1.4705382. URL http://scitation.aip.org/content/aip/journal/jap/111/8/10.1063/1.4705382.
(Cited on page 74.)

[153] Peter Arnold, Guy David Moore, and Laurence G. Yaffe. Transport coefficients in high temperature gauge theories (i): leading-log results. *Journal of High Energy Physics*, 2000(11):001, 2000. doi: 10.1088/1126-6708/2000/11/001. URL http://stacks.iop.org/1126-6708/2000/i=11/a=001.
(Cited on pages 76 and 95.)

[154] Uri M. Ascher, Steven J. Ruuth, and Brian T. R. Wetton. Implicit-explicit methods for time-dependent partial differential equations. *SIAM Journal on Numerical Analysis*, 32(3):797–823, 1995. doi: 10.1137/0732037. URL http://dx.doi.org/10.1137/0732037.
(Cited on pages 84 and 85.)

[155] M. Schütt, P. M. Ostrovsky, M. Titov, I. V. Gornyi, B. N. Narozhny, and A. D. Mirlin. Coulomb drag in graphene near the Dirac point. *Phys. Rev. Lett.*, 110:026601, Jan 2013. doi: 10.1103/PhysRevLett.110.026601. URL http://link.aps.org/doi/10.1103/PhysRevLett.110.

`026601`.
(Cited on page 151.)

[156] Karsten Flensberg, Ben Yu-Kuang Hu, Antti-Pekka Jauho, and Jari M. Kinaret. Linear-response theory of Coulomb drag in coupled electron systems. *Phys. Rev. B*, 52:14761–14774, Nov 1995. doi: 10.1103/PhysRevB.52.14761. URL `http://link.aps.org/doi/10.1103/PhysRevB.52.14761`. (Cited on page 152.)

A Appendix A
Langreth-Wilkins rules

We briefly give a short overview of the necessary rules for analytical continuation of contour ordered correlation functions and their convolution as well as products, the way they are needed in the main text. The definition follow the standard literature on non-equilibrium Green's function methods, see for example Refs. [102, 103].

Given the real-time two-point correlation functions

$$X^{\gtrless}(t_1, t_2) \,, \tag{A.1}$$

we define the following set of additional correlators

$$X^R(t_1, t_2) = \Theta(t_1 - t_2)[X^>(t_1, t_2) - X^<(t_1, t_2)] \,, \tag{A.2}$$

$$X^A(t_1, t_2) = \Theta(t_2 - t_1)[X^<(t_1, t_2) - X^>(t_1, t_2)] \,, \tag{A.3}$$

$$X^T(t_1, t_2) = \Theta(t_1 - t_2)X^>(t_1, t_2) + \Theta(t_2 - t_1)X^<(t_1, t_2)] \,, \tag{A.4}$$

$$X^{\tilde{T}}(t_1, t_2) = \Theta(t_1 - t_2)X^<(t_1, t_2) + \Theta(t_2 - t_1)X^>(t_1, t_2)] \,. \tag{A.5}$$

They are not independent but fulfill the following relations:

$$X^R - X^A = X^> - X^< \,, \tag{A.6}$$

$$X^< + X^> = X^T + X^{\tilde{T}} \,, \tag{A.7}$$

$$X^R(t_1, t_2) = [X^A]^\dagger(t_2, t_1) \,, \tag{A.8}$$

$$X^<(t_1, t_2) = -[X^<]^\dagger(t_2, t_1) \,, \tag{A.9}$$

$$X^>(t_1, t_2) = -[X^>]^\dagger(t_2, t_1) \,. \tag{A.10}$$

From the correlation functions (A.1) we can construct new two-point functions by convolution on the Keldysh contour,

$$Z(t_1, t_2) = \oint_C d\tau \, X(t_1, \tau)Y(\tau, t_2) \,. \tag{A.11}$$

The Langreth-Wilkins rules are simple book-keeping formulas to recover the convolution $Z(t_1, t_2)$ in terms of the real-time correlation functions $X(t_1, t_2)$ and $Y(t_1, t_2)$,

$$Z^{\gtrless} = X^R \circ Y^{\gtrless} + X^{\gtrless} \circ Y^A \,, \tag{A.12}$$

$$Z^{R,A} = X^{R,A} \circ Y^{R,A} \,. \tag{A.13}$$

Here we used the short-hand notation

$$A \circ B = \int \mathrm{d}t_3 \, A(t_1, t_3) B(t_3, t_2) \,. \tag{A.14}$$

Similarly for the product

$$D(\tau_1, \tau_2) = A(\tau_1, \tau_2) B(\tau_2, \tau_1) \,, \tag{A.15}$$

the retarded correlator is for example given by

$$D^R(t_1, t_2) = A^<(t_1, t_2) B^A(t_2, t_1) + A^R(t_1, t_2) B^<(t_2, t_1) \,. \tag{A.16}$$

B

Derivation of the kinetic equation

In this section we are going to give additional details on the derivation of the quantum kinetic equation in graphene. We will also discuss the connection between the Wigner transformation and the projected Green's function technique laid out in Sec. 3.2.1.

B.1 The gradient expansion

We are going to establish a connection between the Wigner transformation of the Green's function in real space representation and the projected GF in the momentum representation. The Wigner transform in real space coordinates of a single particle GF $G(\vec{r}_1, \vec{r}_2)$ reads as

$$G(\vec{R}, \vec{k}) = \int \frac{\mathrm{d}^d r}{(2\pi)^d}\, \mathrm{e}^{+\mathrm{i}\vec{k}\cdot\vec{r}}\, G(\vec{R} + \vec{r}/2, \vec{R} - \vec{r}/2) \,. \tag{B.1}$$

Presume that we have a projected Green's function $g_{k_1 k_2}$ for example as in Sec. Sec. 3.2.1 that depends on two momentum indices. In this case the connection with the Wigner representation is given by

$$g_{k_1 k_2} = \int \mathrm{d}\vec{R}' \mathrm{d}\vec{r}\, \mathrm{e}^{-\mathrm{i}\vec{k}\cdot\vec{R}'} \mathrm{e}^{-\mathrm{i}\vec{K}\cdot\vec{r}} g(\vec{r}, \vec{R}') \,, \tag{B.2}$$

where $\vec{k} = \vec{k}_1 - \vec{k}_2$ and $\vec{K} = (\vec{k}_1 + \vec{k}_2)/2$. We see that assuming $\vec{k}_1 = \vec{k}_2$ leads to an average over the center of mass variable $\vec{R}'$. On the other hand the Green's function in the mixed representation is obtained as

$$g(\vec{R} - \vec{R}_0, \vec{K}) = \int \frac{\mathrm{d}\vec{k}}{(2\pi)^2} \mathrm{e}^{+\mathrm{i}\vec{k}(\vec{R}-\vec{R}_0)} g_{k_1 k_2} \,. \tag{B.3}$$

This yields simply $g(\vec{K}) = g_{KK}$ if we assume that $g_{k_1 k_2} \sim \delta_{k_1 k_2}$.

We are now able to obtain the Liouvillian $[\xi, g]$ in Eq. (3.40) from the main text for equal times ($\tau = 0$) and to leading order in the gradient expansion,

$$\begin{aligned}
[\xi, g] = \int \frac{\mathrm{d}\vec{k}}{(2\pi)^2} \int \mathrm{d}\vec{R}' \int \mathrm{d}\vec{r} \Bigg[&\left(\frac{\vec{K} + \vec{k}/2}{|\vec{K} + \vec{k}/2|} + \frac{\vec{K} - \vec{k}/2}{|\vec{K} + \vec{k}/2|} \right) \cdot \mathrm{i}\nabla_{R'} \\
+ \frac{1}{2} &\left(\frac{\vec{K} + \vec{k}/2}{|\vec{K} + \vec{k}/2|} - \frac{\vec{K} - \vec{k}/2}{|\vec{K} + \vec{k}/2|} \right) \cdot \mathrm{i}\nabla_r \Bigg] \mathrm{e}^{-\mathrm{i}\vec{k}(\vec{R}'-\vec{R})} \mathrm{e}^{-\mathrm{i}\vec{K}\vec{r}} g(\vec{r}, \vec{R}') \,.
\end{aligned} \tag{B.4}$$

Expanding the differential operator in the bracket in Eq. (B.4) in small $\vec{k}$ we obtain to leading order

$$[\xi, g] = 2\hat{K} \cdot \mathrm{i}\nabla_R \int \mathrm{d}^2 r\, \mathrm{e}^{-\mathrm{i}\vec{K}\vec{r}} g(\vec{r}, \vec{R}) = 2\hat{K} \cdot \mathrm{i}\nabla_R\, g_{\vec{K}\vec{K}}(\vec{R}) \,. \tag{B.5}$$

The last equation yields the usual driving term of the Boltzmann equation and links the Wigner transformation with the projection method.

B.2 The collision integral

We will now derive the collision integral of the quantum kinetic equation due to Coulomb scattering. We take into account that the distribution function is in leading order of the gradient expansion linear in the momentum but a 2×2 matrix in sublattice space.

We start out with the projected lesser (greater) component of the self energy due to Coulomb interaction which is given by

$$\sigma_{\nu_1 \nu_2}^{\gtrless} = \mathrm{i} \int \mathrm{d}^2 r_{1,2}\, \phi_{\nu_1}^\dagger(\vec{r}_1) g^{\gtrless}(1, 2)\phi_{\nu_2}(\vec{r}_2)V^{\gtrless}(1, 2) \,. \tag{B.6}$$

Here ϕ_{ν_1} denotes the eigenstates of the clean non-interacting graphene as introduced in Sec. 1.1. The projection of the kinetic equation was explained in the main text in Sec. 3.2.1. For the Coulomb potential we have in Keldysh space

$$V = V_0 + V_0 \circ \Pi \circ V \,. \tag{B.7}$$

Here $\circ$ again denotes convolution in time and space. Furthermore V_0 denotes the bare Coulomb Potential, Eq. (1.1), and Π is the polarization operator defined in Eq. (B.15) below. From the retarded component of the dresses Coulomb potential, Eq. (B.7), we obtain

$$(V^R)^{-1} = V_0^{-1} - \Pi^R \,. \tag{B.8}$$

We now replace Π^R from this expression in the Keldysh component of Eq. (B.7), which reads as

$$V^{\gtrless} = V_0 \circ \Pi^R \circ V^{\gtrless} + V_0 \circ \Pi^{\gtrless} \circ V^A \,. \tag{B.9}$$

We then obtain for the lesser component of the Coulomb potential the expression

$$V^{\gtrless} = V^R \circ \Pi^{\gtrless} \circ V^A \,. \tag{B.10}$$

Inserting Eq. (B.10) into Eq. (B.6) and further use the inverse projection as in Eq. (3.25), we arrive at

$$\sigma_{\nu_1 \nu_2}^{\gtrless} = \mathrm{i} \int \mathrm{d}^2 r_{1,2}\, \phi_{\nu_1}^\dagger(\vec{r}_1) \left(\sum_{\nu_3 \nu_4} \phi_{\nu_3}(\vec{r}_1) g_{\nu_3 \nu_4} \phi_{\nu_4}^\dagger(\vec{r}_2) \right) \phi_{\nu_2}(\vec{r}_2)V^R(1, 1')\Pi^{\gtrless}(1', 2')V^A(2', 2) \,. \tag{B.11}$$

We rearrange and Fourier transform the polarization operator $\Pi^{\gtrless}$, which yields

$$\sigma_{\nu_1 \nu_2}^{\gtrless}(t_1, t_2) = \mathrm{i} \sum_{\nu_{\bar{1}} \nu_{\bar{2}}} g_{\nu_{\bar{1}} \nu_{\bar{2}}}^{\gtrless}(t_1, t_2) \int \frac{\mathrm{d}\vec{k}_{1,2}}{(2\pi)^2} \int \mathrm{d}t_{1',2'} \left(\int \mathrm{d}\vec{r}_{1,1'} \phi_{\nu_1}^\dagger(\vec{r}_1) \phi_{\nu_{\bar{1}}}(\vec{r}_1) V^R(1, 1') \mathrm{e}^{\mathrm{i}\vec{k}_1 \cdot \vec{r}_{1'}} \right)$$
$$\times \left(\int \mathrm{d}\vec{r}_{2,2'} \phi_{\nu_{\bar{2}}}^\dagger(\vec{r}_2) \phi_{\nu_2}(\vec{r}_2) V^A(2, 2') \mathrm{e}^{-\mathrm{i}\vec{k}_2 \cdot \vec{r}_{2'}} \right) \Pi^{\gtrless}(\vec{k}_1, t_{1'}; \vec{k}_2, t_{2'}) \,. \tag{B.12}$$

Inserting the explicit form of the graphene eigenstates (1.7), we obtain the result

$$
\sigma^{\gtrless}_{\nu_1\nu_2}(t_1, t_2) = \mathrm{i} \sum_{\lambda_{\bar{1}}\lambda_{\bar{2}}} g^{\gtrless}_{\nu_{\bar{1}}\nu_{\bar{2}}}(t_1, t_2) \int \frac{\mathrm{d}\vec{q}_{1,2}}{(2\pi)^2} \int \mathrm{d}t_{1',2'} [u^\dagger_{\nu_1} u_{\nu_{\bar{1}}}][u^\dagger_{\nu_{\bar{2}}} u_{\nu_2}]
$$
$$
\times V^R(\vec{q}_1; t_1, t_{1'}) V^A(\vec{q}_2; t_2, t_{2'}) \Pi^{\gtrless}(\vec{q}_1, t_{1'}; \vec{q}_2, t_{2'}) \,.
\tag{B.13}
$$

It is advantageous to introduce the 2×2 matrices

$$
\Theta_{\nu_1\nu_{\bar{1}}} = [u^\dagger_{\nu_1} u_{\nu_{\bar{1}}}] \,,
\tag{B.14}
$$

which are the prototype of the Dirac factors from the main text. We proceed with explicit expressions for the polarization operator $\Pi(\vec{k}_1, t_1; \vec{k}_2, t_2)$. The basic definition in the Keldysh theory is

$$
\Pi^{\gtrless}(1, 2) = -\mathrm{i}N \mathrm{tr}[G^{\gtrless}(1, 2) G^{\lessgtr}(2, 1)] \,.
\tag{B.15}
$$

Inserting the inverse projections (3.25) for the Green's function we obtain

$$
\Pi^{\gtrless}(1, 2) = -\mathrm{i}N \sum_{\nu_i, i=1,...,5} G^{\gtrless}_{\nu_2\nu_3} G^{\lessgtr}_{\nu_4\nu_5} \int \mathrm{d}^2 r_{1,2} \left(\phi^\dagger_{\nu_1}(\vec{r}_1) \phi_{\nu_2}(\vec{r}_1) \phi^\dagger_{\nu_5}(\vec{r}_1) \phi_{\nu_1}(\vec{r}_1) \mathrm{e}^{-\mathrm{i}\vec{k}_1\vec{r}_1} \right)
$$
$$
\times \left(\phi^\dagger_{\nu_3}(\vec{r}_2) \phi_{\nu_2}(\vec{r}_4) \mathrm{e}^{+\mathrm{i}\vec{k}_2\vec{r}_2} \right) \,.
\tag{B.16}
$$

Here $N = 4$ denotes the degeneracy factor in graphene due to valley and spin. Which after using the explicit expression of the graphene eigenstates and their completeness yields

$$
\Pi^{\lessgtr}(\vec{k}_1, t_1; \vec{k}_2, t_2) = -\mathrm{i}N \sum_{\nu_1\nu_2} \sum_{\lambda_{\bar{1}}\lambda_{\bar{2}}} \Theta_{\nu_2\nu_{\bar{2}}} \Theta_{\nu_{\bar{1}}\nu_1} \, g^{\lessgtr}_{\nu_1\nu_2}(t_1, t_2) g^{\gtrless}_{\nu_{\bar{2}}\nu_{\bar{1}}}(t_2, t_1) \,,
\tag{B.17}
$$

Within the Keldysh-theory the gradient expansion of the collision integral leads to the local Boltzmann collision integral. We pursue a strategy developed by Kadanoff and Baym [102] and subsequently refined by others [20, 107] to include higher order correlations on the quantum level. The reconstruction of the two time distribution function from its time diagonal part, usually refered to as the generalized Kadanoff-Baym ansatz, to leading order in the relaxation times in the system reads [107]

$$
G^{\lessgtr}(t_1, t_2) = \mathrm{i}\left[G^R(t_1, t_2) G^{\lessgtr}(t_2, t_2) - G^{\lessgtr}(t_1, t_1) G^A(t_1, t_2) \right] \,.
\tag{B.18}
$$

Since the quantum terms in the kinetic equation are diagonal in momentum space we assume that the Keldysh Green's function remain diagonal in the momentum but may be off-diagonal in the band indices. We write $\nu_i = \{\lambda_i, p_i\}$ and obtain,

$$
G^{\lessgtr}_{\nu_1\nu_2} = G^{\lessgtr}_{\lambda_1, p_1; \lambda_2, p_2} = \delta_{p_1 p_2} G^{\lessgtr}_{\lambda_1\lambda_2} \,.
\tag{B.19}
$$

We therefore allow for interband coherences expressed by the off-diagonal elements of the Green's function (B.19), that will later be identified with the polarization of graphene. In fact, this represents the zeroth order gradient expansion and is not sufficient to restore the convective term $\hat{v} \cdot \nabla_R$ in the Boltzmann equation which is only obtained first order in the gradients (see Appendix B.1). With the relation (B.19), the polarization bubble, Eq. (B.17), becomes diagonal in momentum,

$$
\Pi^{\lessgtr}(\vec{k}_1, t_1; \vec{k}_2, t_2) = -\mathrm{i}N \delta_{k_1, k_2} \sum_{p_1} \sum_{\lambda_1\lambda_2\lambda_{\bar{1}}\lambda_{\bar{2}}} g^{\lessgtr}_{\nu_1\nu_2}(t_1, t_2) \Theta_{\nu_2\nu_{\bar{2}}} g^{\gtrless}_{\nu_{\bar{2}}\nu_{\bar{1}}}(t_2, t_1) \Theta_{\nu_{\bar{1}}\nu_1} \,.
\tag{B.20}
$$

where $\vec{p}_1 = \vec{p}_2$ and $\vec{p}_{\bar{1}} = \vec{p}_1 - \vec{k}_1$ and $\vec{p}_{\bar{2}} = \vec{p}_2 - \vec{k}_2$. Using the Langreth-Wilkins rules (see Appendix A) the collision integral from the main text, Eq. (3.41), can be written as

$$St(t,t) = \frac{1}{4} \int_{-\infty}^{t} dt_3 \left[\sigma^> \circ g^< - g^> \circ \sigma^< + g^< \circ \sigma^> - \sigma^< \circ g^> \right] . \tag{B.21}$$

Here t_3 is the intermediate time in the convolutions of the form $\sigma^>(t,t_3)g^<(t_3,t)$. With this we obtain for the out-scattering term of the collision integral (3.41)

$$- St_{\nu_1\nu_2}^{(\text{out})}(t) = \frac{1}{4} \int_{-\infty}^{t} dt_3 \sum_{\nu_3} \left[\sigma_{\nu_1\nu_3}^>(t,t_3)g_{\nu_3\nu_2}^<(t_3,t) + g_{\nu_1\nu_3}^<(t,t_3)\sigma_{\nu_3\nu_2}^>(t_3,t) \right] , \tag{B.22}$$

the following expression:

$$
\begin{aligned}
- St_{\text{out}} = \frac{N}{4} & \int \frac{d^2q}{(2\pi)^2} \int \frac{d^2p_1'}{(2\pi)^2} \int_{-\infty}^{t} dt_3 \int_{-\infty}^{+\infty} dt_1' \int_{-\infty}^{+\infty} dt_3' \Bigg\{ \\
& V^R(q,t,t_1')V^A(q,t_3',t_3) \\
& \times \Theta_{p_1,p_1-q}g_{p_1-q}^>(t,t_3)\Theta_{p_1-q,p_1}g_{p_1}^<(t_3,t) \, \text{tr}\left[g_{p_1'}^>(t_1',t_3')\Theta_{p_1',p_1'-q}g_{p_1'-q}^<(t_3',t_1')\Theta_{p_1'-q,p_1'} \right] \\
& + V^A(q,t,t_1')V^R(q,t_3',t_3) \\
& \times g_{p_1}^<(t,t_3)\Theta_{p_1,p_1-q}g_{p_1-q}^>(t_3,t)\Theta_{p_1-q,p_1} \, \text{tr}\left[g_{p_1'}^>(t_3',t_1')\Theta_{p_1',p_1'-q}g_{p_1'-q}^<(t_1',t_3')\Theta_{p_1'-q,p_1'} \right] \Bigg\} .
\end{aligned}
\tag{B.23}
$$

Here $\Theta_{p_1p_2}$ and $g_p^{\lessgtr}$ are understood as matrices in band space such that

$$\Theta_{p_1,p_2} = \begin{pmatrix} \cos\varphi_{12}/2 & i\sin\varphi_{12}/2 \\ i\sin\varphi_{12}/2 & \cos\varphi_{12}/2 \end{pmatrix} , \tag{B.24}$$

where $\varphi_{12} = \sphericalangle(\vec{p}_1, \vec{p}_2)$ and

$$g_p^{\lessgtr}(t_1,t_2) = \begin{pmatrix} g_{p,++}^{\lessgtr}(t_1,t_2) & g_{p,+-}^{\lessgtr}(t_1,t_2) \\ g_{p,-+}^{\lessgtr}(t_1,t_2) & g_{p,--}^{\lessgtr}(t_1,t_2) \end{pmatrix} . \tag{B.25}$$

We now insert the Kadanoff-Baym ansatz (B.18) into the collision integral (B.23). Furthermore, we substitute

$$G_{\nu_1\nu_2}^R(t_1,t_2) = -i\delta_{\nu_1\nu_2}\Theta(t_1-t_2)e^{-i\varepsilon_{\nu_1}(t_1-t_2)} , \tag{B.26}$$

$$G_{\nu_1\nu_2}^A(t_1,t_2) = +i\delta_{\nu_1\nu_2}\Theta(t_2-t_1)e^{-i\varepsilon_{\nu_1}(t_1-t_2)} . \tag{B.27}$$

Here, the spectrum is assumed to be unaltered by the external fields. The resulting collision integral is non-Markovian. However if we perform the Markov approximation, that means we set the distribution functions occurring in the collision integral on the external time t and extend the limits of integration

to infinity, we obtain the simpler expression

$$
-St_{\text{out}} = \frac{N}{4} \int \frac{\mathrm{d}\omega}{(2\pi)} \int \frac{\mathrm{d}^2q}{(2\pi)^2} \int \frac{\mathrm{d}^2p_1'}{(2\pi)^2} \Bigg\{
$$

$$
|V^R(q,\omega)|^2 \, \Theta_{p_1,p_1-q} g^>_{p_1-q}(t) \Theta_{p_1-q,p_1} g^<_{p_1}(t) \, \mathrm{tr}\Big[g^>_{p_1'}(t) \Theta_{p_1',p_1'-q} g^<_{p_1'-q}(t) \Theta_{p_1'-q,p_1'} \Big]
$$

$$
\times \int_{-\infty}^{+\infty} \mathrm{d}t_3 \int_{-\infty}^{+\infty} \mathrm{d}t_1' \int_{-\infty}^{+\infty} \mathrm{d}t_3' \, e^{-\mathrm{i}(\omega+\varepsilon_{p_1-q}-\varepsilon_{p_1})t} \, e^{-\mathrm{i}(\omega+\varepsilon_{p_1'}-\varepsilon_{p_1'-q})t_1'}
$$

$$
\times e^{-\mathrm{i}(-\omega+\varepsilon_{p_1'-q}-\varepsilon_{p_1'})t_3'} \, e^{-\mathrm{i}(\omega+\varepsilon_{p_1}-\varepsilon_{p_1-q})t_3} \tag{B.28}
$$

$$
+ \, |V^R(q,\omega)|^2 \, g^<_{p_1}(t)\Theta_{p_1,p_1-q} g^>_{p_1-q}(t) \Theta_{p_1-q,p_1} \, \mathrm{tr}\Big[g^>_{p_1'}(t) \Theta_{p_1',p_1'-q} g^<_{p_1'-q}(t) \Theta_{p_1'-q,p_1'} \Big]
$$

$$
\times \int_{-\infty}^{+\infty} \mathrm{d}t_3 \int_{-\infty}^{+\infty} \mathrm{d}t_1' \int_{-\infty}^{+\infty} \mathrm{d}t_3' \, e^{-\mathrm{i}(\omega+\varepsilon_{p_1}-\varepsilon_{p_1-q})t} \, e^{-\mathrm{i}(\omega+\varepsilon_{p_1'-q}-\varepsilon_{p_1'})t_1'}
$$

$$
\times e^{-\mathrm{i}(-\omega+\varepsilon_{p_1'}-\varepsilon_{p_1'-q})t_3'} \, e^{-\mathrm{i}(\omega+\varepsilon_{p_1-q}-\varepsilon_{p_1})t_3} \Bigg\} \, .
$$

Similar expressions hold for the in scattering term. After evaluating the time integrals which yield the on-shell conditions, we obtain for the diagonal part of the collision integral ($\lambda_1 = \lambda_2$),

$$
-St = \frac{N}{2} \int \frac{\mathrm{d}^2q}{(2\pi)^2} \int \frac{\mathrm{d}\omega}{2\pi} \, V^R(q,\omega) V^A(q,\omega)
$$

$$
\times (2\pi)^2 \delta(\varepsilon_{\bar{\lambda}_1',p_1'-q} - \varepsilon_{\lambda_1',p_1'} + \omega)\delta(\varepsilon_{\bar{\lambda}_1,p_1-q} - \varepsilon_{\lambda_2,p_1} - \omega) \tag{B.29}
$$

$$
\times \mathrm{Re}\Bigg\{ \Theta_{p_1,p_1-q} g^>_{p_1-q}(t) \Theta_{p_1-q,p_1} g^<_{p_1}(t) \, \mathrm{Tr}[g^>_{p_1'}(t)\Theta_{p_1',p_1'-q} g^<_{p_1'-q}(t)\Theta_{p_1'-q,p_1'}] - \{ <\leftrightarrow> \} \Bigg\} \, ,
$$

where the trace also means summation over the intermediate momentum p_1' now. We now define the distribution matrix

$$
g^<_p(t) = \mathrm{i} \begin{pmatrix} \rho_{p,+}(t) & P_p(t) \\ P_p^*(t) & \rho_{p,-}(t) \end{pmatrix} , \tag{B.30}
$$

where the off-diagonal elements P are the polarization of the graphene while $\rho_{p,\pm}$ are the conduction and valence band populations. With this definition we obtain for the trace appearing in the collision integral,

$$
\mathrm{tr}[\delta(\varepsilon_{\bar{\lambda}_1',p_1} - \varepsilon_{\lambda_1'p_2} + \omega)\Theta_{p_1,p_2} g^>_{p_2}(t)\Theta_{p_2,p_1} g^<_{p_1}(t)] = \sum_{\lambda_1',\bar{\lambda}_1'} \delta(\varepsilon_{\bar{\lambda}_1',p_1} - \varepsilon_{\lambda_1'p_2} + \omega)\Bigg\{
$$

$$
\frac{1}{2}(1 + \lambda_1'\bar{\lambda}_1' \cos\varphi_{12})\rho_{\bar{\lambda}_1'}(p_1)\Big(1 - \rho_{\lambda_1'}(p_2)\Big)
$$

$$
+ \frac{\mathrm{i}\sin\varphi_{12}}{2}\Big[\rho_{\bar{\lambda}_1'}(p_1)P_{\lambda_1'}(p_2) - P_{\bar{\lambda}_1'}(p_1)^*\Big(1 - \rho_{\lambda_1'}(p_2)\Big)\Big] \tag{B.31}
$$

$$
- \frac{1}{2}(1 + \lambda_1'\bar{\lambda}_1' \cos\varphi_{12})P_{\bar{\lambda}_1'}(p_1)^* P_{\lambda_1'}(p_2) \Bigg\}
$$

Here we introduced the notation $P_{+1} = P$ and $P_{-1} = P^*$. Furthermore we have for the diagonal parts

$$
\begin{aligned}
[\delta(\varepsilon_{\bar{\lambda}_1,p_2} - \varepsilon_{\lambda_1 p_1} - \omega)\Theta_{p_1,p_2}g^>_{p_2}(t)\Theta_{p_2,p_1}g^<_{p_1}(t)]_{\lambda_1\lambda_1} &= \sum_{\bar{\lambda}_1}\delta(\varepsilon_{\bar{\lambda}_1,p_1} - \varepsilon_{\lambda_1 p_2} - \omega)\Bigg\{ \\
&\frac{1}{2}(1 + \lambda_1\bar{\lambda}_1\cos\varphi_{12})\rho_{\lambda_1}(p_1)\Big(1 - \rho_{\bar{\lambda}_1}(p_2)\Big) \\
&+ \frac{\mathrm{i}\lambda_1\bar{\lambda}_1\sin\varphi_{12}}{2}\Bigg[\rho_{\lambda_1}(p_1)P_{\bar{\lambda}_1}(p_2) - \Big(1 - \rho_{\bar{\lambda}_1}(p_2)\Big)P_{\lambda_1}(p_1)\Bigg] \\
&- \frac{1}{2}(1 + \lambda_1\bar{\lambda}_1\cos\varphi_{12})P_{\lambda_1}(p_1)^*P_{\bar{\lambda}_1}(p_2)\ \Bigg\},
\end{aligned}
\tag{B.32}
$$

while the off-diagonal part reads ($\lambda_2 = -\lambda_1$),

$$
\begin{aligned}
[\delta(\varepsilon_{\bar{\lambda}_1,p_2} - \varepsilon_{\lambda_2 p_1} - \omega)\Theta_{p_1,p_2}g^>_{p_2}(t)\Theta_{p_2,p_1}g^<_{p_1}(t)]_{\lambda_1\lambda_2} &= \sum_{\bar{\lambda}_1}\delta(\varepsilon_{\bar{\lambda}_1,p_2} - \varepsilon_{\lambda_2 p_1} - \omega)\Bigg\{ \\
&\frac{\mathrm{i}\bar{\lambda}_1\lambda_2\sin\varphi_{12}}{2}\rho_{\lambda_2}(p_1)\Big(1 - \rho_{\bar{\lambda}_1}(p_2)\Big) \\
&+ \frac{1}{2}(1 - \lambda_2\bar{\lambda}_1\cos\varphi_{12})\Bigg[P_{\lambda_2}(p_1)^*\Big(1 - \rho_{\bar{\lambda}_1}(p_2)\Big) - P_{\bar{\lambda}_1}(p_2)\rho_{\lambda_2}(p_1)\Bigg] \\
&- \frac{\mathrm{i}\bar{\lambda}_1\lambda_2\sin\varphi_{12}}{2}P_{\lambda_2}(p_1)^*P_{\bar{\lambda}_1}(p_2)\ \Bigg\}.
\end{aligned}
\tag{B.33}
$$

We observe that if the polarization is zero the usual collision integral of Coulomb scattering in graphene including the graphene specific Dirac factors is restored from Eqs. (B.31)-(B.33). We will here only give the total diagonal collision integral neglecting the polarization. And for the off-diagonal collision integral we will assume weak polarization and only consider the out-scattering term that leads to the decay of polarization and defines the decoherence time. In this approximation the usual diagonal part of the collision integral reads

$$
\begin{aligned}
St_{\lambda_1\lambda_1} = -\frac{N}{2}&\int(\mathrm{d}^2q)\int(\mathrm{d}\omega)\,|V(q,\omega)|^2 \\
\times\sum_{\bar{\lambda}_1}&2\pi\delta(\varepsilon_{\bar{\lambda}_1,p_1-q} - \varepsilon_{\lambda_2,p_1} - \omega)\frac{1}{2}(1 + \lambda_1\bar{\lambda}_1\cos\varphi_{12})\rho_{\lambda_1}(p_1)\Big(1 - \rho_{\bar{\lambda}_1}(p_1 - q)\Big) \\
\times\sum_{\lambda'_1,\bar{\lambda}'_1}&\int_{p'_1}2\pi\,\delta(\varepsilon_{\bar{\lambda}'_1,p'_1-q} - \varepsilon_{\lambda'_1,p'_1} + \omega)\frac{1}{2}(1 + \lambda'_1\bar{\lambda}'_1\cos\varphi_{12})\rho_{\bar{\lambda}'_1}(p'_1 - q)\Big(1 - \rho_{\lambda'_1}(p'_1)\Big) \\
+&\{\rho \leftrightarrow (1 - \rho)\}\,.
\end{aligned}
\tag{B.34}
$$

On the other hand for the off-diagonal part in the approximation discussed above we have

$$
\begin{aligned}
St_{\lambda_1,\lambda_2} = -\frac{N}{2} &\int (\mathrm{d}^2 q) \int (\mathrm{d}\omega)\, |V(q,\omega)|^2 \\
\times \sum_{\bar{\lambda}_1} &2\pi\delta(\varepsilon_{\bar{\lambda}_1,p_1-q} - \varepsilon_{\lambda_2,p_1} - \omega)\frac{1}{2}(1 - \lambda_2\bar{\lambda}_1\cos\varphi_{12})P_{\lambda_2}(p_1)^*\Big(1 - \rho_{\bar{\lambda}_1}(p_1-q)\Big) \\
\times \sum_{\lambda'_1,\bar{\lambda}'_1} &\int_{p'_1} 2\pi\,\delta(\varepsilon_{\bar{\lambda}'_1,p'_1-q} - \varepsilon_{\lambda'_1,p'_1} + \omega)\frac{1}{2}(1 + \lambda'_1\bar{\lambda}'_1\cos\varphi_{12})\rho_{\bar{\lambda}'_1}(p'_1-q)\Big(1 - \rho_{\lambda'_1}(p'_1)\Big) \\
&+ \{\rho \leftrightarrow (1-\rho)\}\,.
\end{aligned}
\tag{B.35}
$$

We observe that in the off-diagonal collision integral the Dirac factors are of a different form. As a consequence the integral kernel for the decoherence time will be suppressed at the forward scattering resonance in contrast to the collision kernel for the diagonal collision integral. As a consequence the pure dephasing time τ_φ will not be enhanced by forward scattering and therefore fairly long, i.e. $\tau_\varphi \sim \alpha^2$.

B.3 Calculation of the dephasing rate

We calculate now the dephasing time defined in the previous section. According to Eq. (B.35) for $\lambda_1 = +1$ and $\lambda_2 = -1$ we define the dephasing time as

$$
\begin{aligned}
\tau_\varphi^{-1} = \frac{1}{2} &\int (\mathrm{d}^2 q) \int (\mathrm{d}\omega)\, |V(q,\omega)|^2 \\
\times \sum_{\bar{\lambda}_1} &2\pi\delta(\varepsilon_{\bar{\lambda}_1,p_1-q} - \varepsilon_{\lambda_2,p_1} - \omega)\frac{1}{2}(1 + \bar{\lambda}_1\cos\varphi_{12})\Big(1 - \rho_{\bar{\lambda}_1}(p_1-q)\Big)\mathcal{K}(\omega,q)\,.
\end{aligned}
\tag{B.36}
$$

Here we introduced the kinetic kernel known from Chapt. 4, see Eq. (4.10). After the standard algebra that can be found in Appendix D we have for the decoherence time defined as the out-scattering term in the collision integral for the polarization

$$
\tau_\varphi^{-1} = \frac{\alpha_g^2}{8p_1} \int_0^{+\infty} \mathrm{d}q \int_{-\infty}^{+\infty} \mathrm{d}\omega\, \frac{1}{q}\frac{1 - \rho(\omega - p_1)}{\sqrt{(2p_1 - \omega)^2 - q^2}}\,\mathcal{K}(\omega,q)\,.
\tag{B.37}
$$

Physically, coherences decay into population as can be seen from the factor $[1 - f(\lambda p - \omega)]$ in the scattering rate, expressing the final state of scattering. We split it up into two parts, which we will study separately, i.e.

$$
\tau_{\varphi,1}^{-1}(p) = \frac{N}{8\pi p} \int \mathrm{d}\omega \int \mathrm{d}q\, q\, \frac{|V(\omega,q)|^2}{\sqrt{\mathrm{sgn}(q^2 - \omega^2)(2p - \omega)^2 - q^2}}\,\mathcal{K}(\omega,q)[1 - f(p - \omega)]\,,
\tag{B.38}
$$

$$
\tau_{\varphi,2}^{-1}(p) = \frac{N}{8\pi p} \int \mathrm{d}\omega \int \mathrm{d}q\, q\, \frac{|V(\omega,q)|^2}{\sqrt{\mathrm{sgn}(q^2 - \omega^2)(-2p - \omega)^2 - q^2}}\,\mathcal{K}(\omega,q)[1 - f(-p - \omega)]\,.
\tag{B.39}
$$

Such that

$$
\tau_\varphi^{-1}(p) = \tau_{\varphi,1}^{-1}(p) + \tau_{\varphi,2}^{-1}(p)\,.
\tag{B.40}
$$

In fact the second time is irrelevant close to the Dirac point and we can concentrate on the first contribution or

$$
\tau_\varphi^{-1}(p) = \tau_{\varphi,1}^{-1}(p)\,.
\tag{B.41}
$$

Intraband contribution to the scattering rate

We calculate first the intraband contribution to the decoherence time for small chemical potential, i.e. $|\mu| \ll T$. We introduce the dimensionless quantities $Q = q/2T$, $\Omega = \omega/2T$ and $P = p/T$. In dimensionless variables the decoherence time reads,

$$\tau_{\varphi,1}^{-1}(p)\Big|_{\text{intra}} = \frac{N\alpha^2 T^2}{2p} \underbrace{\int_{-\infty}^{P/2} d\Omega \int_{|\Omega|}^{P-\Omega} dQ \, \frac{\tilde{\mathcal{K}}(\Omega, Q)[1 - f(P - 2\Omega)]}{Q\sqrt{(P-\Omega)^2 - Q^2}}}_{I_{11}} \, . \tag{B.42}$$

Here the dimensionless kinetic kernel $\tilde{\mathcal{K}} = \mathcal{K}/2T^2$, where $\mathcal{K}$ has been defined in Eq. 4.10. We split up the integral in the following subregion amenable to analytic evaluation

$$I_{11} = \int_{-\infty}^{P/2} d\Omega [1 - f(P - 2\Omega)] \left\{ \Theta(1 - |\Omega|) \int_{|\Omega|}^{1} dQ \, [...] + \int_{\max(|\Omega|, 1)}^{P-\Omega} dQ \, [...] \right\} . \tag{B.43}$$

We find that the last integral contains an additional scale given by $P/(1 + \sqrt{2})$,

$$
\begin{aligned}
I_{11} = \int_{-\infty}^{+\infty} d\Omega [1 - f(P - 2\Omega)] &\left\{ \Theta(1 - |\Omega|) \int_{|\Omega|}^{1} dQ \, [...] \right. \\
&\left. + \Theta\left(\frac{P}{1 + \sqrt{2}} - \max(|\Omega|, 1) \right) \int_{\max(|\Omega|, 1)}^{(P-\Omega)/\sqrt{2}} dQ \, [...] + \int_{\max[(P-\Omega)/\sqrt{2}, |\Omega|, 1]}^{P-\Omega} dQ \, [...] \right\} .
\end{aligned} \tag{B.44}
$$

The first integral yields the known logarithmic divergence for small momentum transfer as in the case of the JSD in Appendix D,

$$J_{11} = \int_{|\Omega|}^{1} dQ \, \frac{\tilde{\mathcal{K}}(\Omega, Q)}{Q\sqrt{(P-\Omega)^2 - Q^2}} = \frac{\tilde{\mathcal{K}}(\Omega, Q \to \Omega^+)}{P - \Omega} \ln \frac{1}{|\Omega|} \, . \tag{B.45}$$

The second integral yields

$$
\begin{aligned}
J_{12} = \int_{\max(|\Omega|, 1)}^{(P-\Omega)/\sqrt{2}} dQ \, \frac{\tilde{\mathcal{K}}(\Omega, Q)}{Q\sqrt{(P-\Omega)^2 - Q^2}} &= \frac{e^{+\Omega}}{\sqrt{(P-\Omega)^2 - [\max(|\Omega|, 1)]^2}} \int_{\max(|\Omega|, 1)}^{(P-\Omega)/\sqrt{2}} \frac{\sqrt{2\pi} e^{-Q}}{\sqrt{Q}} \\
&= C \, P^{-1/2} \, ,
\end{aligned} \tag{B.46}
$$

where we used $\tilde{\mathcal{K}} = \sqrt{2\pi Q} e^{-(Q-\Omega)}$ for large momentum transfer and $Q > |\Omega|$. Furthermore, we assumed large momenta $P > 1$ in the last line. The last integral finally gives

$$J_{13} = \int_{\max[(P-\Omega)/\sqrt{2}, |\Omega|, 1]}^{P-\Omega} dQ \, \frac{\tilde{\mathcal{K}}(\Omega, Q)}{Q\sqrt{(P-\Omega)^2 - Q^2}} = \frac{\tilde{\mathcal{K}}(\Omega, Q \to \Omega^+)}{P - \Omega} \arccos \left[\frac{\max(1, |\Omega|, (P-\Omega)/\sqrt{2})}{P - \Omega} \right] , \tag{B.47}$$

For further integration over Ω we use the approximations for the kinetic kernel $\tilde{\mathcal{K}}$. Now that we have all contributions set we evaluate the scattering rate $\tau_{\varphi 1}|_{\text{intra}}$. We see that for high energies the contribution of J_{11} vanishes as $1/P$,

$$\int_{-1}^{+1} d\Omega \underbrace{[1 - f(P - 2\Omega)]}_{\simeq 1} \frac{\tilde{\mathcal{K}}(\Omega, Q \to \Omega^+)}{P - \Omega} \ln \frac{1}{|\Omega|} = \frac{2\tilde{\mathcal{K}}(, Q \to 0^+)}{P} \, . \tag{B.48}$$

The second integral gives the major contribution for $P > 1$, where

$$\int_{-\infty}^{P/(1+\sqrt{2})} \mathrm{d}\Omega \underbrace{[1 - f(P - 2\Omega)]}_{\simeq 1} C\, P^{-3/2} \simeq 2\sqrt{\pi}\, P^{-1/2}\,. \tag{B.49}$$

The contribution from the last integral, basically the peak at $\Omega \sim P/2$, is exponentially small, since

$$\int_{P/(1+\sqrt{2})}^{P/2} \mathrm{d}\Omega \underbrace{[1 - f(P - 2\Omega)]}_{\simeq 1} J_{13} = \frac{\sqrt{2\pi}2^{3/2}\mathrm{e}^{-P}}{\sqrt{P}} \int_{P/(1+\sqrt{2})}^{P/2} \mathrm{d}\Omega\, \frac{\sqrt{\Omega(P/2 - \Omega)}}{P - \Omega} \sim \sqrt{P}\,\mathrm{e}^{-P}\,. \tag{B.50}$$

Interband contribution to the scattering rate

The interband contribution to the decoherence rate $\tau_{\varphi,2}$ is much easier to calculate. Interestingly it is also the dominant contribution for large momenta. Whereas it vanishes for small momenta, where the intraband contribution is more dominant. The latter in turn vanishes essentially as $p^{-3/2}$ as we have seen above.

Again we write the integrals in dimensionless quantities $Q = q/2T$ and $\Omega = \omega/2T$ and $P = p/T$,

$$\tau_{\varphi,1}^{-1}(p)\Big|_{\mathrm{inter}} = \frac{N\alpha^2 T^2}{2p} \underbrace{\int_{P/2}^{P} \mathrm{d}\Omega \int_{|P-\Omega|}^{|\Omega|} \mathrm{d}Q\, \frac{\tilde{\mathcal{K}}(\Omega, Q)[1 - f(P - 2\Omega)]}{Q\sqrt{Q^2 - (P - \Omega)^2}}}_{I_{21}}\,. \tag{B.51}$$

We only need one integration region for the integral I_{21}, namely

$$I_{21} = \int_{P/2}^{P} \mathrm{d}\Omega\, [1 - f(P - 2\Omega)]J_{21}\,. \tag{B.52}$$

$$J_{21} = \int_{|P-\Omega|}^{|\Omega|} \mathrm{d}Q\, \frac{\tilde{\mathcal{K}}(\Omega, Q)}{Q\sqrt{Q^2 - (P - \Omega)^2}}\,. \tag{B.53}$$

In the case of interband transition we always have large momentum transfer since the dominant integration region is $\Omega \simeq P/2$. For higher energies the kernel is exponentially suppressed. Therefore the lower limits of integration in Eq. (B.53) fulfills $|P - \Omega| > 1$. In this limit we use again the asymptotics of the kinetic kernel $\mathcal{K} \simeq \pi Q^2/2$ for $\Omega > 0$. This yields,

$$J_{21} = \frac{\pi}{2} \int_{|P-\Omega|}^{|\Omega|} \frac{\mathrm{d}Q}{\sqrt{1 - (P - \Omega)^2/Q^2}} = \frac{\pi}{2}\sqrt{P(2\Omega - P)}\,. \tag{B.54}$$

So that we finally obtain

$$I_{21} = \frac{\pi}{2} \int_{P/2}^{P} \mathrm{d}\Omega\, \sqrt{P(2\Omega - P)}\mathrm{e}^{-(2\Omega - P)} = \frac{\pi^{3/2}P^{1/2}}{8}\,. \tag{B.55}$$

The dephasing time

We have seen that close to the Dirac point ($|\mu| \ll T$) the dominant contribution to the decoherence time comes from $\tau_{\varphi,1}$. The latter includes two contributions. First intraband scattering ($q > |\omega|$) and second interband scattering ($q < |\omega|$). We find that the latter is dominant for high energies. According to the result (B.55), and Eq. (B.51), the contribution to the rate τ_{φ}^{-1} from interband transitions reads,

$$\tau_{\varphi}^{-1}\Big|_{\text{inter}} = \frac{\alpha^2 \pi^{3/2} T^{3/2}}{4 p^{1/2}} \ . \tag{B.56}$$

On the other hand the contribution due to intraband decay according to the result (B.46) and (B.42), is given by

$$\tau_{\varphi}^{-1}\Big|_{\text{intra}} = \frac{\alpha^2 \, 4\pi^{1/2} \, T^{5/2}}{p^{3/2}} \ . \tag{B.57}$$

The decoherence time is not logarithmically enhanced. This is due to the Dirac electrons topology. More specifically, it is due to the overlap of eigenstates in different bands. In contrast to the usual scattering rates originating from the diagonal collision integral they suppress forward scattering in the decoherence time. In this way the off-diagonal collision integral is intrinsically protected from the forward scattering resonance in the collision integral due to Coulomb scattering.

Short laser pulses in graphene

In this Appendix we are going to apply the quantum kinetic equation to the problem of short laser pulses in graphene. We will in particular derive the formula (3.69) from the main text.

In this section we outline the calculation of the inversion after short laser pulse from Sec. 3.3. In addition to the noninteracting Bloch equations we also introduce a phenomenological dephasing rate Γ_2 and relaxation of the inversion Γ_1 towards its equilibrium values $\Delta\rho(-\infty)$. We start with the solution of the Bloch equations, which we write as

$$\partial_t \vec{S}(t) = [M_1 + M_2(t)]\vec{S}(t) + M_3[\Delta\rho(t_0)\hat{e}_3 - \vec{S}] \,. \tag{C.1}$$

Here we introduced the matrices

$$M_1 = \begin{pmatrix} -\Gamma_2 & \Delta_k & 0 \\ -\Delta_k & -\Gamma_2 & 0 \\ 0 & 0 & 0 \end{pmatrix} \,, \tag{C.2}$$

$$M_2(t) = \begin{pmatrix} 0 & 0 & 0 \\ 0 & 0 & -\frac{ek_y}{k^2}\,E_0(t) \\ 0 & +\frac{ek_y}{k^2}\,E_0(t) & 0 \end{pmatrix} \,, \tag{C.3}$$

and

$$M_3(t) = \begin{pmatrix} 0 & 0 & 0 \\ 0 & 0 & 0 \\ 0 & 0 & -\Gamma_1 \end{pmatrix} \,, \tag{C.4}$$

First, we introduce the deviation of the Bloch vector from its equilibrium value,

$$\vec{u} = \Delta\rho(t_0)\hat{e}_3 - \vec{S} \,, \tag{C.5}$$

for which $\vec{u}(t_0) = 0$ and

$$\partial_t \vec{u}(t) = [M_1 - M_3 + M_2(t)]\vec{u}(t) - \Delta\rho(t_0)M_2(t)\hat{e}_3 \,. \tag{C.6}$$

Now we transform into the interaction picture according to

$$\vec{u}(t) = e^{(M_1 - M_3)t}\vec{r}(t) \,. \tag{C.7}$$

The Bloch equations (C.1) in the interaction picture read

$$\partial_t \vec{r}(t) = M_2^I(t)\vec{r}(t) - \Delta\rho(-\infty)e^{-(M1-M_3)t}M_2(t)\hat{e}_3 \,. \tag{C.8}$$

and again $\vec{r}(0) = 0$. The last term can be rewritten as

$$e^{-(M1-M_3)t}M_2(t)\hat{e}_3 = M_2^I(t)\hat{e}_3\,e^{-\Gamma_1 t} \,, \tag{C.9}$$

so that we obtain

$$\partial_t \vec{r}(t) = M_2^I(t)[\vec{r}(t) - \Delta\rho(-\infty)\hat{e}_3\,e^{-\Gamma_1 t}] \,. \tag{C.10}$$

We see that in the limit $\Gamma_1 \to 0$ the inhomogeneity can simply be eliminated. The general homogeneous solution of Eq. (C.1) ($\Gamma_1 = 0$) is given by

$$\vec{r}_h = Texp\left(\int_{t_a}^t dt' M_2^I(t')\right)\vec{r}(t_a) = O(t,t_a)\vec{r}(t_a) \,. \tag{C.11}$$

We make the following ansatz for the solution of Eq. (C.1),

$$\vec{r}(t) = O(t,t_0)\vec{v}(t) \,, \tag{C.12}$$

with the boundary condition $\vec{v}(t_0) = 0$. We finally obtain for $\vec{v}(t)$,

$$\partial_t \vec{v}(t) = O(t_0,t)M_2^I(t)\hat{e}_3\Delta\rho(t_0)e^{-\Gamma_1 t} \,, \tag{C.13}$$

which has the solution

$$\vec{v}(t) = \int_{t_0}^t dt' O(t_0,t')M_2^I(t')e^{-\Gamma_1 t'}\Delta\rho(t_0)\hat{e}_3 \,. \tag{C.14}$$

Thus we obtain for the initial Bloch vector

$$\vec{S}(t) = \Delta\rho(t_0)\left(\hat{e}_3 - e^{+(M1-M_3)t}\int_{t_0}^t dt' e^{-\Gamma_1 t'}[O(t,t')M_2^I(t')\hat{e}_3]\right) \,. \tag{C.15}$$

Finally, partial integration in the last time integral yields

$$\vec{S}(t) = \Delta\rho(t_0)e^{+(M1-M_3)t}\left(O(t,t_0) + \Gamma_1\int_{t_0}^t dt' e^{-\Gamma_1 t'}O(t,t')\right)\hat{e}_3 \,. \tag{C.16}$$

We are now interested in the imaginary part of the polarization for which we have

$$\frac{\text{Im}[p(t)]}{\Delta\rho(t_0)} = \hat{e}_2^T\,e^{+(M1-M_3)t}\left(O(t,t_0) + \Gamma_1\int_{t_0}^t dt' e^{-\Gamma_1 t'}O(t,t')\right)\hat{e}_3 \,. \tag{C.17}$$

Writing out the time ordered exponential of the first part this yields

$$\hat{e}_2^T\,e^{+(M1-M_3)t}O(t,-\infty)\,\hat{e}_3 = e^{\Gamma_1 t}\sum_{k=0,(n=2k+1)}^{\infty}(-1)^{k+1}\left(\frac{ek_y}{k^2}\right)^n$$
$$\times \int_{-\infty}^t dt_n \int_{-\infty}^{t_n} dt_{n-1}\ldots\int_{-\infty}^{t_2} dt_1\,E(t_n)\cdot\ldots\cdot E(t_1)$$
$$\times e^{-(\Gamma_1+\Gamma_2)(t-t_n)}\cos[\Delta_k(t-t_n)]\times\cdots\times e^{-(\Gamma_1+\Gamma_2)(t_2-t_1)}\cos[\Delta_k(t_2-t_1)] \,. \tag{C.18}$$

The second part yields

$$\Gamma_1 \hat{e}_2^T \, e^{+(M1-M_3)t} \int_{t_0}^t dt' e^{-\Gamma_1 t'} O(t,t') \hat{e}_3 = \Gamma_1 \sum_{k=0,(n=2k+1)}^{\infty} (-1)^{k+1} \left(\frac{ek_y}{k^2} \right)^n$$
$$\times \int_{-\infty}^t dt' \int_{t'}^t dt_n \int_{t'}^{t_n} dt_{n-1} \ldots \int_{t'}^{t_2} dt_1 \, e^{+\Gamma_1(t-t')} \, E(t_n) \cdot \ldots \cdot E(t_1)$$
$$\times e^{-(\Gamma_1+\Gamma_2)(t-t_n)} \cos[\Delta_k(t-t_n)] \times \cdots \times e^{-(\Gamma_1+\Gamma_2)(t_2-t_1)} \cos[\Delta_k(t_2-t_1)] . \tag{C.19}$$

In the limit $\Delta_k \tau \to 0$ the following integrals can be evaluated ($t_0 = 0$):

$$\int_{-\infty}^t dt_n \int_{-\infty}^{t_n} dt_{n-1} \ldots \int_{-\infty}^{t_2} dt_1 \, E(t_n) \cdot \ldots \cdot E(t_1)$$
$$\times e^{-(\Gamma_1+\Gamma_2)(t-t_n)} \cos[\Delta_k(t-t_n)] \times \cdots \times e^{-(\Gamma_1+\Gamma_2)(t_2-t_1)} \cos[\Delta_k(t_2-t_1)]$$
$$\simeq e^{-(\Gamma_1+\Gamma_2)t} \cos[\Delta_k t] \int_{-\infty}^t dt_n \int_{-\infty}^{t_n} dt_{n-1} \ldots \int_{-\infty}^{t_2} dt_1 \, E(t_n) \cdot \ldots \cdot E(t_1) \tag{C.20}$$
$$= e^{-(\Gamma_1+\Gamma_2)t} \cos[\Delta_k t] \frac{1}{n!} \frac{1}{2^n} \left[1 + \mathrm{Erf} \left(\frac{t}{\sqrt{2}\tau} \right) \right]^n .$$

Therefore we have for $\Delta\tau \ll 1$ and $t > \tau$

$$\hat{e}_2^T \, e^{+(M1-M_3)t} O(t,-\infty) \, \hat{e}_3 = -\Theta(t) \sin \left(\frac{ek_y \bar{E}}{k^2} \right) \cos(\Delta t) e^{-(\Gamma_1+\Gamma_2)t} . \tag{C.21}$$

Here we have replaced

$$\frac{1}{2^n} \left[1 + \mathrm{Erf} \left(\frac{t}{\sqrt{2}\tau} \right) \right]^n \to \Theta(t) \tag{C.22}$$

The second part of the imaginary polarization, Eq. (C.17) yields

$$-\Theta(t) \sin \left(\frac{ek_y \bar{E}}{k^2} \right) \cos(\Delta t) \left[e^{-\Gamma_2 t} - e^{-(\Gamma_1+\Gamma_2)t} \right] . \tag{C.23}$$

Such that we obtain for the imaginary part of the polarization

$$\frac{\mathrm{Im}[p(t)]}{\Delta\rho(t_0)} = -\Theta(t) \cos(\Delta t) \sin \left(\frac{ek_y \bar{E}}{k^2} \right) e^{-\Gamma_2 t} \left(2 - e^{-\Gamma_1 t} \right) . \tag{C.24}$$

Inserting Eq. (C.24) into

$$\Delta\rho(t) - \Delta\rho(-\infty) = \frac{ek_y}{k^2} \int_{-\infty}^t dt' E^{-\Gamma_1(t-t')} E_0(t') \mathrm{Im}[p(t')] . \tag{C.25}$$

for the change in the inversion we obtain for $t - t_0 > \Delta\tau^2$ using again $\Delta\tau \ll 1$,

$$\frac{\Delta\rho(t) - \Delta\rho(-\infty)}{\Delta\rho(-\infty)} = -e^{-\Gamma_1 t} \left(\frac{ek_y \bar{E}}{k^2} \right) \sin \left(\frac{ek_y \bar{E}}{2k^2} \right) . \tag{C.26}$$

D

Calculation of the relaxation rate and the JSD from the Boltzmann equation

In this section we derive Eq. (4.7) for the JSD and the relaxation rates from the main text. Furthermore we give the asymptotics of the kinetic kernel.

D.1 Preliminaries

We start from a generic fermionic collision integral as introduced in Sec. 3.2.4,

$$St[f(\lambda, \vec{p})] = \sum_{\lambda_3} \int \frac{\mathrm{d}^2 p_3}{(2\pi)^2} \left\{ W(\lambda, \vec{p}|\lambda_3, \vec{p}_3) f_{\lambda_3}(\vec{p}_3)[1 - f_\lambda(\vec{p})] - W(\lambda_3, \vec{p}_3|\lambda, \vec{p}) f_\lambda(\vec{p})[1 - f_{\lambda_3}(\vec{p}_3)] \right\}, \quad \text{(D.1)}$$

where the transition rates for the Coulomb interaction

$$W(\vec{p}_2, \lambda_2|\vec{p}_1, \lambda_1) = (2\pi)^{-1} \sum_{\lambda_3, \lambda_4} \int \mathrm{d}\vec{p}_{3,4} \int \mathrm{d}\vec{q}\mathrm{d}\omega \delta(\lambda_2 p_2 + \omega - \lambda_1 p_1) \delta(\lambda_4 p_4 - \omega - \lambda_3 p_3)$$
$$\times \delta(\vec{p}_2 + \vec{q} - \vec{p}_1) \delta(\vec{p}_4 - \vec{q} - \vec{p}_3) |M(\vec{q}, \omega, \{\lambda_i\}, \{\vec{v}_i\})|^2 \, f(\vec{p}_3, \lambda_3)[1 - f(\vec{p}_4, \lambda_4)]. \quad \text{(D.2)}$$

Here the interaction kernel

$$|M(\vec{q}, \omega, \{\lambda_i\}, \{\vec{v}_i\})|^2 = N|V(\omega, q)|^2 \Theta_{1,2} \Theta_{3,4}, \quad \text{(D.3)}$$

contains the RPA screened Coulomb matrix element (see Sec. 1.2.2)

$$|V(\omega, q)|^2 = \frac{4\pi^2 \alpha_g^2}{(q + 2\pi\alpha_g N \mathrm{Re}\Pi)^2 + (2\pi\alpha_g N \mathrm{Im}\Pi)^2}, \quad \text{(D.4)}$$

as well as the Dirac factors $(\vec{v}_i = \lambda_i \vec{k}_i/k_i)$ $\Theta_{1,2} = (1 + \vec{v}_1 \cdot \vec{v}_2)/2$. Upon inserting the ansatz (4.1) from the main text, Sec. 4.3.2, into the collision integral (D.1), we obtain the explicit expression for the relaxation rate

$$\Gamma = \sum_{\lambda_1} \int \frac{\mathrm{d}^2 k}{(2\pi)^2} \, W_0(\lambda_1, \vec{k}| + 1, \vec{p})[1 - f_{\lambda_1}(\vec{k})] + W_0(+1, \vec{p}|\lambda_1, \vec{k}) f_{\lambda_1}(\vec{k}). \quad \text{(D.5)}$$

For $\omega < \varepsilon_p$, where interband processes are forbidden, the second term in Eq. (D.6) can be dropped. Using Eqs. (D.2)-(D.3) we then obtain

$$
\Gamma = (2\pi)^2 \sum_{\lambda_{1,3,4}} \int \frac{\mathrm{d}^2 q}{(2\pi)^2} \frac{\mathrm{d}\omega}{2\pi} \frac{\mathrm{d}^2 k_4}{(2\pi)^2} \, \delta(\lambda_2 |\vec{p} - \vec{q}| + \omega - p) \delta(\lambda_4 k_4 - \omega - \lambda_3 |\vec{k}_4 - \vec{q}|)
$$
$$
\times N |V_{RPA}(\omega, q)|^2 \, \Theta_{1,2} \Big|_{1=(\lambda_1, \vec{p}-\vec{q})} \Theta_{3,4} \Big|_{3=(\lambda_3, \vec{k}_4-\vec{q})} \, f_T(\lambda_4 k_4 - \omega)[1 - f_T(\lambda_4 k_4)] \, .
$$
(D.6)

Next we perform the angular integration in the integrals over $\vec{k}_4$ and $\vec{q}$. The arising functional determinants are ($\lambda = +1$),

$$
\left| \frac{\partial}{\partial \varphi_q} \lambda_2 |\vec{p} - \vec{q}| \right| = \frac{pq |\sin(\varphi_q - \varphi_p)|}{|\vec{p} + \vec{q}|} = \frac{\sqrt{q^2 - \omega^2}[(\omega - 2\lambda p)^2 - q^2]^{1/2}}{2|\lambda p - \omega|} \, ,
$$
(D.7)

$$
\left| \frac{\partial}{\partial \varphi_4} \lambda_3 |\vec{k}_4 - \vec{q}| \right| = \frac{k_4 q |\sin(\varphi_4 - \varphi_q)|}{|\vec{k}_4 - \vec{q}|} = \frac{\sqrt{q^2 - \omega^2}[(\omega - 2\lambda_4 k_4)^2 - q^2]^{1/2}}{2|\lambda_4 k_4 - \omega|} \, .
$$
(D.8)

The corresponding Dirac factors are ($\lambda_1 = \lambda = +1$)

$$
\Theta_{1,2} = \frac{1}{2} \left(1 + \frac{\lambda_1 \lambda_2 \vec{k}_1 \cdot (\vec{p} - \vec{q})}{k_1 |\vec{p} - \vec{q}|} \right) = \frac{|(\omega - 2\lambda p)^2 - q^2|}{4p |\lambda p - \omega|} \, ,
$$
(D.9)

$$
\Theta_{3,4} = \frac{1}{2} \left(1 + \frac{\lambda_2 \lambda_3 \vec{k}_4 \cdot (\vec{k}_4 - \vec{q})}{k_4 |\vec{k}_4 - \vec{q}|} \right) = \frac{|(\omega - 2\lambda_4 k_4)^2 - q^2|}{4k_4 |\lambda_4 k_4 - \omega|} \, .
$$
(D.10)

D.2 The JSD $P(\omega)$

Putting together Eqs. (D.6)-(D.10) we finally obtain the JSD

$$
P(\omega) = \int_0^\infty \mathrm{d}q \, \frac{q \, \mathrm{Re} \sqrt{\mathrm{sign}(q^2 - \omega^2)[(\omega - 2\lambda p)^2 - q^2]}}{2p} \frac{N |V(\omega, q)|^2}{|q^2 - \omega^2|} \mathcal{K}(\omega, q) \, .
$$
(D.11)

Here the kinetic kernel is given by Eq. (D.13) below and was also introduced in Sec. 4.3.2. If we assume $p \gg \omega, q$ we obtain the result (4.7) stated in the main text,

$$
P(\omega) = \int_{|\omega|}^\infty \mathrm{d}q \, q \, \frac{N |V(\omega, q)|^2}{|q^2 - \omega^2|} \mathcal{K}(\omega, q) \, .
$$
(D.12)

In the following we again use the dimensionless variables $\Omega = \omega/2T$, $Q = q/2T$, $\beta = \omega/q$ and $\tilde{\mu} = \mu/T$. We also give the asymptotics of the kinetic kernel

$$
\mathcal{K}(\Omega, Q) = 2T^2 \mathrm{e}^\Omega \int_{-\infty}^{+\infty} \mathrm{d}\xi \, \frac{\mathrm{Re}[\mathrm{sign}(1 - |\beta|)(\xi^2 - Q^2)]^{1/2}}{4 \cosh \frac{\xi - \Omega - \tilde{\mu}}{2} \cosh \frac{\xi + \Omega - \tilde{\mu}}{2}} \, ,
$$
(D.13)

for all integration regions. Remember that the kinetic kernel $\mathcal{K}$ roughly describes the phase space of scattering and is connected to the vertex function $\Gamma^{(0)}$ defined in Eq. (E.43) in Appendix E. The asymptotic are summarized in Tab. D.1. Using the asymptotics for the RPA bubble from Sec. 1.2.2 and the asymptotics of the kinetic kernel from Tab. D.1 we obtain limiting expressions for the JSD $P(\Omega)$ presented below for various regimes of temperature, chemical potential and frequency.

$|\tilde{\mu}| \gg 1$	$\beta < 1$		$\beta > 1$	
	$Q \ll \tilde{\mu}$	$Q \gg \tilde{\mu}$	$Q \ll \tilde{\mu}$	$Q \gg \tilde{\mu}$
$\mathcal{K}$	$4T^2\Omega|\tilde{\mu}|(1+\coth\Omega)$	$2T^2\sqrt{2\pi Q}\mathrm{e}^{-(1-\beta)Q}$	$T^2\pi Q^2\mathrm{e}^{-(1-\mathrm{sign}(\Omega))|\Omega|}$	$T^2\pi Q^2\mathrm{e}^{-(1-\mathrm{sign}(\Omega))|\Omega|}$
$|\tilde{\mu}| \ll 1$	$\beta < 1$		$\beta > 1$	
	$Q \ll 1$	$Q \gg 1$	$Q \ll 1$	$Q \gg 1$
$\mathcal{K}$	$4T^2\ln 2\mathrm{e}^{\beta Q}$	$2T^2\sqrt{2\pi Q}\mathrm{e}^{-(1-\beta)Q}$	$T^2\pi Q^2\mathrm{e}^{-(1-\mathrm{sign}(\Omega))|\Omega|}$	$T^2\pi Q^2\mathrm{e}^{-(1-\mathrm{sign}(\Omega))|\Omega|}$

Table D.1: *The asymptotics of the kinetic kernel* (D.13) *expressing the phase space for the thermal electrons participating at the scattering event.*

D.2.1 The limit $T \gg |\mu|$ for $|\Omega| < 1$

The contribution for small momentum transfer ($Q < 1$) reads,

$$P(\Omega)\Big|_{Q<1} = 4\ln 2\,\alpha_g^2\pi^2 N\mathrm{e}^{\Omega}\int_{|\Omega|}^1 \mathrm{d}Q\,\frac{Q}{|Q^2-\Omega^2|(Q+\alpha_g N\ln 2)^2+(\alpha_g N\ln 2\Omega)^2} = \frac{4\pi^2}{N\ln 2}\ln\frac{\alpha_g N\ln 2}{|\Omega|}\,. \tag{D.14}$$

Here the last equality is valid for $|\Omega| < \alpha_g N\ln 2$. The contribution to the JSD with large momentum transfer ($Q > 1$) for frequencies $|\Omega| < 1$ is,

$$P(\Omega)\Big|_{Q>1} = 2\alpha_g^2\pi^2 N\mathrm{e}^{\Omega}\int_1^{\infty}\mathrm{d}Q\,\frac{\sqrt{2\pi}Q^{3/2}\mathrm{e}^{-Q}}{(\sqrt{Q^2-\Omega^2}Q+\alpha_g\pi NQ^2/16)^2+(\alpha_g\pi N\mathrm{e}^{-Q}\sqrt{Q/2\pi})^2}\,. \tag{D.15}$$

The latter can be neglected for $|\Omega| < \alpha_g$.

D.2.2 The limit $T \gg \mu|$ for $|\Omega| > 1$ ($Q > 1$)

For $|\Omega| > 1$, where only intraband transitions with $Q > 1$ are possible, the JSD reads,

$$P(\Omega) = 2\alpha_g^2\pi^2 N\mathrm{e}^{\Omega}\int_{|\Omega|}^{\infty}\mathrm{d}Q\,\frac{\sqrt{2\pi}Q^{3/2}\mathrm{e}^{-Q}}{(\sqrt{Q^2-\Omega^2}Q+\alpha_g\pi NQ^2/16)^2+(\alpha_g\pi N\mathrm{e}^{-Q}\sqrt{Q/2\pi})^2} \simeq \frac{2^9\sqrt{2\pi}}{N}\,|\Omega|^{-5/2}\,, \tag{D.16}$$

where the asymptotics is valid for $|\Omega| \gg 1$.

D.2.3 The limit $|\mu| \gg T$ for $|\Omega| < |\tilde{\mu}|$ ($Q < |\tilde{\mu}|$)

$$P(\Omega) = 4\alpha_g^2\pi^2 N\,\Omega|\tilde{\mu}|(1+\coth(\Omega))\int_{|\Omega|}^{|\tilde{\mu}|}\mathrm{d}Q\,\frac{Q}{(Q^2-\Omega^2)(Q+\alpha_g N|\tilde{\mu}|/2)^2+(\alpha_g N\tilde{\mu}\Omega/2)^2}\,. \tag{D.17}$$

Equation (D.17) can be integrated analytically, similar to Eq. (D.14), yielding a lengthy expression. For brevity we give the limit for $|\Omega| \ll \alpha_g|\mu|$,

$$P(\Omega) \simeq \frac{1}{32\pi}\frac{\ln\alpha_g N|\mu/2\Omega|}{|\mu|^2}\,. \tag{D.18}$$

D.2.4 The limit $|\mu| \gg T$ for $|\Omega| > |\tilde{\mu}|$ ($Q > |\tilde{\mu}|$)

As in the case $|\tilde{\mu}| \ll 1$, here for $|\Omega| > |\tilde{\mu}|$ the JSD is determined by scattering with large momentum transfer,

$$P(\Omega) = 2\alpha_g^2 \pi^2 N \, \mathrm{e}^{+\Omega} \int_{|\Omega|}^{\infty} \mathrm{d}Q \, \frac{\sqrt{2\pi} Q^{3/2} \mathrm{e}^{-Q}}{(\sqrt{Q^2 - \Omega^2} Q + \alpha_g \pi N Q^2/16)^2} \simeq \frac{2^9 \sqrt{2\pi}}{N} |\Omega|^{-5/2} . \tag{D.19}$$

D.3 The relaxation rate Γ

D.3.1 The limit $T \gg |\mu|$

We first calculate the relaxation rate for $T \gg |\mu|$. We find that the contribution from the region with $Q > 1$ is of order α_g^2, whereas $|\Omega| < 1$ yields the leading contribution $\propto \alpha_g$:

$$\Gamma/2T = \int_0^{\alpha N \ln 2} \mathrm{d}\Omega \, P(\Omega) \Big|_{Q<1} + \int_{\alpha N \ln 2}^1 \mathrm{d}\Omega \, P(\Omega) \Big|_{Q<1} . \tag{D.20}$$

Here, $P(\Omega)\Big|_{Q<1}$ is given by Eq. (D.14) and we anticipate that the integrand contains the scale $\alpha_g N \ln 2$ that separates the logarithmic divergence at small frequency from the rest. The first part in Eq. (D.20) yields,

$$\begin{aligned}
\int_0^{\alpha_g N \ln 2} \mathrm{d}\Omega \, P(\Omega) \Big|_{Q<1} &= 4\ln 2 \, \alpha_g^2 \pi^2 N \int_0^{\alpha_g N \ln 2} \mathrm{d}\Omega \left\{ \frac{1}{(\alpha_g N \ln 2)^2} \ln \frac{\alpha_g N \ln 2}{|\Omega|} + \int_{\alpha_g N \ln 2}^1 \mathrm{d}Q \frac{1}{Q(Q^2 - \Omega^2)} \right\} \\
&= 4\alpha_g \pi^2 (1 + \ln 2) .
\end{aligned} \tag{D.21}$$

The second part in Eq. (D.20) yields

$$\int_{\alpha_g N \ln 2}^1 \mathrm{d}\Omega P(\Omega) \Big|_{Q<1} = 4\ln 2 \alpha_g^2 \pi^2 N \int_{\alpha_g N \ln 2}^1 \mathrm{d}\Omega \frac{\mathrm{arccot}(\alpha_g N \ln 2\Omega) - \arctan(\Omega/\alpha_g N \ln 2)}{2\alpha_g N \ln 2\Omega} = 4\alpha_g \pi^2 G/2, \tag{D.22}$$

where $G = 0.916$ is the Catalan constant. Together, Eqs. (D.21) and (D.22) yield the result (4.11) from the main text.

D.3.2 The limit $|\mu| \gg T$

In the case $|\mu| \gg T$ we find that the rate Γ is determined by small energy and momentum transfer, $|\Omega|, Q < \alpha_g N |\tilde{\mu}|/2$.

$$\Gamma = 2T \int_0^{\alpha_g N |\tilde{\mu}|/2} \mathrm{d}\Omega \left(\frac{\alpha_g N |\tilde{\mu}|}{2} \right)^{-2} \int_{|\Omega|}^{\alpha_g N |\tilde{\mu}|/2} \frac{\mathrm{d}Q}{Q} = 8\alpha_g \pi^2 |\mu| . \tag{D.23}$$

Appendix E

E

Calculations for the collision-dominated hydrodynamics in graphene

In this Appendix we give more details on the calculations for the collision dominated hydrodynamics in graphene. These include explicit expressions for all relevant scattering rates to calculate the dissipative corrections to the currents and the viscosity as introduced in the main text.

E.1 Derivation of the hydrodynamic equations

E.1.1 The continuity equations of the densities

Integrating the Boltzmann equation with respect to $\int \mathrm{d}^2 p...$, one obtains

$$\partial_t n_+ + \nabla \cdot \int \frac{\mathrm{d}^2 p}{(2\pi)^2} \hat{v} f_{+,\vec{p}} + e\vec{E} \cdot \int \frac{\mathrm{d}^2 p}{(2\pi)^2} \nabla_p f_{+,\vec{p}} + e \int \frac{\mathrm{d}^2 p}{(2\pi)^2} (\hat{v} \times \vec{B}) \cdot \nabla_p f_{+,\vec{p}} = 0 \,. \tag{E.1}$$

The terms that are proportional to the electric and the magnetic field drop out such that we obtain

$$\partial_t n_+ + \nabla \cdot \frac{1}{2}(\vec{j} + \vec{j}_I) = 0 \,. \tag{E.2}$$

Similarly we get

$$\partial_t n_- + \nabla \cdot \frac{1}{2}(-\vec{j} + \vec{j}_I) = 0 \,. \tag{E.3}$$

From these two equations one obtains the continuity equations for the charge and imbalance density from the main text.

For the energy density we integrate the Boltzmann equation with respect to $\int \mathrm{d}^2 p\, p...$, and obtain

$$\partial_t n_{E,+} + \nabla \cdot \int \frac{\mathrm{d}^2 p}{(2\pi)^2} \varepsilon \hat{v} f_{+,\vec{p}} + e\vec{E} \cdot \int \frac{\mathrm{d}^2 p}{(2\pi)^2} \varepsilon \nabla_p f_{+,\vec{p}} + e \int \frac{\mathrm{d}^2 p}{(2\pi)^2} \varepsilon (\hat{v} \times \vec{B}) \cdot \nabla_p f_{+,\vec{p}} = \int \frac{\mathrm{d}^2 p}{(2\pi)^2} \frac{|\varepsilon|}{2} St[f] \,. \tag{E.4}$$

The term proportional to the magnetic field drops out. Partial integration in the term proportional to the electric field yields

$$\partial_t n_{E,+} + \nabla \cdot \frac{1}{2}(\vec{j}_E + \vec{j}_{E,I}) - e\vec{E} \cdot \frac{1}{2}(\vec{j} + \vec{j}_I) = ... \,. \tag{E.5}$$

Here $\vec{j}_E = \vec{j}_{E,+} - \vec{j}_{E,-}$ and $\vec{j}_{E,I} = \vec{j}_{E,+} + \vec{j}_{E,-}$. Together with the equation for $n_{E,-}$ one obtains the continuity equation from the main text. In this case the finite collision integral on the right-hand site vanishes in the final continuity equation.

E.1.2 The equations of motion for the currents

Averageing the Boltzmann equation with respect to $\int \mathrm{d}^2 p\,\hat{v}...$ we get (α and β are Cartesian indices),

$$\partial_t \frac{1}{2}(\vec{j} + \vec{j}_I)_\alpha + \nabla_\beta \int \frac{\mathrm{d}^2 p}{(2\pi)^2}\,\hat{v}_\alpha \hat{v}_\beta f_{+,\vec{p}} + eE_\beta \int \frac{\mathrm{d}^2 p}{(2\pi)^2}\,\hat{v}_\alpha \nabla_{p,\beta} f_{+,\vec{p}} = \int \frac{\mathrm{d}^2 p}{(2\pi)^2}\,\hat{v}_\alpha\,St[f]\,. \qquad (E.6)$$

Here the term proportional to the magnetic field droped out. Similarly we obtain

$$\partial_t \frac{1}{2}(\vec{j}_I - \vec{j})_\alpha + \nabla_\beta \int \frac{\mathrm{d}^2 p}{(2\pi)^2}\,\hat{v}_\alpha \hat{v}_\beta (1 - f_{-,\vec{p}}) + eE_\beta \int \frac{\mathrm{d}^2 p}{(2\pi)^2}\,\hat{v}_\alpha \nabla_{p,\beta}(1 - f_{-,\vec{p}}) = -\int \frac{\mathrm{d}^2 p}{(2\pi)^2}\,\hat{v}_\alpha\,St[f]\,. \quad (E.7)$$

If we subtract both equations we obtain the equation of motion for the electric current. Partial integration in the term proportional to the electric field and some algebraic manipulation yields

$$\partial_t \vec{j}_\alpha + \nabla_\beta \Pi_{\alpha\beta} - eE_\beta \partial_{\mu_0}(\delta_{\alpha\beta}n - \Pi_{\alpha\beta}) = \int \frac{\mathrm{d}^2 p}{(2\pi)^2}\,\hat{v}_\alpha\,St[f]\,. \qquad (E.8)$$

Similarly adding Eqs. (E.6) and (E.7), yields

$$\partial_t \vec{j}_{I,\alpha} + \nabla_\beta \Pi_{I,\alpha\beta} - eE_\beta \partial_{\mu_0}(\delta_{\alpha\beta}n_I - \Pi_{I,\alpha\beta}) = \int \frac{\mathrm{d}^2 p}{(2\pi)^2}\,\hat{v}_\alpha\,St[f]\,. \qquad (E.9)$$

E.1.3 Local equilibrium and equations of state

We use the local equilibrium ansatz

$$f_{\lambda,\vec{p}} = \frac{1}{1 + \mathrm{e}^{\beta(\varepsilon_{\lambda p} - \mu_\lambda - \vec{u}\cdot\vec{p})}}\,, \qquad (E.10)$$

to obtain the equations of state.

$$n_+ = \int_0^{+\infty} \frac{\mathrm{d}\varepsilon\,\varepsilon}{2\pi} \int_{-\pi}^{+\pi} \frac{\mathrm{d}\varphi}{2\pi}\,f_{+,\vec{p}}\,. \qquad (E.11)$$

Shifting the momentum $\vec{p}$ yields

$$n_+ = \int_{-\pi}^{+\pi} \frac{\mathrm{d}\varphi}{2\pi} \frac{1}{(1 - u\cos\varphi)^2} \int_0^{+\infty} \mathrm{d}p\,\frac{p}{2\pi}\,\left[f_{+,\vec{p}}\right]_{\vec{u}=0}\,. \qquad (E.12)$$

We can perform the angular integration and obtain

$$n_+ = (1 - u^2)^{-3/2}\left(\frac{-T^2}{2\pi}\mathrm{Li}_2(-\mathrm{e}^{+\beta\mu_+})\right) = (1 - u^2)^{-3/2}\,n_{+,0}\,. \qquad (E.13)$$

Similarly we obtain expressions for

$$n_- = \int_{-\infty}^0 \frac{\mathrm{d}\varepsilon\,|\varepsilon|}{2\pi} \int_{-\pi}^{+\pi} \frac{\mathrm{d}\varphi}{2\pi}\,(1 - f)\,. \qquad (E.14)$$

From which we get $n = n_+ - n_-$ and $n_I = n_+ + n_-$.

For the energy density of electrons and holes one obtains

$$n_{E,+} = \int_0^{+\infty} \frac{\mathrm{d}\varepsilon\,\varepsilon^2}{2\pi} \int_{-\pi}^{+\pi} \frac{\mathrm{d}\varphi}{2\pi}\,f = \frac{2+u^2}{2(1-u^2)^{5/2}} \left(\frac{-2T^3}{2\pi}\right) \mathrm{Li}_3(-\mathrm{e}^{+\beta\mu_+})\,, \tag{E.15}$$

and

$$n_{E,-} = \int_{-\infty}^0 \frac{\mathrm{d}\varepsilon\,(-\varepsilon^2)}{2\pi} \int_{-\pi}^{+\pi} \frac{\mathrm{d}\varphi}{2\pi}\,(1-f) = -\frac{2+u^2}{2(1-u^2)^{5/2}} \left(\frac{-2T^3}{2\pi}\right) \mathrm{Li}_3(-\mathrm{e}^{-\beta\mu_-})\,. \tag{E.16}$$

The total energy density than reads as $n_E = n_{E,+} - n_{E,-}$.

Finally we calculate the equation of state for the energy current as well as the electric and imbalance current. In the case of the electric and imbalance current we only calculate the hydrodynamic part without dissipative corrections here. The dissipative corrections are discussed in the main text. For the electric current due to electrons we get

$$\vec{j}_+ = \int_0^{+\infty} \frac{\mathrm{d}k\,k}{2\pi} \int_{-\pi}^{+\pi} \frac{\mathrm{d}\varphi}{2\pi}\,\frac{\vec{k}}{|\vec{k}|}\,f_{+,\vec{k}} = n_+\vec{u}\,, \tag{E.17}$$

whereas holes contribute

$$\vec{j}_- = -\int_0^{+\infty} \frac{\mathrm{d}k\,k}{2\pi} \int_{-\pi}^{+\pi} \frac{\mathrm{d}\varphi}{2\pi}\,\frac{\vec{k}}{|\vec{k}|}\,(1-f_{-,\vec{k}}) = n_-\vec{u}\,. \tag{E.18}$$

From this we get $\vec{j} = \vec{j}_+ + \vec{j}_-$ and $\vec{j}_I = \vec{j}_+ - \vec{j}_-$.

The equation of state for the energy current that is in particular used to replace the energy current by the hydrodynamic velocity field $\vec{u}$ is obtained from the relations

$$\vec{j}_{+,E} = \int_0^{+\infty} \frac{\mathrm{d}k\,k}{2\pi} \int_{-\pi}^{+\pi} \frac{\mathrm{d}\varphi}{2\pi}\,\vec{k}\,f_{+,\vec{k}}\,, \tag{E.19}$$

$$\vec{j}_{-,E} = \int_0^{+\infty} \frac{\mathrm{d}k\,k}{2\pi} \int_{-\pi}^{+\pi} \frac{\mathrm{d}\varphi}{2\pi}\,\vec{k}\,(1-f_{-,\vec{k}})\,. \tag{E.20}$$

From these we obtain the total energy current according to $\vec{j}_E = \vec{j}_{E,+} - \vec{j}_{E,-}$. This yields the desired

$$\vec{j}_E = \frac{3n_E\vec{u}}{2+u^2}\,, \tag{E.21}$$

from the main text.

E.2 Linear response functions

In linear response we linearize the hydrodynamic equations with respect to the linear fluctuations δn, δn_I, δn_E, δu, in the hydrodynamic quantities,

$$n \to n + \delta n\,, \tag{E.22}$$
$$n_I \to n_I + \delta n_I\,, \tag{E.23}$$
$$n_E \to n_E + \delta n_E\,, \tag{E.24}$$
$$u \to \delta u\,. \tag{E.25}$$

We furthermore introduce the response functions to the external perturbation $\vec{E}$

$$\delta n = \chi_n E \,, \tag{E.26}$$
$$\delta n_I = \chi_I E \,, \tag{E.27}$$
$$\delta n_E = \chi_E E \,, \tag{E.28}$$
$$\delta u = \chi_u E \,, \tag{E.29}$$
$$\tag{E.30}$$

The electrical conductivity in linear response for an infinite system follows from $\delta j = en\delta u + \delta\nu$, for which we obtain

$$\sigma = \sigma_0 + en\chi_u + \frac{ieq}{3n_E}\left[\tau_1 n + \tau_2 n_I\right] - \frac{ieq}{2}\left[\tau_1\chi_n + \tau_2\chi_I\right] \,. \tag{E.31}$$

The linear response functions are finally obtained from the matrix equation

$$\begin{pmatrix} -\mathrm{i}\omega + \frac{\tau_2}{2}\,q^2 & +\frac{\tau_2}{2}\,q^2 & -\left(\frac{n\tau_1+n_I\tau_2}{3n_E}\right)q^2 & +\mathrm{i}qn \\ +\frac{\tau_3}{2}\,q^2 & -\mathrm{i}\omega + \frac{\tau_4}{2}\,q^2 & -\left(\frac{n_I\tau_4+n\tau_3}{3n_E}\right)q^2 & +\mathrm{i}qn_I \\ 0 & 0 & -\mathrm{i}\omega & \frac{3}{2}\mathrm{i}n_E\,q \\ 0 & 0 & +\frac{\mathrm{i}}{3n_E}\,q & -\mathrm{i}\omega + \tau_d^{-1} + \frac{2\eta}{3n_E}\,q^2 \end{pmatrix}\begin{pmatrix} \chi_n \\ \chi_I \\ \chi_E \\ \chi_u \end{pmatrix} = \begin{pmatrix} -\mathrm{i}\frac{q\sigma_0}{e} \\ -\mathrm{i}\frac{q\sigma_0^*}{e} \\ 0 \\ \frac{2en}{3n_E} \end{pmatrix}, \tag{E.32}$$

that follows from the linearized hydrodynamic equations. Inverting the matrix in Eq. (E.32) and using the resulting susceptibilities in Eq. (E.31) yields the results (5.57) and (5.58) from the main text.

E.3 Vector-Vertex functions and transport rates

In this section we will give explicit expressions for the scattering times τ_{ij} constituting the matrix collision integral in the space of macroscopic currents, Eq. (5.52) in the main text, appearing in the EOM (5.51) of the currents. We recall that the EOM for the particle and imbalance current is obtained by averaging the BE with respect to the particle velocity $\hat{v}$ and the direction of momentum $\lambda\hat{v}$. Therefore the right-hand side of the defining equation (5.51) is equal to

$$\mathcal{C}_J\begin{pmatrix} \delta\vec{j} \\ \delta\vec{j}_I \end{pmatrix} = \begin{pmatrix} (\hat{v},\mathcal{C}\delta f^{(1)}) \\ (\lambda\hat{v},\mathcal{C}\delta f^{(1)}) \end{pmatrix} = \sum_{j=1}^{3} h_\beta^{(j)}\begin{pmatrix} (\hat{v},\mathcal{C}\phi_j\hat{v}_\beta/T) \\ (\lambda\hat{v},\mathcal{C}\phi_j\hat{v}_\beta/T) \end{pmatrix} \,. \tag{E.33}$$

The scalar product $(\cdot,\cdot)$ was defined in Eq. (5.23). Since $\phi_3\hat{v} = \varepsilon\hat{v} = \vec{p}$ and the momentum is conserved under electron-electron collisions the term for $j = 3$ drops out. Furthermore, note that the dissipative corrections to the macroscopic currents can be defined in a very compact form as

$$\delta\vec{j}_k = \left(\phi_k\hat{v}, -\delta f^{(1)}\partial_\varepsilon f^{(0)}\right), \tag{E.34}$$

with the modes (5.9), and here we labeled the corrections to the macroscopic currents as

$$\delta\vec{j}_k = \begin{cases} \delta\vec{j}\,, k=1 \\ \delta\vec{j}_I\,, k=2 \\ T^{-1}\delta\vec{j}_E\,, k=3 \end{cases}. \tag{E.35}$$

With this notation there is an easy relation between the coefficients $h_\alpha^{(j)}$ that parametrize the corrections to the distribution function, Eq. (5.7), and $\delta j_{k,\alpha}$. This relations reads as

$$\delta j_{k,\alpha} = \sum_{j=1}^{3} h_\beta^{(j)} \left(\phi_k \hat{v}_\alpha, -\phi_j \hat{v}_\beta \partial_\varepsilon f^{(0)}/T \right) = \frac{1}{2} \sum_{j=1}^{3} h_\alpha^{(j)} \left(\phi_k, -\phi_j \partial_\varepsilon f^{(0)}/T \right) = \sum_{j=1}^{3} \mathcal{M}_{kj} h_\alpha^{(j)} \,. \qquad \text{(E.36)}$$

We used the fact that the matrix elements of the linearized collision integral are diagonal in the Cartesian indices α, β. Therefore no summation over the Cartesian index α is implied in Eq. (E.36) and we defined

$$\mathcal{M}_{kj} = \frac{1}{2} \left(\phi_k, -\phi_j \partial_\varepsilon f^{(0)}/T \right) \,. \qquad \text{(E.37)}$$

Using the inverse of Eq. (E.36) in Eq. (E.33), we obtain

$$\underline{\mathcal{C}}_J \begin{pmatrix} \delta\vec{j}_\alpha \\ \delta\vec{j}_{I,\alpha} \end{pmatrix} = \sum_{k=1}^{2} \sum_{j=1}^{2} [\mathcal{M}^{-1}]_{jk} \begin{pmatrix} (\hat{v}_\alpha, \mathcal{C}\phi_j \hat{v}_\alpha/T) \\ (\lambda \hat{v}_\alpha, \mathcal{C}\phi_j \hat{v}_\alpha/T) \end{pmatrix} \delta\vec{j}_{k,\alpha} + \sum_{j=1}^{2} [\mathcal{M}^{-1}]_{j3} \begin{pmatrix} (\hat{v}_\alpha, \mathcal{C}\phi_j \hat{v}_\alpha/T) \\ (\lambda \hat{v}_\alpha, \mathcal{C}\phi_j \hat{v}_\alpha/T) \end{pmatrix} \delta\vec{j}_{E,\alpha} \,.$$
$$\text{(E.38)}$$

Let us drop the last term for now. It will ultimately correspond to a renormalization of the hydrodynamic velocity $\vec{u}$ in the local fluid rest frame and is therefore zero due to the LL-condition. If we thus disregard the second term on the right-hand side of Eq. (E.38), we can immediately read off

$$[\underline{\mathcal{C}}_J]_{lk} = \tau_{lk}^{-1} = \sum_{j=1}^{2} [\mathcal{M}^{-1}]_{jk} (\phi_l \hat{v}_\alpha, \mathcal{C}\phi_j \hat{v}_\alpha/T^2) \,. \qquad \text{(E.39)}$$

We now discuss the second term in Eq. (E.38). Using the expression (E.39) for the collision integral and applying its inverse to Eq. (E.38), we obtain for the right-hand side

$$\begin{pmatrix} \delta\vec{j}_\alpha \\ \delta\vec{j}_{I,\alpha} \end{pmatrix} + \frac{2}{3n_E} \begin{pmatrix} n \\ n_I \end{pmatrix} \delta\vec{j}_{E,\alpha} \,. \qquad \text{(E.40)}$$

Motivated by Eq. (5.50) for small velocity and using the fact that also $\delta n_E = 0$, we introduce the shift of the hydrodynamic velocity $\delta\vec{u}$ via

$$\delta\vec{j}_{E,\alpha} = \frac{3n_E}{2} \delta\vec{u} \,. \qquad \text{(E.41)}$$

From this relation it becomes clear that the second term in Eq. (E.40) is just a shift of the local hydrodynamic velocity field, which however was ruled out by the LL-conditions. From another perspective one can always add or subtract the LL-conditions $\delta\vec{j}_E = 0$ to the collision integral an thus eliminate the second term on the right-hand side of Eq. (E.38).

From Eq. (E.39) we see that in order to calculate the τ_{lk} we need to evaluate the matrix elements $(\phi_l \hat{v}_\alpha, \mathcal{C}\phi_j \hat{v}_\alpha/T^2)$. In order to prepare for the following section we review a method to calculate these matrix elements, given in Refs. [42, 155]. This method relies on the fact that in the integrated electron-electron collision integral, i.e. in the matrix elements $(\phi_l \hat{v}_\alpha, \mathcal{C}\phi_j \hat{v}_\alpha/T^2)$, the summation over scattering states $\{|\lambda, \vec{k}\rangle, |\lambda', \vec{k}'\rangle\}$ and $\{|\nu, \vec{p}\rangle, |\nu', \vec{p}'\rangle\}$ separates and the matrix elements take the form

$$(\phi v_\alpha, \mathcal{C}\phi' v_\beta/T^2) = \frac{1}{16\pi} \int d\omega \int d^2 q \frac{|V(\omega,q)|^2}{\sinh^2(\omega/2T)} \left[\Gamma_{\phi\phi',\alpha\beta}^{(2)}(\omega,q) \Gamma^{(0)}(\omega,q) - \Gamma_{\phi,\alpha}^{(1)}(\omega,q) \Gamma_{\phi',\beta}^{(1)}(\omega,q) \right] \,.$$
$$\text{(E.42)}$$

Here the vertex functions are defined as $[\lambda' = \mathrm{sign}(\varepsilon_{\lambda,p} + \omega)]$,

$$\Gamma^{(0)}(\omega, q) = \frac{1}{T} \int_{\lambda, \vec{p}} \delta(\varepsilon_{\lambda,p} - \varepsilon_{\lambda',\vec{p}+\vec{q}} + \omega) \left(f^{(0)}_{\lambda,p} - f^{(0)}_{\lambda',\vec{p}+\vec{q}} \right) \Theta_{\lambda\vec{p};\lambda',\vec{p}+\vec{q}}, \tag{E.43}$$

$$\Gamma^{(1)}_{\phi,\alpha}(\omega, q) = \frac{1}{T} \int_{\lambda, \vec{p}} \delta(\varepsilon_{\lambda,p} - \varepsilon_{\lambda',\vec{p}+\vec{q}} + \omega) \left(f^{(0)}_{\lambda,p} - f^{(0)}_{\lambda',\vec{p}+\vec{q}} \right) \Theta_{\lambda,\vec{p};\lambda',\vec{p}+\vec{q}} \left[\phi_{\lambda',\vec{p}+\vec{q}} \hat{v}_{\lambda',\vec{p}+\vec{q}} - \phi_{\lambda\vec{p}} \hat{v}_{\lambda\vec{p}} \right]_\alpha, \tag{E.44}$$

$$\Gamma^{(2)}_{\phi\phi',\alpha\beta} = \frac{1}{T} \int_{\lambda, \vec{p}} \delta(\varepsilon_{\lambda,p} - \varepsilon_{\lambda',\vec{p}+\vec{q}} + \omega) \left(f^{(0)}_{\lambda,p} - f^{(0)}_{\lambda',\vec{p}+\vec{q}} \right) \Theta_{\lambda,\vec{p};\lambda',\vec{p}+\vec{q}}$$
$$\times \left[\phi_{\lambda',\vec{p}+\vec{q}} \hat{v}_{\lambda',\vec{p}+\vec{q}} - \phi_{\lambda\vec{p}} \hat{v}_{\lambda\vec{p}} \right]_\alpha \left[\phi'_{\lambda',\vec{p}+\vec{q}} \hat{v}_{\lambda',\vec{p}+\vec{q}} - \phi'_{\lambda\vec{p}} \hat{v}_{\lambda\vec{p}} \right]_\beta. \tag{E.45}$$

The here defined scattering times and matrix elements of the collision integral are relate to the times τ_{ee}, τ_s and τ_{ss} defined in Ref. [42] in the following way:

$$\tau_{ee}^{-1} = (\hat{v}_\alpha, \mathcal{C}\hat{v}_\alpha), \tag{E.46}$$

$$\tau_s^{-1} = (\lambda\hat{v}_\alpha, \mathcal{C}\hat{v}_\alpha), \tag{E.47}$$

$$\tau_{ss}^{-1} = (\lambda\hat{v}_\alpha, \lambda\mathcal{C}\hat{v}_\alpha). \tag{E.48}$$

In the Fermi liquid limit the scattering rates vanish, whereas at the Dirac point $\tau_s^{-1} = 0$. The decomposition into the vertex functions has a simple diagrammatic interpretation illustrated in Fig. E.1. The product $\Gamma^{(1)}_\alpha \Gamma^{(1)}_\beta$ represents the drag or Aslamazov-Larkin type diagram in the Boltzmann limit [156]. Whereas the product $\Gamma^{(0)} \Gamma^{(2)}_{\alpha\beta}$ contains self-energy corrections [diagram b) in Fig. E.1] as well as Maki-Thompson type diagrams [c) in Fig. E.1].
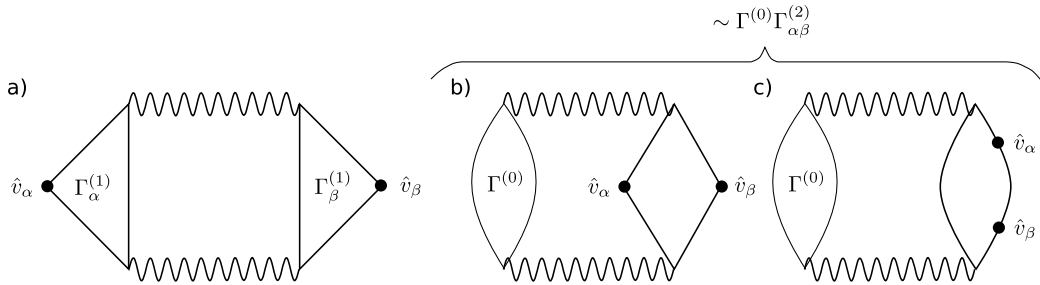

Figure E.1: *a) The diagrammatic correspondence of the term $\Gamma^{(1)}_\alpha \Gamma^{(1)}_\beta$, the Aslamazov-Larkin type diagram. The diagrammatic representation of the product $\Gamma^{(0)} \Gamma^{(2)}_{\alpha\beta}$, that contains self-energy corrections b) as well as Maki-Thompson type diagrams c).*

E.4 Tensor-Vertex functions and viscosity

In this section we are going to give expressions for the collision integral for the energy-stress tensors, and show how the formalism of the vector vertex functions from the preceding section can be generalized for the stress tensors, yielding ultimately the viscosity in graphene. The stress tensors were defined according to

$$\Pi^{(l)}_{\alpha\beta} = \int_{\lambda\vec{k}} \phi_l \, \hat{v}_\alpha \hat{v}_\beta \, f_{\lambda\vec{k}}. \tag{E.49}$$

Here the modes ϕ_l where defined in Eq. (5.9) in the main text. The tensor equations acquire a finite collision integral since they are not hydrodynamic quantities. This collision integral mixes the stress tensors from Eq. (E.49) in the equation of motion

$$(\phi_l \hat{v}_\alpha \hat{v}_\beta, \mathcal{L}f) = -(\phi_l \hat{v}_\alpha \hat{v}_\beta, \mathcal{C}\delta f) = [\underline{\mathcal{C}}_\pi]_{lk} \delta\Pi_{\alpha\beta}^{(k)} \,. \tag{E.50}$$

Here the matrix collision integral $\underline{C}_\pi$ is given by

$$\underline{\mathcal{C}}_\pi \begin{pmatrix} \delta\Pi_{\alpha\beta} \\ \delta\Pi_{I,\alpha\beta} \\ T^{-1}\delta\Pi_{E,\alpha\beta} \end{pmatrix} = \begin{pmatrix} (\hat{v}_\alpha \hat{v}_\beta, \mathcal{C}\delta f^{(2)}) \\ (\lambda \hat{v}_\alpha \hat{v}_\beta, \mathcal{C}\delta f^{(2)}) \\ (\varepsilon \hat{v}_\alpha \hat{v}_\beta / T, \mathcal{C}\delta f^{(2)}) \end{pmatrix} = \sum_{j=1}^{3} g_{\alpha\beta}^{(j)} \begin{pmatrix} (\hat{v}_\alpha \hat{v}_\beta, \mathcal{C}\phi_j \hat{v}_\alpha \hat{v}_\beta / T^2) \\ (\lambda \hat{v}_\alpha \hat{v}_\beta, \mathcal{C}\phi_j \hat{v}_\alpha \hat{v}_\beta / T^2) \\ (\varepsilon \hat{v}_\alpha \hat{v}_\beta / T, \mathcal{C}\phi_j \hat{v}_\alpha \hat{v}_\beta / T^2) \end{pmatrix} \,. \tag{E.51}$$

We used that the matrix elements $(\phi \hat{v}_\alpha \hat{v}_\beta, \mathcal{C}\phi' \hat{v}_\gamma \hat{v}_\delta / T^2)$ are diagonal in Cartesian indices, i.e.

$$(\phi \hat{v}_\alpha \hat{v}_\beta, \mathcal{C}\phi' \hat{v}_\gamma \hat{v}_\delta / T^2) \to \delta_{\alpha\gamma} \delta_{\beta\delta} \,. \tag{E.52}$$

Therefore no summation over α and β is implied in Eq. (E.51). From these equations we obtain the compact expression for the dissipative corrections of the stress tensors in terms of the coefficients $g_{\alpha\beta}^{(l)}$ defining the deviations from equilibrium,

$$\delta\Pi_{\alpha\beta}^{(k)} = \left(\phi_k \hat{v}_\alpha \hat{v}_\beta, -\delta f^{(2)} \partial_\varepsilon f^{(0)} \right) \,. \tag{E.53}$$

Using the representation of the fluctuations $\delta f^{(2)}$, Eq. (5.8),

$$\begin{aligned} \delta\Pi_{\alpha\beta}^{(k)} &= \sum_{j=1}^{3} g_{\gamma\nu}^{(j)} \left(\phi_k \hat{v}_\alpha \hat{v}_\beta, -\phi_j \hat{v}_\gamma \hat{v}_\nu \partial_\varepsilon f^{(0)} / T^2 \right) \\ &= \frac{1}{4} \sum_{j=1}^{3} g_{\alpha\beta}^{(j)} \left(\phi_k, -\phi_j \partial_\varepsilon f^{(0)} / T^2 \right) = \frac{1}{2T} \sum_{j=1}^{3} \mathcal{M}_{kj} g_{\alpha\beta}^{(j)} \end{aligned} \,. \tag{E.54}$$

Here we encounter again the matrix $\mathcal{M}$ given in Eqs. (E.37). We then use this expression in the collision integral (E.51). We note that the coefficients $g_{\alpha\beta}^{(j)}$ are traceless and thus

$$g_{\alpha\beta}^{(j)} \hat{v}_\alpha \hat{v}_\beta = g_{\alpha\beta}^{(j)} (\hat{v}_\alpha \hat{v}_\beta - \delta_{\alpha\beta}/2) = g_{\alpha\beta}^{(j)} I_{\alpha\beta} \,, \tag{E.55}$$

where

$$I_{\alpha\beta} = I_{\alpha\beta,\vec{k}} = \sqrt{2} \left(\hat{v}_\alpha \hat{v}_\beta - \frac{1}{2}\delta_{\alpha\beta} \right) \,, \tag{E.56}$$

with $\text{tr}[I] = 0$. We then obtain

$$\underline{\mathcal{C}}_\pi \begin{pmatrix} \delta\Pi_{\alpha\beta} \\ \delta\Pi_{I,\alpha\beta} \\ T^{-1}\delta\Pi_{E,\alpha\beta} \end{pmatrix} = \sqrt{2}T \sum_{j=1}^{3} \sum_{k=1}^{3} [\mathcal{M}^{-1}]_{jk} \delta\Pi_{\alpha\beta}^{(k)} \begin{pmatrix} (\hat{v}_\alpha \hat{v}_\beta, \mathcal{C}\phi_j I_{\alpha\beta} / T^2) \\ (\lambda \hat{v}_\alpha \hat{v}_\beta, \mathcal{C}\phi_j I_{\alpha\beta} / T^2) \\ (\varepsilon \hat{v}_\alpha \hat{v}_\beta / T, \mathcal{C}\phi_j I_{\alpha\beta} / T^2) \end{pmatrix} \,. \tag{E.57}$$

From this we see that

$$[\underline{C}_\pi]_{lk} = T \sum_{j=1}^{3} [\mathcal{M}^{-1}]_{jk} (\phi_l \hat{v}_\alpha \hat{v}_\beta, \mathcal{C}\phi_j I_{\alpha\beta} / T^2) \,. \tag{E.58}$$

As we mentioned above, the trace of the collision integral in Cartesian indices (Greek subscript α, β) vanishes we can even write,

$$[\underline{C}_\pi]_{lk} = 2T \sum_{j=1}^{3} [\mathcal{M}^{-1}]_{jk} (\phi_l I_{\alpha\beta}, \mathcal{C}\phi_j I_{\alpha\beta}/T^2) \,. \tag{E.59}$$

In order to obtain the collision integral $\mathcal{C}_\pi$, we thus have to calculate the matrix elements $(\phi_l I_{\alpha\beta}, \mathcal{C}\phi_j I_{\alpha\beta}/T^2)$. Due to the symmetries of the collision integral it holds $(\phi_l I_{\alpha\beta}, \mathcal{C}\phi_j I_{\alpha\beta}/T^2) = (\phi_l \hat{v}_\alpha \hat{v}_\beta, \mathcal{C}\phi_j \hat{v}_\alpha \hat{v}_\beta/T^2)$. Similarly to the preceding section the computation can be simplified by the introduction of vertex functions. In fact, the matrix elements can be written as

$$(\phi I_{\alpha\beta}, \mathcal{C}\phi' I_{\gamma\delta}/T^2) = \frac{1}{16\pi} \int d\omega \int d^2q \, \frac{|V(\omega,q)|^2}{\sinh^2(\omega/2T)} \left[\Xi^{(2)}_{\phi\phi',\alpha\beta\gamma\delta}(\omega,q)\Gamma^{(0)}(\omega,q) - \Xi^{(1)}_{\phi,\alpha\beta}(\omega,q)\Xi^{(1)}_{\phi',\gamma\delta}(\omega,q) \right]. \tag{E.60}$$

Here we introduced the tensor vertex functions $[\lambda' = \text{sign}(\varepsilon_{\lambda,\vec{p}} - \omega)]$,

$$\Xi^{(1)}_{\phi,\alpha\beta}(\omega,q) = \frac{1}{T} \int_{\lambda,\vec{p}} \delta(\varepsilon_{\lambda,p} - \varepsilon_{\lambda',\vec{p}+\vec{q}} + \omega) \left(f^{(0)}_{\lambda,p} - f^{(0)}_{\lambda',\vec{p}+\vec{q}} \right) \Theta_{\lambda,\vec{p};\lambda',\vec{p}+\vec{q}} \left[\phi_{\lambda',\vec{p}+\vec{q}} I_{\alpha\beta,\vec{p}+\vec{q}} - \phi_{\lambda\vec{p}} I_{\alpha\beta,\vec{p}} \right], \tag{E.61}$$

$$\begin{aligned} \Xi^{(2)}_{\phi\phi',\alpha\beta\gamma\delta}(\omega,q) = \frac{1}{T} \int_{\lambda,\vec{p}} \delta(\varepsilon_{\lambda,p} - \varepsilon_{\lambda',\vec{p}+\vec{q}} + \omega) \left(f^{(0)}_{\lambda,p} - f^{(0)}_{\lambda',\vec{p}+\vec{q}} \right) \Theta_{\lambda,\vec{p};\lambda',\vec{p}+\vec{q}} \\ \times \left[\phi_{\lambda',\vec{p}+\vec{q}} I_{\alpha\beta,\vec{p}+\vec{q}} - \phi_{\lambda\vec{p}} I_{\alpha\beta,\vec{p}} \right] \left[\phi'_{\lambda',\vec{p}+\vec{q}} I_{\gamma\delta,\vec{p}+\vec{q}} - \phi'_{\lambda\vec{p}} I_{\gamma\delta,\vec{p}} \right]. \end{aligned} \tag{E.62}$$

For further calculations it is useful to express the tensor $I_{\alpha\beta}$ in terms of the basis vectors $\{\hat{q} = \vec{q}/q, \hat{q}_\perp = \hat{z} \times \hat{q}\}$,

$$I_{\alpha\beta} = A_{\vec{k},\vec{q}}(2\hat{q}_\alpha \hat{q}_\beta - \delta_{\alpha\beta}) + B_{\vec{k},\vec{q}}(\hat{q}_{\perp,\alpha}\hat{q}_\beta + \hat{q}_\alpha \hat{q}_{\perp,\beta}) \,, \tag{E.63}$$

where

$$A_{\vec{k},\vec{q}} = \sqrt{2}\left(\frac{(\vec{k}\cdot\vec{q})^2}{(kq)^2} - 1 \right) + \frac{1}{\sqrt{2}} = \tilde{A}_{\vec{k},\vec{q}} + \frac{1}{\sqrt{2}} \,, \tag{E.64}$$

$$B_{\vec{k},\vec{q}} = \sqrt{2}\frac{(\vec{k}\cdot\vec{q}_\perp)(\vec{k}\cdot\vec{q})}{k^2 q^2} \,. \tag{E.65}$$

Due to the conservation laws of the electron-electron interaction we effectively have $A \to \tilde{A}$. Using the δ-function in Eqs. (E.61) and (E.62) one obtains $(\varepsilon = \varepsilon_{\lambda,k})$,

$$\tilde{A}_{\vec{k},\vec{q}} = (\omega^2 - q^2) \frac{(2\varepsilon + \omega)^2 - q^2}{4\sqrt{2}\varepsilon^2 q^2} \,. \tag{E.66}$$

Furthermore, the coefficient B drops out in the vertex function $\Xi^{(1)}$ since it is antisymmetric in the angle between $\vec{q}$ and $\vec{k}$. In the tensor vertex function $\Xi^{(2)}_{\alpha\beta\gamma\delta}(\omega,q)$ we get a separate contribution from A and B but they are orthogonal. For B we obtain with the help of the δ-functions $(\varepsilon = \varepsilon_{\lambda,k})$,

$$B_{\vec{k},\vec{q}} = \text{sign}(\vec{k}\cdot\hat{q}_\perp) \frac{\sqrt{(q^2 - \omega^2)[(2\varepsilon + \omega)^2 - q^2]}\,(\omega^2 - q^2 - 2\varepsilon\omega)}{2\sqrt{2}\varepsilon^2 q^2} \,. \tag{E.67}$$

Finally, with the help of the angular averages

$$\int \mathrm{d}\varphi_q \, \hat{q}_\alpha \hat{q}_\beta \hat{q}_\gamma \hat{q}_\delta = \frac{\pi}{4}(\delta_{\alpha\gamma}\delta_{\beta\delta} + \delta_{\alpha\delta}\delta_{\beta\gamma} + \delta_{\alpha\beta}\delta_{\gamma\delta}) \,, \tag{E.68}$$

$$\int \mathrm{d}\varphi_q \, (2\hat{q}_\alpha \hat{q}_\beta - \delta_{\alpha\beta})(2\hat{q}_\gamma \hat{q}_\delta - \delta_{\gamma\delta}) = \pi(\delta_{\alpha\gamma}\delta_{\beta\delta} + \delta_{\alpha\delta}\delta_{\beta\gamma} - \delta_{\alpha\beta}\delta_{\gamma\delta}) \,, \tag{E.69}$$

$$\int \mathrm{d}\varphi_q \, (\hat{q}_{\perp,\alpha}\hat{q}_\beta + \hat{q}_\alpha\hat{q}_{\perp,\beta})(\hat{q}_{\perp,\gamma}\hat{q}_\delta + \hat{q}_\gamma\hat{q}_{\perp,\delta}) = \pi(\delta_{\alpha\gamma}\delta_{\beta\delta} + \delta_{\alpha\delta}\delta_{\beta\gamma} - \delta_{\alpha\beta}\delta_{\gamma\delta}) \,, \tag{E.70}$$

and the projected $\Xi^{(1,2)}$ obtained after averaging over the angle φ_q of the transfered momentum $\vec{q}$,

$$\Xi_\phi^{(1)}(\omega,q) = \frac{1}{T}\int_{\lambda,\vec{p}} \delta(\varepsilon_{\lambda,p} - \varepsilon_{\lambda',\vec{p}+\vec{q}} + \omega)\left(f_{\lambda,p}^{(0)} - f_{\lambda',\vec{p}+\vec{q}}^{(0)}\right)\Theta_{\lambda,\vec{p};\lambda',\vec{p}+\vec{q}}\left[\phi_{\lambda',\vec{p}+\vec{q}}\tilde{A}_{\vec{k}+\vec{q},\vec{q}} - \phi_{\lambda\vec{p}}\tilde{A}_{\vec{k},\vec{q}}\right] \,, \tag{E.71}$$

$$\Xi_{\parallel,\phi\phi'}^{(2)}(\omega,q) = \frac{1}{T}\int_{\lambda,\vec{p}} \delta(\varepsilon_{\lambda,p} - \varepsilon_{\lambda',\vec{p}+\vec{q}} + \omega)\left(f_{\lambda,p}^{(0)} - f_{\lambda',\vec{p}+\vec{q}}^{(0)}\right)\Theta_{\lambda,\vec{p};\lambda',\vec{p}+\vec{q}}$$
$$\times \left[\phi_{\lambda',\vec{p}+\vec{q}}\tilde{A}_{\vec{p}+\vec{q},\vec{q}} - \phi_{\lambda\vec{p}}\tilde{A}_{\vec{p},\vec{q}}\right]\left[\phi'_{\lambda',\vec{p}+\vec{q}}\tilde{A}_{\vec{p}+\vec{q},\vec{q}} - \phi'_{\lambda\vec{p}}\tilde{A}_{\vec{p},\vec{q}}\right] \,, \tag{E.72}$$

$$\Xi_{\perp,\phi\phi'}^{(2)}(\omega,q) = \frac{1}{T}\int_{\lambda,\vec{p}} \delta(\varepsilon_{\lambda,p} - \varepsilon_{\lambda',\vec{p}+\vec{q}} + \omega)\left(f_{\lambda,p}^{(0)} - f_{\lambda',\vec{p}+\vec{q}}^{(0)}\right)\Theta_{\lambda,\vec{p};\lambda',\vec{p}+\vec{q}} \tag{E.73}$$
$$\times \left[\phi_{\lambda',\vec{p}+\vec{q}}B_{\vec{p}+\vec{q},\vec{q}} - \phi_{\lambda\vec{p}}B_{\vec{p},\vec{q}}\right]\left[\phi'_{\lambda',\vec{p}+\vec{q}}B_{\vec{p}+\vec{q},\vec{q}} - \phi'_{\lambda\vec{p}}B_{\vec{p},\vec{q}}\right] \,, \tag{E.74}$$

we can write the matrix elements for the viscosity as

$$(\phi I_{\alpha\beta}, \mathcal{C}\phi' I_{\gamma\delta}/T^2) = (\delta_{\alpha\gamma}\delta_{\beta\delta} + \delta_{\alpha\delta}\delta_{\beta\gamma} - \delta_{\alpha\beta}\delta_{\gamma\delta})\frac{1}{16\pi}\int \mathrm{d}\omega \int \mathrm{d}^2q \, \frac{|V(\omega,q)|^2}{\sinh^2(\omega/2T)}$$
$$\times \left[\Xi_{\parallel,\phi\phi'}^{(2)}(\omega,q)\Gamma^{(0)}(\omega,q) + \Xi_{\perp,\phi\phi'}^{(2)}(\omega,q)\Gamma^{(0)}(\omega,q) - \Xi_\phi^{(1)}(\omega,q)\Xi_{\phi'}^{(1)}(\omega,q)\right] \,. \tag{E.75}$$

Here we can drop the terms proportional to $\delta_{\alpha\beta}$ since the energy stress tensors are traceless. Due to their symmetry in $\alpha \leftrightarrow \beta$ we effectively have

$$\delta_{\alpha\gamma}\delta_{\beta\delta} + \delta_{\alpha\delta}\delta_{\beta\gamma} - \delta_{\alpha\beta}\delta_{\gamma\delta} \to 2\delta_{\alpha\gamma}\delta_{\beta\delta} \,. \tag{E.76}$$

F Appendix F

Hydrodynamic equations on the staggered grid

In this appendix we give explicit expressions for the finite difference derivatives on the staggered grid which was explained in Sec. 5.6.2. We also give expressions for the conservation laws of energy that are used to check the numerical simulations. Furthermore we briefly discuss the implementation of the implicit scheme.

F.1 The discrete Navier-Stokes equation for graphene

For the numerical simulations it is advantageous to use instead of the velocity u_α the scaled velocity

$$\tilde{u}_\alpha = \frac{3u_\alpha}{2 + u^2} \,. \tag{F.1}$$

From this it follows that $u_\alpha = \tilde{u}_\alpha f(\tilde{u})$ where

$$f(\tilde{u}) = \frac{3 - \sqrt{9 - 8\tilde{u}^2}}{2\tilde{u}^2} \,. \tag{F.2}$$

Let for now n and m denote the indices of the spatial grid point and the index i gives the time step. The we will also write for the function f explicitly f_{nm}^i. We will write in the following

$$\vec{\tilde{u}} = \begin{pmatrix} u \\ v \end{pmatrix} \,. \tag{F.3}$$

We first give expressions for the finite-difference version of the Euler limit of the Navier-Stokes equation (5.55) from the main text. This means we drop the dissipative terms for now. As described in the main text the second order gradients are implemented implicitly and thus discussed below in Sec. F.3. The dissipative terms including linear terms are easily implement analogous to the convective terms. The discretization follows the scheme put forward in Ref. [131]. The spacial discretization in x-direction is given by δx and by δy in y-direction. The subscripts i and j denote the discrete grid index on the

staggered grid depicted in Fig. 5.2. The finite-difference Navier-Stokes equation reads as

$$
\begin{aligned}
\partial_t u_{ij} = \frac{1}{n_E} \Bigg\{ & u_{ij} \left(\frac{\hat{n}_{E,i+1,j}^{(1)} u_{i+1,j} - \hat{n}_{E,ij}^{(1)} u_{ij}}{\delta x} + \frac{\hat{n}_{E,i+1,j}^{\otimes} v_{i+1,j}^{\otimes} - \hat{n}_{E,ij}^{\otimes} u_{ij}^{\otimes}}{\delta x} \right) \\
& - \frac{1}{\delta x} \left[\frac{n_{E,ij} \hat{u}_{ij}^2 \left(3 - \sqrt{9 - 8(\hat{u}_{ij}^2 + \hat{v}_{ij}^2)^2} \right)}{2(\hat{u}_{ij}^2 + \hat{v}_{ij}^2)} - \frac{n_{E,i-1,j} \hat{u}_{i-1,j}^2 \left(3 - \sqrt{9 - 8(\hat{u}_{i-1,j}^2 + \hat{v}_{i-1,j}^2)^2} \right)}{2(\hat{u}_{i-1,j}^2 + \hat{v}_{i-1,j}^2)} \right] \\
& - \frac{1}{\delta y} \Bigg[\frac{\hat{n}_{E,i,j+1}^{\otimes} \hat{u}_{i,j+1}^{\otimes} \hat{v}_{i,j+1}^{\otimes} \left(3 - \sqrt{9 - 8\left([\hat{u}_{i,j+1}^{\otimes}]^2 + [\hat{v}_{i,j+1}^{\otimes}]^2\right)^2} \right)}{2\left([\hat{u}_{i,j+1}^{\otimes}]^2 + [\hat{v}_{i,j+1}^{\otimes}]^2\right)} \\
& \qquad - \frac{\hat{n}_{E,i,j}^{\otimes} \hat{u}_{i,j+1}^{\otimes} \hat{v}_{i,j+1}^{\otimes} \left(3 - \sqrt{9 - 8\left([\hat{u}_{ij}^{\otimes}]^2 + [\hat{v}_{ij}^{\otimes}]^2\right)^2} \right)}{2\left([\hat{u}_{ij}^{\otimes}]^2 + [\hat{v}_{ij}^{\otimes}]^2\right)} \Bigg] \\
& + e E_{x,ij} n_{ij}^{(1)} - u_{ij} \left(E_{x,ij} i_{ij} + \hat{E}_{y,ij}^{(2)} \hat{v}_{ij}^{(2)} \right) e \hat{n}_{ij}^{(1)} \frac{3 - \sqrt{9 - 8\left(u_{ij}^2 + [\hat{v}^{(2)}]^2\right)}}{2\left(u_{ij}^2 + [\hat{v}^{(2)}]^2\right)} \Bigg\} = F_u[...] \,.
\end{aligned}
\tag{F.4}
$$

Here we introduced the following averages on the staggered grid:

$$
\hat{u}_{ij} = \frac{u_{i+1,j} + u_{ij}}{2} \,,
\tag{F.5}
$$

$$
\hat{v}_{ij} = \frac{v_{i+1,j} + v_{i,j-1}}{2} \,,
\tag{F.6}
$$

$$
\hat{n}_{E,i,j} = \frac{n_{E,i-1,j} + n_{E,ij}}{2} \,,
\tag{F.7}
$$

$$
\hat{v}_{ij}^{(2)} = \frac{v_{ij} + v_{i,j-1} + v_{i-1,j} + v_{i-1,j-1}}{4} \,,
\tag{F.8}
$$

$$
\hat{u}_{ij}^{(2)} = \frac{u_{ij} + u_{i+1,j} + u_{i,j+1} + u_{i+1,j+1}}{4} \,,
\tag{F.9}
$$

$$
\hat{n}_{E,ij}^{\otimes} = \frac{n_{ij} + n_{i-1,j} + n_{i,j-1} + n_{i-1,j+1}}{4} \,,
\tag{F.10}
$$

$$
\hat{u}_{i,j+1}^{\otimes} = \frac{u_{i,j+1} + u_{ij}}{2} \,,
\tag{F.11}
$$

$$
\hat{v}_{i,j+1}^{\otimes} = \frac{v_{ij} + u_{i-1,j}}{2} \,.
\tag{F.12}
$$

The equation for v looks analogous. The continuity equations are discretized in the standard manner. The finite-difference equation for the particle density reads as

$$
\begin{aligned}
\partial_t n_{ij} = -\frac{1}{\delta x} &\left[\frac{n_{i+1,j} + n_{ij}}{2} \frac{3 - \sqrt{9 - 8\left(u_{i+1,j}^2 + [\hat{v}_{i+1,j}^{(2)}]^2\right)}}{2\left(u_{i+1,j}^2 + [\hat{v}_{i+1,j}^{(2)}]^2\right)} u_{i+1,j} \right. \\
&\left. - \frac{n_{ij} + n_{i-1,j}}{2} \frac{3 - \sqrt{9 - 8\left(u_{ij}^2 + [\hat{v}_{ij}^{(2)}]^2\right)}}{2\left(u_{ij}^2 + [\hat{v}_{ij}^{(2)}]^2\right)} u_{ij} \right] \\
-\frac{1}{\delta x} &\left[\frac{n_{i,j+1} + n_{ij}}{2} \frac{3 - \sqrt{9 - 8\left([\hat{u}_{ij}^{(2)}]^2 + v_{ij}^2\right)}}{2\left([\hat{u}_{ij}^{(2)}]^2 + v_{ij}^2\right)} v_{ij} \right. \\
&\left. - \frac{n_{ij} + n_{i,j-1}}{2} \frac{3 - \sqrt{9 - 8\left([\hat{u}_{i,j-1}^{(2)}]^2 + v_{i,j-1}^2\right)}}{2\left([\hat{u}_{i,j-1}^{(2)}]^2 + v_{i,j-1}^2\right)} v_{i,j-1} \right] = F_n[...] .
\end{aligned}
\tag{F.13}
$$

The continuity equations for the energy density and the imbalance density are analogous.

F.2 Conservation of energy

In the absence of dissipative terms the energy and in either case with or without dissipative terms the particle number is conserved. Using the expression

$$
eE_\alpha n = \partial t(n_E \tilde{u}_\alpha) + \nabla_\beta \Pi_{\alpha\beta} ,
\tag{F.14}
$$

for the electrical, which is obtained from the equation for the energy current without dissipative terms, in the continuity equation for the energy one obtains

$$
\partial_t \int dV \, n_E = \int dV \, n_E [\partial_t \tilde{u}] \frac{3 - \sqrt{9 - 8\tilde{u}}}{2\tilde{u}} .
\tag{F.15}
$$

Here we integrated the resulting equation over the volume of the system. Therefore without dissipative terms the total energy, i.e. the integral

$$
E = \int dV \, n_E \left(1 - \frac{1}{2} \left[\ln\left(3 + \sqrt{9 - 8\tilde{u}^2}\right) - \sqrt{9 - 8\tilde{u}^2} \right] \right) ,
\tag{F.16}
$$

is conserved. As long as boundary effects can be neglected the energy (F.16) is well preserved by the numerical simulation scheme employed for the hydrodynamic simulation in Chapt. 5.

F.3 The second order gradients - the semi-implicit scheme

We consider finite differences in time and space now. we use the subscripts n and m for the position of the spatial grid point and the index i for the time step. The difference in two time steps is denoted

δt and we assume $\delta x = \delta y = \delta l$. If we include the finite viscosity η in the Navier-Stokes equation and parametrize the viscous terms by a backward Euler scheme as explained in the main text the finite-difference equation for the velocity component u from Eq. (F.3) reads as

$$u_{nm}^{i+1}\left(1 + \frac{\eta \delta t}{n_E \delta l^2}\, 4 f_{nm}^i\right) - \frac{\eta \delta t}{n_E \delta l^2}\left(f_{n+1,m}^i u_{n+1,m}^{i+1} + f_{n-1,m}^i u_{n-1,m}^{i+1}\right)$$
$$- \frac{\eta \delta t}{n_E \delta l^2}\left(f_{n,m+1}^i u_{n,m+1}^{i+1} + f_{n,m-1}^i u_{n,m-1}^{i+1}\right) = F_u[...]\,. \tag{F.17}$$

Here the right-hand site $F_u[...]$ stands for the finite-difference on the staggered grid given by Eq. (F.4). It is now obvious that Eq. (F.17) is a tridiagonal matrix equation for the velocity component u. Similarly the matrix equation for v is obtained. Both have to be solved in the hydrodynamic simulations in Chapt. 5 in conjunction with the continuity equations. In the latter the coupled diffusion between imbalance and particle density makes it necessary to solve the coupled matrix equation that is schematically depicted in the following equation:

$$\begin{pmatrix} \mathbf{M}_1 & \mathbf{M}_2 & 0 \\ \mathbf{M}_3 & \mathbf{M}_4 & 0 \\ 0 & 0 & \mathbb{I} \end{pmatrix} \begin{pmatrix} \overline{\overline{n}} \\ \overline{\overline{n}}_I \\ \overline{\overline{n}}_E \end{pmatrix} = \begin{pmatrix} \overline{F}_n[...] \\ \overline{F}_I[...] \\ \overline{F}_E[...] \end{pmatrix}\,. \tag{F.18}$$

Here we used

$$\overline{\overline{n}} = \begin{pmatrix} \vdots \\ n_{ij} \\ \vdots \end{pmatrix}, \qquad \overline{\overline{n}}_I = \begin{pmatrix} \vdots \\ n_{I,ij} \\ \vdots \end{pmatrix}, \qquad \overline{\overline{n}}_E = \begin{pmatrix} \vdots \\ n_{E,ij} \\ \vdots \end{pmatrix}\,. \tag{F.19}$$

Here n_{ij}, $n_{I,ij}$ and $n_{E,ij}$ label the densities on every grid point. We note that we evaluate the function f from Eq. (F.2) explicitly at the current time step. The matrices $\mathbf{M}_i$ operating in the space of grid points are proportional to the scattering times τ_i from Sec. 5.4. They represent the standard discrete version of the Laplace operators on the lattice [131]. Furthermore F_{dens} denotes the right-hand site of the continuity equations on the staggered grid as shown in Eq. (F.13) for the particle density. All the linear gradients due to dissipative terms are discretized in the standard manner and added to the right-hand site of Eq. (F.18).